Study of Future On-board GNSS/INS Hybridization Architectures

Jérémy Vezinet

THÈSE

En vue de l'obtention du

DOCTORAT DE L'UNIVERSITÉ DE TOULOUSE

Délivré par : *l'Institut National Polytechnique de Toulouse (INP Toulouse)*

Présentée et soutenue le *18 décembre 2014* **par :**

Jérémy VEZINET

Study of Future On-board GNSS/INS Hybridization Architectures

---

JURY

Thierry Chonavel	Professeur	Président de jury
Maarten Uijt de Haag	Professeur	Rapporteur
Naser El-Sheimy	Professeur	Rapporteur
Christophe Macabiau	Docteur	Directeur de thèse
Anne-Christine Escher	Docteur	Co-Directeur de thèse
Alain Guillet	Ingénieur	Encadrant

École doctorale et spécialité :
MITT : Domaine SIAO : Signal, Image, Acoustique et Optimisation

Unité de Recherche :
Ecole Nationale de l'Aviation Civile - Laboratoire TELECOM/SIGNAV

Directeur de Thèse :
Christophe MACABIAU

Abstract

The quick development of air traffic has led to the improvement of approach and landing operations by using flexible flight paths and by decreasing the minima required to perform these operations. The direct consequence is that the aircraft navigation systems, which compute and provide navigation parameters such as 3D position, 3D velocity, attitude angles and heading, are more and more constrained in terms of accuracy, integrity, availability and continuity performance requirements.

Nowadays, most of the aircraft operations are supported by the Global Navigation Satellite System (GNSS) augmented with Ground Based Augmentation System (GBAS), Satellite Based Augmentation Systems (SBAS) or Aircraft Based Augmentation System (ABAS). SBAS and GBAS allow supporting navigation operations down to Precision Approaches. However, these augmentations do require an expensive network of reference receivers and real-time broadcast to the airborne user. To overcome, the ABAS system integrates on-board information that can be provided by an Inertial Navigation System (INS) to enhance the navigation performance. Inertial navigation being based on dead-reckoning principle small errors affecting the accelerations and angular rotation rates measurements can cause non-negligible integration drift and induce a horizontal position error of more than 1 Nm after 1 hour of navigation.

In the perspective of the ABAS system, INS is coupled on board with a GPS receiver (L1 C/A code pseudorange measurements) through a GPS/baro-INS hybridization solution, already performed on current commercial aircraft. This solution allows reaching better performance in terms of accuracy, integrity, availability and continuity than the two separated solutions. The basic principle of such a hybridization is that the GPS measurements are used to estimate and correct the inertial drift. Hybridization compensates GPS and INS drawbacks (unavailability for GPS and drifting errors for INS), allowing navigation from oceanic en-route operations down to non-precision approaches for long range aircraft. The hybridized solution also allows coasting when GPS is unavailable for a limited period of time and can improve integrity monitoring of GPS data. Moreover, on most of the commercial aircraft, the Air Data Inertial Reference Unit provides air data parameters such as Barometric Altitude and Vertical Speed. Indeed, the hybridization architecture integrates the barometric altitude measurement within a baro-inertial loop and estimates the altitude and the vertical velocity.

However the most stringent requirements for precision approaches or automatic landings cannot be fulfilled with the current GPS/baro-INS hybridization schemes. The main idea in the framework of this Ph.D. study is then to extend the hybridization process by including other sensors or other information sources already available on commercial aircraft or not and, to assess the performance reached by this global hybridization architecture. More precisely, the objective is to propose a system that will be able to fuse the multiple sources of information or measurements in a global architecture. Thus, it aims

at providing most of the navigation parameters (3D position, 3D velocity, attitude and heading) in all conditions and operations with the required level of performance in terms of accuracy, integrity, availability and continuity. The integration of multiple sources of on-board measurements allows improving the performances of the navigation solution by gathering the advantages of each source while adding redundancy. The operations targeted by this hybridization are the ones requiring very stringent performances, as precision approaches, with a particular focus on CAT III precision approach and roll out on the runway. In that way, the Ph.D. thesis proposes a hybridized solution integrating several sensors in a global filter, which estimates several navigation parameters.

The Ph.D. thesis particularly focused on the study of vision sensors. Indeed, as an alternative navigation mean, more and more considered in navigation applications, video-based navigation is a complete autonomous navigation opportunity because it is only based on sensors that provide information from the dynamic of the vehicle and from the observation of the scenery. From a possible compensation of any loss or degradation of a navigation system to the improvement of the navigation solution during the most critical operations, the interests of video are numerous. In addition to the study on video, the thesis addresses several issues on navigation for civil aviation including standardized requirements, navigation means and hybridization algorithms.

The dissertation begins with the introduction of the definition and identification of navigation requirements in the context of civil aviation. The standardized requirements are presented and the requirements that we focused during our study are reminded.

Then the presentation of the current GNSS/INS on-board hybridization is done in the third chapter. This chapter deals with the presentation of the two systems (GNSS and INS) and describes briefly the main interest of a coupled solution. A description of the existing configuration is done with a comparison of the corresponding properties. Finally, a proposition of a set of new sensors or systems that can provide interest in being integrated is given.

The fourth chapter is a detailed study on video-based navigation. This chapter presents the results of a state of the art on video based navigation methods done during the Ph.D. thesis. A general description of the video sensors is also provided. Finally the preliminary results of a study focusing on detecting specific features in a given image are given.

The fifth chapter deals with the detailed description of the proposed solution. This solution is an Extended Kalman Filter that integrates GNSS, INS, barometer, Wheel Speed Sensors and a Video system.

The sixth chapter is the presentation of the different results obtained with the proposed solution. Several configurations of the filter are proposed and the results are compared with the focused requirements.

Finally, the last chapter concludes on the works done during the Ph.D. and put the stress on some perspective that could be considered or future works that could be conducted.

Résumé

Un développement rapide et une densification du trafic aérien ont conduit à l'introduction de nouvelles opérations d'approches et d'atterrissage utilisant des trajectoires plus flexibles et des minimas plus exigeants. La conséquence directe est que les systèmes de navigations, qui calculent et fournissent les paramètres de navigation tels que la position et vitesse 3D, les angles d'attitude et le cap, sont de plus en plus se doivent d'être de plus en plus exigeants en termes d'exigences de performances de précision, intégrité, disponibilité et continuité.

La plupart des opérations de navigation aérienne sont actuellement réalisées grâce au GNSS, augmenté par les systèmes GBAS, SBAS ou ABAS qui permettent d'atteindre des opérations jusqu'aux d'approches de précision. Cependant ces systèmes nécessitent la mise en place d'un réseau de station de référence relativement couteux et des diffusions constantes de messages aux utilisateurs de l'espace aérien. Afin de surmonter ces contraintes, le système ABAS intègre à bord des informations fournies par les systèmes de navigation inertielle (INS) ainsi améliorant les performances de navigation. La navigation inertielle étant basé sur le principe de la navigation à l'estime, de faibles erreurs entachant les mesures d'accélérations et de vitesses angulaires de rotation du véhicule peuvent engendrer des dérives dues à l'intégration non négligeables et induire une erreur d'estimation de la position horizontale allant jusqu'à 1 Nm après 1 heure de navigation.

Dans la perspective du système ABAS, l'INS est couplé avec un récepteur GPS (les mesures de pseudodistance de code L1 C/A) en une solution d'hybridation GPS/baro-INS déjà utilisée à bord. Cette solution permet d'atteindre des niveaux de performance en termes de précision, intégrité, disponibilité et continuité supérieurs aux deux systèmes pris séparément. Le principe de base de l'hybridation est que les mesures GPS sont utilisées afin d'estimer puis de corriger la dérive des systèmes inertiels. L'hybridation compense les désavantages du GPS et de l'inertie (principalement la disponibilité pour le GPS et les dérives d'erreur pour l'inertie), tout en permettant de réaliser des opérations de navigation océaniques en-route jusqu'aux approches de non précision pour les avions long-courriers. La solution d'hybridation peut également fonctionner en « coasting », qui permet de fournir une solution de navigation exploitable pendant une durée limitée lors d'une perte du signal GPS. L'hybridation peut également améliorer le contrôle d'intégrité des données GPS. De plus, sur la plupart des avions commerciaux, un ADIRU fournit des paramètres « air » tel que l'altitude barométrique et la vitesse verticale. Dans cette configuration, l'architecture d'hybridation intègre la mesure de baro-altitude au sein d'une boucle baro-inertielle et estime ainsi l'altitude et la vitesse verticale.

Malheureusement, les niveaux d'exigences requis par les opérations de précision ou les atterrissages automatiques ne peuvent pas encore être totalement couverts par les solutions d'hybridation actuelles. L'idée principale de cette thèse a été d'étendre le processus d'hybridation en incluant d'autres capteurs ou systèmes actuellement

disponibles ou non à bord and d'analyser les niveaux de performance atteints par cette solution de filtre d'hybridation global.

Plus précisément, l'objectif est de proposer une architecture capable de fusionner les multiples sources de mesures dans un filtre global. L'objectif ciblé est de pouvoir fournir la plupart des paramètres de navigation (position et vitesse 3D, attitude et cap) en toute conditions et pour les opérations les plus critiques avec le niveau de performance requis par les exigences OACI. L'intégration de différentes sources d'informations à bord permet d'améliorer les performances de la solution de navigation en cumulant les avantages de chacune des sources tout en ajoutant une redondance sur les potentiels systèmes de navigation. Les opérations ciblées pendant l'étude étaient les approches de précision (en particulier les approches CAT III) et le roulage sur la piste. La thèse propose ainsi une solution d'hybridation multi-capteurs qui fournit une estimation de plusieurs paramètres de navigation.

L'étude des systèmes vidéo a fait l'objet d'une attention particulière pendant la thèse. La navigation basée sur la vidéo est une solution autonome de navigation de plus en plus utilisée de nos jours axée sur des capteurs qui mesurent le mouvement du véhicule et observent l'environnement. Que cela soit pour compenser la perte ou la dégradation d'un des systèmes de navigation ou pour améliorer la solution existante, les intérêts de l'utilisation de la vidéo sont nombreux. En plus de l'étude sur la vidéo la thèse développe certaines notions sur la navigation en aviation civile telles les exigences standardisées, les moyens de navigations et les algorithmes d'hybridation.

Ce mémoire de thèse débute en introduisant les définitions et en identifiant les exigences de navigation officielles en aviation civile. Les exigences standardisées sont présentés et les exigences sur lesquelles nous sommes focalisés pendant l'étude sont rappelées.

Ensuite la présentation des hybridations GPS/INS embarquées actuelles est faite dans le chapitre 3. Ce chapitre introduit les deux systèmes majeurs de navigations (le GNSS et l'INS) et décrit brièvement les intérêts d'une solution de couplage entre ces deux systèmes. Finalement la description des configurations existantes est réalisée avec une comparaison des propriétés de chaque solution. Finalement, de nouveaux systèmes ou capteurs qui pourraient être couplés avec la solution existante et apporter une amélioration significative à la solution sont proposés.

Le quatrième chapitre est une étude détaillée de la navigation basée sur la vidéo. Ce chapitre présente les résultats d'un état de l'art sur ces techniques réalisé pendant la thèse. Une description générale des capteurs vidéo est apportée. Finalement, les résultats préliminaires d'une étude sur un algorithme de traitement d'image visant à détecter des points d'intérêt sont donnés.

Le cinquième chapitre est une description détaillée de la solution proposée. Cette solution est un filtre de Kalman étendu qui intègre un récepteur GNSS, une INS, un baromètre, des WSS et un système vidéo.

Le sixième chapitre synthétise les divers résultats obtenus avec la solution proposée. Plusieurs configurations du filtre sont analysées et les résultats sont comparés avec les exigences correspondantes.

Finalement, le dernier chapitre conclut sur le travail réalisé durant la thèse et met l'accent sur les perspectives qui pourraient être envisagées et les travaux futurs qui pourraient être entrepris.

Remerciements

Mes premiers mots de remerciements sont tout d'abord pour Christophe Macabiau qui a eu l'idée de me proposer cette thèse il y a maintenant 4 ans, a été mon directeur de thèse et a toujours pris le temps de répondre à mes (nombreuses…) questions et corriger mes rapports, articles ou chapitres. Je remercie également Anne-Christine Escher, ma co-directrice de thèse et encadrante qui m'a beaucoup aidé pendant ces 3 (presque 4) années. Enfin je remercie Alain Guillet mon encadrant à Airbus pour ses conseils et son investissement.

I gratefully acknowledge Professor Maarten Uijt de Haag and Professor Naser El-Sheimy for reviewing my PhD thesis, providing me some useful remarks and comments and participating as a member of the jury during my PhD defence. Je remercie le professeur Thierry Chonavel pour avoir accepté la présidence de mon jury de thèse.

Je remercie par ailleurs Airbus et l'ENAC pour avoir financé ces travaux et en particuliers le laboratoire TELECOM de l'ENAC pour l'accueil.

Je remercie particulièrement les personnes du laboratoire TELECOM qui ont pu contribuer tous les jours à la bonne ambiance : Paul, Anais, Olivier, Antoine, Carl, Axel, Remi, Alexandre, Christophe. Un merci aux personnes de l'ENAC qui m'ont aidé ou qui ont su répondre à mes questions : Colette, Cathy et Yves Rouillard pour son aide sur Flight Simulator. Je remercie tous les stagiaires et étudiants ENAC (il y en a eu beaucoup…) qui ont participé de près ou de loin à mes travaux de thèse ou à mes projets pendant la rédaction de mon manuscrit : Grégoire et Anne-Claire, Elodie, Christophe et Christophe (Nassif et Charbo), Adrien et Damien, Thomas et Anne, Antoine et Kevin, Claire, François et Pauline (J'espère que je n'en oublie pas…).

Je remercie toutes les personnes qui ont un jour été mes « co-bureau » : Sébastien et Myriam avant qu'on émigre au rez-de-chaussée avec Leslie, Ludo, Marion, Jimmy, Damien et Kevin, puis J-B, Quentin, Enik qui ont pris la relève, ainsi que Giuseppe, Alizé, Philippe et Amani. Je remercie également Lina et Daniel qui m'ont beaucoup aidé pour toutes mes questions sur le filtrage de Kalman et autres joyeusetés… Je remercie particulièrement Leslie avec qui j'ai partagé mon bureau et quelques travaux pendant toute la thèse. Enfin, un merci à toutes les personnes que j'aurais pu oublier (il doit y en avoir…).

Un petit mot d'encouragement aux futurs docteurs : Ludo, Philippe, Amani, Alizé, Giuseppe, Enik, J-B, Quentin et plus récemment arrivés : Jade, Enzo et Amandine. Courage !

Je finis par remercier ma famille et mes amis qui ont été présents pendant ces années de hauts et de bas et qui m'ont permis de tenir le coup dans les moments compliqués.

Table of Contents

List of Figures

List of Tables

Abbreviations

AAIM	Aircraft Autonomous Integrity Monitoring
ABAS	Aircraft Based Augmentation System
ADIRS	Air Data Inertial Reference System
ADIRU	Air Data Inertial Reference Unit
AHRS	Attitude and Heading Reference System
AL	Alert Limit
AOD	Age of Data
APV	Approach with Vertical Guidance
A-SMGCS	Advanced Surface Movement Guidance and Control Systems
ATM	Air Traffic Management
BTAC	Bus Tie AC Contactor
CAST	Commercial Aviation Safety Team
CCD	Charge-Coupled Device
CICTT	CAST/ICAO Common Taxonomy Team
CMOS	Complementary Metal-Oxyde-Semiconductor
CNS	Communication, Navigation and Surveillance
DEM	Digital Elevation Model
DH	Decision Height
DLC	Direct Lift Control
DLL	Delay Locked Loop
DME	Distance Measuring Equipment
EKF	Extended Kalman Filter
EMLP	Early-Minus Late Power
ESG	Electrostatically Suspended Gyroscope
FAA	Federal Aviation Administration
FANS	Future Air Navigation Systems
FMS	Flight Management System
FOG	Fiber optic gyroscope
FTAC	Fuel Tank Access Cover
FTE	Flight Technical Error
GBAS	Ground Based Augmentation System
GCA	Great Circle Angle
GM	Gauss-Markov
GNSS	Global Navigation Satellite System
GPS	Global Positioning System
HAL	Horizontal Alert Limit
HPL	Horizontal Protection Level
IAF	Initial Approach Fix
ICAO	International Civil Aviation Organization
IFR	Instrument Flight Rules
IKF	Information Kalman Filter
ILS	Instrument Landing System
IMU	Inertial Measurement Unit

INS	Inertial Navigation System
IRS	Inertial Reference System
IR	Integrity Risk
IRS	Inertial Reference System
KF	Kalman Filter
MEMS	Microelectromechanical systems
MLG	Main Landing Gear
NLG	Nose Landing Gear
NPA	Non-Precision Approach
NSE	Navigation System Error
PA	Precision Approach
PDE	Path definition Error
RAIM	Receiver Autonomous Integrity
RLG	Ring laser gyroscope
RMS	Root Mean Square
RNAV	Area Navigation
RTCA	Radio Technical Commission for Aeronautics
RVR	Runway Visual Range
SARPS	Standards And Recommended Practices
SBAS	Satellite Based Augmentation System
SIS	Signal In Space
SISA	Signal In Space Accuracy
SLAM	Simultaneous Localization and Mapping
SP	Strategic Planner
TP	Tactical Planner
TSE	Total System Error
TTA	Time-To-Alert
UAV	Unmanned Aerial Vehicle
UERE	User Equivalent Range Error
UKF	Unscented Kalman Filter
URA	User Range Accuracy
VAL	Vertical Alert Limit
VFR	Visual Flight Rules
VHF	Very High Frequency
VOR	VHF Omnidirectional Range
VPL	Vertical Protection Level
WSS	Wheel Speed Sensor
ZOAD	Zero Age of Data

Notations

This part introduces the notations that are used in the manuscript. If any simplification is done in the following, additional indications will be given at the beginning of the chapter in question.

First, note that the different coordinate frames used in the document are defined in Appendix A.

In the whole document, the Earth reference ellipsoid parameters are as follows:

- a is the equatorial radius: $a = 6378137m$.
- e is the eccentricity: $e = 0.0818$.
- R_M is the radius of curvature along a meridian at a given latitude.

$$R_M = \frac{a \cdot (1-e^2)}{(1-e^2 \cdot \sin^2(\lambda))^{1.5}}$$

- R_N is the transverse radius of curvature.

$$R_N = \frac{a}{(1-e \cdot \sin^2(\lambda))^{0.5}}$$

For any parameter or vector:

- x denotes the *true value*.
- $\tilde{x}$ denotes a *measurement* of x.
- $\hat{x}$ denotes an *estimate* of x.
- For an estimated parameter, we will denote δx the difference between the *true value* of the parameter and the *estimated* one:

$$\delta x = x - \hat{x}$$

- For a measured parameter we will denote δx the difference between the *true value* of the parameter and the *measured* one:

$$\delta x = x - \tilde{x}$$

- X denotes the *state vector* in the system state representation.
- δX denotes the corresponding *error state vector*:

$$\delta X = X - \hat{X}$$

- $\hat{X}_{k|k-1}$ denotes the estimation of X at instant k based on the estimation of X at instant $k-1$, also called *"a-priori"* estimation.

- $\hat{X}_{k|k}$ denotes the estimation of X at instant k, also called *"a-posteriori"* estimation

- R_{a2b} denotes the rotation matrix from the *a-frame* coordinates system to the *b-frame* coordinates system.
- $v^a_{b/c}$ denotes the instantaneous velocity vector of the *b-frame* with respect to the *c-frame* expressed in the *a-frame* coordinates system.
- $\omega^a_{b/c}$ denotes the instantaneous angular rotation vector of the *b-frame* with respect to the *c-frame* expressed in the *a-frame* coordinates system.
- $\Omega^a_{b/c}$ denotes the *skew-symmetric matrix* associated to $\omega^a_{b/c}$. If $\omega^c_{a/b} = \begin{bmatrix} \omega_x \\ \omega_y \\ \omega_z \end{bmatrix}$, it is defined as follows:

$$\Omega^a_{b/c} = \begin{bmatrix} 0 & -\omega_z & \omega_y \\ \omega_z & 0 & -\omega_x \\ -\omega_y & \omega_x & 0 \end{bmatrix}$$

- For any vector v the notation $(v\wedge)$ denotes the associated skew symmetric matrix.
- The coordinates of a vector v expressed in the *n-frame* coordinates system will be denoted with the subscripts as follows: (v_N, v_E, v_D).
- The coordinates of a vector v expressed in the *w-frame* coordinates system will be denoted with the subscripts as follows: (v_x, v_y, v_z).
- The Earth geodetic coordinates of the vehicle - latitude, longitude and altitude, will be designed by the notation $p_{m/e} = (\lambda, \phi, h)$.
- The attitude of the vehicle - roll, pitch, heading angles, will be denoted $\rho_{m/n} = (\varphi, \theta, \psi)$.
- The velocity of the mobile frame with respect to the earth frame also denoted as the Earth relative velocity will be denoted v^a_e (where a is the frame in which the coordinates of the vector are expressed).
    - In the *n-frame*, $v^n_e = \begin{bmatrix} v_N \\ v_E \\ v_D \end{bmatrix}$
    - In the *w-frame*, $v^w_e = \begin{bmatrix} v_x \\ v_y \\ v_z \end{bmatrix}$

Chapter 1 : Introduction

1.1 Thesis Motivations

Civil aviation navigation has been ensured for many years with conventional radionavigation means such as VHF Omnidirectional Range (VOR), Distance Measuring Equipment (DME) or Instrument Landing System (ILS). However their ground dependence and their reduced coverage led to install the Global Navigation Satellite System (GNSS) as a main provider for navigation services. GNSS is a concept from the Future Air Navigation Systems (FANS) committee of the International Civil Aviation Organization (ICAO) [ICAO, 1991]. Indeed, aircraft navigation rules are currently evolving to go along with this change from conventional radionavigation to what is known as Area Navigation (RNAV). This commitment has been established by the ICAO in the early nineties and this agreement is part of the Communication, Navigation and Surveillance/Air Traffic Management (CNS/ATM) concept. Yet, the use of GNSS signals for aircraft navigation is today limited to the GPS L1 C/A signal broadcasted by the US Global Positioning System (GPS).

However, civil aviation navigation requirements are very stringent in terms of accuracy, integrity, availability and continuity so that GPS receivers cannot be used on board as a mean of navigation. Therefore, in order to improve the performances and reach the requirements level, ICAO defined and developed standard augmentation systems: the Ground Based Augmentation System (GBAS), the Satellite Based Augmentation System (SBAS) and the Aircraft Based Augmentation System (ABAS). Each augmentation system has specific characteristics, coverage areas and purpose.

In particular, ABAS is an augmentation system that augments and/or integrates the information obtained from the other GNSS elements with information available on board the aircraft [ICAO, 2006]. It also allows providing on-board integrity monitoring for the positon solution: either using a Receiver Autonomous Integrity Monitoring (RAIM) function, which is based on GNSS measurements redundancy only, or using an Aircraft Autonomous Integrity Monitoring (AAIM) function, which is based on GNSS measurements redundancy and information provided by additional on-board sensors measurements. ABAS may thus provide improvement in terms of accuracy by combining a GNSS receiver and an Inertial Navigation System (INS) within a hybridization architecture, and also, may provide availability and continuity of service improvement allowing inertial coasting performance of navigation when GNSS service is unavailable.

Inertial navigation appears to the historical navigation means used for aircraft navigation. In that way, most of the high-end commercial aircraft possess Inertial Navigation Systems on board. Inertial navigation is based on dead reckoning estimation: inertial sensors measurements are integrated so as to estimate the next positon from the current one. Inertial navigation performance is then strongly dependent on the quality of motion sensors on board (accelerometers and gyroscopes). Indeed, the major drawback of inertial system is the drift caused by successive integrations of measurement errors.

Therefore, standalone inertial navigation cannot be used for long term 3D-navigation (for altitude estimation in fact) because of the natural exponential drift of the estimated vertical position. In that context, on-board INS is coupled with an additional source of altitude measurements (classically a barometer).

GNSS/baro-INS hybridization is then a high performing navigation solution that is justified by the complementarities of the systems. Hybridization creates a system whose performance exceeds that of each system taken independently. On-board today GNSS/baro-INS hybridization process aims at using GNSS measurements for estimating and correcting the inertial drift. Two types of architectures are currently implemented on board: the loose coupling architecture that integrates the GNSS receiver position solution with the INS and the tight coupling architecture that integrates the GNSS code pseudorange measurements with the INS. In terms of performances, these hybridizations allow high-end commercial aircraft navigating oceanic en-route operations down to non-precision approaches.

Nevertheless, the requirements of the most stringent operations such as approaches with vertical guidance (APV) and precision approach operations (PA), cannot be fulfilled with the current GNSS/baro-INS hybridization. Indeed, current standardization of integration of GNSS and baro-inertial information is only done for en route through Non-Precision Approaches (NPA) [ICAO, 2006]. The current integrated systems do not provide a sufficient vertical integrity monitoring for performing approaches beyond NPA [ICAO, 2008]. That issue is clearly one of the main motivations of this Ph.D. work. In addition, the future evolutions of the GNSS systems - use of measurements from GPS L5 frequency and the GALILEO constellation signals - may lead to consider these evolutions as future improvements of the existing solutions. A major possible improvement of current solutions can concern the optimization or the selection of new algorithms, more performing, more robust and more reliable in terms of integrity monitoring. Therefore, a potential improvement of current hybridization architectures goes mainly through the introduction of new technologies, new sensors, or new systems so as to extend the current GNSS/INS hybridization to all the measurement sources available on board. Thus, a part of the study conducted was focused on some sensors that are currently available on board but are not yet integrated in the hybridization architecture: radio-altimeters, Wheel Speed Sensors (for airport operations), redundant systems (fuse several receivers or INS) or backup inertial instruments. In addition to that, the study was focused on systems or sensors that are not present on board or are not currently used for navigation purpose. In that Ph.D. thesis, a detailed study has been conducted on how to integrate video sensor information in the hybridized solution.

Integration of Video technology within the current hybridization solutions is mainly driven by the fact that video sensors are nowadays used in a lot of navigation applications – such as robotic applications, indoor navigation, Unmanned Aerial Vehicles (UAV) navigation, localization and mapping…. Basic principle of visual navigation is defined by a simple fact: the observation of the world and objects around us is the most reliable information for deducing our relative position with respect to our environment. Cameras

are currently available on board on some aircraft and they are mainly used for pilot assistance during ground navigation operations or for passenger entertainment during the flights. However, the observation of the surrounding scenery can be seen as a source of information for navigation purpose. But a correct transcription of the details in the landscape can only be done taking into consideration physical limitations and characteristics of the video sensor: its resolution, its field of view (or aperture), its dimensions and its position.

As said, a wide range of navigation information can be drawn from video sensors measurements. Optical flow measurements can be used for position, velocity and orientation estimation such as proposed in [Cheng et al., 2013], [DeSouza and Kak, 2002] or [Hagen and Heyerdahl, 1992]. The use of a stereovision system (a couple of camera with a known baseline) allows providing range estimations such as in [Sabater, 2009] or [Urmson et al., 2002]. Line following algorithms can be used for optimization of the ground operations. Several applications can be found in [Bibuli et al., 2008], [Konaka et al., 2001] or [Silveira et al., 2003]. Targets of known location around the navigation area can be used for relative positioning as in [Cesetti et al., 2010] or [Jia et al., 2008].

Hence, video offers a lot of possibilities promising for aircraft navigation in approach operations, that is why an objective of the thesis work was to propose a solution for integrating video in a future hybridization architecture.

The objectives of the Ph.D. work are detailed in the next section.

1.2 Thesis Objectives

The global objective of this Ph.D. is to study the possible integration of multiple sensors within a global hybridization architecture on board that can be used for aircraft navigation, for all the phase of flight.

In that way, this overall objective has been divided in the following sub-objectives:

1. The review of the current hybridization architectures on board. This objectives includes:
    - The review of GNSS, INS and their hybridization.
    - The review of existing coupling architectures and hybridization filters.
2. The study of sensors or systems that can provide an improvement for the navigation by being included in a hybridization architecture. This objective includes:
    - The study of on-board sensors that are not currently integrated.
    - The study of sensors that are not available on board.

3. The selection of sensors that will be integrated in the future solution. The description of the measurement model and the development of a simulator for each considered sensor have been done.
4. The development of a global hybridization architecture that will integrate the considered sensors.
5. The assessment of the performances reached with that architecture.

1.3 Thesis Contributions

The major contributions of the thesis are listed as follows:

A detailed inertial measurement model (specific force and gyrometer) has been studied and developed in an IMU measurements simulator, as well as a basic baro-altimeter measurements simulator. Then, a strapdown INS platform mechanization coupled with a third order baro-inertial loop has been implemented. All those simulation tools were used to generate inertial data with different sensors classes' assumptions. The entire INS simulator (including the generation of IMU measurements) has been validated regarding the expected drift, the Schuler oscillations, and the global performances.

A WSS measurement model has been studied and implemented in a WSS simulator. The simulation of WSS measurements takes into account the variation of the radius of the wheels in function of the velocity that has been obtained with a linear regression from real data.

A GNSS code pseudorange model has been studied and implemented in a GNSS receiver simulator. The simulator allows generating GPS and GALILEO single or dual frequency code pseudorange measurements.

A state of the art on video based navigation methods has been done during the thesis work. This state of the art has leaded to the proposition of a classification of video methods for navigation, to the identification of some key-elements for navigation with video-aid and, to the development of a solution for integration of video measurements within a hybridization architecture existing on board, for aircraft navigation during approach and landing operations.

A Video measurement model has been proposed and implemented. The Video system simulator models the pixels coordinates and optical angular measurements provided by a camera for a given target of known location. The image processing algorithm that aims at detecting targets in an image has not been assessed in the thesis but an initial feasibility study has been conducted and some results are presented in the Ph.D. thesis manuscript.

An Extended Kalman Filter architecture has been implemented. In that context, a detailed wander azimuth inertial mechanization has been developed. The observation functions for integration of GNSS code pseudorange measurements, WSS measurements and Video measurements have also been developed. Finally, the architecture allows integrating all possible combinations of the considered measurements.

Two papers have been published. The first one [Vezinet et al., 2013], in the proceedings of the 2013 ION/ITM conference, presents a video-based navigation state of the art. The second [Vezinet et al., 2014], in the proceedings of the 2014 IEEE/ION PLANS conference, presents a first description of the integration of the video measurements within a Extended Kalman Filter architecture.

Finally, the performances of several combinations of sensors have been assessed. A comparison study has been provided and a conclusion on this Ph.D. thesis is done at the end of the document.

1.4 Thesis Outline

In order to constitute the most complete synthesis of the work done during this Ph.D. thesis, the document is organized as follows:

Chapter 2 introduces the main definitions and identifies the civil aviation requirements established by the ICAO. For that, the main phases of flights and their standard definitions are reminded. Then the navigation system requirements are presented with the definition of the requirements criteria and the GNSS Signal-In-Space performance requirements. Finally, the requirements used in the framework of our study are described and an extension for parameters other than position is proposed.

Chapter 3 deals with the presentation of the current on-board GNSS/baro-INS hybridization. The chapter starts with an overview of these two navigation means used for commercial aircraft navigation, which are the GNSS and the INS. Then, the properties and characteristics of the hybridized architectures are provided with a focus on the solution currently implemented on board. Finally, the chapter initiates the discussion by introducing new sensors or systems that can be considered for their integration in future global hybridization architecture. A brief and synthetic analysis of the interest for each sensor is proposed.

Chapter 4 synthesizes a large study done during the Ph.D. on video-based navigation methods and the potential integration of a video system within a hybridization architecture. The chapter starts with an overview of video-based navigation methods done during a state of the art study. The synthesis of the state of the art leads to the establishment of a classification the navigation methods using video. Then, a description of the video sensor is provided and a measurement model is introduced. In a third part, the first results of a study assessing the feasibility of using the video system in the particular

context of commercial aircraft navigation during approach and landing is proposed. This chapter is one of the most innovative aspects of the study.

Chapter 5 describes in details the implemented hybridization solution. The chapter starts with a general description of the characteristics of the proposed solution and the details of the theoretical models of our solution. Then, the description of the error state vector and the state system equations is provided. The chapter also presents the observation models for the sensors and the systems considered in the study. The detailed equations are demonstrated in the Appendices.

Chapter 6 presents the different simulation results obtained with the implemented solution, and concludes on the performances obtained. The chapter first reminds the global architecture detailed in the previous chapter and describes the main hypothesis for the simulation tests. In the last part, the results with the different combination and simulations are commented and compared to the intended accuracy performances required for estimation of the position, altitude, velocity and heading parameters.

Finally, **Chapter 7** synthetizes the main results of this Ph.D., concludes on the works done and proposes perspectives and recommendations than could be addressed in the future.

Chapter 2 : Requirements Definition and Identification

The International Civil Aviation Organization (ICAO), a United Nations agency, is a global authority aiming at regulating principle and techniques of international air navigation. In that way, ICAO adopts Standards And Recommended Practices (SARPs) concerning air navigation. Global Navigation Satellite System (GNSS) can be used as a navigation aids provided that it supports requirements established by the different standardization bodies. In particular, ICAO defines in the Volume 1 of Annex 10 of the Convention on international Civil Aviation [ICAO, 2006] the standards and the Signal-In-Space (SIS) navigation performance requirements for radio navigation aids.

The main objective of the chapter is to remind the definitions and identify requirements for all phases of flight.

In that way, the first part reminds the definition of the phases of flight according to the ICAO.

The second part defines the performance requirement criteria for the Navigation System requirements. It also reminds the GNSS SIS performance requirements.

Finally, as an extension to other navigation parameters, we propose a table of expected level of performance of on-board systems.

2.1 Phases of Flight

The International Civil Aviation Organization (ICAO) and the Commercial Aviation Safety Team (CAST), which includes Government officials and aviation industry leaders, have jointly chartered the CAST/ICAO Common Taxonomy Team (CICTT). A document of the CICTT defines the different phases of flight [ICAO, 2010].

We can retain 8 major phases of flight. 6 of them are illustrated in Figure 1 with some specified navigation performances associated with each phase. We can see for example that the "Climb" phase starts at the altitude of 400ft.

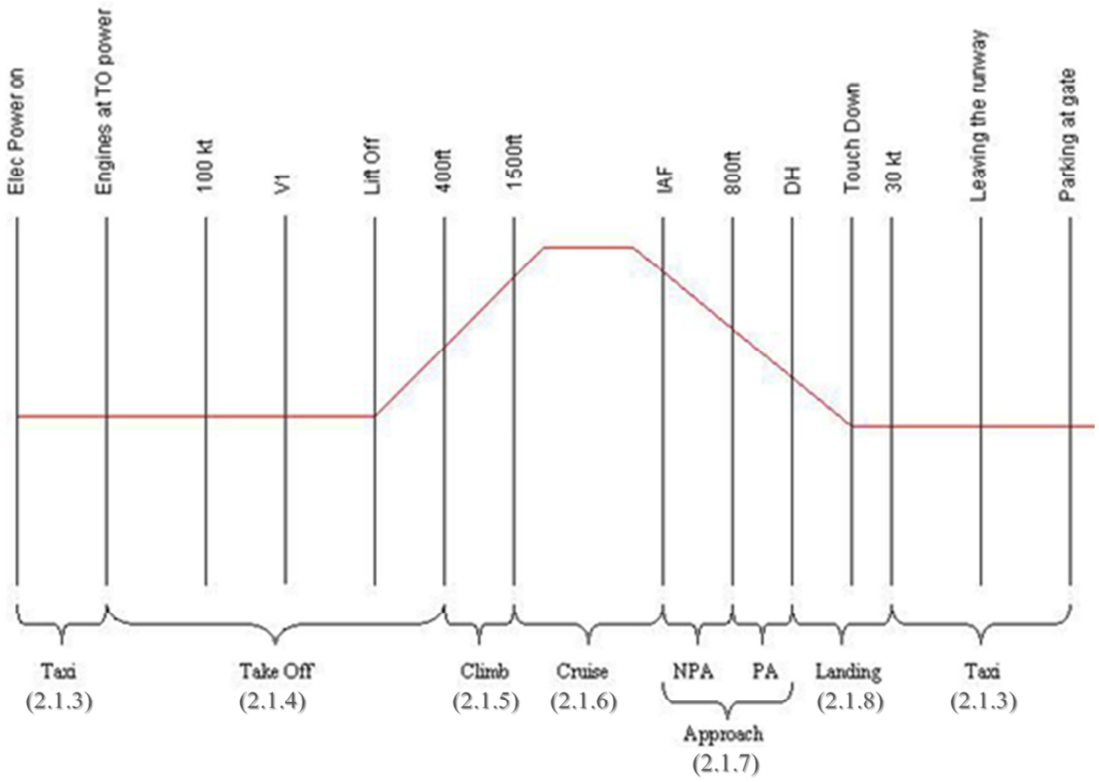

Figure 1 – Flight phases definition [AIRBUS, 2009]

The illustration also provides numbers corresponding to the following sections that provide definitions of those 8 phases of flight.

2.1.1 Standing

Standing phase corresponds to the following operation: "prior to pushback or taxi, or after arrival, at the gate, ramp, or parking area, while the aircraft is stationary".

2.1.2 Pushback/Towing

Pushback (or Towing) corresponds to the following operation: “aircraft is moving in the gate, ramp, or parking area, assisted by a tow vehicle”.

2.1.3 Taxi

Taxi corresponds to the following operation: “the aircraft is moving on the aerodrome surface under its own power prior to takeoff or after landing”.

2.1.4 Takeoff

Takeoff corresponds to the following operation: “from the application of takeoff power, through rotation and to an altitude of 35 feet above runway elevation”.

2.1.5 Initial climb

Initial climb corresponds to the following operation: “from the end of the takeoff sub-phase to the first prescribed power reduction, or until reaching 1000 feet above runway elevation or the Visual Flight Rules (VFR) pattern, whichever comes first”.

2.1.6 Cruise or En route

The definition of this phase depends on the flight rules:

- Instrument Flight Rules (IFR): from completion of departure through cruise altitude and completion of controlled descent to the initial approach fix.
- Visual Flight Rules (VFR): from completion of departure through cruise and controlled descent to the VFR pattern altitude or 1000 feet above runway elevation, whichever comes first.

And generally, the en-route phase includes the following sub-phases:

- Climb to Cruise:
    - IFR: “from completion of Initial Climb to arrival at initial assigned cruise altitude”,
    - VFR: “from completion of Initial Climb to initial cruise altitude”.
- Cruise: “any level flight segment after arrival at initial cruise altitude until the start of descent to the destination”.
- Descent (or arrival):
    - IFR: “descent from cruise to either initial approach fix or VFR pattern entry”,

  - VFR: “descent from cruise to the VFR pattern entry or 1000 feet above the runway elevation, whichever comes first”.

– Holding: “execution of a predetermined maneuver, which keeps the aircraft within a specified airspace while awaiting further clearance. Descent during holding is also covered in this sub-phase”.

Descent and holding phases correspond to terminal area operations. Terminal area operations are characterized by moderate to high traffic densities, converging routes, and transitions in flight altitudes.

2.1.7 Approach

The definition of this phase depends on the flight rules:

– Instrument Flight Rules (IFR): From the Initial Approach Fix (IAF) to the beginning of the landing flare.
– Visual Flight Rules (VFR): From the point of VFR pattern entry, or 1000 feet above the runway elevation, to the beginning of the landing flare.

ICAO presents in the Annex 6 of the ICAO Convention [ICAO, 2010] three classes of approaches and landing operations.

2.1.7.1 Non precision Approach

Non precision approach is a standard instrument approach and landing, which utilizes lateral guidance but does not meet the requirements established for precision approach and landing operations.

2.1.7.2 Approach operations with vertical guidance: APV

This kind of approach is an instrument approach and landing, which utilizes lateral and vertical guidance but does not meet the requirements established for precision approach and landing operation.

We can define actually two main classes of APV approaches depending on the type of vertical guidance used. The first one is APV BaroVNAV: it uses GNSS for lateral guidance and barometric measurements for vertical guidance.

Since barometric guidance has many limitations, there is a second class of precision approach with vertical guidance, which describes the use of GNSS vertical guidance instead of barometric vertical guidance: APV I and APV II. Actually GPS augmented with SBAS supports APV I&II performance level and in the future Galileo should be able to support it.

2.1.7.3 Precision approach

A precision approach is a standard instrument approach and landing, which utilizes lateral and vertical guidance (a glideslope/glide path is provided for the vertical guidance).

There are three types of precision approaches (CAT I, CAT II, CAT III), which are specified by a Decision Height and two visual requirements, distance of visibility and Runway Visual Range. The official definition of these parameters appears in the DO 245A of the Radio Technical Commission for Aeronautics [ICAO, 2004], the Annex 2 of the ICAO Convention [ICAO, 2005] and the Federal Meteorological Handbook No. 1 [OFCM, 2005]

Decision Height *(DH): A specified altitude or height in the precision approach at which a missed approach must be initiated if the required visual reference to continue the approach has not been established. DH is referenced to the threshold elevation* [ICAO, 2004].

Distance of Visibility *is the greatest distance, determined by atmospheric conditions and expressed in units of length, at which it is possible with the unaided eye to see and identify, in daylight a prominent dark object, and at night a remarkable light source* [ICAO, 2005].

Runway Visual Range *(RVR) is the maximum distance at which the runway, or the specified lights or markers delineating it, can be seen from a position above a specified point on its center line. This value is normally determined by visibility sensors located alongside and higher than the center line of the runway. RVR is calculated from visibility, ambient light level, and runway light intensity* [OFCM, 2005].

These categories of precision approaches are defined as following [ICAO, 2006]:

- **Category I**: A precision instrument approach and landing with a decision height not lower than 60m (200 ft) and with either a visibility not less than 800m (2400 ft), or a runway visual range not less than 550m (1800 ft).
- **Category II**: A precision instrument approach and landing with a decision height lower than 200 feet (61 m) above touchdown zone elevation but not lower than 100 feet (30 m), and a runway visual range not less than 350 meters (1148 ft).
- **Category III**: This category is subdivided in three categories:
    - Category III A - A precision instrument approach and landing with:
      a) a decision height lower than 100 feet (30 m) above touchdown zone elevation, or no decision height; and
      b) a runway visual range not less than 200 meters (656 ft).
    - Category III B - A precision instrument approach and landing with:
      a) a decision height lower than 50 feet (15 m) above touchdown zone elevation, or no decision height; and

b) a runway visual range less than 200 meters (656 ft) but not less than 75 meters (246 ft).

- Category III C - A precision instrument approach and landing with no decision height and no runway visual range limitations. A Category III C system is capable of using an aircraft's autopilot to land the aircraft and can also provide guidance along the runway surface.

Table 1 summarizes classification of precision approaches according to decision height and visual requirements.

Operation		Decision Height	Visual Requirement
CAT I		DH ≥ 60 m (200 ft)	Visibility ≥ 800 m RVR ≥ 550 m
CAT II		(100 ft) 30 m ≤ DH ≤ 60 m	RVR ≥ 300 m
CAT III	A	0 m ≤ DH ≤ 30m	RVR ≥ 175 m
	B	0 m ≤ DH ≤ 15 m	50 m ≤ RVR ≤ 175 m
	C	DH = 0 m	RVR = 0 m

Table 1 – Decision heights and Visual requirements [ICAO, 2010]

2.1.8 Landing

This phase starts from the beginning of the landing flare until aircraft exits the landing runway, comes to a stop on the runway, or when power is applied for takeoff in the case of a touch-and-go landing. The sub-phase from the contact of the wheels on the runway to exit to the taxiway is called the Roll-out.

2.2 Navigation System Requirements

The concept of Area Navigation (RNAV) is a method of navigation, which permits aircraft operation on any desired flight path within the coverage of station-referenced navigation aids or within the limits of the capability of self-contained navigation aids, or a combination of these [ICAO, 2003].

Within this concept, ICAO defines Required Navigation Performance (RNP) as statement of the navigation performance necessary for a given operation. In that way, the navigation performance requirements for RNAV operations are defined in terms of accuracy, integrity, availability and continuity, specified for the Total System Error (TSE), illustrated in Figure 2.

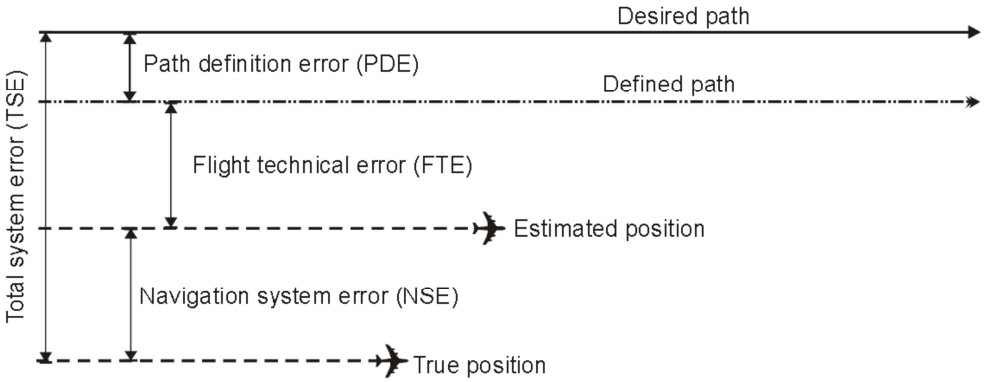

Figure 2 – Total System Error [ICAO, 2008]

The TSE is the difference between the true position and the desired position. It is equal to the sum of the following terms:

The Path Definition Error (PDE), which is the difference between the desired path (the path that the crew and air traffic control can expect the aircraft to fly) and the path defined by the Flight Management System (FMS).

The Flight Technical Error (FTE), which is the difference between the estimated position of the aircraft and the path defined by the FMS.

The Navigation System Error (NSE), which is the: difference between the estimated position and the true position of the aircraft.

The total system performance requirements on TSE are allocated in requirements expressed in terms of PDE, FTE and NSE. These navigation performance requirements are also defined by four criteria that are the accuracy, integrity, availability and continuity.

2.2.1 Performance Requirements Criteria

Operational requirements for each phase of flights are specified in terms of Accuracy, Integrity, Availability and Continuity. The following definitions are official definitions collected from [ICAO, 1991], [ICAO, 2006] and [ICAO, 2006].

2.2.1.1 Accuracy

Accuracy is the degree of conformance between the estimated or measured position and/or velocity of a platform at a given time and its true position and/or velocity [ICAO, 1991].

In order to characterize the accuracy on the estimated quantity, ICAO has defined a 95%-confidence level. It means that for any estimated position at a specific location, the probability that the position error is within the former requirement should be at least 95%.

2.2.1.2 Availability

Availability is the ability of the navigation system to provide the required function and performance at the initiation of the intended operation [ICAO, 2006]. It is expressed as a percentage of time.

2.2.1.3 Continuity

Continuity of service of a system is the capability of the system to perform its function without unscheduled interruptions during the intended operation [ICAO, 2006].

2.2.1.4 Integrity

Integrity is a measure of the trust that can be placed in the correctness of the information supplied by the total system. Integrity includes the ability of a system to provide timely and valid warnings to the user (alerts) when the system must not be used for the intended operation (or phase of flight) [ICAO, 2006].

ICAO and RTCA define the Integrity criteria for GNSS through three parameters:

- The time to alert
- The alert limit
- The integrity risk

2.2.1.4.1 Time to alert (TTA)

Time to alert is the maximum allowable elapsed time from the onset of a positioning failure until the equipment annunciates the alert [ICAO, 2006]. If the equipment is aware of the navigation mode/alert limit, a positioning failure is defined to occur whenever the difference between the true position and the indicated position exceeds the applicable alert limit (HAL or VAL). If the equipment is not aware of the navigation mode/alert limit, a positioning failure is defined to occur whenever the difference between the true position and the indicated position exceeds the applicable protection level (HPL or VPL) [ICAO, 2004].

2.2.1.4.2 Alert limits (AL)

To ensure that the position error is acceptable, an alert limit is defined that represents the largest position error allowable for a safe operation. The position error cannot exceed this alert limit without annunciation [ICAO, 2006].

- **The Horizontal Alert Limit (HAL)** is the radius of a circle in the horizontal plane (the local plane tangent to the WGS-84 ellipsoid), with its center being at the true position, that describes the region that is required to contain the indicated

horizontal position with the required probability for a particular navigation mode [ICAO, 2006]

- **The Vertical Alert Limit (VAL)** is half the length of a segment on the vertical axis (perpendicular to the horizontal plane of WGS-84 ellipsoid), with its center being at the true position, that describes the region that is required to contain the indicated vertical position with the required probability for a particular navigation mode [ICAO, 2006]

2.2.1.4.3 Integrity Risk (IR)

Integrity risk is the probability of an undetectable (latent) failure of the specified accuracy [ICAO, 2006].

2.2.2 GNSS Signal in Space Performance Requirements

The navigation system performance requirements are the part of the total system performance requirements allocated to the navigation system and are expressed in terms of NSE. GNSS is the primary navigation system used to support defined and standardized operations. The NSE requirements allocation is then divided in two components which are: the airborne radio-navigation receiver performance requirements, defined by the RTCA and the EUROCAE for GPS and GALILEO airborne receivers respectively; and the other GNSS elements (constellation, ground system and augmentations) performance requirements. Thus, ICAO SARPS in Volume 1 of ICAO Annex 10 defines the Signal in Space (SIS) navigation performance requirements for radio-navigation aids.

The SIS is the aggregate of guidance signals arriving at the antenna of an aircraft. The concept of a fault-free user receiver is applied only as a means of defining the performance of combinations of different GNSS elements. The fault-free receiver is assumed to be a receiver with nominal accuracy and time-to-alert performance. Such a receiver is assumed to have no failures that affect the integrity, availability and continuity performance. Table 2 and Table 3 present the SIS requirement.

Typical Operation	Accuracy		Integrity		Continuity	Availability
	Horizontal 95%	Vertical 95%	IR	TTA		
En-route	3.7 km (2.0 NM)	N/A	$1–1\times10^{-7}$/h	5 min	$1–1\times10^{-4}$/h to $1–1\times10^{-8}$/h	0.99 to 0.99999
En-route, Terminal	0.74 km (0.4 NM)	N/A	$1–1\times10^{-7}$/h	15 s	$1–1\times10^{-4}$/h to $1–1\times10^{-8}$/h	0.99 to 0.99999
Initial approach, Intermediate approach, NPA, Departure	220 m (720 ft)	N/A	$1–1\times10^{-7}$/h	10 s	$1–1\times10^{-4}$/h to $1–1\times10^{-8}$/h	0.99 to 0.99999
APV I	16 m (52 ft)	20 m (66 ft)	$1–2\times10^{-7}$ per approach	10 s	$1–8\times10^{-6}$/h in any 15 s	0.99 to 0.99999
APV II	16 m (52 ft)	8 m (26 ft)	$1–2\times10^{-7}$ per approach	6 s	$1–8\times10^{-6}$/h in any 15 s	0.99 to 0.99999
CAT I	16 m (52 ft)	4 m to 6m (20 ft to 13ft)	$1–2\times10^{-7}$ per approach	6 s	$1–8\times10^{-6}$/h in any 15 s	0.99 to 0.99999

Table 2 – SIS performance requirements [ICAO, 2006]

Typical Operation	Horizontal Alert limit	Vertical Alert limit
En-route (Oceanic/continental low density)	7.4 km	N/A
En-route (continental)	3.7 km	N/A
En-route, Terminal	1.85 km	N/A
NPA	556 m	N/A
APV I	40 m	50 m
APV II	40 m	20 m
CAT I	40 m	35.0 m to 10 m

Table 3 – Alert Limit requirement [ICAO, 2006]

Ranges of values are given for the continuity requirement for en-route, terminal, initial approach, NPA and departure operations, as this requirement is dependent upon several factors including the intended operation, traffic density, and complexity of airspace

and availability of alternative navigation aids. The lower value given is the minimum requirement for areas with low traffic density and airspace complexity. The higher value given is appropriate for areas with high traffic density and airspace complexity.

A range of values is also given for the availability requirements as these requirements are dependent upon the operational need, which is based upon several factors including the frequency of operations, weather environments, the size and duration of the outages, availability of alternate navigation aids, radar coverage, traffic density and reversionary operational procedures.

2.3 Current Study Requirements

Annex 10 of the Chicago convention defined SARPS for SIS and position requirements for GNSS. In addition, the PBN and Advanced Surface Movement Guidance and Control Systems (A-SMGCS) manuals proposed recommendations intended as guidance to enable manufacturers, operators and certifying authorities to develop and introduce these concepts.

PBN concept defines performance requirements instead of systems requirements. Consequently, requirements on SIS and position defined in the SARPS can be considered as the NSE requirements for a fault-free GNSS receiver and do not concern the TSE requirements.

Current standardization (in SARPS and MOPS) establishes only requirements on position that have been presented in the current chapter. However, in the framework of our study, we did not focus on horizontal and vertical position only, but also on velocities, vertical speed, attitude angles and heading. Thus, we needed to extend the current standardized requirements on position to these other parameters.

Thus to complete the standard ICAO GNSS requirements Table 2 and Table 3, we propose to use the following ones that stands for the performance level expected from each individual system on board; for position we propose to retain the most stringent value between the two tables. Those requirements have been proposed in the framework of the PhD thesis based on previous studies done by the navigation department of Airbus. Indeed, Flight commands and auto-pilot research projects have led to the proposition of these values so as to fulfill specific operations or navigation functions. The following table is an extract of the parameters and performances document provided by Airbus that will be retained as requirements for the PhD thesis.

Type	Parameters	Required Accuracy (95%)	
		Primary	Secondary
Position	Standard Altitude	± 30 to 180 ft (≈ 9 to 60 m) up to 50 000 ft	± 350 ft (≈ 120 m) up to 50 000 ft
	Baro-corrected Altitude		
Accelerations	Longitudinal and Lateral Accelerations	± 10 mg or 1 %	± 20 mg
	Normal Acceleration	± 5 mg or 1 %	
Rotations	Yaw Rate	± 0.025 °/s or 0.25 %	± 0.05 °/s
	Pitch and Roll Rates		
Angles	Heading Angle	± 0.4 °	± 8 °
	Pitch and Roll Angles	± 0.1 °	± 1° in static ± 2.5° in dynamic
Speeds	Ground Speed	Inertia: ± 8 kt (4 m/s) Hybrid: ± 1 kt (0.5 m/s)	
	Vertical Speed	± 30 ft/mn or 5 %	
Positions	Latitude and Longitude	Inertia: < 2 NM/H Hybrid: ± 130 m (0.07 Nm)	
	Geometric Altitude	± 150 ft (45m)	

Table 4 – Expected level of performance of on-board systems [AIRBUS, 2011]

2.4 Conclusion

The current chapter has introduced the notions of requirements for aircraft navigation systems. Those requirements are standardized in documents delivered by the ICAO. The requirements gathered in the beginning of the chapter are GNSS SIS requirements for position. In that way the chapter proposed an extension of these requirements for other parameters than position.

The first section of the chapter introduced the official definition of the phases of flight by the ICAO.

The second part presented the navigation system requirements definition and reminds the GNSS SIS performance requirements.

Finally, as explained before, we proposed an extension of the given requirements by proposing the expected level of performance of on-board systems for other parameters.

Chapter 3 : Current On-board GNSS/INS Hybridization

Inertial Navigation System (INS) and GNSS are currently the two main navigation systems that provide the user position and velocity estimates. INS main characteristics are short term accuracy and autonomy but long term drift resulting from the successive integrations of measurement errors and initialization errors (INS navigation being based on dead-reckoning estimation). GNSS at the opposite offers a global coverage but has a high sensitivity to external perturbations and a limited accuracy, integrity and availability.

GPS/INS hybridization for navigation is then a good solution for compensating weak points of both systems and providing a better navigation solution while improving continuity of service and integrity monitoring performances. In the context of tight performance requirements for navigation systems that are used on commercial aircraft (see previous chapter), coupling GNSS and INS represents a high efficiency solution for navigation.

In that way, this chapter aims at presenting current on-board GNSS/INS hybridization architectures. The first part is a presentation of the main properties and characteristics of inertial navigation.

The second part is an overview of the Global Navigation Satellite System with a focus on the model of the code pseudorange measurements and the detail of the error contributions.

The third part describes the properties and characteristics of GNSS/INS hybridization in the civil aviation context.

Finally, the last part is a presentation of some additional sensors, signals or systems that have been studied for integration in our proposed solution. It has to be noticed that description and properties of video as a navigation mean is discussed in details in the next chapter. This part only introduces video as a potential innovative sensor for the design of a global hybridization architecture.

3.1 Inertial Navigation Overview

This first section presents an overview of inertial navigation with the description of the main principle, the measurement models of the inertial sensors, some properties and characteristics and a description of the baro-inertial data fusion.

3.1.1 Principle

Inertial navigation is based on dead-reckoning navigation, which is the process of estimating the current position of a mobile from a previously determined position knowing the vehicle motion. The navigation principle relies on the measurements provided by on-board sensors, which sense the absolute movement of the aircraft. For aircraft navigation, inertial sensors are generally composed of three accelerometers and three gyroscopes orthogonally mounted.

These sensors can be basically integrated into two main types of inertial systems: stabilized-platform systems and strap-down systems.

– Stabilized-platform uses a set of actuators to stabilize the gyro-accelero unit. The platform is isolated from any external rotational motion and the role of the actuators is to maintain the platform frame aligned with a specific navigation coordinate system, when achieved, the accelerometers mounted on the platform are used to measure the specific force along the navigation axes. These measurements are then processed to compute the position of the vehicle. The attitude of the vehicle is measured as the relative angles between the platform and the vehicle axes. Figure 3 illustrates the navigation processing of a stabilized platform.

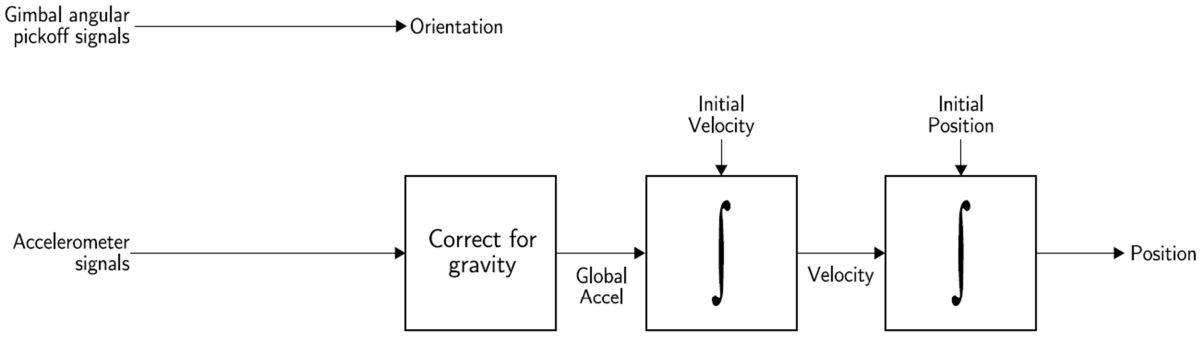

Figure 3 – Stabilized platform inertial navigation algorithm [Woodman, 2007]

– In strapdown systems, the gyro-accelero unit is directly attached to the vehicle. The sensors measure the dynamic of the vehicle so that the relationship between the measurements and the navigation state of the vehicle must be permanently computed. In most cases gyroscope axes form a trihedron parallel to the axes formed by the mobile frame (*m-frame* defined in Appendix A). Then, accelerometers measure the specific

force in the mobile frame: $f_{m/i}^{m}$ is the non-gravitational acceleration of the aircraft relative to the inertial frame expressed in the mobile frame. Gyroscopes are used to characterize the angular motion between the aircraft and the computational frame, which is the rotation of the mobile frame relative to the navigation frame, and determines the components of the aircraft angular rate. They provide the measurement of $\omega_{m/i}^{m}$, the mobile angular rate relative to the inertial frame in the mobile coordinate frame. The orientation of the mobile frame relative to the navigation frame is obtained analytically through integration of $\omega_{m/i}^{m}$. This integration is shown in Figure 4. Compared to stabilized-platform system, the computation load is increased. Such a drawback is currently not a problem due to major improvements in computer technology. Moreover, strap-down systems allow the reduction of the sensors size as well as its cost but at the expense of some accuracy.

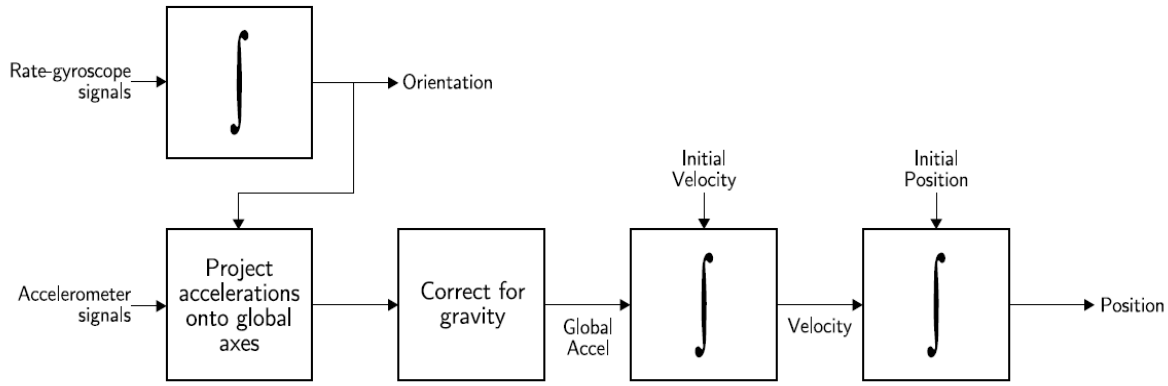

Figure 4 – Strapdown inertial navigation algorithm [Woodman, 2007]

Nowadays, most of the commercial aircraft are equipped with strapdown inertial navigation systems. The current computing power of on-board computers and the development of high technology inertial sensors allow providing high accuracy navigation with strapdown systems while space-stabilized inertial systems require high expensive and more sizeable mechanical parts.

Whatever the configuration, inertial navigation is first based on integration of inertial measurements of a vehicle. Those inertial measurements are the specific force and angular rotation rate and they are respectively sensed by accelerometers and gyroscope (or gyrometers). The next section deals with the detailed description of the two measurements: a description of the potential error sources that can affect the measurements, the measurement model and a classification of several types of sensor are provided.

3.1.2 Inertial Measurements

Inertial measurements are of two types:

The specific force also called the non-gravitational acceleration (expressed in m/s²). Despite of its name, specific force is not a force but an acceleration. More precisely, specific force is the measure of the acceleration relative to a free-fall reference. .In that way, a free-falling accelerometer measures a zero specific force while an accelerometer on the surface of the Earth measures the gravitational acceleration.

The angular rotation rate also called angular velocity, expressed in rad/s (or deg/s). It is defined as the rate of change of angular position, or the angular speed of an object about the axis the object is rotated.

In civil aviation equipment, inertial sensors block is called the Inertial Measurement Unit (IMU). An IMU traditionally contains three accelerometers and three gyroscopes, which are orthogonally mounted.

The IMU is a part of the Inertial Navigation System (INS), see Figure 5, which provides raw inertial measurements (specific forces $f^m_{m/i}$ and rotation rates $\omega^m_{m/i}$) as well as inertial 3D position $p_{m/e} = (\lambda, \phi, h)$, 3D velocity $v^n_{m/e} = (v_{North}, v_{East}, v_{Down})$ and attitude angles $\rho_{m/n} = (\varphi, \theta, \psi)$.

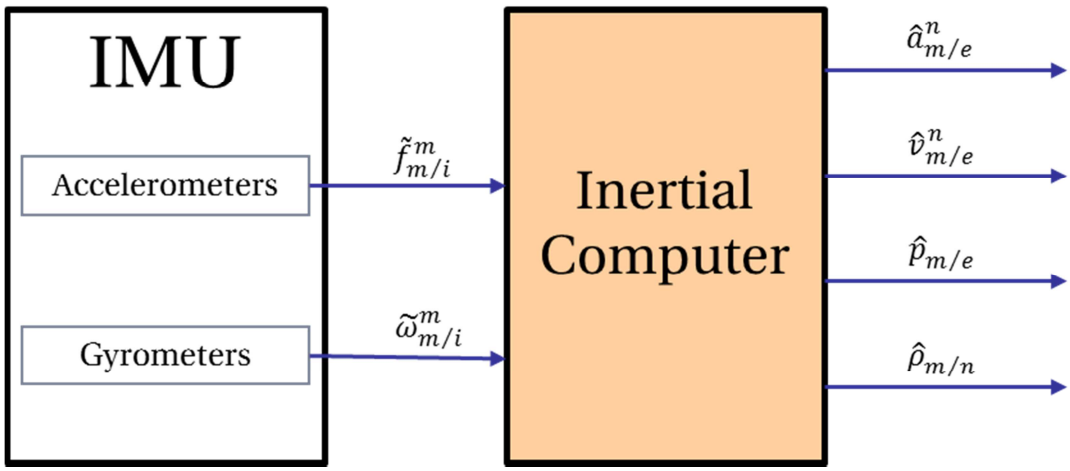

Figure 5 – Inertial Navigation System

As it is presented in the introduction, INS is a navigation system based on dead-reckoning principle: estimate the current position by using the previous one and the movement measured by inertial sensors. However, this principle is strongly subject to errors on the previous position estimates and on quality of the measured parameters because of the successive integrations. In order to characterize the dimension of the estimation errors it is important to know the characteristics of the errors that can affect the inertial measurements. They are detailed in the next part.

3.1.2.1 Error Characteristics

A measurement error is basically defined as the difference between the measured value and the true value. In the following, different error characteristics that typically affect inertial measurements are presented.

3.1.2.1.1 Bias

Bias is defined as the output of the sensor when no input movement is applied. This bias on the measurement can be divided in three components:

- *A constant bias*, which characterizes the mean output from the sensor when there is no input. It can be estimated and compensated by taking a long term average of the output while no movement is experienced.
- *A repeatability bias (or run-to-run bias)*, which is also a constant bias but changes every time the sensor is switched on. It characterizes the variation on measured bias between successive turn-on.
- *A stability bias (or in-run bias)*, which characterizes the short term in-run variation on the measured bias after turn-on. Stability bias is impacted by temperature variations and high acceleration profiles.

3.1.2.1.2 Amplitude response

Amplitude response error can be separated in three components:

- *A Linear component*, which characterizes by the slope in the linear amplitude response of the sensor, also called scale factor. Usually, scale factor is not constant and can vary during a run (Scale factor stability) and from a run to another (Scale factor repeatability).
- *A Non-linear component,* which characterizes the non-linear deviation from the expected response to a change in input (hysteresis cycle for example). Non-linear errors are usually expressed as polynomial coefficients.
- *A Non-symmetric component,* which is characterized by the difference in response to positive and negative inputs of the same absolute value.

In our measurement model presented in 3.1.2.2, we will only model the amplitude response as a constant scale factor parameter uniformly distributed in a given interval.

3.1.2.1.3 Axes misalignment/Non-Orthogonality

This error can be separated in two components:

– *The Non-Orthogonality,* which characterizes manufacturing errors of orthogonality between the axes.

– *The Misalignment,* which characterizes the error between the sensitive axis of the sensor and the axis of the body.

The misalignment of sensor axes is illustrated in Figure 6.

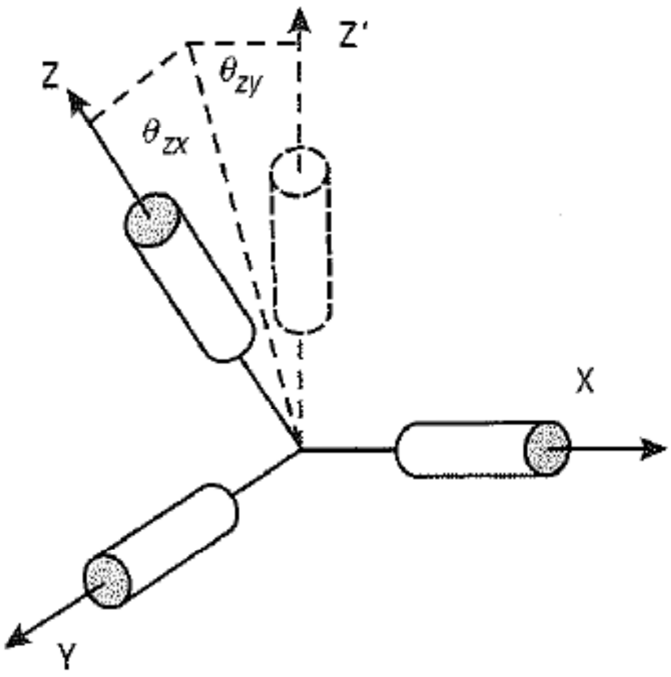

Figure 6 – Misalignment of accelerometer and gyro axes [Aggarwal et al., 2010]

In our measurement model presented in 3.1.2.2, we will model the non-orthogonality/misalignment error contribution as a matrix factor of the true inertial measurements. In addition, we fused all misalignment angles on one axis: $\theta_{ZX} = \theta_{ZY} = \theta_Z$. The matrix is the following:

$$M = \begin{bmatrix} \cos\theta_X & -\sin\theta_Z & \sin\theta_Y \\ \sin\theta_Z & \cos\theta_Y & -\sin\theta_X \\ -\sin\theta_Y & \sin\theta_X & \cos\theta_Z \end{bmatrix} \tag{3.1}$$

Where: θ_X, θ_Y and θ_Z are the misalignment angles for the platform axes.

3.1.2.1.4 Quantization/Resolution

This characterizes the minimum change in the output signal.

The quantization/resolution error contribution is not modeled in our measurement model.

3.1.2.1.5 Dead-Band

This characterizes the maximum output from zero before a change in the output signal. The quantization/resolution error contribution is not modeled in our measurement model.

3.1.2.1.6 Noise

This component is usually modeled as a White Gaussian noise.

3.1.2.1.7 Synthesis

The different error contributions presented in this part are the main error sources for accelerometers and gyrometers. However, several classes of sensors can be distinguished, depending on the way these errors can impact the specific force or rotation rate measurement. Some of the main inertial classes are described in the following part.

3.1.2.2 Measurement Models

Previous parts described in details some error characteristics that contribute to the nominal measurement errors for inertial sensors. However, in our study we will not consider all these contributions: scale factor, misalignment, thermal noise and time-correlated uncompensated bias will be considered, only. The measurement models that will be used in our study are detailed in 6.2.

In that way, the measurement models for the specific force and rotation rate provided by an IMU are as follows:

$$\tilde{f}^m_{m/i} = (SF_a + M_a) \cdot f^m_{m/i} + b_a + n_a \tag{3.2}$$

Where:

- $\tilde{f}^m_{m/i}$ is the accelerometer measurement
- $f^m_{m/i}$ is the real specific force of the mobile
- SF_a is the Scale Factor error coefficient of the accelerometer
- M_a is the Misalignment error coefficient of the accelerometer
- b_a is the uncompensated accelerometer bias
- n_a is the white Gaussian measurement noise

$$\tilde{\omega}^m_{m/i} = \left(SF_g + M_g\right) \cdot \omega^m_{m/i} + b_g + n_g \tag{3.3}$$

Where:

- $\tilde{\omega}_{m/i}^{m}$ is the gyrometer measurement
- $\omega_{m/i}^{m}$ is the real instantaneous rotation rate of the mobile
- SF_g is the Scale Factor error coefficient of the gyrometer
- M_g is the Misalignment error coefficient of the gyrometer
- b_g is the uncompensated gyroscope bias
- n_g is the white Gaussian measurement noise

For generation of accelerometer and gyrometer measurements according to these models, we will use the Table 5 values in order to obtain class A to class C simulated inertial measurements.

3.1.2.3 Sensors Classification

The computation of inertial parameters on board is not always done with the same equipment. It depends on the type of aircraft and its operational usage. An inertial classification can be established and is mainly described as a function of the quality and technology of the sensor and the targeted performance.

3.1.2.3.1 IRS

Long range commercial aircraft are equipped with Inertial Reference Systems (IRS) offering an inertial positioning capability compliant with international certification regulations for flying in oceanic or remote areas. These IRS also provide high accurate velocities, accelerations, attitudes, true and magnetic heading, track, rotation rates and rotation accelerations. It is constituted of three accelerometers and three optical gyroscopes orthogonally mounted.

The IRS can be a component of the Air Data and Inertial Reference Unit (ADIRU), which can be associated to two other ADIRUs to constitute an Air Data and Inertial Reference System (ADIRS). In addition to the IRS, an ADIRU is composed of an Air Data Reference System (ADR) that provides to the pilot and various systems inertial data as well as air data (airspeed, angle of attack, temperatures, altitude…). An ADR provides parameters such as Total Pressure, Static Pressure, Computed Air Speed, Altitude, Vertical Speed, Mach number, Angle of Attack, Total Temperature, Static Temperature etc…

3.1.2.3.2 AHRS

On short-range aircraft flying over continental areas, positioning was traditionally ensured by radio navigation means, like VOR or DME; nowadays supplanted by GPS as primary mean of navigation. Autonomous inertial navigation is not required. And inertial parameters delivery may be fulfilled using Attitude Heading Reference System (AHRS), which provides sufficient performance for display or flight control.

AHRS is generally composed of optical or Microelectromechanical systems (MEMS) gyroscopes, accelerometers and magnetometers on all three axes. A form of non-linear estimation such as a Kalman filter is typically used to compute the solution from these multiple sources. AHRS differ from traditional inertial navigation systems by attempting to estimate only attitude states, rather than attitude, position and velocity as is the case with an IRS. Magnetometers are generally needed in order to perform heading initialization and maintain its computation.

AHRS have proven themselves to be highly reliable and are in common use in commercial and business aircraft. AHRS are typically integrated with Electronic Flight Information Systems (EFIS) to form the Primary Flight Display (PFD). AHRS can be combined with air data computers to form an "air data, attitude and heading reference systems" (ADAHRS), which provide additional information such as airspeed, altitude and outside air temperature.

Halfway between IRS and AHRS in term of performance, an offer for so-called Super-AHRS has emerged in the last years; this type of product implements inertial sensors whose performance is sufficient to allow autonomous heading determination, but not enough to provide positioning capability with an acceptable level of performance.

3.1.2.3.3 Standby Instruments

A back up and independent inertial reference source can be available through a stand-by instrument like IESI (Integrated Electronic Standby Instrument) or an Integrated Standby Instrument Systems (ISIS).

ISIS instrument can provide the following parameters:

- Attitude (pitch and roll);
- Standard or barometric-corrected altitude and associated barometric pressure;
- Indicated airspeed;
- Indicated Mach number

Standby instruments are intended to replace separate mechanical instruments to serve as backups in case of failures of main instrument systems. In that way, they are supposed to operate reliably and independently from aircraft's main instrument systems.

3.1.2.3.4 Performance Classification

Quality of inertial sensors will be the main contributor to inertial system performance. Based on a previous study, Table 5 provides a performance classification for gyrometers and accelerometers sensors in terms of error characteristics. That classification allows identifying numerical parameters for describing the nominal measurement error model. It will be used in our study in order to generate inertial measurements for considered classes of inertia.

Sensor parameter		ADIRU	Super AHRS+	Super AHRS-	AHRS	Stand-by instrument
		CLASS A	CLASS B+	CLASS B-	CLASS C+	CLASS C-
Gyro	Repeatability (run to run drift)	0.01°/h	0.05°/h	0.5°/h	2.5°/h	300°/h
	Stability (in run drift)	0.005°/h	0.025°/h	0.25°/h	2.5°/h	15°/h
	Scale Factor	12ppm	50ppm	50ppm	300ppm	3000ppm
	Misalignment	12μrd	50μrd	200μrd	200μrd	1000μrd
	Random Walk	0.003°/ $\sqrt{h}$	0.01°/ $\sqrt{h}$	0.02°/ $\sqrt{h}$	0.04°/ $\sqrt{h}$	10°/ $\sqrt{h}$
	Correlation Time	1800s	1200s	800s	700s	600s
Accel	Repeatability (run to run bias)	80μg	100μg	100μg	1000μg	4000μg
	Stability (in run bias)	Negligible	20 μg	20 μg	1000 μg	2000 μg
	Scale Factor	80ppm	80ppm	80ppm	150ppm	700ppm
	Misalignment	20μrd	50μrd	50μrd	200μrd	1000μrd
	Random Walk	10µg/√Hz	20µg/√Hz	20µg/√Hz	50µg/√Hz	100µg/√Hz
	Correlation Time	3600s	1200s	1200s	300s	150s

Table 5 – Inertial Classes Performances [THAV, 2009]

3.1.3 Inertial Properties and Performance

3.1.3.1 General Properties

Compared with other means of navigation, one of the main advantages of inertial navigation is that it is a self-contained system (it is not reliant on external information with the exception of a vertical channel limitation). Inertial systems are insensitive to any external perturbation like meteorological phenomena, jamming, interference, multipath and can operate in all medium (air, space and water).

The accuracy of inertial navigation systems is mainly limited by the quality of inertial sensors (position and velocity degrades with time due to sensors error sources) and the knowledge of the earth's gravity field, shape and spin rate.

Initialization process, also called alignment, is needed in order to establish an initial reference point (position is determined relatively to the initial position; inertial sensors

measure change in location and not an absolute location). This initialization process is usually done from accelerometer measurements (in order to estimate the local gravitation constant and Earth's angular rate) and gyros or external heading reference system for heading initialization. A bad alignment can introduce some errors that will not stop growing after integration process.

The coupling of an INS with some complementary means of navigation, such as GNSS, allows improving performance of both systems and correcting position drift. This coupling can be performed in several configurations (presented in section 3.4.2). Current on-board integrated solutions only couple single frequency GPS L1 C/A code pseudorange measurements and inertial sensors in order to estimate a hybrid position.

3.1.3.2 IMU Performance

The classification proposed in Table 5 quantifies the error characteristics of inertial sensors associated to each class. In addition, [Kenneth, 2008] proposed a classification that relates IMU performance, sensors technology , usage domain and performance in terms of position. This classification is depicted in Table 6.

Class	Position performance	Gyro technology	Accelerometer technology	Gyro bias	Accel bias
Military grade	1 NM / 24h	ESG, RLG, FOG	Servo accelerometer	< 0.005°/h	< 30µg
Navigation grade	1 NM /h	RLG, FOG	Servo accelerometer, Vibrating beam	0.01°/h	50 µg
Tactical grade	> 10 NM /h	RLG, FOG	Servo accelerometer, Vibrating beam, MEMS	1°/h	1 mg
AHRS	NA	MEMS, RLG, FOG, Coriolis	MEMS	1 - 10°/h	1 mg
Control system	NA	Coriolis	MEMS	10 - 1000°/h	10 mg

Table 6 – IMU technology and performance [Kenneth, 2008]

Current on-board IMUs are "navigation grade" class and provide a pure inertial position that drifts at 1 nautical mile (NM) per hour. This value is currently reached with good quality inertial sensors.

3.1.3.3 INS Mechanization

Inertial mechanization describes the process for providing navigation parameters (position, velocity, attitude and acceleration) from inertial sensor measurements.

Strapdown inertial navigation mechanization is illustrated in Figure 7.

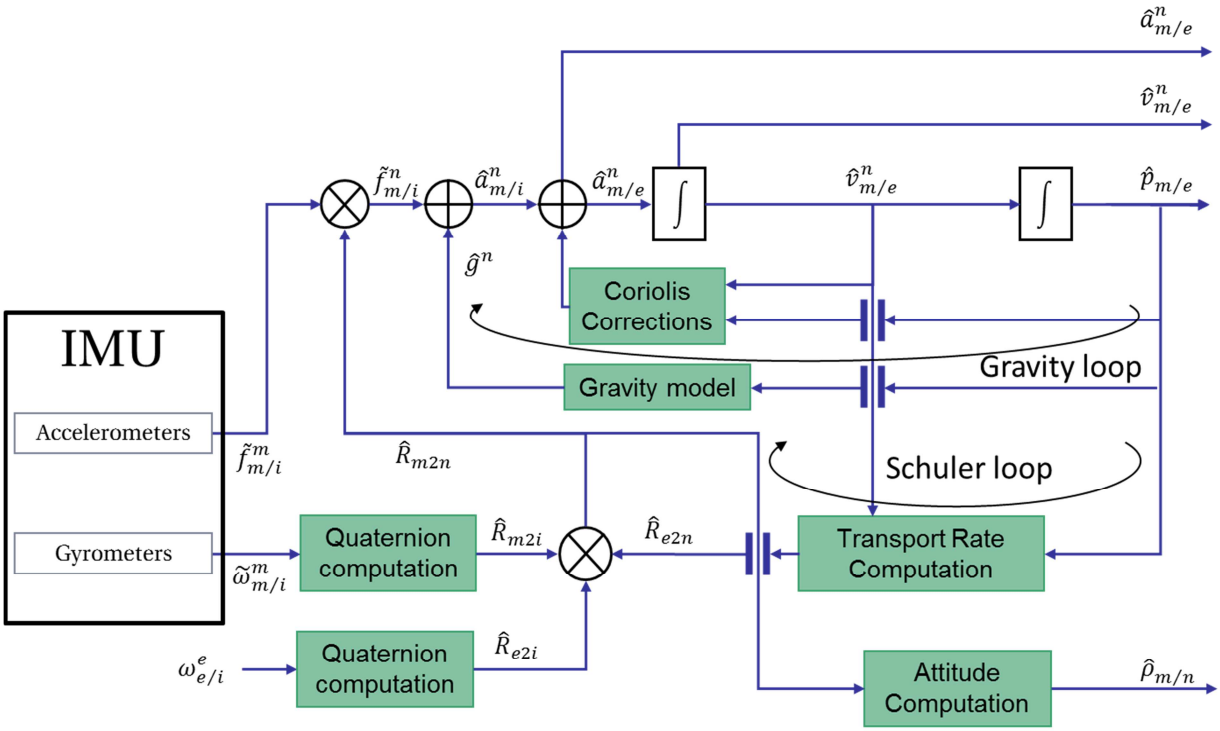

Figure 7 – Strapdown INS Mechanization

Basic mechanization of a strapdown INS starts with the compensation of the specific force measurement provided by the accelerometers with the local gravity vector computed at the previous estimated position. Then a correction of the Coriolis inertial acceleration is done allowing a double integration to obtain position and velocity. In the same time, gyrometers measurements are used for estimating rotation matrices using directly the Direct Cosine Matrices (DCM) or the quaternion vector. The DCM, or the quaternion vector, is then used for attitude estimation.

In such mechanization, two particular “loops” can be identified:

- The gravity loop, which aims at computing the local gravity vector for specific force compensation in function of the estimated position. That helps slowing the inertial drifts by using an adaptive gravity model (as the Somigliana model for example, described in 5.4.1.3) that depends on the previously computed position. The use of a good gravity model is important because an error in the computation of the local gravity vector will be seen as a measured acceleration error and will grow the inertial estimation error. Gravity loop can be more complex when the INS is aided with an external source of altitude measurement (such as a barometer). In that way, the barometer helps correcting the fast vertical inertial drift due to the curvature of the earth and the dependency of the gravity with the altitude (gravity decreases as the square of the altitude). A more complex gravity loop is depicted in 3.1.4.2.
- The Schuler loop, which consists in using the position and velocity for computation of the transport rate vector $\omega^n_{e/n}$ of the platform. This rotation vector is used to

stabilize horizontally the platform axes (or to keep a local vertical). The use of the transport rate vector to compute R_{e2n} rotation matrix is called the Schuler tuning because it gives to the system the property of a Schuler pendulum (also called Schuler oscillations) described in the next part.

3.1.3.4 Schuler Oscillations

Since the Earth's surface is not flat, a strapdown INS constantly needs to keep the platform axis virtually horizontal, or more accurately to keep the platform perpendicular to the local gravity vector. This process that intends maintaining a local vertical, is supposed to keep the platform not impacted by any acceleration felt by the platform and then maintain the platform perfectly horizontal.

Theoretically, a system that obeys the property of being insensitive to any acceleration is called a Schuler pendulum, which is a pendulum of length the distance between the platform and the center of the earth. Such a pendulum would oscillate at a frequency of 84,4 min, when close to the earth's surface, called the Schuler frequency.

Anyway, this pendulum cannot be realized in reality. However, the property of that is intended to be reproduced virtually. This process is called Schuler tuning. In that way, the INS is tuned in order to exhibit the same properties as a Schuler pendulum. Thus, the platform becomes insensitive to all acceleration felt and can maintain the local vertical. In fact, the Schuler tuning makes the platform not directly rotated by the incident accelerations.

The Schuler tuning is done by computing the transport rate vector (rotation velocity vector of the *n-frame* with respect to the *e-frame*), directly proportional to the velocity in the North and East directions. The transport rate vector characterizes the change in the alignment of the platform with respect to the horizontal plane. Then it can be used to compensate this rotation.

In that configuration, acceleration or rotation rate measurement errors will induce a velocity and a transport rate error. Transport rate error will then cause an alignment error of the platform with respect to the horizontal plane. Error in the alignment of the platform makes that the platform will sense a component of the gravity along one of the horizontal sensitive axis. This gravity contribution on a sensitive axis will be seen as an additional acceleration error and converted into a velocity and a transport rate error. This error is increasing until the velocity error changes its sign. Finally, this phenomenon appears to be periodic at the Schuler frequency and position, velocity and attitude estimations are affected by this oscillation.

Paradoxically, the advantage of these oscillations is that they bound the error growth and slow the drift, in the horizontal plane.

3.1.4 Baro-inertial Data Fusion

As described in the previous parts, one of the INS main drawbacks is the fast vertical inertial drift that prevents estimation of the altitude during a long period of time. For short term navigation, this phenomenon can be neglected but when the duration increases, altitude error estimation will exponentially drift. This drift will then impact the horizontal position estimation because of the dependency of the local gravity vector with the altitude estimation.

For civil aviation application, a barometric altimeter (or barometer) is used in order to provide an additional altitude measurement. This sensor allows compensating the vertical drift of an INS and then maintaining inertial navigation possible during hours. The process for correcting the vertical inertial drift with a barometer is described in the next part. But, in a first part, a brief description of the main error sources that can affect a barometer measurement is presented and a measurement model is given. For the following, measurement errors affecting the baro-altitude will have to be taken into account when deriving performance of a solution using a baro-INS system.

3.1.4.1 Baro-altimeter Error Sources

Two main sources of barometric altitude errors can be identified:

Height Difference between Mean Sea Level (MSL) and the Geoid: The barometric altitude measurement provided by a barometer is with respect to the MSL. The other navigation systems involved in the thesis do not provide altitude information with respect to the MSL but to the WGS84 coordinate system. In the study we will assume that the difference is corrected by the baro-altimeter system before using it in the baro-inertial loop (described in the next part). That error will not be considered in the measurement model for the barometric altitude.

Pressure Error: The conversion of measured air pressure to altitude is based on a theoretical standard atmosphere and a corresponding pressure versus altitude curve as well as the assumption that air is a perfect gas. The conversion of measured air pressure to altitude is based on the following equation [Jan, 2003]:

$$\hat{h}_B = \frac{T_0}{\lambda} \cdot \left[1 - \left(\frac{P_m}{P_0} \right)^{\frac{\lambda R}{g}} \right] \tag{3.4}$$

Where

- $\hat{h}_B$ is estimated altitude
- T_0 is temperature at the level of reference
- λ is lapse rate

- P_0 is pressure at the level of reference
- P_m is pressure measured
- R is universal gas constant
- g is acceleration of gravity

The pressure error contributions correspond to the error in the reference pressure used in the previous equation. The pressure error is the major error source of a barometric altimeter.

Commercial aircraft currently uses inertial systems for en-route navigation since decades. However, the navigation solution is only provided in the horizontal plane. Vertical positioning is provided with the help of a baro-altimeter that corrects the vertical inertial acceleration, vertical inertial velocity and inertial altitude.

The baro-altimeter sensor measures a pressure level converted in mean sea level altitude h_B.

Current aircraft are in fact equipped with ADIRUs, meaning that the baro-altimeter is coupled with the inertial mechanization within a baro-inertial loop architecture. An example of such an architecture is illustrated in [Kayton and Fried, 1997]. In that reference, a inertial mechanization using a second order baro-inertial loop for vertical channel drift compensation is described.

In our study we decided to model the pressure error as a simple white Gaussian noise with a standard deviation of 10m (as it is proposed in [Jan, 2003]). The measurement model is then as follows:

$$\tilde{h}_B = h_B + n_B \tag{3.5}$$

Where:

- $\tilde{h}_B$ is the baro-altitude measurement
- h_B is the real altitude
- n_B is the white Gaussian measurement noise

3.1.4.2 Baro-inertial loop

The INS vertical channel mechanization is done by integrating twice the vertical acceleration. This acceleration is obtained from the specific force measurement corrected from the local gravitational acceleration, which decreases proportionally to R_e^2. In that case a small error in the altitude estimation will grow exponentially due to the positive feedback within the vertical gravity loop. Even in high performance navigation systems, estimated altitude error becomes unacceptable after few minutes. The vertical channel is then usually stabilized using an altitude reference as a barometric altimeter.

In our study we have implemented a third order baro-inertial loop (meaning that the loop uses three integrators). The error model of the loop is illustrated in Figure 8.

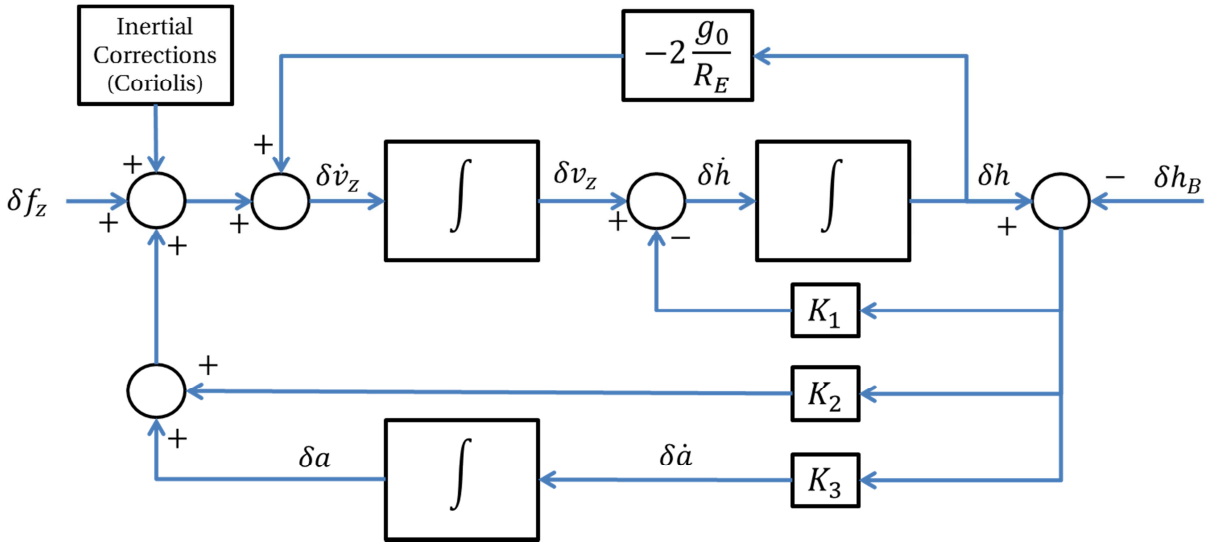

Figure 8 – Error model of a third order baro-INS loop [Seo et al., 2004]

Where:

- δf_z is the bias on the vertical-axis of the specific force vector
- $\delta \dot{v}_z$ is the derivative of the vertical velocity error
- δv_z is the vertical velocity error
- $\delta \dot{h}$ is the derivative of the baro-INS altitude error
- δh is the baro-INS altitude error
- δh_B is the barometric altitude error
- $\delta \dot{a}$ is the derivative of the output error of the compensator of the feedback loop
- δa is the output error of the compensator of the feedback loop
- g_0 is the magnitude of gravity at the equator and at sea level
- R_E is the earth's equatorial radius

The vertical channel error mechanization presented in Figure 8, allows introducing the equations that relates the error on the sensed vertical acceleration to the altitude and vertical velocity estimation errors. Those relations will be used so as to define precisely the state transition function for the vertical channel in the description of the filter implemented in the thesis (see section 5.4). As introduced before, we use a third order baro-inertial loop, identified with the presence of three integrators in the functional diagram of the loop. This architecture also introduces three gains (K_1, K_2 and K_3) that allows stabilizing the loop.

3.1.5 Synthesis

An INS is a self-contained and autonomous navigation system based on the dead reckoning principle. For any class of sensors, inertial navigation is characterized by a very

good short term accuracy and being totally insensitive to external perturbation such as atmospheric disturbances and interferences, it is not impacted by external error sources. In return, inertial navigation presents a long term drift, which results of successive integrations of accelerometers and gyrometers measurement errors. In that way, the position, velocity and attitude provided by an INS are potentially unbounded. Moreover, INS provides high bandwidth data estimates at a high rate, useful for navigation and guidance purpose.

One of the main drawbacks when using INS is that the sensor platform needs to be perfectly aligned. Indeed, an INS requires an initialization process, called alignment, that establishes the relation between the vehicle frame (supposed aligned with the platform frame) and the navigation frame. Usually, alignment is done maintaining the vehicle stationary for a period of time depending on the technology involved. It may also require data from other systems (GPS, magnetometers…). Alignment is strongly essential because an alignment error will increase projection errors and then integration errors (especially when INS is used as a sole means of navigation).

Finally, INS main advantage is the ability to provide continuous estimates of the position without being impacted by the external environment. Depending on the technology, the accuracy at short term is relatively important but fast degrades after a short period of time. This last point remains the major drawback of inertial navigation that cannot be compensated or corrected even with the best technology.

3.2 Global Navigation Satellite System Overview

GNSS stands for Global Navigation Satellite System; it allows any user equipped with a receiver obtaining its position and time. A GNSS receiver uses pseudorange measurements obtained by estimation of the propagation delay of the signal between the receiver antenna and the different satellite antennas of the GNSS constellation to compute the position and time of the user. The satellite's antenna to user's antenna range measurement is called pseudoranges because of the user's receiver clock error (the offset between the receiver clock and the GNSS reference clock), which affect that measurement.

The difference between the true pseudorange and the measured one are due to several sources of error. In civil aviation, some of these errors are partially corrected with adequate error models (for example the Klobuchar model for GPS single frequency ionospheric delays). In that way, some models (ionospheric error, tropospheric error, multipath) describing the residual error after application of these corrections are standardized in ICAO's documents [ICAO, 2006] or [ICAO, 2009]. For models not specific for civil aviation (ephemeris errors, satellite errors, receiver noise), a standard can be found in the literature [Farrel and Barth, 1998] or [Kaplan and Hegarty, 2006]. The following part describes in details the major error sources for pseudorange measurements.

3.2.1 GNSS Error Sources

GPS errors sources can be detailed in six main classes [Parkinson and Spilker, 1996]. These errors can be generalized for a GNSS:

- ***Ephemeris data:*** Errors in the transmitted location of the satellite
- ***Satellite clock:*** Errors in the satellite clock prediction
- ***Ionosphere:*** Errors during propagation through ionosphere
- ***Troposphere:*** Errors during propagation through troposphere
- ***Multipath:*** Errors caused by reflected signals entering the receiver antenna
- ***Receiver:*** Errors in the receiver's measurement of range caused by thermal noise, software accuracy, and inter-channel biases

Ephemeris and satellite clock errors will be modeled as a single error component whose characteristics are detailed in this part.

The pseudorange errors caused by each independent source can be modeled with a zero-mean normal distribution that overbounds the real error distribution.

$$\epsilon_{Sat/Eph} \sim \mathcal{N}\left(0, \sigma^2_{Sat/Eph}\right) \tag{3.6}$$

$$\epsilon_{iono} \sim \mathcal{N}\left(0, \sigma^2_{iono}\right) \tag{3.7}$$

$$\epsilon_{tropo} \sim \mathcal{N}\left(0, \sigma^2_{tropo}\right) \tag{3.8}$$

$$\epsilon_{mp} \sim \mathcal{N}\left(0, \sigma^2_{mp}\right) \tag{3.9}$$

$$\epsilon_{noise} \sim \mathcal{N}\left(0, \sigma^2_{noise}\right) \tag{3.10}$$

3.2.1.1 Ephemeris and Satellite Clock Errors

3.2.1.1.1 Ephemeris

Estimations of ephemerides for all satellites are computed and uplinked to the satellites with other navigation data message parameters for rebroadcast to the user [Kaplan and Hegarty, 2006]. These ephemeris errors can be represented with three components: radial, tangential and cross track. Radial component is in general the smallest and has the most important impact on ranging accuracy. Tangential and cross track errors may be larger but don't affect the ranging accuracy [Farrel and Barth, 1998].

3.2.1.1.2 Satellite Clock Errors

Satellites contain atomic clocks that control all on board timing operations including broadcast signal generation. These clocks are highly stable and deviate approximately up to 1ms from time system but an offset of 1ms translates to a 300km pseudorange error [Kaplan and Hegarty, 2006]. The control segment estimates and monitors the satellite clock error but does not correct the clock. It only sends the correction parameter to the user. The user is then able to read these parameters and correct the predicted portion of the satellite clock error. Remaining satellite clock error will bias the corrected range [Farrel and Barth, 1998].

This residual error results in ranging error that typically vary from 0.3 to 4m depending on the type of the satellite and age of the broadcast data. More precisely residual clock error slowly degrades over time until the next upload. At zero age of data (ZOAD), clock errors for a typical satellite are on the order of 0.8m [Dieter et al., 2003] and [Taylor and Barnes, 2005]. 24 hours after an upload, errors are generally within the range of 1–4m. User equipment that is tracking all visible satellites will observe satellites with ages of data (AODs) varying from 0 to 24 hours. The nominal 1-sigma clock error for the constellation in 2004 averaged over AOD was 1.1m, based on the data presented in [Dieter et al., 2003] and [Taylor and Barnes, 2005]. It is expected that residual clock errors will continue to decrease as newer satellites are launched with better performing clocks and as improvements are made to the control segment [Yinger et al., 2003]. Average clock errors are also influenced by the frequency of uploads to each satellite [Kaplan and Hegarty, 2006].

3.2.1.1.3 Synthesis

For GPS, the User Range Accuracy (URA) is a bound of the standard deviation of the range component of clock and ephemeris error. We assume that the distribution of the ephemeris and clock range error of each satellite is over bounded by a zero mean Gaussian distribution with standard deviation equal to URA. In the case of GALILEO, we assume that the clock and ephemeris error of each satellite is over bounded by a nonbiased Gaussian distribution with the minimum standard deviation called Signal-In-Space Accuracy (SISA). This parameter is assumed to have the same definition as the GPS URA. The integrity performance requirement, in [ESA, 2005], specifies a SISA value, for both nominal and degraded mode of 0.85m. GPS URA depends on the assumed type of satellite and therefore on the considered modernization step of the GPS constellation. For the study we will assume future GNSS constellations and we will make the assumption that both GALILEO and GPS satellites will achieve at least the URA of 0.85m [Neri, 2011]:

$$\sigma_{Sat/Eph} = 0.85\ m \tag{3.11}$$

3.2.1.2 Ionosphere Error

The ionosphere is a dispersive medium located primarily in the region of the atmosphere between about 70 km and 1,000 km above the Earth's surface. Within this region, ultraviolet rays from the sun ionize a portion of gas molecules and release free electrons. These free electrons influence electromagnetic wave propagation, including the GPS satellite signal broadcasts [Kaplan and Hegarty, 2006].

The modulation on the signal is delayed in proportion to the number of free electrons encountered and is also proportional to the inverse of the carrier frequency squared. The phase of the radio frequency carrier is advanced by the same amount because of these effects. All users will correct the raw pseudoranges for the ionospheric delay. The simplest correction will use an internal diurnal model of these delays. The parameters can be updated using information in the GPS communication message [Parkinson and Spilker, 1996]. One important example of correction used is the Klobuchar model, which removes (on average) about 50% of the ionospheric delay at midlatitudes through a set of coefficients included in the GPS navigation message. This model assumes that the vertical ionospheric delay can be approximated by half a cosine function of the local time during daytime and by a constant level during nighttime [Jorgensen, 1989].

As the ionosphere is a dispersive medium, the use of a dual frequency signals allows correcting entirely the ionosphere delay.

The following parts detail the standard deviations of the residual error model for the ionospheric propagation delay for GPS and GALILEO single frequency and GPS/GALILEO dual frequency.

3.2.1.2.1 GPS Single Frequency Mode

GPS signals currently apply the Klobuchar model for estimation of ionospheric delays. As depicted in [Salos, 2012], the standard deviation of the residual error model of the ionospheric propagation delay for GPS L1 C/A signal can reasonably be taken as the product of the Slant factor F (see equation (3.13)) and the vertical standard deviation of the ionospheric error (see equation (3.12)). That standard deviation depends on the latitude λ of the receiver as follows:

$$\sigma_{iono,vertical,E1} = \begin{cases} 9\,m & \text{if } 0° \le |\lambda| \le 20° \\ 4.5\,m & \text{if } 20° < |\lambda| \le 55° \\ 6\,m & \text{if } 55° < |\lambda| \end{cases} \tag{3.12}$$

$$F = 1.0 + 16 \cdot \left(0.53 - \frac{elev}{\pi}\right)^3 \tag{3.13}$$

$$\sigma_{iono,L1} = \sigma_{iono,vertical,L1} \cdot F \tag{3.14}$$

By extension, for GPS L5 frequency, the standard deviation of the residual ionospheric error is as follows:

$$\sigma_{iono,L5} = \left(\frac{f_{L1}}{f_{L5}}\right)^2 \cdot \sigma_{iono,L1} = 1.79 \cdot \sigma_{iono,L1} \tag{3.15}$$

Where:

- $\sigma_{iono,L1}$ is the standard deviation of the residual error model of the ionospheric propagation delay for GPS L1 C/A signal.
- $f_{L1} = 1572.42\ MHz$ and $f_{L5} = 1176.45\ MHz$.

3.2.1.2.2 GALILEO Single Frequency Mode

In the case of GALILEO, a more recent model is considered for ionospheric error corrections. It is called the NeQuick algorithm and is assumed to correct 70% of the ionospheric delay when operating on E5a, E5b and E1 frequencies. However, in the framework of our study, we will use Klobuchar algorithm to model ionospheric delay on GALILEO frequencies. Thus, as it is considered for GPS single frequency mode, we can reasonably set the standard deviation of the residual error model of the ionospheric propagation delay for GALILEO E1 as the product of the Slant factor F (see equation (2.5)) and of the vertical standard deviation of the ionospheric error. The vertical $\sigma_{iono,vertical,E1}$ is in the range [7.5m; 3.9m], where 7.5m corresponds to $\lambda = 0°$ and 3.9m corresponds to $\lambda = 75°$ (see [Montloin, 2011],[Salos, 2012]).

By extension, for GALILEO E5a frequency, the standard deviation of the residual ionospheric error is as follows:

$$\sigma_{iono,E5a} = \left(\frac{f_{E1}}{f_{E5a}}\right)^2 \cdot \sigma_{iono,E1} = 1.79 \cdot \sigma_{iono,E1} \tag{3.16}$$

Where:

- $\sigma_{iono,E1}$ is the standard deviation of the residual error model of the ionospheric propagation delay for GALILEO E1 signal.
- $f_{E1} = 1572.42\ MHz$ and $f_{E5a} = 1176.45\ MHz$.

3.2.1.2.3 GPS and GALILEO Dual Frequency Mode

As presented before, the dispersive property of the ionosphere allows correcting entirely the ionospheric delay when using dual receivers. In that way, the first order ionospheric delay is completely removed. Higher orders remain but are neglected when comparing their magnitudes to other error sources (between 0 and 2 cm at the zenith for

second order ionospheric delays and between 0 and 2 mm for third order ones, [Salos, 2012]). The standard deviation of the residual ionospheric error is then as follows:

$$\sigma_{iono,L1/L5} = \sigma_{iono,E1/E5a} = 0 \tag{3.17}$$

Even if dual frequency measurements are iono-free pseudoranges, a main drawback is the amplification of the errors caused by thermal noise and multipath. Nonetheless, standard deviation of the residual error with iono-free measurements remains lower than with a single frequency receiver. The amplification of the thermal noise and multipath due to iono-free combination is illustrated in 3.2.1.4.2 and 3.2.1.5.2.

3.2.1.3 Tropospheric Error

The troposphere is the lower part of the atmosphere that is non-dispersive for frequencies up to 15 GHz. Within this medium, the phase and group velocities associated with the GNSS carrier and signal information (PRN code and navigation data) are equally delayed with respect to free-space propagation. This delay is a function of the tropospheric refractive index, which is dependent on the local temperature, pressure, and relative humidity [Kaplan and Hegarty, 2006]

Tropospheric delay is normally represented as having a wet component and a dry component. The wet component is difficult to model because of local variations in the water-vapor content of the troposphere and accounts for approximately 10% of the tropospheric delay. The dry component is relatively well modeled and accounts for approximately 90% of the tropospheric delay [Farrel and Barth, 1998].

For civil aviation GNSS receivers, the tropospheric model to correct the troposphere code delay is specified in [ICAO, 2006]. The standard deviation of the residual tropospheric error model is the product of the vertical error standard deviation $\sigma_{tropo,vertical}$ and a mapping function F_{tropo}, exclusively dependent upon the satellite's elevation angle θ, as follows ([ICAO, 2006] and [EUROCAE, 2010]):

$$\sigma_{tropo} = F_{tropo} \cdot \sigma_{tropo,vertical} \tag{3.18}$$

Where:

$$F_{tropo} = \begin{cases} \dfrac{1.001}{\sqrt{0.002001 + \sin^2\theta}} & for\ \theta \geq 4° \\ \dfrac{1.001}{\sqrt{0.002001 + \sin^2\theta}} \cdot (1 + 0.015 \cdot (4° - \theta)^2) & for\ 2° \geq \theta > 4° \end{cases} \tag{3.19}$$

$$\sigma_{tropo,vertical} = 0.12m \tag{3.20}$$

3.2.1.4 Multipath Error

The receiver determines the GNSS signal transit time by correlating a locally generated version of the satellite PRN code with the received satellite signal. The internally generated signals can be shifted in time until maximum correlation occurs. The time corresponding to maximum correlation of the two signals minus to the known time at which the satellite generated the signal is stands for the transit time. Ideally, the correlation envelope is symmetric about a maximum value. This symmetry simplifies the process of determining the peak correlation time.

Multipath errors are due to reflected signals from surface near the receiver shift the correlation peak and corrupt the theoretically symmetric receiver correlation envelope. These changes to the correlation envelope result in erroneous pseudorange measurements.

3.2.1.4.1 Single Frequency Mode

A model for multipath error has been established by RTCA for GPS L1 C/A code users. The results are presented in the ICAO's SARPs [ICAO, 2006] as a standard curve describing the standard deviation of the smoothed error due to multipath for airborne equipment as a function of the GPS satellite elevation angle. The Federal Aviation Administration (FAA), Boeing and Honeywell validated this model for GPS L1 C/A thanks to data collected during a real flight [Murphy and Booth, 2000].

Thus, the standard deviation of the smoothed multipath error for GPS-L1 C/A airborne equipment during approaches (NPA to CAT 1, including runway rolling) is described in [ICAO, 2006] is as follows:

$$\sigma_{multipath,smoothed} = 0.13 + 0.53 \times e^{-\frac{\theta}{10}} \tag{3.21}$$

Where θ is the elevation angle of the satellite.

Firstly, to be conservative and before further validation, the L1 C/A SARPs [ICAO, 2006] error curve is used for the other GNSS signals in the European MOPS [EUROCAE, 2010]. Studies have shown that smaller error can be anticipated for GPS L1C, GPS L5, Galileo E1 and E5a since a flat sigma curve referring to a constant deviation of 7 cm for any elevation is proposed [Macabiau et al., 2006].

Secondly, as it will be explained later, we will not consider the code carrier smoothing of the pseudorange measurements in our study. In that way, we decided to use by extension of the unsmoothed standardized model, an unsmoothed multipath error model. Then, the standard deviation of the unsmoothed multipath error GPS-L1 C/A (and by extension for GPS L1C, GPS L5, GALILEO E1 and E5a) airborne equipment for en-route to CAT 1 operations (including runway rolling) is set to:

$$\sigma_{multipath,smoothed} = \frac{\sigma_{multipath,unsmoothed}}{\sqrt{2 \cdot \tau_{smooth}}} \tag{3.22}$$

Where $\tau_{smooth} = 100\ s$ correspond to the standard smoothing time constant after code carrier smoothing(see [ICAO, 2006]).

3.2.1.4.2 Dual Frequency Mode

As described in 3.2.1.2, the use of iono-free measurements removes most of the ionospheric delays but amplifies the receiver thermal noise. Assuming that the multipath error sources are independent at each frequency, residual multipath standard deviation error in dual frequency is as follows:

$$\sigma^2_{mp,iono-free} = k^2_{L1/E1} \cdot \sigma^2_{mp,L1/E1} + k^2_{L5/E5a} \cdot \sigma^2_{mp,L5/E5a} \tag{3.23}$$

Where:

- $k^2_{L1/E1} = \frac{f^2_{L1/E1}}{f^2_{L1/E1} - f^2_{L5/E5a}}$.
- $k^2_{L5/E5a} = \frac{f^2_{L5/E5a}}{f^2_{L5/E5a} - f^2_{L1/E1}}$.
- Both signals (GPS and GALILEO) multipath standard deviations can be modeled in that way and assuming: $\sigma_{mp,L1/E1} = \sigma_{mp,L5/E5a} = \sigma_{multipath,\mathrm{un}smoothed}$, as defined in (3.21) and (3.22), the iono-free standard deviation for the unsmoothed multipath error is:

$$\sigma_{mp,iono-free} = \sigma_{multipath,unsmoothed} \cdot \sqrt{k^2_{L1/E1} + k^2_{L5/E5a}} \tag{3.24}$$

3.2.1.5 Receiver Thermal Noise Error

3.2.1.5.1 Single Frequency Mode

The presence of thermal noise at the receiver front-end perturbs the tracking process and causes thermal noise errors on the code pseudo-range measurement estimates [Kaplan and Hegarty, 2006]. The standard deviation of the nominal thermal noise code errors depends on the DLL discriminator. In the case of the Early-Minus Late Power (EMLP) discriminator, which is widely used in civil aviation applications, the variance is given by Betz formula [Betz and Kolodziejski, 2009]:

$$\sigma^2_{noise} = c^2 \frac{B_L(1 - 0.5B_L T_I)\int_{-B/2}^{B/2} G_S(f)\sin^2(\pi f d)\,df}{\frac{C}{N_0}\left(\int_{-B/2}^{B/2} 2\pi f G_S(f)\sin(\pi f d)\,df\right)^2} \cdot \left[1 + \frac{\int_{-B/2}^{B/2} G_S(f)\cos^2(\pi f d)\,df}{\frac{C}{N_0} T_I \left(\int_{-B/2}^{B/2} G_S(f)\cos(\pi f d)\,df\right)^2}\right] \tag{3.25}$$

Where :

- c is the speed of light.
- B_L is the one-sided equivalent rectangular bandwidth of the DLL.
- T_I is the integration time.
- G_S is the normalized signal power spectral density.
- d is the two-sided early-late spacing.
- $\frac{C}{N_0}$ is the signal to noise ratio.

Note that this model is adequate when the loops implemented are derived from an analog loop model using an approximate analog to discrete-time transform. When the loops are directly designed in the digital domain using [Stephens and Thomas, 1995], the term $(1 - 0.5B_L T_I)$ can be removed.

As we will not consider code carrier smoothing in our study, the variance of the thermal noise residual error for a single frequency receiver will be as presented in (3.25)

3.2.1.5.2 Dual Frequency Mode

As detailed in 3.2.1.5.2 for iono-free unsmoothed multipath error standard deviation, we can set the iono-free unsmoothed receiver noise error standard deviation as follows:

$$\sigma^2_{noise,iono-free} = k^2_{L1/E1} \cdot \sigma^2_{noise,L1/E1} + k^2_{L5/E5a} \cdot \sigma^2_{noise,L5/E5a} \tag{3.26}$$

Where:

- $k^2_{L1/E1} = \frac{f^2_{L1/E1}}{f^2_{L1/E1} - f^2_{L5/E5a}}$.
- $k^2_{L5/E5a} = \frac{f^2_{L5/E5a}}{f^2_{L5/E5a} - f^2_{L1/E1}}$.

3.2.1.6 Synthesis

The User Equivalent Range Error (UERE) reflects the error budget of pseudorange measurements. It is based on the computation of the different error contribution presented in the current part: Ephemeris errors and satellite clock offset, troposphere, ionosphere, multipath and receiver thermal noise residual error.

Assuming all the contributions are independent of each other, the UERE Is variance is as follows:

$$\sigma^2_{UERE} = \sigma^2_{Sat/Eph} + \sigma^2_{iono} + \sigma^2_{tropo} + \sigma^2_{mp} + \sigma^2_{noise} \tag{3.27}$$

3.2.2 Temporal Correlation

3.2.2.1 First Order Gauss-Markov process

All of the errors described previously are also correlated in time. That time correlation is usually modeled with a first order Gauss-Markov (GM) process and is standardized in ICAO's documents [ICAO, 2009]. A GM process is a stationary process that has exponential autocorrelation function. GM processes are described with a relatively simple mathematical formulation and can represent a large number of physical processes with a good accuracy. These two points are very important because, GM processes will be largely used in our study: for generating nominal measurement errors or for modeling bias that we want to estimate in our solution (the complete description of the solution will be done in a next chapter).

A first order GM process is described by the following continuous equation of time:

$$\dot{x} = -\frac{1}{\tau} \cdot x + w \tag{3.28}$$

Where:

- x is the GM random process with zero mean and variance σ_x^2
- τ is the correlation time of the error.
- w is the driven noise of the process with zero mean and variance σ_w^2

The autocorrelation function of a first order Gauss-Markov process is exponential with the following expression and is illustrated in Figure 9 [El-Diasty and Pagiatakis, 2009].

$$R(T) = E[x(t) \cdot x(t+T)] = \sigma_x^2 \cdot e^{-\frac{|T|}{\tau}} \tag{3.29}$$

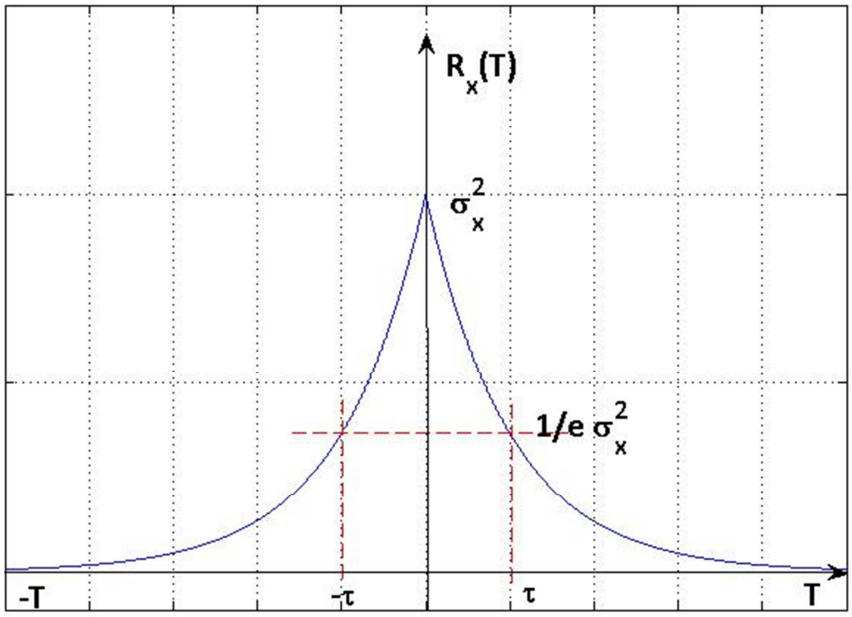

Figure 9 – Autocorrelation function of the first-order Gauss-Markov process

The discrete time model of the GM random process (for implementation) is as follows:

$$x(k) = e^{-\frac{\Delta t}{\tau}} \cdot x(k-1) + w(k) \tag{3.30}$$

Where:

- $x(k)$ is the value of the process at instant k
- Δt is the sampling period
- τ is the correlation time of the process
- $w(k)$ is value of the driven noise at instant k

Finally as explained previously, the expression of the discrete time GM process presented in (3.30) will be largely used in our study for modeling error contributions on pseudorange measurements (for the generation of simulated data) and for modeling biases in our solution. Only two parameters are needed for entirely describing the GM process: the correlation time τ and the driven noise variance σ_w^2.

In discrete time, the driven noise variance can be easily deduced from the variance of the global process using the following relation:

$$\sigma_w^2 = \sigma_x^2 \cdot \left(1 - e^{-\frac{2\Delta t}{\tau}}\right) \tag{3.31}$$

The second parameter needed for the generation of adapted GM processes for the different error contribution on GNSS pseudorange measurements is the correlation time. The next part presents the values of correlation time for the nominal error components introduced in 3.2.1.

3.2.2.2 Ephemeris and Satellite Clock Error Correlation Time

Orbital parameter errors and ranging errors due to inaccuracies in the clock drift corrections are currently re-initialized every few hours through updates from the control segment [ICAO, 2009]. In addition, these errors vary slowly then the correlation time is long (about 2 hours). Thus, the correlation time of the raw code ranging errors due to satellite clock and ephemeris inaccuracies can be set to $\tau_{Sat/Eph} = 3600\ s$ as presented in [ICAO, 2009] and [EUROCAE, 2010]. This reduction is based on the average satellite visibility.

3.2.2.3 Ionospheric Error Correlation Time

Ionospheric errors are modeled using the International Ionosphere Reference 2001 model [ICAO, 2009]. For both GPS and GALILEO signals, the correlation time of the raw code residual ionospheric ranging errors is set to $\tau_{iono,GPS} = 1800\ s$ in [ICAO, 2009] and [EUROCAE, 2010].

3.2.2.4 Tropospheric Error Correlation time

Tropospheric errors are modeled using the standard civil aviation model assuming in [ICAO, 2009] that the correlation time can be set to $\tau_{tropo} = 1800\ s$. This correlation time is representative of a typical storm system passing through.

3.2.2.5 Multipath Error Correlation Time

Usual multipath errors, whose model is standardized for civil aviation [ICAO, 2006] and applicable in flight, is impacted by the carrier phase smoothing process. In that way, the resulting multipath correlation time is similar to the value of the smoothing time constant ($\tau_{smooth} = 100\ s$). However, when assuming an integrated inertial/GNSS solution as we proposed in our study, carrier phase smoothing is not performed. As we derived an unsmoothed multipath error model in 3.2.1.4, the correlation time used for the following of the study will be set at $\tau_{mp} = 1\ s$.

3.2.2.6 Receiver Thermal Noise Correlation Time

The receiver noise error correlation time is driven by the DLL bandwidth [Martineau, 2008]. Hence, the correlation time of the single-frequency and iono-free raw code ranging errors due to receiver noise is $\tau_{noise} = 1/B_L = 1\ s$ [Salos, 2012].

3.2.3 GNSS Code Pseudorange Measurement Model

Finally, the nominal code pseudorange measurement, after corrections based on standard models, made by a receiver for a given satellite *i* at epoch *k* can be modeled as follows:

$$\tilde{P}^i(k) = \rho^i(k) + cb_H(k) + \epsilon^i_{Sat/Eph}(k) + \epsilon^i_{iono}(k) + \epsilon^i_{tropo}(k) + \epsilon^i_{mp}(k) + \epsilon^i_{noise}(k) \quad (3.32)$$

Where:

- $\tilde{P}$ is the code pseudorange measurement in meters.
- ρ is the geometrical distance between the receiver and the satellite.
- c is the speed of light.
- b_H is the user time offset.
- $\epsilon_{Sat/Eph}$ is bias induced by the residual ephemeris and the satellite clock errors.
- ϵ_{iono} is the bias induced by the residual ionosphere delay.
- ϵ_{tropo} is the bias induced by the residual tropospheric delay.
- ϵ_{mp} is the bias induced by the residual code multipath delay.
- ϵ_{noise} is the bias induced by the residual thermal noise on the measurement.

3.2.4 Synthesis

A GNSS receiver provides high fidelity position and velocity estimates with bounded errors. However, GNSS SIS is very sensitive to external perturbations, which can degrade the navigation solution performance of even interrupt the service. An important issue when using GNSS as a stand-alone navigation means is the signal interruption, which can be caused by shading of the receiver antenna by any obstacle (natural or not) or by interference from an external source.

In addition, when only three satellites signals are available, most of the receivers revert to a two-dimensional mode by using either the last known height or a height computed from an external source. Indeed a complete resolution of the 3D positioning equation using pseudorange measurements requires the reception of at least four signals.

Finally, GNSS advantage is mainly the ability to provide a position in almost every location on the Earth with a bounded position error. In the civil aviation context, the main issue remains the difficulty to ensure the continuity of the coverage during a critical operation and the ability to detect failures or non-nominal errors affecting the GNSS measurements that can induce catastrophic position errors without alerting the user.

3.3 GNSS and INS Error Model Synthesis

Table 7 aims at summarizing the error models for the GNSS code pseudorange and inertial measurements.

Sensor	Error Source	Model	Error Characteristics	
			PSD	Temporal
GNSS	URA	GM*	$\sigma_{Sat/Eph} = 0.85\ m$	$\tau_{Sat/Eph} = 3600\ s$
	Ionosphere	GM	$\sigma_{iono,L1} = \sigma_{iono,vertical,L1} \cdot F$ (Klobuchar)	$\tau_{iono,GPS} = 1800\ s$
			$\sigma_{iono,L5} = \left(\frac{f_{L1}}{f_{L5}}\right)^2 \cdot \sigma_{iono,L1}$	
			$\sigma_{iono,E1} = \sigma_{iono,vertical,E1} \cdot F$ (NeQuick)	
			$\sigma_{iono,E5a} = \left(\frac{f_{E1}}{f_{E5a}}\right)^2 \cdot \sigma_{iono,E1}$	
			$\sigma_{iono,L1/L5} = 0$	
			$\sigma_{iono,E1/E5a} = 0$	
	Troposphere	GM	$\sigma_{tropo} = 0.12 \cdot F_{tropo}$	$\tau_{tropo} = 1800\ s$
	Multipath	GM	$\sigma_{mp} = 0.13 + 0.53 \times e^{-\frac{elevation}{10}}$	$\tau_{mp} = 1\ s$
			$\sigma_{mp,iono-free} = \sigma_{mp} \cdot \sqrt{k_{L1/E1}^2 + k_{L5/E5a}^2}$	
	Receiver Thermal Noise	GM	$\sigma_{noise,L1/E1}$ (Betz Formula)	$\tau_{noise} = 1\ s$
			$\sigma_{noise,L5/E5a}$ (Betz Formula)	
			$\sigma_{noise,iono-free} = \sqrt{k_{L1/E1}^2 \cdot \sigma_{L1/E1}^2 + k_{L5/E5a}^2 \cdot \sigma_{L5/E5a}^2}$	
Accel	Repeatability Bias	C*	/	/
	Stability Bias	GM or FN*	See Table 5	See Table 5
	Scale Factor	C	/	/
	Misalignment	C		
	Noise	G	See Table 5	
Gyro	Repeatability	C	/	/
	Stability	GM or FN	See Table 5	See Table 5
	Scale Factor	C	/	/
	Misalignment	C		
	Noise	G	See Table 5	
Baro	Measurement Noise	G	$\sigma_b = 5m$	/

*GM: Gauss-Markov
*G: Gaussian
*C: Constant
*FN: Flicker Noise
*PSD: Power Spectrum Density for the Random Entities

Table 7 – Error models synthesis

3.4 GNSS/INS Hybridization

3.4.1 Interest in GNSS/INS Hybridization

Hybridized navigation systems consist in combining navigation means that have complementary performances. In the case of GNSS/INS hybridizations, strong and weak points (synthetized in 3.1.5 and 3.2.4 and reminded in the Table 8) have very complementary characteristics. Navigation employing GNSS and inertial sensors is a synergistic relationship. Integration of these two types of sensors produces a system whose performance exceeds that of each of the individual sensors.

System	Strong points	Weak points
GNSS	– Bounded Accuracy, – Global coverage, – Reduced cost and size	– Very sensitive to external perturbations – Integrity monitoring required – Continuity of Service not always ensured
INS	– Very good short term accuracy (and stability), – Continuity of service, – High rate data and dynamic – Immunity from external perturbations, self-contained and autonomous system – Provides a full navigation solution (position, attitude, velocity and acceleration)	– Unbounded errors (error drift), – Alignment required, – Important cost and size – Vertical channel fast divergence

Table 8 – GNSS/INS complementarities

Advantage in coupling GNSS receivers with INS is not only an improvement in terms of accuracy but an improvement in availability and integrity of the system. In addition, when GNSS data are no more available, the inertial solution may still be estimated for few minutes using the propagation model of the inertial sensors. It is called coasting and it represents an important improvement in terms of continuity of service.

As reminded in the previous table, strong and weak points of GNSS and INS are numerous. However, depending on the characteristics of the solution we want to provide, several configuration exists. They allow insisting on a particular advantage or focusing on the compensation of a certain drawback. The next section will introduce the main types of existing hybridization architectures with a brief description of the interest of each configuration.

3.4.2 Hybridization Architectures

There are three main ways of coupling INS with GNSS receiver. The integration mainly depends on the GNSS measurements available and on the hybridized solution.

In a ***loose coupling architecture***, GNSS receiver and INS operate as independent navigation systems. Outputs of the two systems are coupled using an estimator in order to form a third navigation solution. This solution is the simplest and least expensive because it only deals with the separate outputs of the INS and GNSS receiver. However, the main drawback of this solution is that the integration can be done only if the GNSS receiver is able to compute a position solution (that is to say if there are 4 available pseudorange measurements at least).

In a ***tight coupling architecture***, GNSS receiver and INS do not provide a navigation solution but are only considered as sensors. The fusion algorithm provides a single navigation solution. Generally, the tight coupled architecture provides a more accurate solution than the loose coupled architecture. In addition this architecture integrates directly pseudoranges measurements and then does not use a GNSS position solution (that requires at least 4 visible satellites). However, only one navigation solution is provided instead of three in the loose coupling architecture.

Finally, in ***a deep (or ultra-tight) coupling architecture***, GNSS receiver architecture is no longer considered as a navigation system able to provide a navigation solution. The INS is a constituent of the GNSS receiver. In that case, GNSS receiver robustness is improved and the solution is better than in the tight coupling architecture. However, complexity of the deep coupling architecture is the major drawback of that integration and the redundancy is also sacrificed.

In the particular cases of a loose coupling or tight coupling architectures, there are two types of configurations: *open-loop* or *closed-loop*.

- In an *open-loop configuration*, the GNSS receiver processes the pseudoranges of the tracked satellites without using feedback of the integration filter output. Movements of the platform are experienced by the sensors and all the measurements are processed to get the position, velocity and attitude of the IMU. Data from the two navigation systems are then combined and fed into the Kalman filter as measurements. The filter estimates the INS errors according to the models implemented, and the corrections are added to the output of the inertial navigation algorithm. The INS platform outputs keep on drifting due to sensor errors, which are not compensated, and due to the integration errors. When high quality sensors are used, this solution is preferred because of the relative independence between the GNSS errors and the INS mechanization.
- In a *closed-loop configuration*, a feedback loop is used to correct the raw sensor output and other mechanization parameters using the error estimates obtained from the integration filter. The feedback configuration has better accuracy since the linearization error is smaller. But a detected error in any of the navigation sources is more difficult to correct since the complete solution is defected by this error. This configuration is particularly employed when low-cost inertial sensors are used. In a tight coupling architecture, the feedback loop can also return in the GNSS receiver to help tracking loops; in particular during high dynamics movement when tracking

signals is more difficult. A major drawback of this configuration is that GNSS receiver delivers a solution, which depends on inertial solution and a failure of an inertial sensor will affect hybridized solution and then the receiver solution.

In a tight or loose coupling architecture, closed or open loop configurations integrate outputs of a GNSS receiver (pseudorange or positon) with an INS. In both architectures, GNSS data are directly used in order to correct inertial drifting errors and to compensate alignment defaults. However, several types of perturbations can affect the GNSS SIS and induce failures or non-nominal measurement errors or strong erroneous position that will impact and corrupt the INS. In that way, in current on-board GNSS/INS hybridized solutions, it is required to provide an integrity monitoring solution for the GNSS data before or during the hybridization. The next section presents the main existing solution already implemented on-board.

3.4.3 GNSS in On-board Hybridization

GNSS/INS coupling solutions on board assume that the data provided by the GNSS receiver have been monitored. Nevertheless, the current integrity monitoring provided by the ground segment of GNSS does not fulfill the requirements established by the ICAO. Then, an additional integrity monitoring should be provided in order to use a GNSS/INS hybridized navigation solution. This additional integrity monitoring can be ensured by the ground (using SBAS or GBAS augmentations) or on board (using the ABAS augmentation).

In the case of the loose coupling architecture, the GNSS data must be monitored before the coupling process. A Receiver Autonomous Integrity Monitoring (RAIM) algorithm is then used. This algorithm is only based on the use of the redundant GNSS measurements. In the case of the tight coupling hybridization, the integrity monitoring is ensured by an Aircraft Autonomous Integrity Monitoring (AAIM) algorithm is performed, allowing using INS data for the integrity monitoring.

Finally, current on-board hybridization architectures only integrate GPS L1 C/A code pseudorange measurements. In that configuration, the GPS receiver is considered as an aiding source for INS error compensation. The coupling is performed in open-loop so as to avoid any propagation of the errors between the two systems. In addition, since the hybridization process induces a smoothing on the estimated parameters, the code pseudorange measurements provided by the receiver are not smoothed by the code carrier filter.

3.4.4 Synthesis

The current hybridized solution used on board is relatively limited with respect to the potential possibilities of coupling between the several aircraft systems. Moreover, future GNSS receivers will integrate dual constellation and dual frequencies signals, then the first upgrades should be the integrations of these new signals. As a first step, the

expected improvements can be an additional redundancy and a reduction of some error pseudorange residual errors (use of iono-free measurements).

Anyway, the current solution estimates several hybrid parameters (position, velocity, attitude, altitude, vertical speed…) but for now, only the hybrid position is really used for navigation solution. The reason is mainly because position is nowadays the most important parameter for navigation. But, another reason is because there is no standardized solution providing an integrity monitoring solution for other parameters (velocity, attitude…). Our study did not focus only on position estimation, but on providing most of the navigation parameters that can be used in the future on board. This idea goes along with the global multi-sensor architecture concept that can be seen as the main provider of most of the parameters needed for navigation.

Finally, the most stringent requirements for precision approaches or automatic landings cannot be reached with the current GNSS/INS hybridization. Then, the integration of multiple sources of measurement on board should allow improving the reliability of the solution by gathering all the advantages of each source. In addition, such architecture could allow performing more stringent operations such as precision approaches using sensor that are not currently involved in the hybridization filter.

3.5 Other sensors

3.5.1 GNSS

As depicted previously, current GNSS signal use in hybridization architecture is only the GPS L1 C/A signal. A first improvement should be to consider more GNSS signals. Then, in the framework of the Ph.D. thesis, the considered GNSS measurements are GPS and Galileo code pseudorange measurements on L1, L5, E1 and E5a frequencies. The set of possible combinations is as follows:

- GNSS single frequency single constellation receiver (GPS L1, GPS L5, GALILEO E1 or GALILEO E5a)
- GNSS dual frequency single constellation receiver (GPS L1 and L5 or GALILEO E1 and E5a)
- GNSS single frequency dual constellation (GPS L1 and GALILEO E1)
- GPS dual frequency dual constellation (GPS L1, GPS L5, GALILEO E1 and GALILEO E5a)

Interest in considering new signals for hybridization is mainly the multiplication of aiding source measurements integrated into the filter. Compared with the current GPS L1 C/A integration, dual frequency pseudorange measurements allows removing most of the ionosphere delay (see section 3.2.1.2). In addition, in a tight coupling configuration (when the GNSS receiver provides pseudorange measurements), the multiplication of signals and satellites adds redundancy, useful for integrity monitoring or simply for compensation of any loose of satellites (masking or failure). Finally, a coupling architecture able to integrate

most of the signals provided by a GNSS receiver (GPS L1/L5, GALILEO E1,E5a) could be an advantage for establishing a robust hybrid navigation solution.

3.5.2 Wheel Speed Sensor

A Wheel speed sensor (WSS), or tachometer, is a motion sensor, mounted on a wheel, which can directly sense the rotation rate of the associated wheel. The measurement provided can be an angular rate but can also be a linear velocity when the radius of the wheel is well known. However, the true value of the radius of the wheel (in real-time) is really hard to estimate, mainly because of variations in the pressure of the ties, of the nominal radius of the wheel, of the velocity of the mobile (that causes tire stretching) or of the state of the road. A tachometer can also measure the distance traveled by the wheel, in that case it is called odometer.

In our study, we decided to focus on the velocity measurement provided by the sensor. This decision has been taken because we wanted to develop a WSS measurement generator to measurements of WSS linear velocity obtained during a real flight. The radius variation issues have been considered in our study and the measurement model is described in Appendix B.

Thus, the measurement provided by the tachometer that is considered in the thesis is the longitudinal earth relative velocity of the mobile $v_{WSS} = \left(v^m_{m/e}\right)_1$. The subscript 1 denotes the first component of the velocity vector.

Interest in tachometer sensors mounted on an aircraft landing gear is mainly provided by their redundancy and the reliability of their measurements. Yet, in our study an important hypothesis has to be set when using a tachometer measurement: the wheel is not affected with lateral drift as any lateral displacement of the wheel cannot be measured by the tachometer. This hypothesis is called the non-holonomic hypothesis. That assumption can be considered as valid as the operations concerned by the use of tachometer and considered in the Ph.D. thesis are runway take-off and landing; and especially during take-off, the motion can be considered as a linear motion without any drift. However landing operations can present some drift sequences so that the non-holonomic hypothesis could be adjusted in a future work.

The idea of integrating WSS has also been driven knowing that on current aircraft (for example on an A380), we can have access to up to 20 tachometer measurements. Figure 10 presents a diagram of the repartition of wheel speed sensors on the A380 landing gear. In a scenario where we use real WSS measurements, the lever arm between the different WSS and the other sensors integrated in our solution should be taken into account. However, in our simulations we only focused on simulated data so we did not add lever arm compensation.

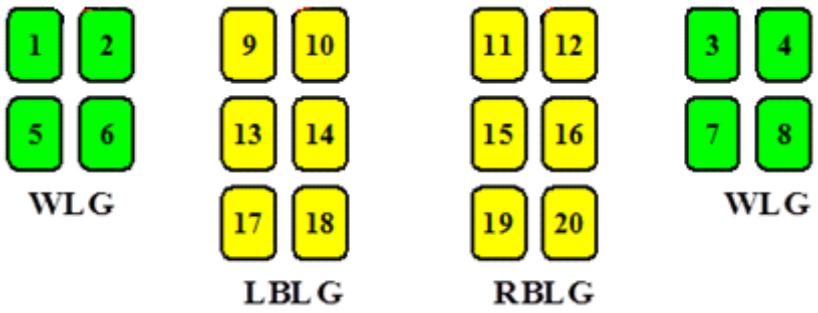

Figure 10 – Identification and location of tachometers on a A380 [AIRBUS, 2012]

3.5.3 Video

Video is currently more and more used for navigation purpose: in robotic [Jia, 2008] or [Blaer and Allen, 2002], indoor navigation [Wang et al., 2006] or Unmanned Aerial Vehicles (UAVs) [Conte and Doherty, 2008], [Azinheira and Rives, 2008] or [Merino et al., 2006]. Video based navigation offers a wide range of possibilities mainly driven by the context, the performance requirements, the mobile, the environment, the sensors, the meteorological conditions and many other parameters.

In the particular context of civil aviation, video based navigation is currently limited to an aid provided to the pilot during ground maneuvers (following taxilanes, when reaching gate…). The only other use of video in an aircraft is for passenger entertaining when we can observe several views of the aircraft during a long flight.

In addition, some aircraft are already equipped with cameras: for example on the A380 and A350 there are three cameras:

- The Bus Tie AC Contactor (BTAC) camera is a forward pointing camera mounted under the fuselage. The image is centered on the Nose Landing Gear (NLG).
- The Fuel Tank Access Cover (FTAC) camera is a forward pointing camera mounted on the leading edge of the tailfin. The image is centered on the Main Landing Gear (MLG).
- The Direct Lift Control (DLC) camera (only on A350) is a down pointing camera mounted under the fuselage.

In that way, a particular interest has been found in the study of the video for navigation purpose. Indeed, image provided by a video sensor contains geometrical information useful for navigation in flight or on the ground. This information may be extracted from an image with an adapted image processing algorithm. It is fundamental to understand that this process has not been studied in the framework of this thesis. We will only focus on the type of measurements generated by this image processing block. However, some parallel studies have been launched trying to assess the feasibility of the proposed solution (see Chapter 4).

One of the most important parts of the Ph.D. thesis was to study video based navigation possibilities and to propose a solution for integrating measurement obtained from a camera able to improve navigation performance (improve accuracy, replace other sensors or simply add redundancy). A detailed study of video in the context of our study is proposed in the Chapter 4.

Image sensor technology can be of different types: those that can sense visible light, infrared (or thermal) or low light (night vision cameras). We decided to free from this constraint by considering that an image processing algorithm could treat images provides by a visible light camera as well as images provided by a night vision camera.

The idea was then to try to use video in order to provide geometrical information that can be used for navigation during approach and landing operations (translation vectors and rotations between successive images, lateral, vertical or angular deviations with respect to a reference trajectory, velocity with respect to the ground or to the environment, obstacle relative position…

3.6 Conclusion

The current chapter has introduced the two current main navigation system used as navigation means for commercial aircraft: GNSS and INS. It has also detailed and presented the characteristics and properties of coupling those systems in a global architecture called hybridization. In that way, interest of hybridizing a GNSS receiver with an INS has been described with a particular focus on strong and weak points of the existing solutions.

Finally, the last section of the chapter has introduced other sensors or systems that could be interesting for extending the hybridization architecture. Based on the characteristics of the existing solution, a globalization of the hybridization integrating more sensors can provide benefits for reaching the most stringent navigation requirements.

In the framework of the thesis, the study of the video for navigation has been particularly focused. In that way, the next chapter provides a detailed study of video-based navigation methods and interest in coupling a video system with the existing navigation systems.

Chapter 4 : Video Aiding

The current chapter introduces video as a sensor that can be used for navigation purposes. Studies involving video as a navigation mean are currently conducted for a large set of applications and in various contexts. Possible uses are numerous and strongly depend on the environment, the level of performance needed or required, the number of degrees of freedom of the vehicle, the knowledge of the environment, the visibility conditions, the sensor characteristics and some other parameters. Before trying to integrate video in our solution, it was required to detail the main video based navigation methods in order to propose, describe and justify a concrete scheme of integration of video in a global hybridization architecture.

The first part of the chapter synthetizes the main results of a review of the state of the art of video based navigation methods that gives an overview of what can be find in the literature involving video sensors. At the end of this review a general classification is proposed for video-based navigations methods.

The second part describes more precisely the video sensor (focusing on the camera models and image representations). This part also provides context elements and characteristics of the video solution proposed in our study. It gives the detailed measurement model for the measurements provided by the video system that we are considering.

The third part presents the preliminary results of an algorithm that deals with the detection of a runway in an image.

4.1 Video Based Navigation Overview

Visual navigation is one of the oldest known navigation method based on the observation of the heavens (it was called celestial navigation). Some of the navigators used equipment to determine angles between stars and horizon or vertical, and then to estimate their position. Basic principle of visual navigation is defined by a simple fact: the observation of the world and objects around us is the most reliable information for deducing our relative position with respect to our environment. In that way, video seems to be a sensor that offers a wide range of applications.

Improvement of low-cost, light and high resolution video sensors has led to an interest in extracting accurate navigation information such as position, velocity or attitude from an optical measurement. Cameras are currently available on board of some aircraft and they are mainly used to assist the pilot for ground navigation or to entertain the passengers during flights. However, observation of the surrounding scenery can be considered as a good source of information for navigation purpose. For instance, an image flow measurement can be representative of the position, the velocity and the orientation of the aircraft. But a correct transcription of the details in the landscape can only be done taking into consideration physical limitations and characteristics of the video sensor: resolution, field of view, dimension and position of the sensor.

Visual measurements can provide a lot of information from a simple image. A basic digital optical sensor measures the intensity of the light entering an aperture with a Charge-Coupled Device (CCD) or a Complementary Metal-Oxyde-Semiconductor (CMOS). This measurement, as a snapshot of the surrounding scenery, provides information of light intensity at each pixel that constitutes the sensor. An optical sensor is most of the time associated to an image processing algorithm that allows detecting particular pixels in the image. These pixels are image points of specific areas in the scenery that we want to detect and the resulting structure in the image (a dot, an edge, a line, a particular shape) is called a feature. Finally, the information that can be extracted from these features, such as their absolute or relative positions in the image plane can contain geometric information that can be used for navigation purpose.

A lot of methods and algorithms involving video sensors for navigation can be found in the literature. The next section tends to provide some important aspects that have been identified during a detailed state of the art done in our study.

4.1.1 *Topological Localization*

Topological cartography deals with a discrete representation of the environment without scale metric necessity. The localization then aims at recovering a location in the topological space. This topological representation appears in video-based navigation methods described in [Gaspar et al., 2000], [Angeli et al., 2009] and [Fraundorfer et al., 2007]. [Ulrich and Nourbakhsh, 2000] used a topological approach for the localization of a

mobile robot in a relatively closed environment (indoor or along a road). Figure 11 presents an example of a topological map of an environment.

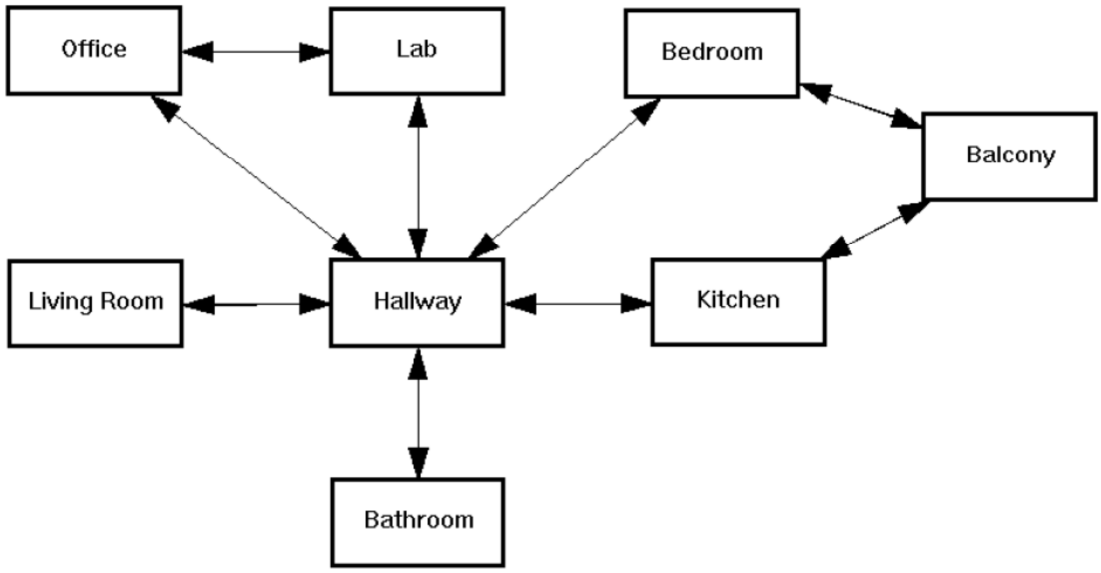

Figure 11 – Environment graph of an apartment [Ulrich and Nourbakhsh, 2000]

In that figure, a topological map of an example environment is proposed that illustrates only relationships between rooms of the apartment. The map is reduced to the most simple elements and links between them for localization in that environment. Interest in that representation is proved only when the objective is to navigate within a restrained environment (indoor or in limited areas with interest points like tours). Navigation functions in that context are only limited to find our location in the topological representation of the environment. We have a good example of topological maps with the metro network. Most of the cities that have metro use a topological map for the illustrations of the network. In such a map, scale and distance are not realistic but we can correctly identify connections and localizations of the stations within the network.

Topological localization is directly opposed to geometric localization because it avoids maintaining a metric map of the environment and allows operating directly in the image space. Indeed, geometric localization usually uses a grid as a map representation (in two or three dimensions). Such an application allows keeping track of the mobile's exact position with respect to the map's coordinate system.

Topological map only constitutes a representation of the environment but does not provide a way for navigating or localizing in the map. In that way, [Segvic et al., 2007] presents a method of localization in a topological map for an autonomous mobile robot in two steps: a learning step and a localization step. The first step is called mapping components and it aims at acquiring images through a learning stage and then extracting interest points (or features) in these images. Construction of the "map", called environment graph is done during a previous navigation procedure with other means of

navigation (or human interaction). During this procedure, some images provided by the camera are recorded as key images, also called nodes, in order to constitute the graph. The selection of image that will constitute the graph is done based on a criterion of difference between two successive nodes: they have to be sufficiently separated to minimize the number of nodes in the final graph; but they have to have enough similarities to find common sets of features. Once the map has been constructed, the graph is completed with the set of features X_i and the scale metric s_i in each image I_i; the two-view geometry W_i, which is the relative camera pose between the two views (including rotation, translation and metric between the surrounding images) and match arrays M_i between common features in I_{i-1} and I_i in each arc i.

The topological map with all elements associated (key image, scale metric, features, two view geometry and match arrays) is illustrated in Figure 12. Each Square in the Figure represents a node of the graph.

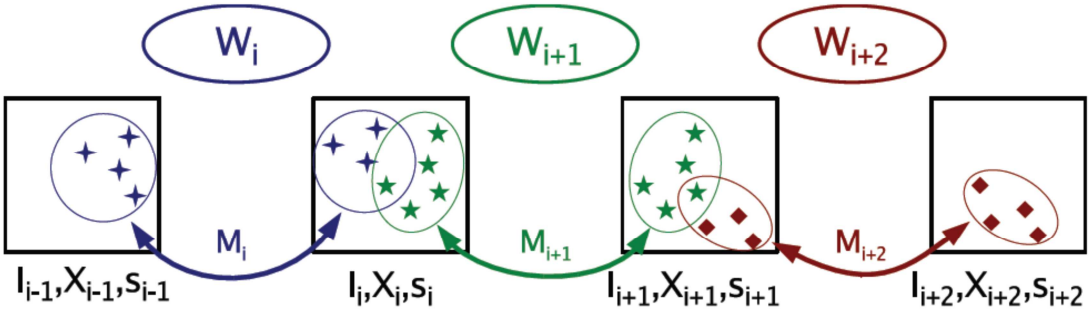

Figure 12 – Linear environment graph [Segvic et al., 2007]

The second step presented in [Segvic et al., 2007] is the localization component and aims at locating in the map previously created the current image registered by the camera. The principle of localization among the nodes of the graph is based on comparison between the current image and the reference image. It allows localizing the vehicle among the topological graph. The process of tracking features during the passing from a node to another is done by computing the two view-geometries and three-view geometries between the surrounding nodes and current image. The tracking of a feature is defined as the process of locating the feature over time in the image. The process aims at keeping the consistent features and updating the topological localization of the vehicle.

Figure 13 illustrates the localization of a given image in the topological map previously described.

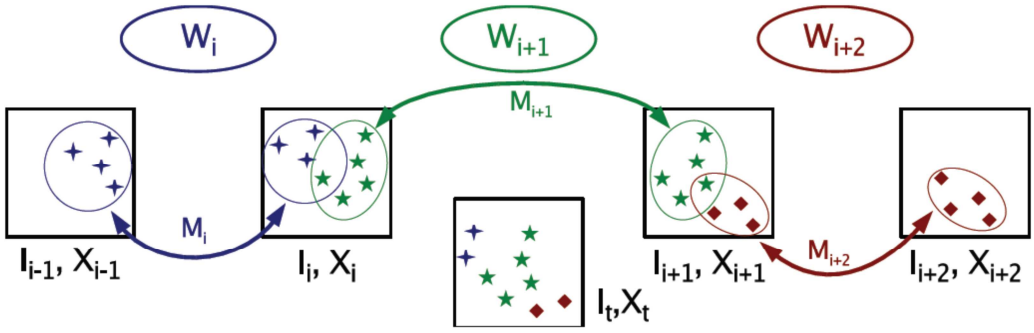

Figure 13 – Localization of the current image in the environment graph [Segvic et al., 2007]

Applications involving a topological map of the environment imply repetitive trajectories like a tour or navigation indoor. Even if the topological localization approach allows freeing from a metric constraint, it seems not really adapted for an application in an open and unknown place. In addition, this particular method does not aim at navigating with a high level of accuracy; localization is only done within a set of nodes identified in the topological map. In addition; this method does not associate the recorded images to the camera position coordinates as it only deals with localization relative to a map.

4.1.2 *Visual Servoing*

Visual servoing can be defined as the use of vision sensors to provide closed-loop feedback control of some moving component. In visual servoing, the system aims at minimizing an error function. Visual servoing methods are usually used for controlling the pose of industrial robots arms but it is also used in aircraft landing applications. [Bourquardez and Chaumette, 2007], [Goncalves et al., 2010], [Azinheira and Rives, 2008], [Rives and Azinheira, 2004], [Le Bras et al., 2009] and [Coutard et al., 2011] present image-based visual servoing for an aircraft during approach and landing. [Miller et al., 2008] uses, in addition, image registration for landing a UAV on a runway. This method is based on the comparison between a test frame composed of previously recorder image and a reference frame previously registered. The approach presented in [Miller et al., 2008] only uses visual measurements and a stack of reference frames. The navigation process is in 3 steps: the localization of the runway in each image, the estimation of the attitude of the UAV and the steering of the UAV towards the runway maintaining the correct glideslope. A forward pointing camera is mounted on the UAV and its intrinsic calibration matrix C is known (C is one of the matrix that links the homogeneous coordinates of a 3D-point with coordinates of the point projected in the image plan; it depends on the focal length, the size of the image and the coordinates of the optical center).

Navigation method used in this paper implies that during a previous flight, images have been registered to create a stack of reference frames. During this previous flight the flown trajectory is considered as the reference trajectory, the ideal glide path (see Figure 14). The set of reference images contains frames taken as the UAV gets closer to the runway and that are sampled at an increasing frequency as the altitude decreases. A preprocessing

step is necessary to annotate two particular points: the vanishing point (intersection between the horizon line and runway axis) and the beginning of the runway (more precisely the spot where the UAV should touch the ground). They are circled in yellow in Figure 14. The vanishing point and a point at the beginning of the runway (the spot where the UAV should touch down) are annotated in each frame.

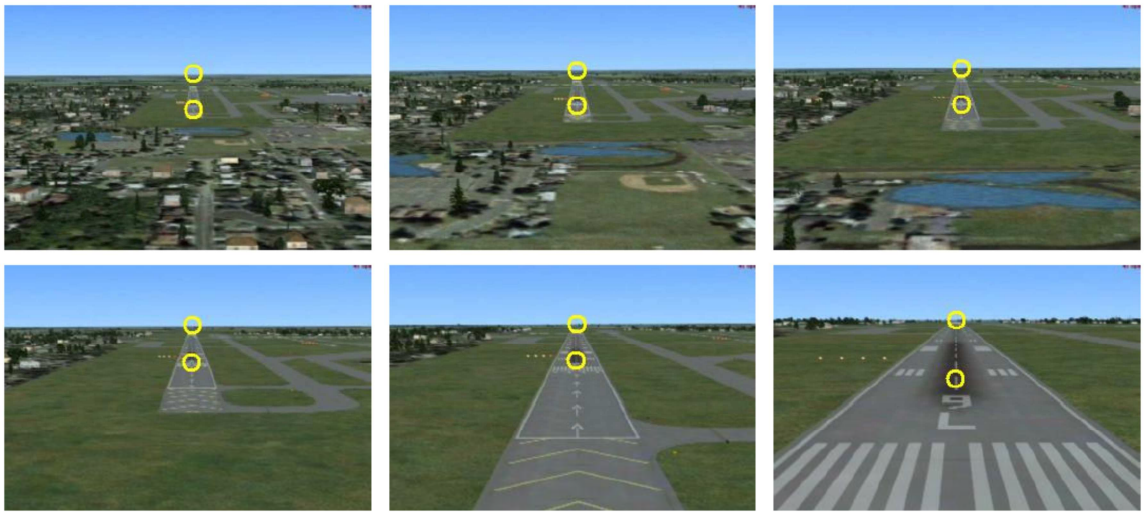

Figure 14 – Set of reference frames taken from a video as the UAV gets closer to the runway [Miller et al., 2008].

From the measured image (current frame) during landing, a Scale-Invariant Feature Transformation (SIFT) algorithm is used to compute the planar homography H. The planar homography relates any point on the ground in a particular view (the reference view) to the corresponding point in a different view (the current view). This planar homography is established between the test frame and the reference frame so that they have the most correlations. Once the best reference frame identified and H matrix computed, it is possible to project the two points annotated in the reference frame to the corresponding points in the test frame (see Figure 15).

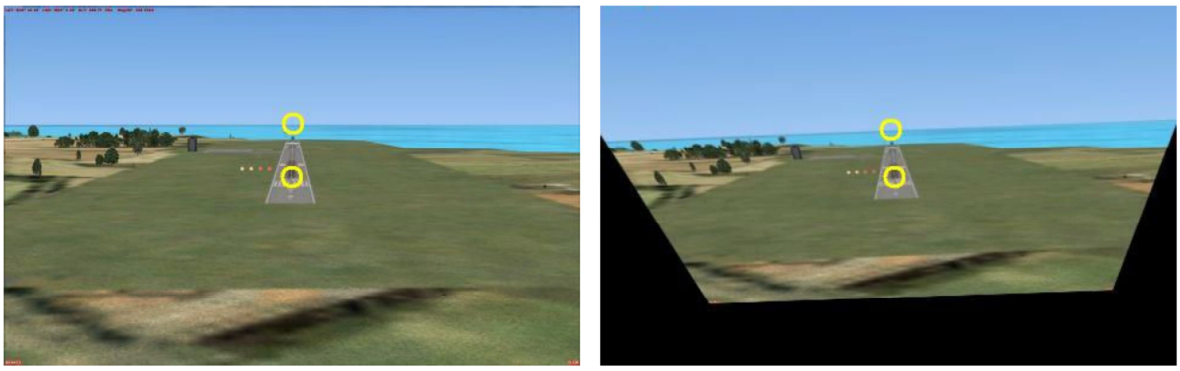

Figure 15 – Projection of two points in the test frame (on the left the reference frame, on the right the transformed reference frame in the same view as the test frame) [Miller et al., 2008]

The relative position of these two points in the test frame allows estimating the UAV attitude and steering. This technique is similar to the runway analysis conducted by a pilot during landing. Finally the geometrical information read in the test image is directly converted into a command for the actuators of the UAV. The underlying property is that the relative position of the two points in the image frame is related with the UAV attitude because usually this is based on the same interpretation as that done by the pilots when landing. The reading of the coordinates of the two annotated points (vanishing and threshold points) permits to estimate three geometrical parameters: the runway offset, the runway angle and the runway distance (see Figure 16).

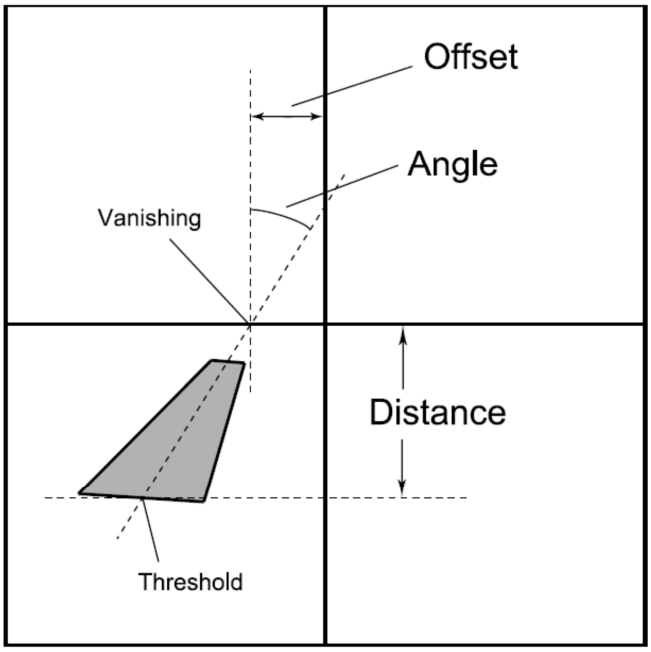

Figure 16 – Interpretation of the measured parameters in the test frame [Miller et al., 2008]

Extraction of geometric features from the image measurement allows using visual servoing techniques to minimize error of position or orientation during landing. Furthermore, it is possible to interpret these geometric features in a different way by using a metric scale. The image measurements can then provide real position parameters (height, range, and attitude). Such a method is detailed in [Doehler and Korn, 2003].

Visual servoing described in [Miller et al., 2008] appears as a way to extract geometric parameters (relative position of two features: runway threshold and runway horizon) that characterize deviation with respect to a previous trajectory, considered as the reference one. In the application described by the authors, the deviation parameters obtained with this video process are directly used as steering commands for piloting the UAV along the ideal glide path. Major interest of this method is that the video acts as a system able to provide an Instrument Landing System (ILS) axis during an approach. It is not directly an ideal descent axis but by steering the actuators of the UAV, the video tends to correct the deviation with respect to the reference axis. Indeed, this method is based on two main ideas: the video system uses a set of reference images taken during a previous

flight, which was flown with another navigation system. In other words, this method needs a reference (image database registered during a “perfect” flight). This assumption is really important because it does not allow doing that in an unknown environment or on a new airport. However, the idea highlighted here, is that it is possible to directly relate the geometry of the visible runway during an approach to provide a measurement for navigation (in that case: a deviation). The second idea is that the results of the video processing directly feed the flight commands and are not interpreted as parameter for a potential navigation computer. It seems to be possible only because of the type of vehicle presented here (a UAV) and its particular flight dynamic and the targeted level of performance.

Finally, focusing on our context of civil aircraft during approach and landing, we can identify some similarities with the previous method as the navigation toward an environment constituted of a runway (with this common rectangular shape all over the world), the targeted trajectory that the vehicle has to fly (a descent axis) or the type of vehicle, which while being an UAV has the same degrees of freedom as an aircraft. The image database assumptions cannot be considered in our study because it would represent a strong constraint for navigation (need to register images in all airports and for all aircraft). However, we could imagine replacing the reference images by reference or estimated positions and then use the video to provide deviation between the recorded images and the estimated position.

4.1.3 *Path Planning*

Path planning is the act of finding an optimal path between two locations (in other words to optimize the navigation between these two locations). Most of the time, path planning processes involve a global path planner and a local path planner. The main difference between global and local path planners is the resolution of the path: global path planning deals with large obstacles avoidance and approximated navigation and local path planning deals with small obstacles avoidance and precise navigation among the global path.

[Sinopoli et al., 2001] presents a video-based navigation method for a UAV (a helicopter) without a complete knowledge of the environment. It is based on optimal path planning trough a hierarchical approach. The method is detailed through a four-part algorithm implemented on a Flight Management System (FMS), as the vision system is coupled with the FMS. The first two steps of the algorithm, called the Strategic Planner (SP) and the Tactical Planner (TP), are respectively an offline path planning and an online local trajectory computation. The SP is the global path planner and the TP is the local path planner.

The SP step consists in creating a set of waypoints. This first part of the algorithm is not performed with the video system. However a wavelet transformation from a Digital Elevation Model (DEM) of the environment then a Dijkstra optimization algorithm are

employed to find the shortest path between two waypoints on the transformed grid (see Figure 17). The shortest path defined by the optimization algorithm also includes flight altitude information in order to guarantee a 3-D navigation.

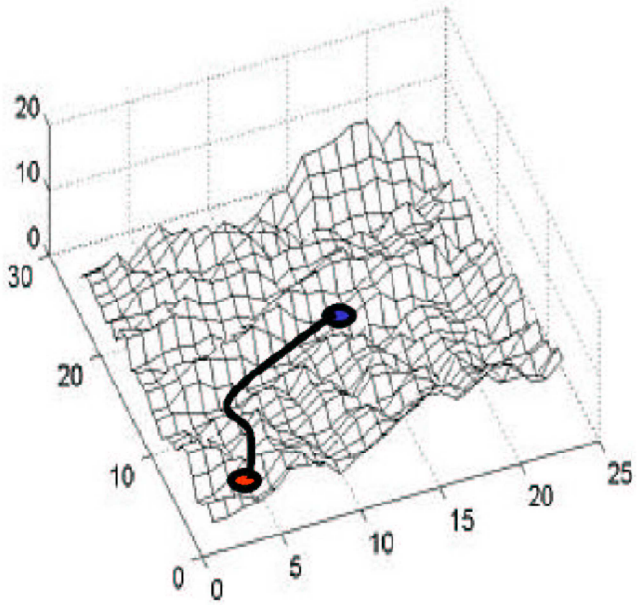

Figure 17 – Path between two waypoints on a DEM [Sinopoli et al., 2001]

The UAV is equipped with an initial knowledge of the surrounding environment through an a priori risk map. The TP is then a vision-based technique and is based on local obstacles avoidance and update of the risk map. TP consist in connecting the waypoints provided by the SP. It builds a sub-grid (see Figure 18) of known dimensions, connecting two successive waypoints and updating the risk map from the video measurements.

The method involved for updating the risk map is to use the a-priori knowledge of the trajectory (position estimated with other sensors) and of the map (established by the SP) to derive a depth parameter: the distance between the vehicle and the obstacles of the map. This depth parameter is then compared with the current video measurement that provides, thanks to an adapted image processing algorithm, the depth between the camera and the objects in the image. The result of this comparison allows modifying the risk map by deciding if the obstacle seems to be closer or not than predicted. The optimal trajectory is currently updated by choosing the path with the least risk.

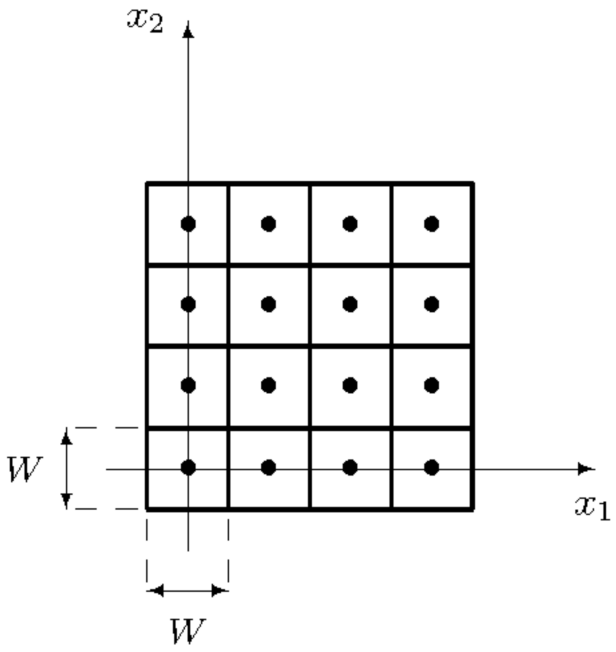

Figure 18 – Sub-grid decomposition [Sinopoli et al., 2001]

Finally, the method presented allows finding an optimal path between two selected waypoints. The navigation is done by coupling GPS, inertial measurements and a video system for obstacles detection. Such a method can be employed for autonomous navigation in a constrained area (with high relief variations or urban area). The area has to be partially known to establish an initial guess about the optimal path through a "risk map". The video main contribution is to update the path in real time in case of erroneous a-priori DEM, the apparition of an obstacle or any error in the predicted navigation path.

Video is here introduced as a sensor able to check and modify the truth of predicted and planned navigation path. Main interest is obstacle avoidance for navigation in a partially known environment: a DEM is used.

4.1.4 *Simultaneous Localization and Mapping and Visual Odometry*

Simultaneous Localization and Mapping (SLAM) techniques deal with the problem of building a map of an environment unknown by the mobile while navigating this environment using the created map. SLAM algorithms generally consist of multiple parts: landmark extraction, data association, state estimation, state update and landmark update. Each of these parts can be done in many ways [Riisgaard and Blas, 2005]. SLAM algorithms are usually implemented from a basic odometry system coupled with a range measurement sensor to locate the landmarks (laser, sonar or stereovision).

[Mirisola et al., 2007] presents a vision-based navigation method using an AHRS. The inertial sensor is mounted on the camera and provides orientation measurements. The

navigation method deals with the reconstruction of a trajectory from a sequence of images. The employed process is denoted as visual odometry because the video system aims at estimating translation vector between two successive images. The principle detailed in [Mirisola et al., 2007] is based on the estimation of the translation vector by pure homography, that is to say the determination of the relation between two sets of homogeneous pixel coordinates that represent the same points imaged from two different positions.

In that case the homography H (equation (5.1)) provides the rotation R and the translation vector t between the two views $\{\mathcal{C}\}|_i$ and $\{\mathcal{C}\}|_{i+1}$ (see Figure 19). d is the height of the camera in the view i and n is the 3D plane normal vector. λ represents the scale factor between the two successive images.

$$\lambda H = \lambda\left(R - \frac{t}{d}n^T\right) \tag{4.1}$$

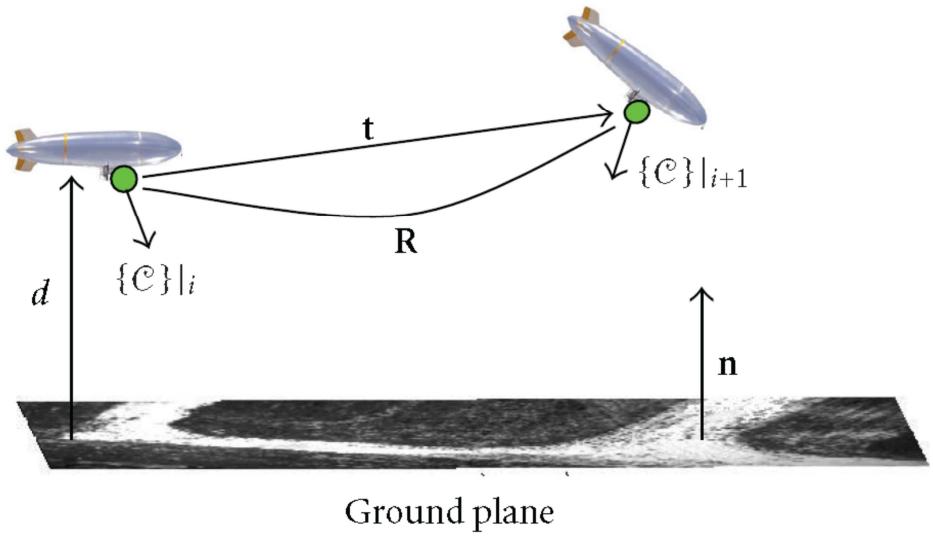

Figure 19 – Image of a 3D plane by a moving camera [Mirisola et al., 2007]

The presented method shows that the principle is to estimate the trajectory of the camera through its successive poses and the associated image of the ground. Indeed, that method starts with the projection of the recorded image on a virtual horizontal plane (i.e. plane with normal n parallel to gravity). This transformation is done with the computation of the infinite homography. The infinite homography literally represents the transformation generated when the plane is moved at the infinity but it is also the homography between two images taken from the same point but only rotated (the rotation corresponds to the orientation of the camera with respect to the normal view of the horizontal plane). In the method presented by [Mirisola and Dias, 2009], the computation of the infinite homography is only done from AHRS attitude measurements.

When the entire set of images is transformed through this infinite homography, the sequence corresponds to image measurements taken from a camera constantly oriented along the vertical. Then after the selection and matching of a set of features and their

correspondence in the next image, a Procrustes routine, aiming at finding the optimal transformation (translation, rotation and scaling) that minimizes the shape difference between two objects, is done to find the transformation and generate the 2D translation vector, the rotation matrix and the scale factor between the two images (see Figure 20).

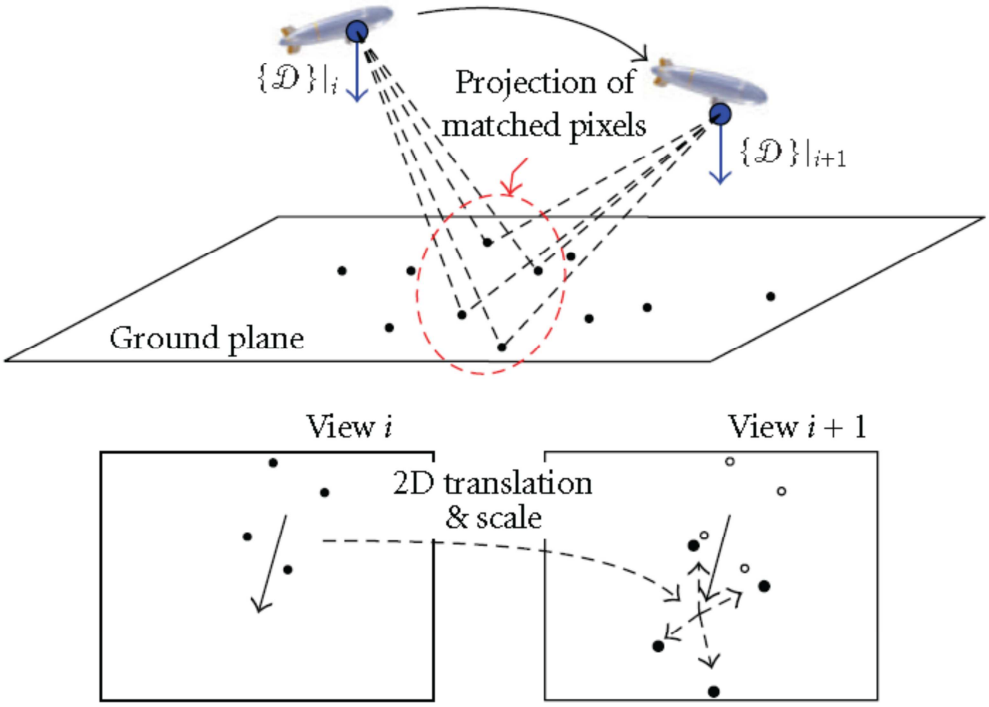

Figure 20 – Principle of trajectory recovery [Mirisola et al., 2007]

The method detailed in [Mirisola et al., 2007] is at the end coupled with a SLAM algorithm that aims at performing the visual odometry. Some methods involving SLAM are also described in [Huang, 2008] and [Angeli et al., 2009]. However a straight movement seems to be a major constraint in visual odometry and SLAM techniques.

For general SLAM applications, the low dynamic constraint is mainly driven by the fact that a high dynamic trajectory can be estimated only if the SLAM algorithm (including the video system and the image processing algorithm) is able to follow the same high dynamic and then provide high frequency real-time processing. For modern cameras, providing a high frame rate is possible (some commercial cameras can provide 100 images per second), but the main drawback is that the SLAM process that cannot be achieved at this frequency. In addition to that, SLAM algorithm processing time is not the only obstacle to high dynamic trajectories: the feature matching ability also limits the use of SLAM for high dynamics. Indeed, SLAM is based on the detection and tracking of specific features from an image to another. Thus, a loss of tracking of the image features induces an interruption in the SLAM process. In a high dynamic trajectory profile coupled with an outdoor unknown environment in which mobile features can be detected, the loss of feature tracking represents a highly relevant risk.

Based on those constraints (low dynamic, high frequency real time processing, loss of tracking risk…), SLAM algorithms seem not to be adapted for our application (approach and landing of an aircraft) so the study will not deal with a SLAM algorithm. Anyway, SLAM technics are in constant development, aiming at focusing on very specific applications and compensating the main drawbacks. In that way, SLAM could be a serious perspective for a lot of navigation applications in the future.

4.1.5 *Fusion of Imaging and Inertial Sensors*

Most of the methods presented in previous sections deal with the use of video as a main navigation mean (in some cases with a sensor aiding: altimeter or AHRS). In addition to that, the simplest case that involves video as a navigation sensor is only to consider a video system (camera plus an image processing algorithm) as a source of measurements than can be coupled with other systems (basically an INS, a GPS receiver, or other sensors).

This coupling concept is in fact directly related to the objective of the PhD study of integrating several sensors in a global hybridization architecture. In that way, the study of methods that are describing such a solution in the literature has been done and compiled in a review of the state of the art. The current section is highlighting a possible solution for integrating video within a hybridization architecture.

[Raquet and Giebner, 2003], [Veth and Raquet, 2007], [Veth, 2006] and [Ebcin and Veth, 2007] detail a tight-coupled image-aided inertial navigation through a Kalman Filter (KF) or an extended Kalman Filter (EKF). In a classic GPS/INS tight coupled integration, GPS receiver is used as an aiding source providing code pseudorange measurements. The fundamental mechanism of such a solution is that the state vector of the KF contains the inertial position estimation errors, i.e. the estimated difference between the true position driving the GPS measurements and the INS estimated position. GPS observation are used in order to correct the inertial reference, basically by comparing the measurements with the measurements that would be obtained if the position estimated by the INS was the true one. The idea developed here is that the concept is extended with video measurements. In that case, the video measurement model must be well defined and if we want to estimate the inertial error using video observation we need to be able to derive the video measurements that would be obtained is the estimated inertial position was the true one.

In [Raquet and Giebner, 2003], the measurement model from video sensors is described with its integration in a KF. The particularity of the state vector of the KF is that it contains positions of targets that are considered as features for the video. Indeed, these targets are at unknown locations and their positions will be estimated. The paper also presents the relationships between the video measurements and the target locations so as to compute the observation function (see (4.2)(5.2) to (4.4)).

The image measurements for a target in the environment are the angles depicted in Figure 21. They are constituted of two angles that define the Line-Of-Sight vector between

the true aircraft positon (more precisely the camera center) and the tracked target in the *n-frame.*

$$d_n = R_N(\lambda_i - \lambda_{INS} - \delta\lambda) \tag{4.2}$$

$$d_e = R_E(\phi_i - \phi_{INS} - \delta\phi) \tag{4.3}$$

$$d_d = h_{INS} - h_i + \delta h \tag{4.4}$$

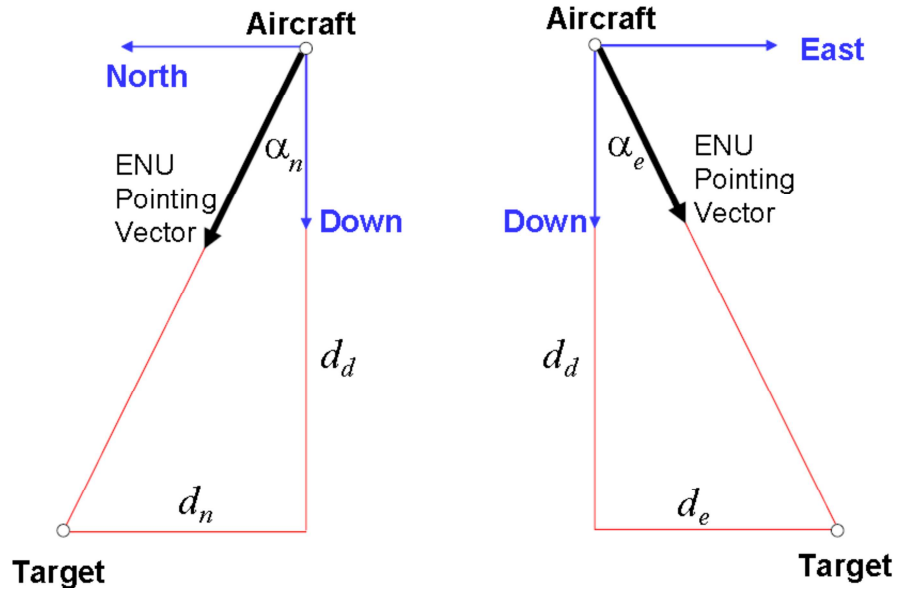

Figure 21 – Definition of image measurements [Raquet and Giebner, 2003]

In these equations d_n, d_e and d_d are respectively the distances between the target and the camera projected in the North, East and Down directions as depicted in Figure 21. λ_{INS}, ϕ_{INS} and h_{INS} define the position of the aircraft estimated by the INS. λ_i, ϕ_i and h_i are the i^{th} target position and $\delta\lambda$, $\delta\phi$ and δh are the INS position estimation error. These distances allows computing the geometrical angles that defines the Line-Of-Sight (LOS) vector between the estimated inertial position of the aircraft (more precisely of the camera) and of the estimated targets locations.

The proposed method is based on navigation using video during GPS outages and the paper shows that position error is reduced in that case. However in [Veth and Raquet, 2007], [Veth, 2006] and [Ebcin and Veth, 2007] the algorithm is depicted as a pure image-aided inertial navigation. GPS is not used in the method and the video system is based on stochastic feature projection aided by inertial measurements. Finally this tight fusion of optical and inertial sensors can provide an autonomous navigation and good performance. The model of video measurements and their integration in a KF presented in [Raquet and Giebner, 2003] represents a very good way to provide a navigation solution that can reach high level of performance.

Finally, fusing imaging sensors with other sensors seems to be an interesting alternative. The first reason is that based on some elements that were identified previously,

a pure video solution (or partially aided with additional sensors like AHRS or altimeters) requires a complex and constrained algorithm. Especially for high dynamic vehicle, a real time navigation solution using SLAM techniques or path planning cannot be implemented. The second reason is that video would be considered as a sensor providing data for navigation at the same level as for GNSS in the current hybridized solutions. Video would be considered as a redundant navigation aid that perfectly integrates our context (integrating several sources of navigation data within a global hybridization architecture). Fundamental aim of integrating video in our study is not to replace existing solution but to increase the number of the potential aids for the estimation of a navigation solution. GPS/INS hybridization started from the idea that INS and GNSS are rather complementary and the drawbacks of each system can be compensated thanks to the coupled solution.

In that way, video is there seen as an additional, redundant source of information, which has some advantages (independency with other sources, provides a pure geometrical information, already mounted on some aircraft, technology and methods currently in development) and drawbacks (complex image processing algorithm, risk of loss of tracking of features…) that fit with the general idea of a global multi-sensor hybridization. This idea is to fuse in a transparent solution any source of measurement available at a given instant and that can improve the navigation solution performance.

4.1.6 *Synthesis and Classification*

The previous analysis is based on a state of the art done during our study [Vezinet et al., 2013] in order to have the most complete overview of what can be done using video for navigation. Thus, this analysis allows identifying and highlighting some properties of video-based navigation and proposing a classification scheme. This classification can be considered as a possible classification of video-based navigation techniques and should not be considered as a standard. The classification is presented in Figure 22.

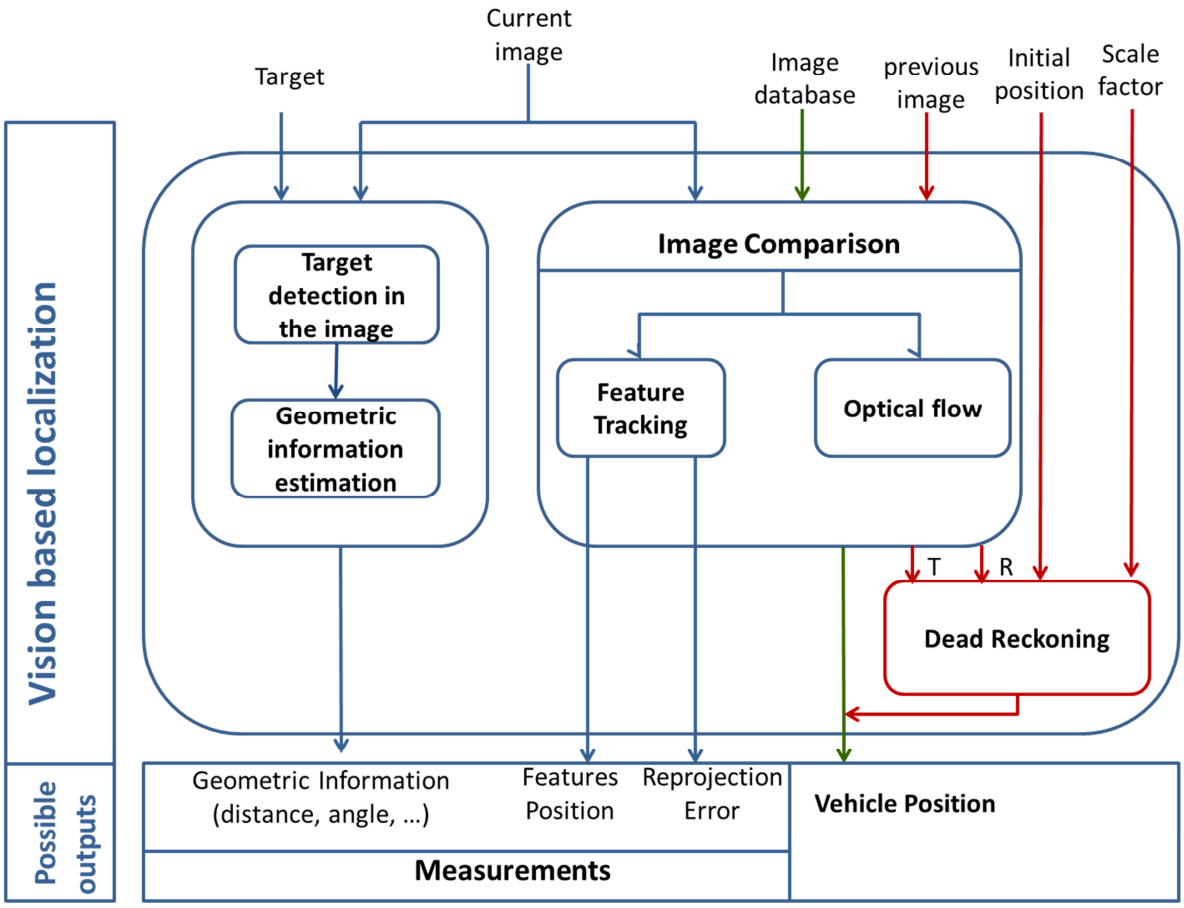

Figure 22 – Proposed video-based navigation techniques classification [Ben Afia, 2013]

The figure presents some of the key elements involved in the different video based navigation techniques. At the top of the diagram, we find the major inputs or elements needed in a video based navigation solution. The central element is the current image provided by a camera. From this image two paths can be distinguished: the first one includes every technique that deals with target detections and extraction of geometrical information from the feature (a distance, an angle, a set of coordinates,...); the second one deals with comparison with a second image that can be from a dataset, a previous image or a second current image (in stereovision applications for example). In that second branch, the comparison between two images can provide various information: the translation and rotation of the camera between the two images (dead-reckoning), the feature's positions (feature localization), the velocity of the camera (analyzing the optical flow).

This diagram does not represent so far an exhaustive classification of video based navigation but it helped in establishing basis for introducing video in our study. In that way based on our context and assumptions, we could decide to focus on the feature tracking part and not to deal with the image comparison. The choice of not considering the image comparison solution is justified by the fact that we do not want any dependency with any other image: no database (too heavy and too complex, would be needed whatever the aircraft and wherever the airport), no comparison with a previous image (we assumed that

the video provides one measurement per image), no stereovision (a single camera is assumed, two camera only offers a redundancy but no stereovision algorithm).

Finally, we will focus on a solution constituted by a single camera that detects and tracks targets in the environment and provides associated measurements. These measurements will be used in our hybridization architecture in order to add redundancy and improve performance of the navigation solution in terms of accuracy, integrity, availability and continuity (our study will focus on accuracy performance assessment and improvement provided by video in different configurations: loss, unavailability or degradation of a sensor). The next section of the chapter details the video sensor and its characteristics. It also deals with the presentation of models for video measurements as well as the description.

The PhD study only focused on integration of video measurement and multi-sensor hybridization thus we did not work on the implementation of an image processing algorithm that would aim at detecting specific targets in the image. However, we lead during the PhD some studies about the feasibility of such a solution and a set of preliminary results is presented in the last section of the chapter.

4.2 Sensor Description

The fundamental element in a video system is the image sensor usually called a camera. Camera is an optical instrument that records images. These images may be from the visible spectrum or from other portion of the electromagnetic spectrum. As we do not focus especially on the image processing part in the study, we will not consider a specific type of camera (visible, infrared or ultraviolet). A camera is defined trough a set of characteristic parameters presented in the following.

4.1.7 *Camera Characteristics*

4.1.7.1 Resolution

The resolution of a camera corresponds to the density of pixels in the recorded image (and not the number of pixels). The resolution characterizes the fineness of the image.

The resolution has to be distinguished from the definition of a camera, which defines the total number of pixels.

The definition and the size of a sensor define a resolution.

4.1.7.2 Focal Length

Usually, the focal length is the basic description of a photographic lens. It characterizes the optical distance from the point where light rays converge to the image sensor.

The focal length has an impact on the angle of view (or field of view of an image sensor).

4.1.7.3 Field of View

The field of view characterizes the extent of the observable world. It is designed by a solid angle, which is mapped to the sensitive area of the image sensor.

The field of view is impacted by the focal length of the camera: the longer the focal length, the narrower the angle of view.

4.1.7.4 Sensor Dimensions

The sensor dimensions are the physical dimensions of the image sensor.

4.1.8 *Video Measurements Model*

4.1.8.1 Pinhole Camera Model

The pinhole camera model is a usual model for cameras that defines the geometric relationship between a 3D point and its 2D corresponding projection onto the image plane. The geometric mapping from 3D to 2D is called a perspective projection when using the pinhole camera model. The center of the perspective projection (the point in which all the rays intersect) is denoted the optical center (or focal point). The line perpendicular to the image plane passing through the optical center is denoted the optical axis and the intersection point of the image plane with the optical axis is called the principal point (or image center) [Ben Afia et al., 2014]. Finally, the distance between the focal point and the image plane is called the focal length.

The pinhole camera that models a perspective projection of 3D points onto the image plane can be illustrated as follows:

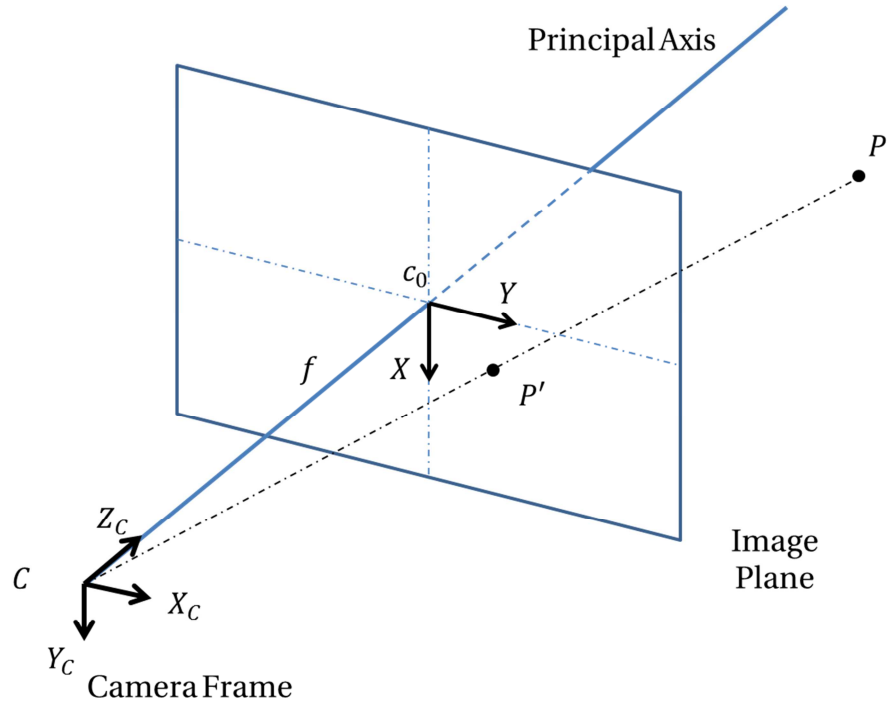

Figure 23 – The pinhole camera model [Morvan, 2009]

(X_c, Y_c, Z_c) represents the camera frame C, f is the focal length of the camera, (X, Y) are the image plane axes and c_0 is principal point (defined as the intersection between the optical axis and the image plane). P is a point in the 3D environment and P' its projection in the image plane. In our study, we will use the classic pinhole camera model in order to simulate pixel and angular coordinates of the image of targets that can be detected by the video system. This simple model is entirely depicted by the focal length, the size of the sensor, the number of pixels and the resolution. The next section introduces the basic pixel coordinates measurement model.

4.1.8.2 Pixel Coordinates Measurement Model

The fundamental measurement provided by a camera sensor that detects and tracks targets is the coordinates of the associated features in the image plane. Usually, we use the Cartesian representation for pixels coordinates. In most of cameras, distortion effects affect the recorded images as well as the pixels locations. However, distortion effects on pixels coordinates can be modeled and corrected. In that way, we will not take into account distortion effect on pixels coordinates in the study but only a measurement noise. This choice is mainly justified by the fact that there are some solutions to correct and cancel the distortion effects. We will assume that the residual distortion after correction is included in the measurement noise.

For the measurement model, we will only consider a White Gaussian measurement noise, which models any image noise, feature detection error, calibration residual error and

target location uncertainty. In that way, the pixel coordinates measurement model is as follows:

$$\tilde{X} = X + n_X \tag{4.5}$$

$$\tilde{Y} = Y + n_Y \tag{4.6}$$

Where:

- $\tilde{X}$ and $\tilde{Y}$ are the measured pixel coordinates
- X and Y are the true pixel coordinates
- n_X and n_Y are the white Gaussian measurement noises

Details on the nominal measurement error model are depicted in 4.1.8.4.

4.1.8.3 Angular Coordinates Measurement Model

Based on the previous section, we can describe the raw measurement provided by a camera as a particular pixel in the image plane. This pixel corresponds to a three-dimensional pointing vector in the camera frame, which can be uniquely defined by two angles. However, there are several possibilities for defining this pointing vector with two angles. The selected option was to describe the pointing vector with a series of two rotations around the axes of the *m-frame*: a first one around the lateral y-axis and a second one around the vertical z-axis. In that way these two angles will constitute the raw measurement provided by our video system. This system will then be considered as a self-contained box, which can provide two angular measurements per detected feature independent from the previous measurements, the aircraft state or the other sensors.

A typical representation of an image that can be provided by a camera is presented in Figure 24.

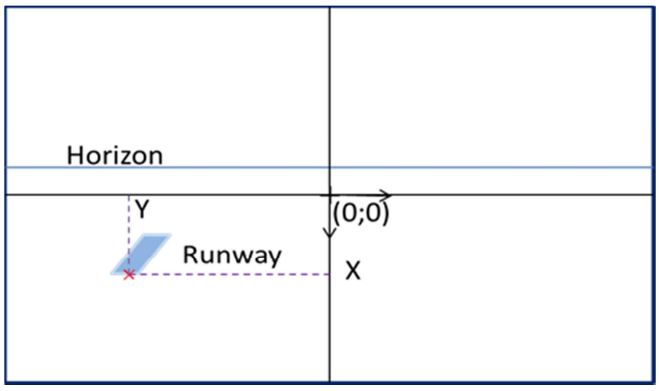

Figure 24 – Image plane configuration

The image frame origin is located at the center of the image also considered as the optical center (the projection of the focal points in the image). The x-axis is down oriented

and the y-axis is right oriented. In this particular example, if we supposed that the video system detects a feature that corresponds to a specific target (of known location) like corners of the runway, the coordinates of the pixel are designated by (X, Y).

The corresponding measurement angles are then denoted α_X and α_Y. The first angle is illustrated in Figure 25. The second one is illustrated in Figure 26.

If we consider the angle between the x-axis of the aircraft frame and the Line-of-Sight between the focal point of the camera and the target, α_X is the angle between the normal vector from the point and the projection of the point of interest p in the image frame on the x axis. α_Y is then the angle between the normal vector from the focal point and the projection of the point of interest p in the image frame on the y axis.

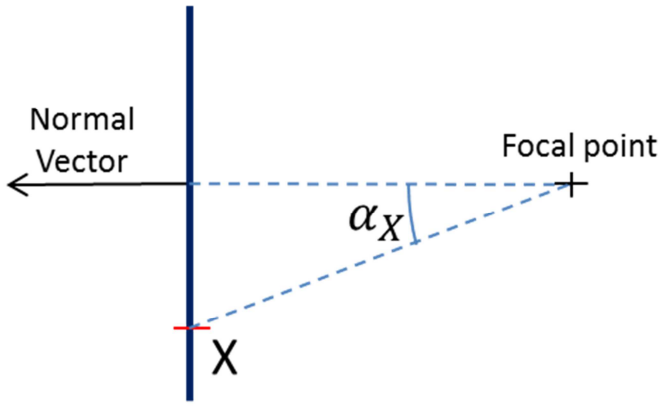

Figure 25 – First optical angular measurement – Side View

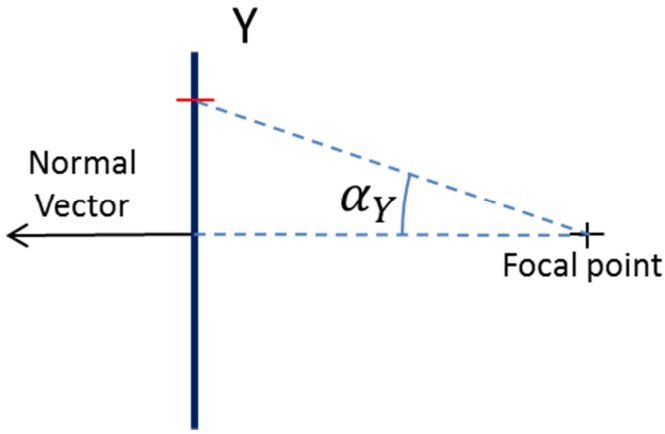

Figure 26 – Second optical angular measurement – Upper View

By convention established in the image frame in Figure 24, the coordinate (angular or pixels) are counted positively toward the right direction for y and positively toward the down direction for x. A global view is represented in Figure 27.

In that configuration, another view of Figure 24 illustrating the measurements angles is presented in Figure 27.

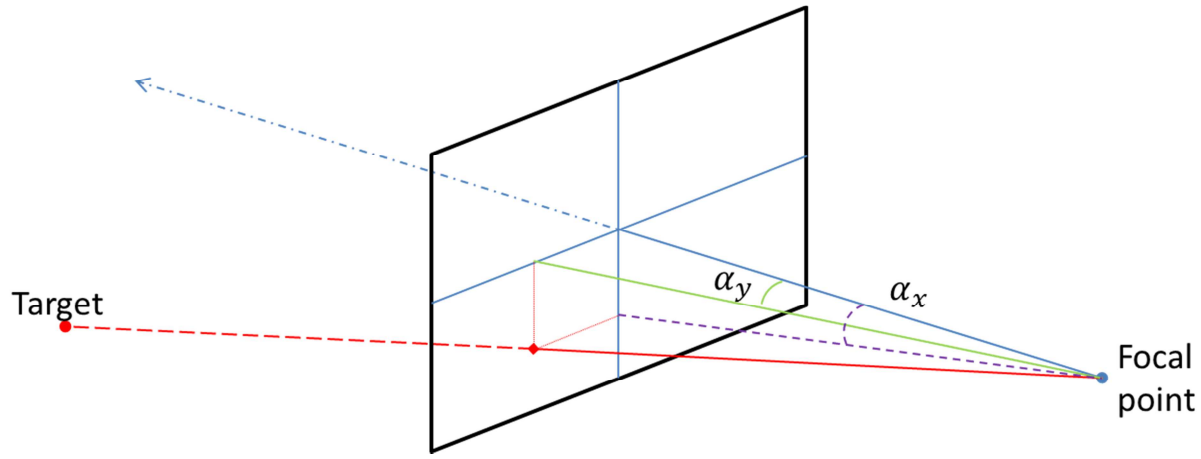

Figure 27 – Angular measurements representation

It is evident that for any feature detection in the image plane, both angular measurements will be in the interval $\left[-\frac{\pi}{2};\frac{\pi}{2}\right]$. In that way, it allows us using symmetrically, the angular measurements (α_X, α_Y) and their tangent (because of the bijection induced by the tangent function on this interval). The interest in using the tangent is that it turns the measurements into the metrical domain (just by dividing the pixel coordinate in meters by the focal length). In addition, we assume that the measurement noise on the proposed measurement is Gaussian.

The video measurement model for a target is then as follows:

$$\tan(\tilde{\alpha}_X) = \tan(\alpha_X) + n_X \tag{4.7}$$

$$\tan(\tilde{\alpha}_Y) = \tan(\alpha_Y) + n_Y \tag{4.8}$$

Where:

- $\tilde{\alpha}_X$ and $\tilde{\alpha}_Y$ are the video measurements
- α_X and α_Y are the true geometrical angles
- n_X and n_Y are the white Gaussian measurement noises

In order to integrate these video measurements in a hybridization architecture like a Kalman Filter, it will be necessary to relate these measurements to the state vector of our filter. This step is presented in the next chapter. The following section discuss on the nominal measurement error model, here modeled as a White Gaussian noise.

4.1.8.4 Nominal Measurement Error Model

The nominal measurement error model for a video sensor is quite difficult to define because it depends on lots of factors. We can divide the contributions in two parts: the one

that comes from the sensor and its calibration and the one that comes from the image processing algorithm during detection and tracking.

The first component of the error contribution is related to the sensor quality, is strongly dependent on the type of sensor and the calibration procedure. As an example, in [Giebner, 2003] the calibration procedure permits to estimate a bias in the optical angular measurements that depends on the position of the pixel. The Figure 28 represents an angular measurement error as a function of the location of the pixel in the image:

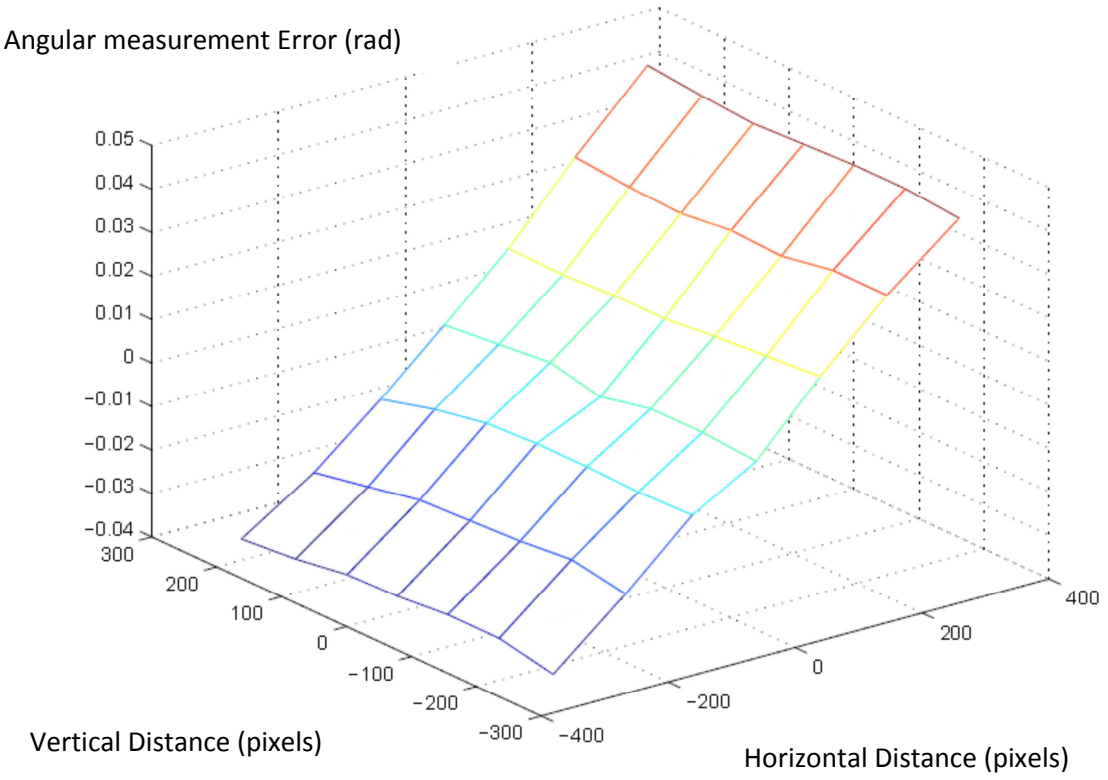

Figure 28 – Optical angular measurement error [Giebner, 2003]

The second component is related to the image processing performances. It corresponds to an error done when the selected pixel is not the good one. This error can be produced by a too low resolution that does not allow selecting the target with enough precision, or by an error in the image processing algorithm, or by a size of pixel too high, which would induce a rounding error, or by the image noise. There are no standardized values for modeling these errors. However, lots of studies using a similar measurement model [Giebner, 2003], [Raquet and Giebner, 2003], [Ebcin and Veth, 2007], [Veth, 2006], [Veth and Raquet, 2007] stated that an error of several pixels can be considered in the nominal case.

In conclusion for the Ph.D. study, we consider a white Gaussian centered noise with a standard deviation of 3 pixels on the pixel coordinates. This value has been used for generating the noise on the angular measurements after conversion of the pixel coordinate in angular coordinate.

4.3 Preliminary Results of Runway Detection Algorithm

When we chose to introduce a video system as a sensor that can be integrated within an hybridization architecture, we wanted to consider that the video system should be able to provide measurements at any time in any location without need of any help or complementary data (no image database, no dead reckoning and no dependency with a previous measurement). Of course, in order to provide measurements, the video system must be able to detect specific objects in the world. As soon as we decided to focus on stringent operations, like approach and landing (partly because current less stringent operations are performed with GPS/INS hybridization), it seemed pretty clear that the element in common between all airports and landing environments was the runway. In that way, the basic target, which was assumed to be detected by the video system, is the shape of the runway. More particularly, we will focus on the detection of specific points in the runway that define the rectangular shape. Such an approach has already been chosen in the literature for using video for approach and landing. Indeed, as presented in section 4.1, [Doehler and Korn, 2003] and [Miller et al., 2008] present applications in which the runway is also targeted during landing. The study described here is supported by the text in those references.

These considered specific points are the two runway threshold's corners as illustrated in Figure 29. The image has been taken from a camera mounted behind the panes of the cockpit during a final approach at Blagnac airport in Toulouse in France. These corners describe the rectangular shape of the visible runway.

The horizontal distance between the camera and the threshold when this image has been taken is around 230 meters. The visibility of the four corners of the runway is not ensured in every condition and at every moment but the idea is that the video system is able to detect points among these four ones. Even though we did not develop an image processing algorithm able to provide such detections, we conducted some studies on the feasibility of this solution.

Figure 29 – Runway's corners detection during landing taken at 230m of the runway's threshold

Locations of these specific targets will be considered as known in the current study. The location, length and size of the runways during approaches and landings are supposed to be known. In further studies, this location could be considered to be known with a certain inaccuracy. The target's locations could also be estimated as it was explained in 4.1.5. Therefore, in the presented scenario, we assume that the position of the targets is known on-board. That can be done assuming that during an approach, the runway's position and characteristics (width and length) are known. The runway's corners position can then be deduced.

The study lead for trying to detect corners of the runway of specific images has been done on the set of images in Figure 30. These images were all taken by the same camera at different instants during the final approach segment.

Figure 30 – Raw images taken during the final segment approach in Blagnac airport in Toulouse respectively taken at 4500 m, 2500 m and 800 m of the runway's threshold

The set of images allows describing the results of the algorithm with different visibility conditions. In the first image, the dense urban environment induces difficulties to locate the runway even to the naked eye and we can assume that the details among the airport will produce detection error if we want to detect only the runway.

The first step of the algorithm is the conversion in binary images and the application of a morphological filter aiming at closing every contour in the image. The results are illustrated in Figure 31.

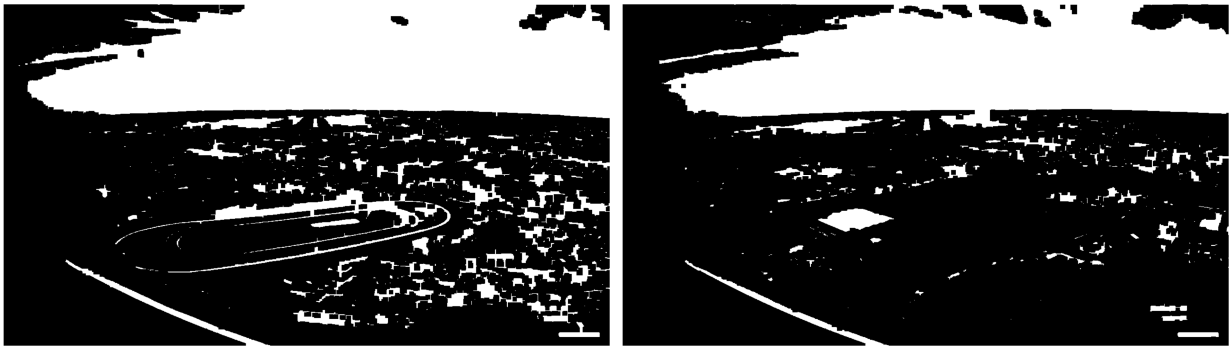

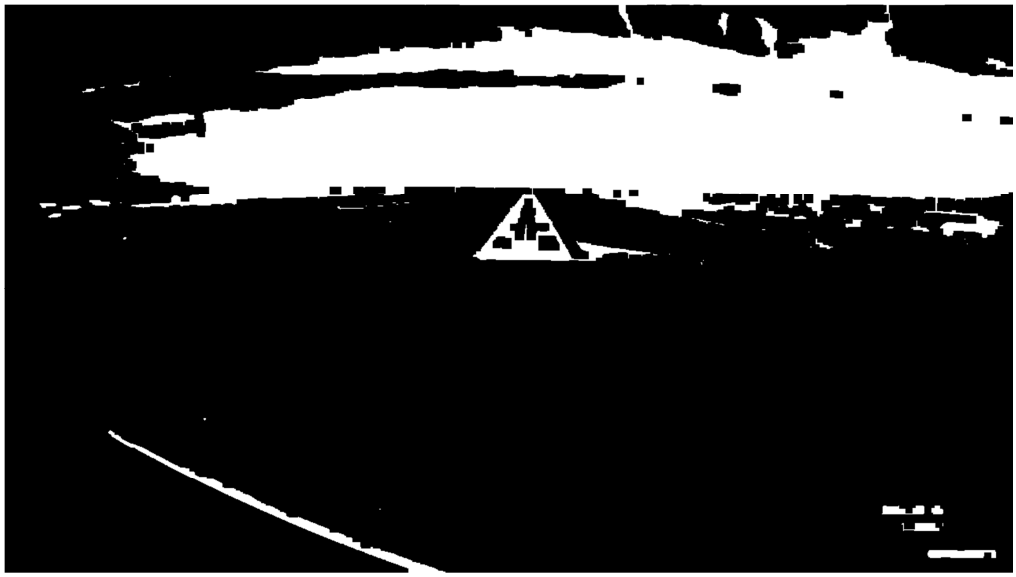

Figure 31 – Images after application of a morphological filter respectively taken at 4500 m, 2500 m and 800 m of the runway's threshold

The next step is a Canny edge detector aiming at detecting each contour represented by a transition in the image colors. The Canny edge detector is described in public references such as [Wang and Fan, 2009], [Maini and Aggarwal, 2009] or [McAndrew, 2004]. The results after use of the detector appear in Figure 32.

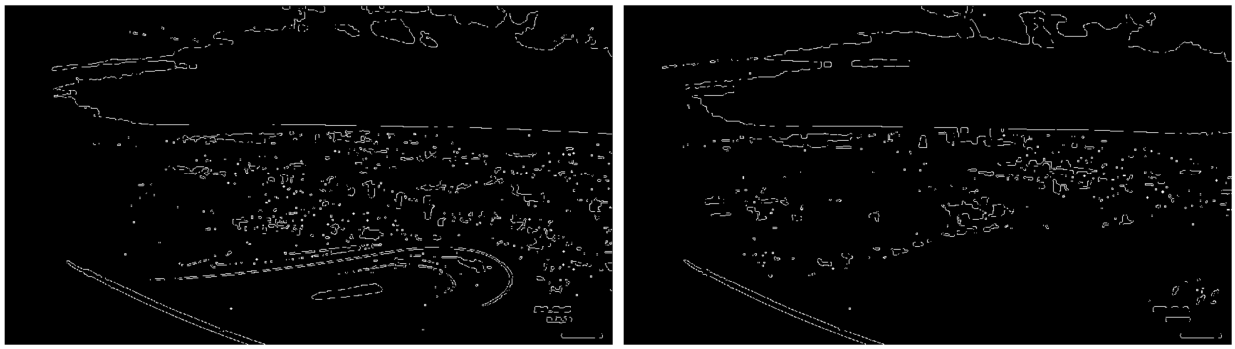

Figure 32 – Images after a Canny edge detector respectively taken at around 4500 m, 2500 m and 800 m of the runway's threshold

At this moment, all preprocessing steps have been applied and this image will be used in an image processing algorithm in order to detect and track the corners of the runway. Several complex algorithms can be implemented but we first decided to use a simple Hough transform [Maitre, 1985], [Damary et al.], [McAndrew, 2004], which aims at detecting lines in the input image. Using this transformation we obtain the images presented in Figure 33.

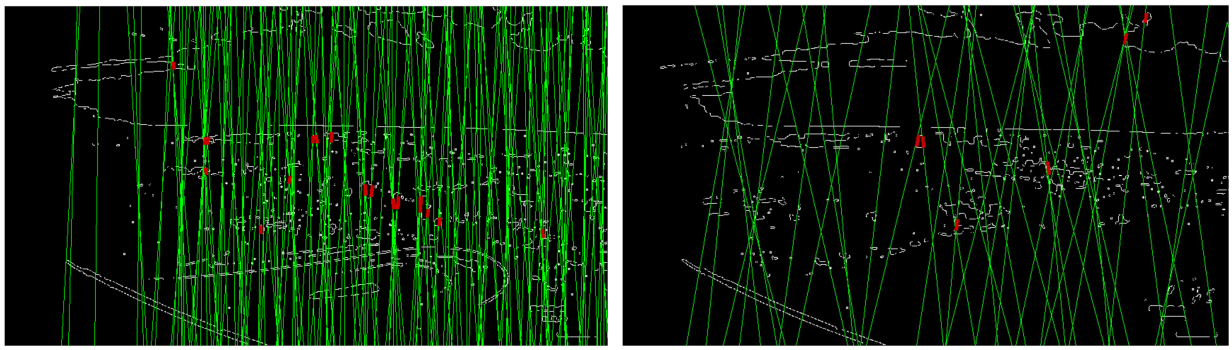

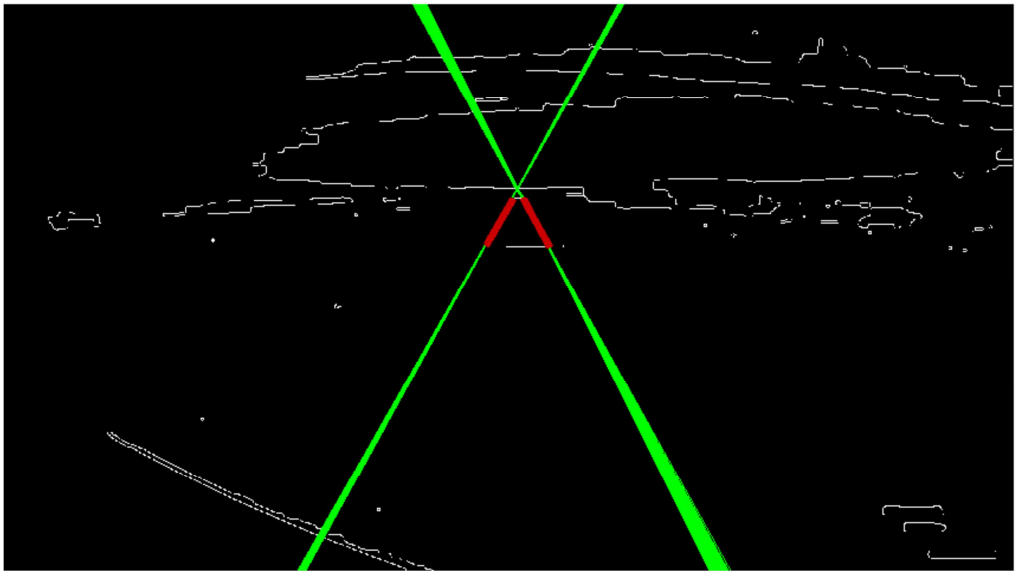

Figure 33 – Images after a Hough transform respectively taken at 4500 m, 2500 m and 800 m of the runway's threshold

From these resulting images we could imagine a combination of another Hough transform for horizontal line detection and track the intersection. Based on this idea, the result of the detection of the four corners is as illustrated in Figure 34.

Figure 34 – Runway's corners detection in the images respectively taken at 4500 m, 2500 m and 800 m of the runway's threshold

The process described in that part is just a snapshot of the study that has been led in order to assess the feasibility of the solution proposed concerning the detection of the runway's corners. Firstly, in that configuration it seems to provide good results: even in the first image the four corners are detected. Secondly, we have to take into account the fact that each transform and process involved in the previous steps needs a correct tuning as a compromise between wrong detection and no detection. This tuning might be really difficult to accomplish and could have important impact on the resulting image. In addition, a good tuning needs to be adapted in all conditions and for all images but in our study the tuning was adapted to these images in particular. A more complete study has been done in [Ressouche and Decneudt, 2014]. Thirdly, this is not the only method that allows detecting the runway's shape in a set of images. Similar studies have been led defining other criteria for runways detection. In [Schertler, 2012], a method aiming at detecting the symmetry axis of the runway is presented. The robustness of the algorithm is highlighted and it shows that even in poor visibility conditions, the axis is found.

Finally, the idea of detecting specific targets is important because we wanted to detect targets of known locations. In particular for simplicity reasons and for limiting source of errors, which could results from a wrong estimation of their positions, in our solution. Considering the development of applications using video, of image processing algorithms and of camera technologies, this principle totally seems to be realizable with an accuracy that needs to be determined.

The entire process described in the current part is summarized in Figure 35.

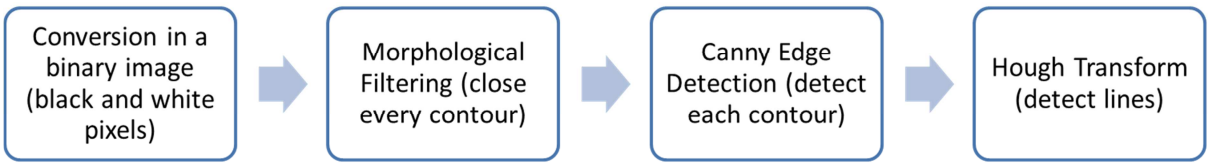

Figure 35 – Image processing algorithm overview

4.4 Conclusion

The current chapter has introduced some video based navigation methods and highlighted the characteristics of video systems. It has justified the choice of using angular coordinates of features as raw video measurements. These features are related to specific targets of known location in an airport environment that are runway's corners. These points appear in fact to be the only common elements between every airport. In that way it does not limit the context to a particular airport or to a particular approach.

The ability of the video system to detect these points has not been proven but it is assumed for the following that the system provides these measurements. However, even if the image processing part was no included in the study, some results of an algorithm for detecting the targeted points are presented in the chapter and provide good results.

As an anticipated axis of development, we can discuss about the fact that only four features are identified in the described procedure. The reason is mainly because the rectangular shape of the runway easily defines those four points. However, we could address in particular the addition of other known features in the recorded images so as to multiply the sources of measurement, add redundancy and increase the optical flow provided by the video sensor. As discussed in [Veth, 2006], when the aircraft is moving toward the runway the optical flow is limited when the number of features is limited. Indeed, an increased optical flow is important for estimation of velocity.

The next chapter will provide in details the integration of the proposed video measurements in a global hybridization architecture.

Chapter 5 : Algorithm Implementation

The current GNSS/INS hybridization performed on board uses a tight-coupling or loose-coupling Kalman Filter architecture in an open-loop configuration. Yet, the possibilities for data fusion algorithms are numerous. It can be done with a simple Kalman Filter, with its variants such as Linearized Kalman Filter, Extended Kalman Filter, or Unscented Kalman Filter, with the more complex Information Kalman Filter, with a Particle Filter or with any other filter that can combine data from different systems or sensors.

The current chapter deals with the description of the proposed solution for a global hybridization solution integrating a GNSS receiver, an INS, Wheel Speed Sensors and a Video System. In the study, the hybridization architecture is a tight coupled solution in an open loop configuration using an Extended Kalman Filter.

The first part of the chapter is an overall description of the proposed solution with some justifications for the selection of the architecture.

The second part is a presentation of a theoretical model of the Kalman Filter.

The third part details the error state vector used in our model.

The fourth part defines the state transition model of the Kalman Filter.

The fifth part defines the observation model of the Kalman Filter.

5.1 Hybridization Architecture

5.1.1 Global Overview

Figure 36 is a schema that aims at describing the global hybridization architecture in which the PhD thesis takes place.

The schema illustrates in the upper part, the possible inputs (or sources of measurements) that could be considered in the global architecture such as the INS, the GNSS receivers, the tachometer the video system and the barometer. This part describes also the possible redundancy of every measurement sources.

The hybridization architecture is then divided into two parts denoted “FUSION” part and “MONITORING” part. The “FUSION” bloc deals with the estimation of the targeted parameters with algorithms that aims at providing the best estimates, including an expected level of accuracy of these estimations. The second part, the “MONITORING” bloc aims at providing an integrity monitoring algorithm for the GNSS SIS as well as for the other sources of measurement integrated within the architecture. In fact, this part aims at estimating an integrity level for every parameter (for example a protection level) and a flag indicating if a sensor can be used or not.

The “FUSION” and the “MONITORING” parts are supposed to communicate for providing estimates of the navigation parameters and proposing a new configuration of the implemented filter. It is important to notice that the solution implemented in the PhD thesis is only included in the “FUSION” bloc and do not focus on the “MONITORING” part that has not been developed yet.

That scheme illustrates the PhD thesis with a more extended view of the global project and gives some indications on the future development that will be held in the framework on that study.

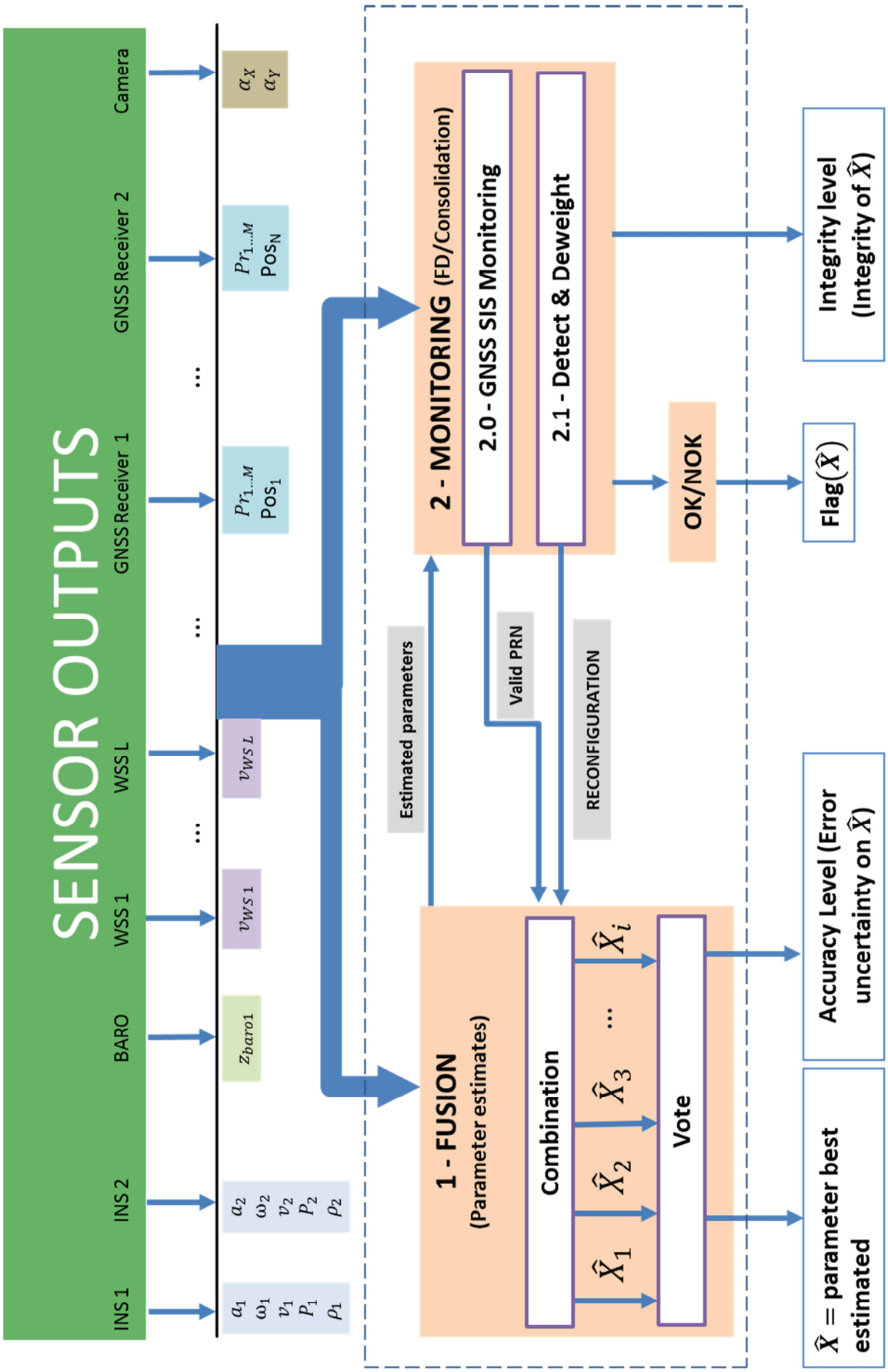

Figure 36 – Global Hybridization Architecture Overview

5.1.2 Architecture Description

The hybridization solution that we develop in the thesis is an open-loop tight coupling EKF architecture integrating an INS, a GNSS receiver, WSSs and a Video system. As it was described in 3.1.3.3, we implemented a wander azimuth inertial mechanization and the EKF deals with estimating the inertial navigation errors.

Most of the choices that have been done concerning the characteristics of the hybridization solution are based on the well-known existing and regular solutions used in civil aviation. Indeed, the wander azimuth mechanization does not maintain a North-pointing orientation of the local navigation frame. This navigation mechanization solves particular navigation issues near the poles, where the transport rate vector tends to become infinite and causes severe instabilities.

The tight-coupling architecture is, with the loose coupling, one of the two main architectures implemented on board. In our case we decided to focus on the tight-coupling architecture because we assume that we have a better knowledge of the GNSS code pseudorange measurement model than of the GNSS position measurement model. In addition, with the future consideration of GALILEO signals, the redundancy of the GNSS measurements appears to be a great advantage for integrity monitoring solutions.

The criteria for the selection of the EKF algorithm deals with the resolution of non-linear problems for solving the navigation state system. EKF provides an important improvement when linearizing the state transition model and observation model of the system. In the framework of the thesis, we also started to focus on the implementation of an Unscented Kalman Filter (UKF), stronger with the non-linearity issues because it does not linearize the state space model.

Finally, the open loop configuration has been considered because of the potential multiplication of sensors for integration in the global architecture. Indeed, the closed loop configuration induces the potential propagation of a sensor error mode to other sensors. So the open-loop allows avoiding this possible issue and reinforcing the redundancy of the sensors.

5.2 Theoretical Model

The usual Kalman Filter is a recursive estimator of the internal state of a linear stochastic system. In most of the cases, dynamic systems are not linear and the Kalman Filter cannot be used for system state estimation. The Extended Kalman Filter is then a solution for non-linear systems but is not an optimal estimator contrary to the KF.

The following section describes the state space model of a non-linear stochastic system and introduces the equations of the Extended Kalman Filter.

5.2.1 State Space Description

From the next section, for simplification of the notation, the time indicator t or k will be denoted as a subscript (F_t or X_k instead of $F(t)$ or $X(k)$).

A continuous non-linear stochastic system can be modeled with the two following equations:

$$\dot{X}(t) = f(X,t) + U(t) \tag{5.1}$$

$$Y(k) = h(X,k) + V(k) \tag{5.2}$$

Where:

- X is the state vector of the system
- Y is the observation vector
- f is the state transition function (or dynamic matrix)
- h is the observation function
- U is the additive process noise vector assumed centered, white and Gaussian
- V is the additive observation noise vector assumed centered, white and Gaussian

(5.1) and (5.2) are respectively denoted the state transition model and the observation model.

The estimation of the system space for non-linear system models using an EKF is based on the linearization of the state space representation. The entire description of the linearization process is described in Appendix B. In a GNSS/INS hybridization with an EKF, the linearization of the state transition equation is usually done around a reference state (the estimation provided by INS, denoted $\hat{X}_{INS}$)). The observation equation is then linearized around the predicted state $\left(\hat{X}_{k|k-1}\right)$. At the opposite, in a simple linearized Kalman Filter the observation equation is also linearized around the reference state.

After linearization, the state space model is rewritten as following:

$$\delta\dot{X}(t) = F(t) \cdot \delta X(t) + U(t) \tag{5.3}$$

$$Z(k) = H(k) \cdot \delta X(k) + V(k) \tag{5.4}$$

Where:

- δX is the error state vector of the system
- Z is the observation vector
- F is the linearized state transition function (or state transition matrix)
- H is the linearized observation function or observation matrix

- U is the additive process noise vector assumed centered, white and Gaussian
- V is the additive observation noise vector assumed centered, white and Gaussian
- t is the continuous time variable

The non-linear state space model described by equations (5.1) and (5.2) is then completely equivalent to the linearized state space described by equations (5.3) and (5.4). This new representation introduces two new terms: the error state vector δX and the observation vector Z. The error state vector describes the error between the true state of the system and the state estimated by the reference solution (the INS). In that way, the EKF will estimate the INS error. The observation vector is the difference between the input measurement Y and the prediction of the measurement at the linearization point (the predicted state $\hat{X}_{k|k-1}$).

For implementation purpose, we will consider the discrete time state space model of the system. It can be easily deduce from the continuous state space representation and is as follows:

$$\delta\dot{X}(t) = \Phi(t) \cdot \delta X(t) + U(t) \tag{5.5}$$

$$Z(k) = H(k) \cdot \delta X(k) + V(k) \tag{5.6}$$

Where Φ is the discrete form of the state transition matrix F.

After the linearization process, the estimation of the error state vector can be done using the equations of a classic Kalman Filter. Contrary to the KF, the EKF is not optimal because it is based on approximations of the linearization process (Taylor series development).

5.2.2 Extended Kalman Filter Equations

The principle of the KF is to estimate the state vector at instant k from the prediction of the state vector from the previous instant $k-1$ and the measurement observed at the current instant k. Applied to the linearized state space model described by equations (5.3) and (5.4), the EKF equations are those of a KF applied to the error state vector δX. They can be divided in five steps detailed in the current section.

5.2.2.1 Prediction

The prediction step defines the relation between the previous estimation of the error state vector $\delta\hat{X}_{k-1|k-1}$ to the new estimation only based on the state transition model $\delta\hat{X}_{k|k-1}$. This estimation is called the “a-priori” estimation and corresponds to the estimation of the error state vector before considering the observations.

$$\text{State prediction} \quad \delta\hat{X}_{k|k-1} = \Phi_k \cdot \delta\hat{X}_{k-1|k-1} \tag{5.7}$$

The particularity of a Kalman Filter is that while estimating the error state vector of a system, it also estimates the variance of the estimation error. The variance estimation is based on the same principle than the state estimation and its prediction is obtained with the following equations:

$$\begin{matrix}\text{Covariance} \\ \text{prediction}\end{matrix} \quad P_{k|k-1} = \Phi_k \cdot P_{k-1|k-1} \cdot \Phi_k^T + Q_k \tag{5.8}$$

Where Q_k is the covariance of the additive process noise vector U_k.

The prediction is often called the "first stage" of a KF. The "second stage", called the update, is done after computation of the Innovation and Gain of the KF.

5.2.2.2 Innovation and Gain

The innovation in a KF is defined as the difference between the measurements and a prediction of the measurements that should be observed at the predicted state. The innovation is then as follows:

$$\text{Innovation} \quad I_k = Y_k - h\left(\hat{X}_{k|k-1}\right) \tag{5.9}$$

The computation of the Kalman Gain is then as follows:

$$\text{Gain} \quad K_k = P_{k|k-1} \cdot H_k^T \cdot \left[H_k \cdot P_{k|k-1} \cdot H_k^T + R_k\right]^{-1} \tag{5.10}$$

Where R_k is the covariance of the additive observation noise vector V_k.

5.2.2.3 Update

Once the Gain and Innovation are computed, the predicted state from the "first stage" of the KF is updated (or corrected) using the Kalman Gain and the Innovation. The updated state, also called the "a-posteriori" state, is computed as follows:

$$\text{State update} \quad \delta\hat{X}_{k|k} = \delta\hat{X}_{k|k-1} + K_k \cdot I_k \tag{5.11}$$

As for the state update, the predicted covariance matrix of the state is updated using the Gain and Innovation as follows:

$$\text{Covariance update} \quad P_{k|k} = P_{k|k-1} - K_k \cdot H_k \cdot P_{k|k-1} \tag{5.12}$$

Those five equations are the EKF equations used for estimation of the error state vector of the system. This error state vector is defined in the next section.

5.3 Error State Vector

The system model is based on a wander-azimuth mechanization and the position, velocity and attitude error states of the error state vector are the difference between the quantities estimated by the INS platform and the true ones.

5.3.1 Position and Baro-Inertial Altitude

The first two states are horizontal angular position error expressed in the *w-frame*. These parameters are denoted $\delta\theta_x$ and $\delta\theta_y$ and can be expressed in the *n-frame* as follows:

$$\begin{aligned} \delta\theta_x &= \delta\theta_N \cdot \cos w + \delta\theta_E \cdot \sin w \\ \delta\theta_y &= -\delta\theta_N \cdot \sin w + \delta\theta_E \cdot \cos w \end{aligned} \tag{5.13}$$

Then the invert transformation is:

$$\begin{aligned} \delta\theta_N &= \delta\theta_x \cdot \cos w - \delta\theta_y \cdot \sin w \\ \delta\theta_E &= \delta\theta_x \cdot \sin w + \delta\theta_y \cdot \cos w \end{aligned} \tag{5.14}$$

These horizontal angular position errors are related to the errors in latitude and longitude with the following relationships:

$$\begin{aligned} \delta\lambda &= -\delta\theta_E \\ \delta\phi &= \frac{\delta\theta_N}{\cos\lambda} \end{aligned} \tag{5.15}$$

The next two states δh_B and δa_B describe the baro-inertial error state. δa_B being the output error of the compensator of the feedback loop illustrated in 3.1.4.2.

5.3.2 Velocity and Baro-Inertial Vertical Velocity

The two following states are the earth relative horizontal velocity error coordinates expressed in the *w-frame*, δv_x and δv_y.

The next state is the baro-inertial vertical speed error δv_z also illustrated in 3.1.4.2.

5.3.3 Attitude

The three following states are the *w-frame* alignment errors $\delta\phi_x$, $\delta\phi_y$ and $\delta\phi_z$.

5.3.4 Sensors Measurements Errors

The next 6 states are the three-axis gyrometer errors bg_x, bg_y and bg_z, and the three-axis accelerometer errors ba_x, ba_y and ba_z.

5.3.5 Receiver Clock Bias and Drift

As we are in a tight coupling architecture, bias and drift of the GNSS receiver clock b_H and d_H need to be estimated. They are the next two elements of the error state vector.

5.3.6 GNSS Pseudoranges Correlated Errors

Identically, using a tight coupling architecture and integrating GNSS code pseudorange measurements, we estimate in the error state vector the time-correlated pseudoranges measurement errors: $b_{GNSS\,1}, \dots, b_{GNSS\,N}$.. The time-correlated pseudorange errors are described in the GNSS code pseudorange measurement model reminded in 3.2.1.

5.3.7 Synthesis

The complete error state vector δX is presented in (5.16) it can be divided in three sub-states as illustrated in the following equations. They are respectively related to INS estimates, IMU sensor biases and GNSS pseudorange bias.

$$\delta X = \begin{bmatrix} \left.\begin{matrix} \delta\theta_x \\ \delta\theta_y \\ \delta h_B \\ \delta a_B \\ \delta V_x \\ \delta V_y \\ \delta V_z \\ \delta\phi_x \\ \delta\phi_y \\ \delta\phi_z \end{matrix}\right\} \delta X_{INS} \\ \left.\begin{matrix} bg_x \\ bg_y \\ bg_z \\ ba_x \\ ba_y \\ ba_z \end{matrix}\right\} \delta X_{IMU} \\ \left.\begin{matrix} b_H \\ d_H \\ b_{GNSS\,1} \\ \vdots \\ b_{GNSS\,N} \end{matrix}\right\} \delta X_{GNSS} \end{bmatrix} \tag{5.16}$$

5.4 State Transition Model

5.4.1 State Transition Matrix

The state transition matrix of the Kalman filter is the linearized matrix of the state transition function f, denoted F in equation (5.3) in its continuous form and denoted Φ in equation (5.5) in its discrete-time form.

The next part will present the main steps for obtaining the continuous state transition matrix that relates the error state vector to its derivative. The description of the dynamic matrix is presented for each state.

5.4.1.1 Position Error Propagation Equation

The first block of the state transition matrix F, $F_{pos/velo}$, define the relationship between the derivatives of the horizontal angular position error expressed in the *w-frame*: $[\delta\theta_x, \delta\theta_y]$ and the state of the velocity error expressed in the *w-frame*:

$$\begin{bmatrix} d\dot{\theta}_x \\ d\dot{\theta}_y \end{bmatrix} = \underbrace{\begin{bmatrix} \frac{1}{R_{xy}+h_B} & \frac{1}{R_y+h_B} \\ -\frac{1}{R_x+h_B} & -\frac{1}{R_{xy}+h_B} \end{bmatrix}}_{F_{pos\backslash velo}} \cdot \begin{bmatrix} \delta v_x \\ \delta v_y \end{bmatrix} \tag{5.17}$$

Details of the computation are in Appendix B.

5.4.1.2 Baro-Inertial Altitude Error Propagation Equation

The principle of the baro-inertial loop integration has been briefly described in 3.1.4.2. The baro-inertial vertical channel error model is illustrated in Figure 8. We can deduce from that error model the following equations:

$$\begin{aligned} \delta\dot{h}_B &= -\delta V_z - K_1 \cdot (\delta h_B - \delta h_{baro}) \\ \delta\dot{a}_B &= K_3 \cdot (\delta h_B - \delta h_{baro}) \end{aligned} \tag{5.18}$$

The transition state matrix part for the vertical channel states $[\delta h_B, \delta a_B]$ denoted F_{baro} is then as follows:

$$F_{baro\_alti} = \begin{bmatrix} 0 & 0 & -K_1 & 0 & 0 & -1 & 0 & \cdots & 0 \\ 0 & 0 & 0 & K_3 & 0 & 0 & 0 & \cdots & 0 \end{bmatrix} \tag{5.19}$$

With K_1 and K_3 the gains of the baro-inertial loop.

5.4.1.3 Velocity Error Propagation Equation

Appendix B details the Earth-relative velocity dynamic equation in the inertial frame and then in the wander frame (*w-frame)*.

It is reminded in the following:

$$\delta \dot{v}_e^w = \underbrace{\delta f^w}_{ba^w} + \left(-\tilde{f}^w \wedge\right) \cdot \rho + \delta g^w + \left(\hat{v}_e^w \wedge\right) \cdot \left(\delta \omega_{w/e}^w + 2\delta \omega_{e/i}^w\right) - \left(\hat{\Omega}_{w/e}^w + 2\hat{\Omega}_{e/i}^w\right) \times \delta v_e^w \tag{5.20}$$

Where:

- $\delta \dot{v}_e^w$ is the derivative of the Earth-relative horizontal velocity error.
- δf^w is the specific force error, so the accelerometer bias.
- $\tilde{f}^w$ is the specific force measurement.
- ρ is the attitude error vector.
- δg^w is the gravity error vector.
- $\hat{v}_e^w$ is the Earth-relative horizontal velocity.
- $\delta \omega_{w/e}^w$ is the angular velocity error vector of the *w-frame* with respect to the *e-frame*.
- $\delta \omega_{e/i}^w$ is the angular velocity error vector of the *e-frame* with respect to the *i-frame*.
- $\hat{\Omega}_{w/e}^w$ is the skew symmetric matrix associated to the estimated angular velocity error vector of the *w-frame* with respect to the *e-frame*.
- $\hat{\Omega}_{e/i}^w$ is the skew symmetric matrix associated to the estimated angular velocity error vector of the *e-frame* with respect to the *i-frame*.
- δv_e^w is the horizontal Earth-relative velocity error vector.

All these components are expressed in the wander azimuth coordinates frame. It allows deducing the following horizontal velocity error state transition matrix (detailed in Appendix B):

$$F_{velo\ INS} = [F_{velo/pos} \quad F_{velo/velo} \quad F_{velo/att} \quad F_{velo/bg} \quad F_{velo/ba}] \tag{5.21}$$

With:

- $F_{velo/pos} = (\hat{v}_e^w \wedge) F_{velo/pos\ 1} + F_{velo/baro}$, is the position error to velocity error derivative transition matrix. $F_{velo/pos\ 1}$ and $F_{velo/baro}$ are defined in Appendix B.
- $F_{velo/velo} = (\hat{v}_e^w \wedge) F_{velo/velo\ 1} - F_{velo/velo\ 2}$ is the velocity error to velocity error derivative transition matrix. $F_{velo/velo\ 1}$ and $F_{velo/velo\ 2}$ are defined in Appendix B.
- $F_{velo/att} = \left(-\tilde{f}^w \wedge\right)$ is the attitude error to velocity error derivative transition matrix (defined in Appendix B).
- $F_{velo/bg} = 0$ is the gyrometer measurement error to velocity error derivative transition matrix (defined in Appendix B).

- $F_{velo/ba} = \hat{R}_{m2w}$ is the accelerometer measurement error to velocity error derivative transition matrix (defined in Appendix B).

5.4.1.4 Baro-Inertial Vertical Velocity Error Propagation Equation

The baro-inertial vertical channel error model is illustrated in Figure 8. In the same way than for baro-inertial altitude, the baro-inertial vertical speed error model equation is described as follows:

$$\delta\dot{V}_z = \delta f^z_{corr} - \frac{2g_0}{R_E} \cdot \delta h_B + \delta a_B + K_2 \cdot (\delta h_B - \delta h_{baro}) \tag{5.22}$$

Where f^z_{corr} is the vertical specific force of the aircraft once inertial corrections (Coriolis) are applied.

The transition state matrix is then:

$$F_{baro\_velo} = \begin{bmatrix} 0 & 0 & \left(K_2 - \frac{2g_0}{R_E}\right) & 1 & 0_{1\times 8} & 1 & 0 & \cdots & 0 \end{bmatrix} \tag{5.23}$$

5.4.1.5 Attitude Error Propagation Equation

The attitude error propagation is given by:

$$\dot{\rho} = -\widehat{\Omega}^w_{w/i} \cdot \rho + \hat{R}_{m2w} \cdot \delta\omega^m_{m/i} - \delta\omega^w_{w/i} \tag{5.24}$$

Where:

- $\dot{\rho}$ is the derivative of the attitude error vector.
- $\widehat{\Omega}^w_{w/i}$ is the skew symmetric matrix associated to the estimated angular velocity error vector of the *w-frame* with respect to the *i-frame*.
- ρ is the attitude error vector.
- $\hat{R}_{m2w}$ is estimated rotation matrix, from the *m-frame* coordinates system to the *w-frame* coordinates system.
- $\delta\omega^m_{m/i}$ is the angular velocity error vector of the *m-frame* with respect to the *i-frame* expressed in the *m-frame* coordinates system.
- $\delta\omega^w_{w/i}$ is the angular velocity error vector of the *w-frame* with respect to the *i-frame* expressed in the *w-frame* coordinates system.

The steps to obtain that equation are entirely detailed in Appendix B. This equation defines the following state transition matrix of the attitude error state:

$$F_{att} = [F_{att/pos} \quad F_{att/velo} \quad F_{att/att} \quad F_{att/bg} \quad F_{att/ba}] \tag{5.25}$$

With:

- $F_{att/pos} = -F_{pos\,1}$ is the position error to attitude error derivative transition matrix. $F_{pos\,1}$ is defined in Appendix B.
- $F_{att/velo} = -F_{velo\,1}$ is the position error to attitude error derivative transition matrix. $F_{velo\,1}$ is defined in Appendix B.
- $F_{att/att} = \left(-\hat{\Omega}^{w}_{w/i}\right)$ is the attitude error to attitude error derivative transition matrix (defined in Appendix B).
- $F_{att/bg} = \hat{R}_{m2w}$ is the gyrometer measurement error to attitude error derivative transition matrix (defined in Appendix B).
- $F_{att/ba} = 0$ is the accelerometer measurement error to attitude error derivative transition matrix (defined in Appendix B).

5.4.1.6 IMU Measurements Error Propagation Equation

The estimation of IMU measurement errors in the Kalman Filter is based on a measurement model supposed as follows:

$$\tilde{f}^{m}_{m/i} = f^{m}_{m/i} + b_{accel} + n_a \tag{5.26}$$

Where:

- $\tilde{f}^{m}_{m/i}$ is the accelerometer measurement
- $f^{m}_{m/i}$ is the real specific force of the mobile
- b_{accel} is the accelerometer measurement error
- n_a is the white Gaussian measurement noise

$$\tilde{\omega}^{m}_{m/i} = \omega^{m}_{m/i} + b_{gyro} + n_g \tag{5.27}$$

Where:

- $\tilde{\omega}^{m}_{m/i}$ is the gyrometer measurement
- $\omega^{m}_{m/i}$ is the real instantaneous rotation rate of the mobile
- b_{gyro} is the gyrometer measurement error gyroscope bias
- n_g is the white Gaussian measurement noise

Considering these measurement models, b_{accel} and b_{gyro} will be estimated in the filter assuming that they follows a first order Gauss Markov process, which model is entirely described in the Chapter 3. Indeed, we saw that this model is described with a correlation time the variance of the driven noise generating the process. This driven noise has a variance related to the variance of the process as presented in equation (3.31). In that case, the IMU measurement errors propagation matrix is as follows:

$$F_{IMU\_biases} = \begin{bmatrix} -\frac{1}{\tau_{gyro}} & 0 & 0 & 0 & 0 & 0 \\ 0 & -\frac{1}{\tau_{gyro}} & 0 & 0 & 0 & 0 \\ 0 & 0 & -\frac{1}{\tau_{gyro}} & 0 & 0 & 0 \\ 0 & 0 & 0 & -\frac{1}{\tau_{accel}} & 0 & 0 \\ 0 & 0 & 0 & 0 & -\frac{1}{\tau_{accel}} & 0 \\ 0 & 0 & 0 & 0 & 0 & -\frac{1}{\tau_{accel}} \end{bmatrix} \tag{5.28}$$

Where τ_{accel} and τ_{gyro} are the assumed measurement error correlation times.

5.4.1.7 Receiver Clock Bias and Drift Propagation Equation

As in [Farrel and Barth, 1998], we assume a continuous-time two-state clock model. Figure 37 presents the block diagram of this model:

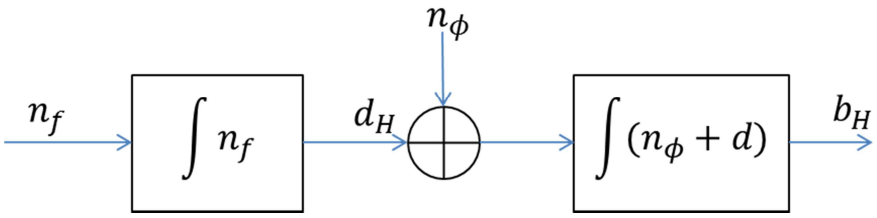

Figure 37 – Continuous-time two-state clock model [Farrel and Barth, 1998]

The associated process that describes the clock model is then as follows:

$$\begin{bmatrix} \dot{b}_H \\ \dot{d}_H \end{bmatrix} = \underbrace{\begin{bmatrix} 0 & 1 \\ 0 & 0 \end{bmatrix}}_{F_{clock}} \cdot \begin{bmatrix} b_H \\ d_H \end{bmatrix} + \begin{bmatrix} u_\phi \\ u_f \end{bmatrix} \tag{5.29}$$

Where F_{clock} is the state transition matrix of the receiver clock bias and drift states.

5.4.1.8 GNSS Pseudoranges Correlated Errors Propagation Equation

In the studied hybridization solution, presented in 5.1 as an open loop tight coupling EKF architecture, we integrate GNSS code pseudorange measurements. In order to improve the performance of an integrated solution, it is important to estimate most of the errors of the system integrated in the global solution. In that way, we will introduce on the error state vector, a state that should represents the biggest component of the error affecting the GNSS measurements. The section 3.2.1 introduced the different error sources

that can affect the GNSS pseudorange measurements and described their amplitude and temporal behavior. Based on the knowledge of these potential errors (depending on the GNSS receiver configuration: single or dual frequency, single or dual constellation) and on the fact that a KF is able to estimate a time correlated process, we will be able to estimate the major component of the time-correlated errors on the GNSS measurements.

The time-correlated error on the GNSS pseudorange measurements is then modeled as first order Gauss-Markov processes with the same assumed correlation time $\tau_{b_{GNSS}}$ and the same variance whatever the satellite the signal is emitted from. And, the state transition matrix for the GNSS code pseudorange measurements is as follows:

$$F_{b_{GNSS}} = \begin{bmatrix} -\frac{1}{\tau_{b_{GNSS}}} & 0 & 0 \\ 0 & \ddots & 0 \\ 0 & 0 & -\frac{1}{\tau_{b_{GNSS}}} \end{bmatrix} \tag{5.30}$$

The correlation time $\tau_{b_{GNSS}}$ used for modeling the time-correlated error on the code pseudorange measurements is set at the maximum correlation time of all errors affecting the measurements (and presented in Chapter 2) so as to focus on estimating the error with the slowest variation.

5.4.2 Process Noise Covariance Matrix

The process noise covariance matrix is by definition the covariance of the state noise vector U, as defined in (5.3).

U may be divided in four parts as follows:

$$U = \begin{bmatrix} U_{INS} \\ U_{IMU} \\ U_{clock} \\ U_{b_{GNSS}} \end{bmatrix} \tag{5.31}$$

The process noise for the horizontal position error states is due to implementation and rounded errors. For the velocity and attitude error states, the process noises are mainly due to the accelerometer and gyrometer noises, respectively. The process noise for the baro-inertial error states is mainly driven by the barometer noise. The process noise vector for the “INS” states is then as follows:

$$U_{INS} = \begin{bmatrix} u_{\theta_x} \\ u_{\theta_y} \\ u_{h_B} \\ u_{a_B} \\ u_{v_x} \\ u_{v_y} \\ u_{v_z} \\ u_{\phi_x} \\ u_{\phi_y} \\ u_{\phi_z} \end{bmatrix} \tag{5.32}$$

In a second part, considering that we model the inertial biases as first order GM processes, the state noise vector of the six inertial biases states is the driven noise of the GM that models the processes. The "IMU" state noise vector is then as follows:

$$U_{IMU} = \begin{bmatrix} u_{bg_x} \\ u_{bg_y} \\ u_{bg_z} \\ u_{ba_x} \\ u_{ba_y} \\ u_{ba_z} \end{bmatrix} \tag{5.33}$$

The receiver clock bias and drift states noises are defined by Allan constants and depend on the receiver clock quality performance [Farrel and Barth, 1998]. The noise vector is defined in (5.29):

$$U_{clock} = \begin{bmatrix} u_{\phi} \\ u_f \end{bmatrix} \tag{5.34}$$

Finally, the process noise associated to the time-correlated GNSS biases are characterized by the variance of the driven noise of the GM process. The details of the GM process are presented in Chapter 3. In fact, the process is the same as for inertial measurement errors: the variance of the driven noise for generating the GM process is related to the variance of the bias as in equation (3.31). The noise vector is denoted as follows:

$$U_{b_{GNSS}} = \begin{bmatrix} u_{b_{GNSS\,1}} \\ \vdots \\ u_{b_{GNSS\,N}} \end{bmatrix} \tag{5.35}$$

Assuming inertial error state noises are not correlated, mutually independent, and independent from GNSS error state noise, the continuous time state noise covariance matrix is the covariance of the previously described noise vector.

5.5 Observation Model

5.5.1 Observation Function

The observation function of the Kalman Filter is the function that relates the state vector X to the measurement vector Y. In the EKF equations (5.3) and (5.4), the observation function is linearized so as to relate the error state vector δX to the observation evctor of the EKF Z. The linearized observation matrix is denoted H.

That section presents the main steps for obtaining the observation functions the different aiding systems involved in the thesis: GNSS code pseudorange measurements, WSS measurements and Video system measurements. Then a brief part describes how to compute the linearized observation matrix.

5.5.1.1 GNSS Pseudorange Observation Function

The mathematical model of GNSS code pseudorange measurements provided by a receiver for a given satellite i at epoch k for integration within a Kalman Filter architecture can be written as:

$$\tilde{P}^i(k) = \rho^i(k) + cb_H(k) + b^i_{GNSS}(k) + n^i(k) \tag{5.36}$$

Where:

- $\tilde{P}$ is the code pseudorange measurement in meters.
- ρ is the true geometrical distance between the receiver and the satellite.
- c is the speed of light.
- b_H is the receiver clock bias.
- Δt_s is the satellite clock bias.
- b_{GNSS} is the bias on the measurement assumed to be time-correlated.
- n is the receiver thermal noise error, assumed to be centered, white and Gaussian.

Let h^i_{GNSS} be the observation function that relates the measurement P^i to the aircraft current location X. The measurement model (5.36) can be rewritten as:

$$\tilde{P}^i(k) = h^i_{GNSS}\big(X(k)\big) + n^i(k) \tag{5.37}$$

With:

$$h^i_{GNSS}\big(X(k)\big) = \rho^i(k) + cb_H(k) + b^i_{GNSS}(k) \tag{5.38}$$

And then depends on:

- b_{GNSS}: the bias on the pseudorange measurement.
- b_H: the receiver clock bias.
- ρ: the geometrical range.

The geometrical range is related to the user antenna position as follows:

$$\rho^i(k) = \sqrt{\left(x^i(k) - x(k)\right)^2 + \left(y^i(k) - y(k)\right)^2 + \left(z^i(k) - z(k)\right)^2} \tag{5.39}$$

Where:

- $(x, \mathrm{y}, \mathrm{z})$ are the coordinates of the position estimated by the INS in the *e-frame*.
- $\left(x^i, y^i, z^i\right)$ are the coordinates of the i^{th} satellite position in the *e-frame*.

In the model for GNSS code pseudorange measurement detailed in (5.37), the noise on the measurement is supposed to be a pure White Gaussian uncorrelated noise. This measurement noise is assumed to describe the receiver thermal noise, however, when we proposed a GNSS code pseudorange measurement model in 3.2.3, the receiver residual noise was assumed to be modeled as a first order Gauss Markov process with a 1s correlation time. In the current model, the correlated noise in included in the bias component and only a noise assumed centered, white and Gaussian remains.

5.5.1.2 WSS Measurement Observation Function

The mathematical model of the WSS velocity measurements provided by the i^{th} WSS at epoch k for integration within a Kalman Filter architecture can be described as follows:

$$\tilde{v}^{\mathrm{i}}_{WSS}(k) = R_{w2m}(k) \cdot v^w_{m/e}(k) + n^i_{WSS}(k) \tag{5.40}$$

Where:

- $\tilde{v}_{WSS}$ is the WSS velocity vector measurement.
- R_{w2n} is the rotation matrix from the *w-frame* to the *m-frame*.
- $v^w_{m/e}$ is the Earth-relative velocity of the aircraft expressed in the *w-frame*.
- n_{WSS} is the measurement noise assumed to be white and Gaussian.

As described in 3.5.2, if we assume the non-holonomic hypothesis, we can consider the WSS velocity measurement is a measurement along the longitudinal axis, only. In other words, the WSS velocity vector components along the *y-axis* and *z-axis* of the *m-frame* are equal to zero. In that way only the first component of the vector will be considered.

Let h^i_{WSS} be the WSS observation function:

$$\tilde{v}^{i}_{WSS}(k) = h^{i}_{WSS}\big(X(k)\big) + n^{i}_{WSS}(k) \tag{5.41}$$

With:

$$h^{i}_{WSS}\big(X(k)\big) = R_{w2m}(k) \cdot v^{w}_{m/e}(k) \tag{5.42}$$

And then depends on:

- R_{w2m}: the rotation matrix from the *w-frame* coordinates system to the *m-frame* coordinates system.
- $v^{w}_{m/e}$: the Earth-relative velocity of the aircraft expressed in the *w-frame*.

5.5.1.3 Video Measurement Observation Function

The video angular measurement mathematical model provided by the video system for a given target i at epoch k for integration within a Kalman Filter, is described in 4.1.8.3 and reminded in the following:

$$\tan\left(\tilde{\alpha}^{i}_{X}(k)\right) = \tan\left(\alpha^{i}_{X}(k)\right) + n^{i}_{X}(k) \tag{5.43}$$

$$\tan\left(\tilde{\alpha}^{i}_{Y}(k)\right) = \tan\left(\alpha^{i}_{Y}(k)\right) + n^{i}_{Y}(k) \tag{5.44}$$

Where:

- $\tilde{\alpha}_X$ and $\tilde{\alpha}_Y$ are the video angular measurements.
- α_X and α_Y are the true video angular measurements.
- n_X and n_Y are the measurement noise assumed to be centered, white and Gaussian.

Let h^{i}_{video} be the observation function. Equations (5.43) and (5.44) can be rewritten using the observation function as:

$$\tan\big(\alpha^{i}(k)\big) = h^{i}_{video}\big(X(k)\big) + n^{i}_{Y}(k) \tag{5.45}$$

Where $\alpha = [\alpha_X; \alpha_Y]$ and $n = [n_X; n_Y]$.

with:

$$h^{i}_{video}\big(X(k)\big) = \tan\left(\alpha^{i}(k)\right) \tag{5.46}$$

The relationship between the video observation function and the aircraft position is not as straight forward as for GNSS and WSS.

This process starts with the introduction of an "intermediate" set of angular measurements that we will name $\alpha' = (\alpha'_X, \alpha'_Y)$. These angles correspond to optical angular measurement in the particular case where the aircraft roll angle, ϕ, is equal to zero (the camera is considered perfectly horizontal). The consideration of a non-zero roll angle will be presented in section 5.5.1.3.3. The first section focusses on the first intermediate angular coordinate, α'_X.

5.5.1.3.1 α'_X Angular Coordinate Function

The determination of the observation function for the first intermediate angular measurements is done through a complex process involving angular and trigonometric relations. The first measurement α_X is defined as the angle between the normal axis of the image plane and the LOS of the target in the vertical plane (see section 4.1.8.3). In the case of a zero roll angle, Figure 38 illustrates the current configuration.

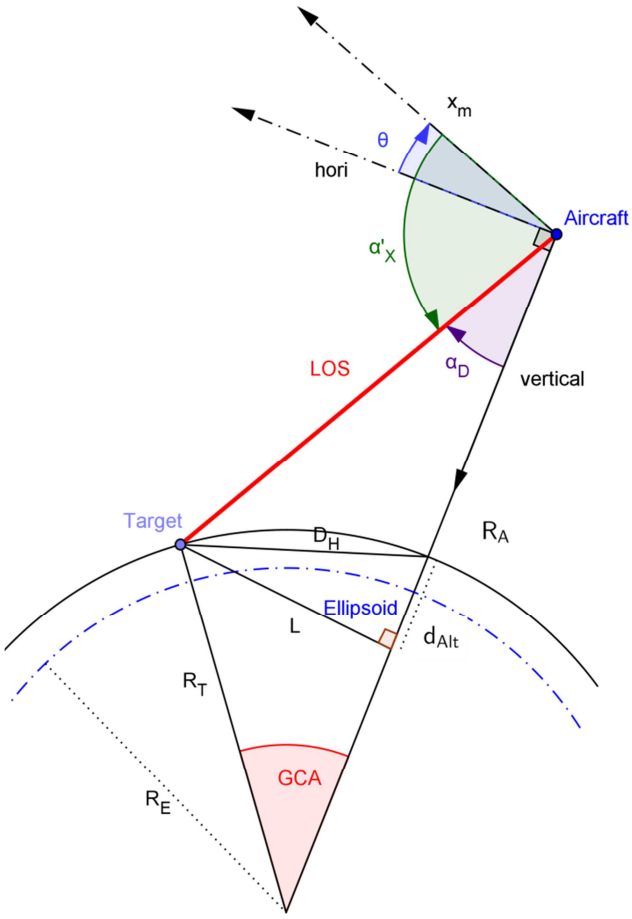

Figure 38 – Observation model for the vertical optical angular measurement

This figure introduces several parameters that are:

- x_m is the x-axis of the *m-frame* (the longitudinal axis of the aircraft).
- $hori$ is the projection of the x_m axis in the local horizontal plane.
- θ is the pitch angle.

- α_D is the angle between the local vertical axis and the LOS.
- R_E is the radius of the Earth.
- R_A is the distance between the aircraft and the center of the Earth: $R_A = R_E + h_B$.
- R_T is the distance between the target and the center of the Earth: $R_T = R_E + h_T$, where h_T is the altitude of the target.
- GCA is the Great Circle Angle between the target and the Aircraft.
- D_H is the horizontal distance between the target and the projection of the aircraft positon at the target's altitude.
- d_{Alt} and L define the rectangle triangle illustrated in the figure.

The representation allows establishing the following relationship between the intermediate measurement α'_X (the angle is counted positive in the anti-trigonometric direction), α_D and the pitch angle θ.

$$\alpha'_X = \theta + \frac{\pi}{2} - \alpha_D \tag{5.47}$$

Then as explained above, considering the tangent of the angles, we can introduce the following equation:

$$\tan(\alpha'_X) = \tan\left(\theta + \frac{\pi}{2} - \alpha_D\right) \tag{5.48}$$

The development of (5.48) leads to the following relationship:

$$\tan(\alpha'_X) = \frac{1 + \tan\alpha_D \cdot \tan\theta}{\tan\alpha_D - \tan\theta} \tag{5.49}$$

This last equation, equation (5.49), shows that the intermediate measurement α'_X depends on the pitch angle of the aircraft and the α_D angle. This relationship is introduced as a function f_X in the following, which leads to the following equation:

$$\tan(\alpha'_X) = f_X(\tan(\alpha_D), \tan(\theta)) \tag{5.50}$$

With the following definition of f_X for a given set (x, y):

$$f_X(x, y) = \frac{1 + x \cdot y}{x - y} \tag{5.51}$$

In a second step, focusing on the development of the expression of α_D using Figure 38, we get the following equations:

$$R_A = R_E + h_B \tag{5.52}$$

$$R_T = R_E + h_T \tag{5.53}$$

Where:

- R_A is the distance from the center of the Earth to the aircraft.
- h_B is the altitude of the aircraft.
- R_T is the distance from the center of the Earth to the target.
- h_T is the altitude of the target.
- R_E is the radius of the Earth.

In addition,

$$\tan(\alpha_D) = \frac{L}{d_{Alt} + \Delta Alt} \tag{5.54}$$

Where $\Delta Alt = h_B - h_T$ is the difference between the altitude of the aircraft and the altitude of the target.

Thus, it can be easily shown that in the triangle described by the sides L, d_{Alt} and D_H, the angle between D_H and L is equal to $\frac{GCA}{2}$ where GCA is the great circle angle illustrated in Figure 38. The sides of this triangle can be expressed in function of the GCA and R_T as follows:

$$L = R_T \cdot \sin GCA \tag{5.55}$$

$$D_H = 2 \cdot R_T \cdot sin\left(\frac{GCA}{2}\right) \tag{5.56}$$

$$\begin{aligned} d_{Alt} &= D_H \cdot sin\left(\frac{GCA}{2}\right) \\ &= 2 \cdot R_T \cdot sin^2\left(\frac{GCA}{2}\right) \\ &= R_T \cdot (1 - cos(GCA)) \end{aligned} \tag{5.57}$$

And finally, using (5.54), (5.55) and (5.57) we obtain the following expression of $\tan(\alpha_D)$:

$$\begin{aligned} \tan(\alpha_D) &= \frac{R_C \cdot \sin(GCA)}{2R_C \cdot \sin^2\left(\frac{GCA}{2}\right) + \Delta Alt} \\ &= \frac{R_C \cdot \sin(GCA)}{R_C \cdot (1 - \cos(GCA)) + \Delta Alt} \\ &= \frac{R_C \cdot \sin(GCA)}{R_E + h_B - R_C \cdot \cos(GCA)} \end{aligned} \tag{5.58}$$

The last expression defines the tangent of the angle α_D as a function of the GCA, the aircraft altitude and other parameters (R_E and R_T). This relationship will be introduced as a function g_X in the following, which leads to the following equation:

$$\tan(\alpha_D) = g_X(GCA, h_B) \tag{5.59}$$

With the following definition of g_X for a given set of (x, y, R_C, R_E):

$$g_X(x, y) = \frac{R_C \cdot \sin(x)}{R_E + y - R_C \cdot \cos(x)} \tag{5.60}$$

If we synthetize the two previous steps (5.50) and (5.59), we can express tangent of α'_X using f_X and g_X:

$$\tan(\alpha'_X) = f_X(g_X(GCA, h_B), \theta) \tag{5.61}$$

Then, the third step consists in developing the expression of the GCA. This development is done introducing the relationship called "haversine formula".

The haversine formula expresses the haversine of the GCA (defined as half the versine: 1 − cos) between two points on a sphere in function of the spherical geodetic coordinates of the two points (in our case the latitude λ and longitude ϕ of these two points). The haversine formula is given in (5.62).

$$haversine(GCA) = haversine(\Delta\lambda) + \cos(\lambda_1)\cos(\lambda_2)\, haversine(\Delta\phi) \tag{5.62}$$

Where:

- $\Delta\lambda = \lambda_2 - \lambda_1$ is the difference in latitude of the two points on the sphere
- $\Delta\phi = \phi_2 - \phi_1$ is the difference in longitude of the two points on the sphere
- λ_i, ϕ_i are respectively the latitude and longitude of the i^{th} point on the sphere

The haversine function and its inverse are defined as follows for a given angle x:

$$haversine(x) = \sin^2\left(\frac{x}{2}\right) = \frac{1 - \cos(x)}{2} \tag{5.63}$$

$$haversine^{-1}(x) = 2 \cdot \arcsin\left(\sqrt{x}\right) \tag{5.64}$$

The haversine formula can be extended to the "law of haversines" (5.66) using the law of spherical cosines (5.65) and considering three points on a sphere as illustrated in Figure 39.

$$\cos(a) = \cos(b) \cdot \cos(c) + \sin(b) \cdot \sin(c) \cdot \cos(\hat{A}) \tag{5.65}$$

$$haversine(a) = haversine(b - c) + \sin(b) \cdot \sin(c) \cdot haversine(\hat{A}) \tag{5.66}$$

Where a, b, c and A are defined in Figure 39 (a, b, c are the angles subtended by the labeled sides of the triangle).

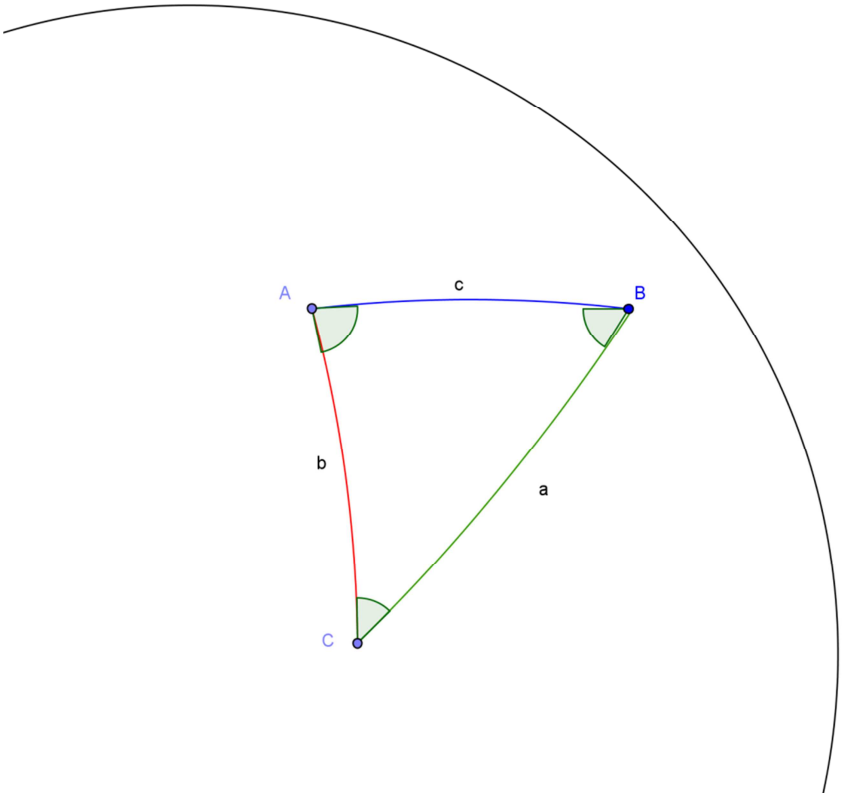

Figure 39 – Spherical triangle solved by the law of haversines

The use of the previously introduced law of haversines in our context can be done considering that apexes B and C are the target and the aircraft locations, respectively. In addition, apex A is defined such that b and c sides are respectively along a meridian and along a parallel.

We thus obtain the following relation:

$$\begin{aligned} haversine(GCA) &= haversine(\Delta\lambda - \Delta\phi) + \sin(\Delta\lambda) \cdot \sin(\Delta\phi) \cdot haversine\left(\frac{\pi}{2}\right) \\ &= \frac{1 - \cos(\Delta\lambda - \Delta\phi)}{2} + \frac{1 - \sin(\Delta\lambda - \Delta\phi)}{2} \\ &= \frac{1 - \cos(\Delta\lambda) \cdot \cos(\Delta\phi)}{2} \end{aligned} \tag{5.67}$$

Where $\Delta\lambda = \lambda - \lambda_T$ and $\Delta\phi = \phi - \phi_T$. (λ, ϕ) being the geodetic coordinates of the aircraft and, (λ_T, ϕ_T) being the geodetic coordinates of the target.

From the definition of the haversine function and its inverse in (5.63) and (5.64), we can obtain an expression of the cosine (5.68) and the sine (5.69) of the GCA and, an expression of the GCA (5.70).

$$\cos(GCA) = \cos(\Delta lat) \cdot \cos(\Delta long) \tag{5.68}$$

$$\sin(GCA) = \sqrt{1 - \cos^2(\Delta lat) \cdot \cos^2(\Delta long)} \tag{5.69}$$

$$\begin{aligned} GCA &= 2 \arcsin\left(\sqrt{\frac{1 - \cos(\Delta lat) \cdot \cos(\Delta long)}{2}}\right) \\ &= \arccos(\cos(\Delta lat) \cdot \cos(\Delta long)) \end{aligned} \tag{5.70}$$

The last expression defines the GCA between the aircraft and the target as a function of the aircraft and target positions. This relationship will be introduced as a function k in the following, which leads to the following equation:

$$GCA = k(\lambda, \phi) \tag{5.71}$$

With the following definition of k for a given set of $(x, y, \lambda_T, \phi_T)$:

$$k(x, y) = \arccos(\cos(x - x_T) \cdot \cos(y - y_T)) \tag{5.72}$$

If we synthetize the different steps (5.61) and (5.71), we can express the tangent of α'_X using the functions f_X, g_X and k:

$$\tan(\alpha'_X) = f_X(g_X(k(\lambda, \phi), h_B), \theta) \tag{5.73}$$

The entire relationship between the tangent of α'_X and $(\lambda, \phi, h_B, \theta)$ will be simplified in the following using the notation h_X. In that way, (5.73) becomes:

$$\tan(\alpha'_X) = h_X(\lambda, \phi, h_B, \theta) \tag{5.74}$$

5.5.1.3.2 α'_Y Angular Coordinate Function

The determination of the observation function for the second intermediate angular measurements is done in a similar way. The second measurement α_Y is defined as the angle between the normal axis of the image plane and the LOS of the target in the horizontal plane (see section 4.1.8.3). In the case of a zero roll angle, Figure 40 illustrates the current configuration.

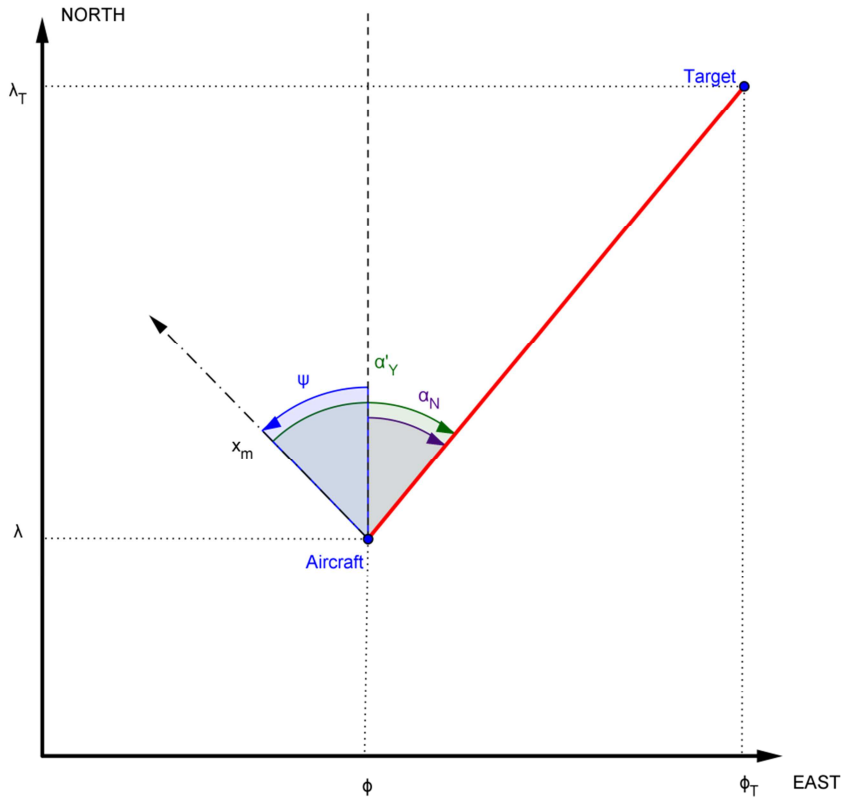

Figure 40 – Observation model for the horizontal optical angular measurement

This figure introduces several parameters that are defines as follows:

- x_m is the x-axis of the *m-frame* (the longitudinal axis of the aircraft).
- ψ is the heading angle.
- α_N is the angle between the North and the LOS.
- (λ, ϕ) are the geodetic coordinates of the aircraft (latitude and longitude)
- (λ_T, ϕ_T) are the geodetic coordinates of the target.

The representation allows establishing the following relationship between the intermediate measurement α'_Y (the angle is counted positive in the anti-trigonometric direction), α_N and the heading angle ψ.

$$\alpha'_Y = \alpha_N - \psi \tag{5.75}$$

In the following, we will assume that the video measurement will be the same for any variation in altitude. In other words, for two measurement made at the same latitude and longitude but at two different altitudes, α'_Y angle will be identical. In that way for the computation, we will consider that the two objects are on a sphere, and then the aircraft point is considered to be the projection of the aircraft at the same altitude as the target.

Then as explained above, considering the tangent of the angles, we can introduce the following equation:

$$\tan(\alpha'_Y) = \tan(\alpha_N - heading) \tag{5.76}$$

The development of (5.76) leads to the following relationship:

$$\tan(\alpha'_Y) = \frac{\tan(\alpha_N) - \tan(\psi)}{1 + \tan(\alpha_N) \cdot \tan(\psi)} \tag{5.77}$$

This last equation (5.77) shows that the intermediate measurement α'_Y depends on the heading angle of the aircraft and α_N angle. This relationship is introduced as a function f_Y in the following, which leads to the following equation:

$$\tan(\alpha'_Y) = f_Y(\tan(\alpha_N), \tan(\psi)) \tag{5.78}$$

With the following definition of f_Y for a given set (x, y):

$$f_Y(x, y) = \frac{x - y}{1 + x \cdot y} \tag{5.79}$$

In a second step, focusing on the development of the expression of α_N using Figure 40, we can introduce the following parameters:

- d_{lat}, which is the arc segment length between the aircraft and the target along a meridian line
- d_{long}, which is the arc segment length between the aircraft and the target along a parallel line

Their expressions are given as:

$$d_{lat} = 2 \cdot R_T \cdot \sin\left(\frac{\Delta\lambda}{2}\right) \tag{5.80}$$

$$d_{long} = 2 \cdot R_T \cdot \sin\left(\frac{\Delta\phi}{2}\right) \tag{5.81}$$

Using (5.69) and (5.70), the tangent of α_N can be expressed as:

$$\begin{aligned} \tan\alpha_N &= \frac{d_{long}}{d_{lat}} \\ &= \frac{\sin\left(\frac{\Delta\phi}{2}\right)}{\sin\left(\frac{\Delta\lambda}{2}\right)} \end{aligned} \tag{5.82}$$

The last expression defines the tangent of the angle α_N as a function of the aircraft and target positions. This relationship will be introduced as a function g_Y in the following, which leads to the following equation:

$$\tan \alpha_N = g_y(\lambda, \phi) \tag{5.83}$$

With the following definition of g_Y for a given set (x, y):

$$g_Y(x, y) = \frac{\sin\left(\frac{\phi - \phi_T}{2}\right)}{\sin\left(\frac{\lambda - \lambda_T}{2}\right)} \tag{5.84}$$

If we synthetize the two previous steps (5.78) and (5.83), we can express tangent of α'_Y using the functions f_Y and g_Y:

$$\tan(\alpha'_Y) = f_Y(g_Y(\lambda, \phi), \tan(\psi)) \tag{5.85}$$

The entire relationship between tangent of α'_Y and (λ, ϕ, ψ) will be simplified in the following using the notation h_Y. In that way, (5.73)(5.85) becomes:

$$\tan(\alpha'_Y) = h_Y(\lambda, \phi, \psi) \tag{5.86}$$

5.5.1.3.3 Roll angle φ contribution

The two previous observation functions described by equations (5.74) and (5.86) express a relationship between the video angular measurements and the aircraft location through its position, altitude and attitude. However, the two functions were established under the assumption that the roll angle of the aircraft, φ, was equal to zero. To extend that model for any value of φ, we will use the basic set of pixel coordinates. Indeed, the pixel coordinates of a feature in a given image are observed with respect to the image frame. Then applying any rotation of the image frame, effect of a roll movement of the aircraft will induce a rotation transformation on the pixel coordinates.

The zero roll angle assumption used for establishing the measurement model in the vertical and horizontal directions can be justified by the fact that the observation function defines the LOS vector in the camera frame. Thus, the application of a roll angle rotation can be seen as a coordinate transformation and can be applied in a second step. The idea behind this process is that it simplifies the observation function determination by doing it sequentially in the same way as we apply a rotation composed of three sub-rotations to a vector.

For describing the roll angle contribution on the observation function, we introduce the set of pixel coordinates of a feature under the assumption of a roll equal to zero as (X', Y'). Identically, the coordinates of the same pixel considering the roll of the aircraft are (X, Y). The notations are illustrated in Figure 41. The difference between the two sets is a rotation between the axis frames of an angle equal to φ.

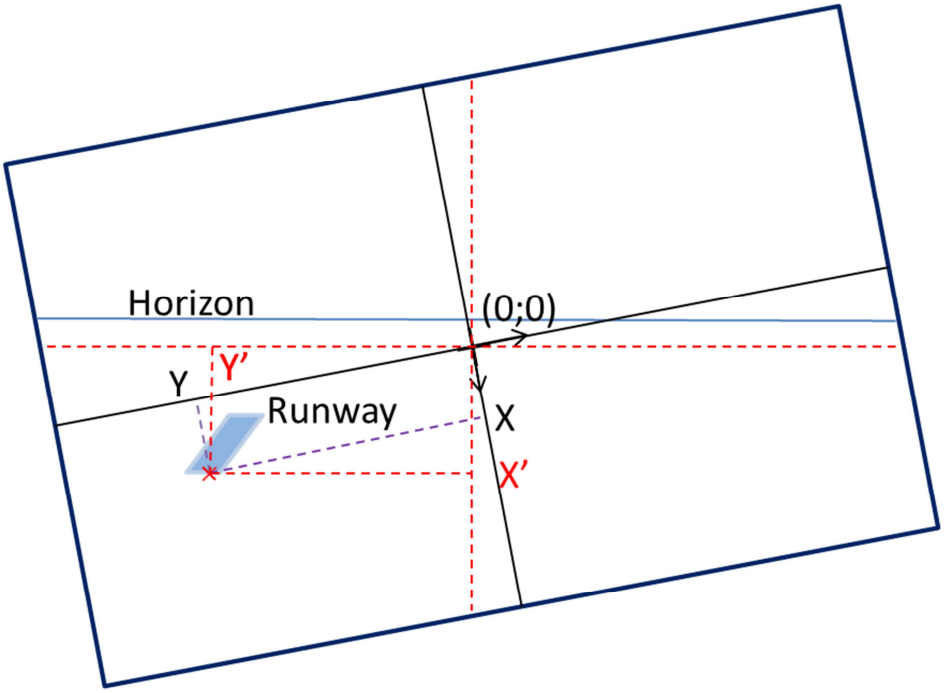

Figure 41 – Optical angular measurements in presence of roll

In a first step we define the relationship between the angular coordinates and the pixel coordinates and, the focal length of the camera of the video system:

$$\tan(\alpha_X) = \frac{X}{f} \tag{5.87}$$

$$\tan(\alpha_Y) = \frac{Y}{f} \tag{5.88}$$

Where:

- X is the vertical coordinate of the image of the target, positive toward the down direction.
- Y is the horizontal coordinate of the image of the target, positive toward the right direction.
- f is the focal length

Under the “no-roll” assumption, in a similar way, we have:

$$\tan(\alpha'_X) = \frac{X'}{f} \tag{5.89}$$

$$\tan(\alpha'_Y) = \frac{Y'}{f} \tag{5.90}$$

After the introduction of the pixel coordinates and based on the illustration in Figure 41, the relationship between the two sets of pixel coordinates is simply as follows:

$$\begin{aligned} X &= X' \cdot \cos(\varphi) + Y' \cdot \sin(\varphi) \\ Y &= -X' \cdot \sin(\varphi) + Y' \cdot \cos(\varphi) \end{aligned} \tag{5.91}$$

By dividing both sides by the focal length of the camera we have the same relationship between the two sets of angular coordinates:

$$\begin{aligned} \tan(\alpha_X) &= \tan(\alpha'_X) \cdot \cos(\varphi) + \tan(\alpha'_Y) \cdot \sin(\varphi) \\ \tan(\alpha_Y) &= -\tan(\alpha'_X) \cdot \sin(\varphi) + \tan(\alpha'_Y) \cdot \cos(\varphi) \end{aligned} \tag{5.92}$$

Finally, introducing the rotation matrix R_φ, equation (5.92) can be rewritten as follows:

$$\begin{pmatrix} \tan(\alpha_X) \\ \tan(\alpha_Y) \end{pmatrix} = \underbrace{\begin{pmatrix} \cos(\varphi) & \sin(\varphi) \\ -\sin(\varphi) & \cos(\varphi) \end{pmatrix}}_{R_\varphi} \cdot \begin{pmatrix} \tan(\alpha'_X) \\ \tan(\alpha'_Y) \end{pmatrix} \tag{5.93}$$

In conclusion, simply by applying the rotation matrix R_φ to the observation functions h_X and h_Y under the "no-roll" assumption, defined in (5.74) and (5.86), we can establish the general observation functions using (5.93):

$$\tan(\alpha_X) = h_X(\lambda, \phi, h_B, \theta) \cdot \cos(\varphi) + h_Y(\lambda, \phi, \psi) \cdot \sin(\varphi) \tag{5.94}$$

$$\tan(\alpha_Y) = -h_X(\lambda, \phi, h_B, \theta) \cdot \sin(\varphi) + h_Y(\lambda, \phi, \psi) \cdot \cos(\varphi) \tag{5.95}$$

The entire relationship will be simplified in the following using the notations h_1 and h_2 that relate the true angular video coordinate to the position, altitude and attitude of the aircraft. In that way, (5.73)(5.94) and (5.95) become:

$$\tan(\alpha_X) = h_1(\lambda, \phi, h_B, \varphi, \theta, \psi) \tag{5.96}$$

$$\tan(\alpha_Y) = h_2(\lambda, \phi, h_B, \varphi, \theta, \psi) \tag{5.97}$$

These two functions h_1 and h_2 represent the general observation functions for the two optical angular measurements.

Finally, we summarize the video observation functions for a target i at an epoch k in its vector form as:

$$\begin{bmatrix} \alpha_X^i(k) \\ \alpha_Y^i(k) \end{bmatrix} = h_{video}^i\big(X(k)\big) = \begin{bmatrix} h_1^i\big(X(k)\big) \\ h_2^i\big(X(k)\big) \end{bmatrix} \tag{5.98}$$

5.5.2 Linearized Observation Matrix

The equations of the EKF presented in (5.3) and (5.4) introduce the linearized observation matrix H. The linearization process is described in details in Appendix D. In simple terms, the H matrix is the Jacobian of the observation function h computed around the predicted aircraft state $\hat{X}_{k|k-1}$. This predicted state is obtained after the prediction stage of the Kalman Filter by compensating the inertial position, velocity and attitude of the aircraft $\hat{X}_{INS}$ with the estimation of the error state vector $\delta\hat{X}_{k|k-1}$.

The linearized observation matrix is defined as follows:

$$H = \left.\frac{\partial h}{\partial X}\right|_{\hat{X}_{k|k-1}=\hat{X}_{INS}+\delta\hat{X}_{k|k-1}} \tag{5.99}$$

5.5.3 Measurement Noise Covariance Matrix

The measurement noise covariance matrix is by definition the covariance of the measurement noise vector, V, assumed to be a White Gaussian noise. As we have three types of measurement sources, the measurement noise vector is divided as follows:

$$V = \begin{bmatrix} V_{GNSS} \\ V_{WSS} \\ V_{video} \end{bmatrix} \tag{5.100}$$

The measurement noise on GNSS code pseudorange measurements is assumed to be White Gaussian noise whose variance is equal to the σ_{UERE}^2 for a given satellite. Assuming in addition that all receiver channels are independent and the noise on the measurements is centered and normal distributed, the covariance matrix is diagonal with its components equal to the UERE.

In the same way, for WSS measurements, we will assume that all WSS measurements are independent and the noise on the measurements is centered and normal distributed. The covariance matrix is then diagonal with its components equal to the assumed standard deviation of the velocity noise (depending on the quality of the WSS).

Finally, the noise covariance matrix for Video measurement is diagonal because each target is supposed to be independent from another and the noise is assumed centered and normal distributed. In addition, as presented in 4.1.8.4, a correct value for the noise on the coordinates of the detected feature can be set within some pixels. However, this value strongly depends on the image processing algorithm, the camera characteristics, the environment and the aircraft dynamic. For future works, a more developed model could be assessed in order to be more confident in the estimated noise variance.

5.6 Conclusion

The current chapter developed in details the implemented hybridization solution and introduced the general theoretical equation for solving a state problem using the Kalman Filter estimator. The state space problem has been entirely described in the chapter and, the state transition model and observation model have been particularly detailed.

The observation model for the video system part introduced a solution for the integration of video measurements by defining a detailed observation function for optical angular measurements. The linearization of the obtained observation function is provided in Appendix D.

The next chapter deals with the presentation of the simulation results of the implemented solution.

Chapter 6 : Simulation Results

The current chapter is a presentation of the results obtained after the different simulation tests done with the implemented solution. The simulations tests are based on the assessment of the hybridized solution estimation error for position, velocity and attitude. For that, this chapter also describes the simulation assumptions and details the configurations for every set of simulations.

It aims at assessing the performance of the implemented solution by comparing the estimation results of the different architectures. It proposes a conclusion on the feasibility of such a solution and the optimization or perspective that can be addressed for validating the implementation.

The first part of the chapter is a description of the architecture implemented in a global view. A brief description of the different modules that compose the architecture is reminded.

The second part presents the simulation assumptions for the generation of the measurements and the simulation tests.

The third part is an overview of the simulations, describing some results that were obtained with the filter and detailing some intermediate results.

The last part presents a synthesis of the results by introducing coherent comparisons between the simulation scenarios. We also discuss about the contribution of the different combinations. A performance analysis is proposed based on the criteria chosen for the assessment, the simulation assumptions and the implementation choices.

6.1 Architecture Overview

The global architecture of the implemented multi-sensor hybridization simulator is reminded in Figure 42.

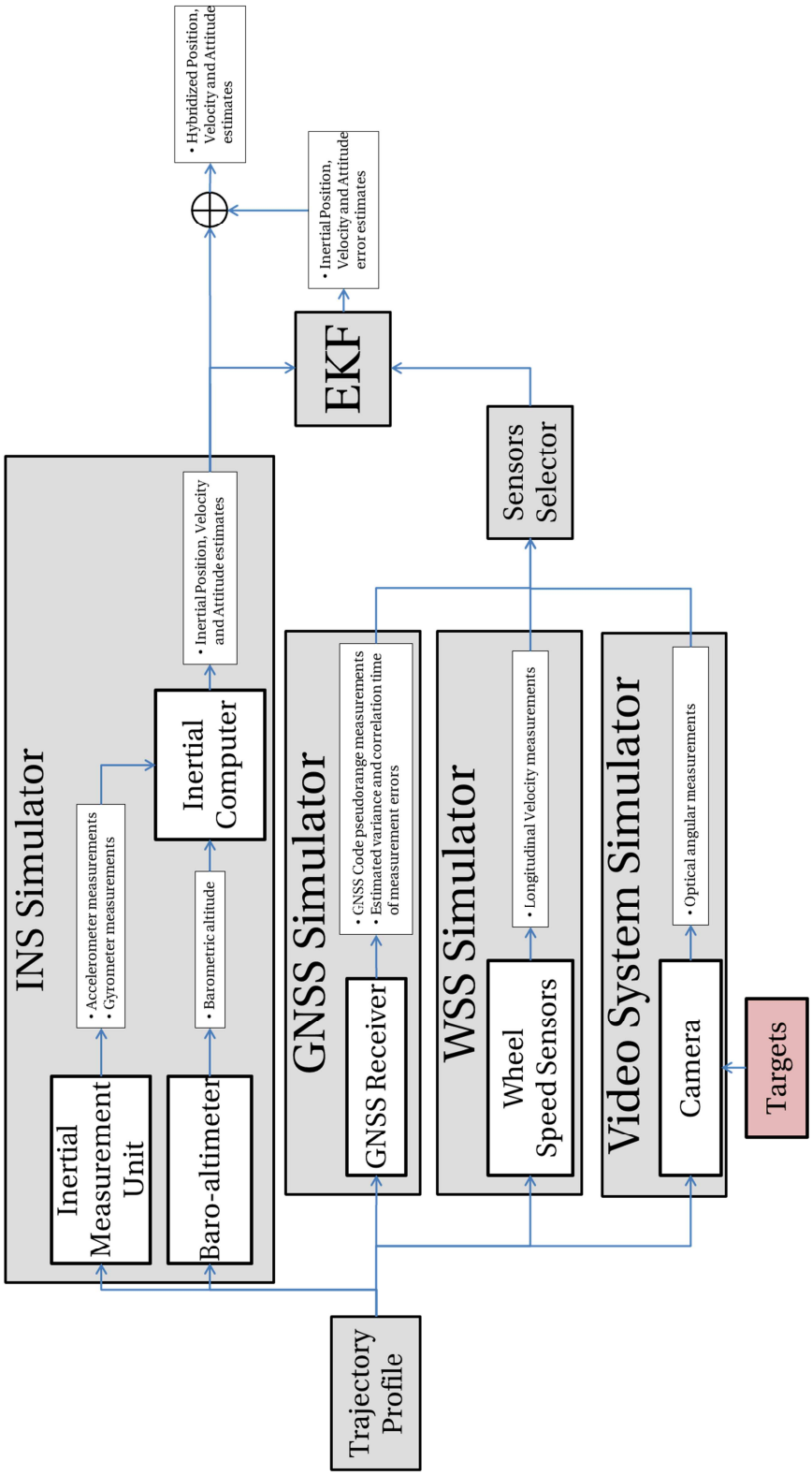

Figure 42 – Global Simulator Architecture Overview

The architecture presented in Figure 42 is composed of a trajectory module that was used for converting the dataset from the different trajectories in the correct input variables for the other simulation modules.

The Strapdown baro-inertial navigation system simulator is composed of different sub-modules that were implemented during the Ph.D. thesis. The IMU module simulator has been implemented with the development of a measurement model detailed in 3.1.2.2. The measurement model can be set according to the IMU performance class that we want to simulate. Interest in that module is that INS performance can be degraded in order to assess and compare hybridization performance with different classes of inertia. The inertial computer is a standard strapdown baro-inertial INS.

The GNSS receiver simulator allows generating code pseudorange measurements for GPS and GALILEO satellites in single or dual frequency. Measurements simulated are modeled as described in 3.2.3.

The WSS simulator is a module that can generate multiple WSS velocity measurements whose model is described in the next part (6.2.1.3).

The Video System simulator generates optical angular measurements as described in the Chapter 4. The generation has been done using the observation function detailed in Appendix D.

The EKF module is the filter described in Chapter 5. The filter can easily allow integrating different configurations of sensors and assessing the hybridization performances in those cases.

The next part reminds the assumptions and models for the simulations of the baro-INS, GNSS, WSS and Video measurements.

6.2 Simulation Assumptions

The current part introduces the mathematical models that have been used for the generation of the simulated measurements for each sensor considered in the thesis. Then, we present the characteristics of the trajectory.

6.2.1 Measurement Models

6.2.1.1 Inertial Measurement Model

The mathematical model for the generation of the IMU measurements (specific force and angular rotation rate) has been detailed in Chapter 3. It is reminded in the following:

$$\tilde{f}^m_{m/i} = (SF_a + M_a) \cdot f^m_{m/i} + b_a + n_a \tag{6.1}$$

Where:

- $\tilde{f}^m_{m/i}$ is the accelerometer measurement
- $f^m_{m/i}$ is the real specific force of the mobile
- SF_a is the Scale Factor error coefficient of the accelerometer
- M_a is the Misalignment error coefficient of the accelerometer
- b_a is the uncompensated accelerometer bias
- n_a is the white Gaussian measurement noise

$$\tilde{\omega}^m_{m/i} = \left(SF_g + M_g\right) \cdot \omega^m_{m/i} + b_g + n_g \tag{6.2}$$

Where:

- $\tilde{\omega}^m_{m/i}$ is the gyrometer measurement
- $\omega^m_{m/i}$ is the real instantaneous rotation rate of the mobile
- SF_g is the Scale Factor error coefficient of the gyrometer
- M_g is the Misalignment error coefficient of the gyrometer
- b_g is the uncompensated gyroscope bias
- n_g is the white Gaussian measurement noise

In our simulations, the uncompensated gyroscope and accelerometer biases b_a and b_g are modeled as the sum of two components:

- The first one models the stability bias (or in-run variation of the bias). This component is modeled as a flicker noise [Kasdin and Walter, 1992]. Time correlation and variance detailed in Table 5 are used in order to model specific classes of IMUs.
- The second one models the repeatability bias (or run-to-run variation of the bias). This component is a constant bias uniformly chosen at each simulation run. The variance of the repeatability bias defined in Table 5 is used to define the width of the interval where the bias is chosen.

The Scale Factor and Misalignment coefficient are constant numbers uniformly chosen at each simulation run. The variances of the parameters defined in Table 5 are used to define the width of the interval where the biases are chosen.

6.2.1.2 Code GNSS Pseudorange Measurement Model

The mathematical model for the generation of the GNSS code pseudorange measurements has been detailed in Chapter 3. It is reminded in the following:

$$\tilde{P}^i(k) = \rho^i(k) + cb_H(k) + \epsilon^i_{Sat/Eph}(k) + \epsilon^i_{iono}(k) + \epsilon^i_{tropo}(k) + \epsilon^i_{mp}(k) + \epsilon^i_{noise}(k) \tag{6.3}$$

Where:

- $\tilde{P}$ is the code pseudorange measurement in meters.
- ρ is the geometrical distance between the receiver and the satellite.
- c is the speed of light.
- b_H is the user time offset.
- $\epsilon_{Sat/Eph}$ is bias induced by the residual ephemeris and the satellite clock errors.
- ϵ_{iono} is the bias induced by the residual ionosphere delay.
- ϵ_{tropo} is the bias induced by the residual tropospheric delay.
- ϵ_{mp} is the bias induced by the residual code multipath delay.
- ϵ_{noise} is the bias induced by the residual thermal noise on the measurement.

$\epsilon_{Sat/Eph}$, ϵ_{iono}, ϵ_{tropo}, ϵ_{mp} and ϵ_{noise} are obtained by generating a first order Gauss-Markov process with using a correlation time constant and a variance as presented in 3.2. We also assumed code pseudorange measurements without code carrier smoothing and unsmoothed measurement error models for tropospheric, noise, satellite clock and ephemeris errors. In particular, multipath error model appears to be a highly conservative model.

GNSS measurements were simulated at a frequency of 1Hz.

6.2.1.3 WSS Measurement Model

The mathematical model for the generation of the WSS velocity measurements is as follows [Li, 2009]:

$$\tilde{v}_{WSS} = (R_{nominal} + \epsilon_R) \cdot (1 + SF_{WSS})\Omega_{WSS} + n_{WSS} \tag{6.4}$$

Where:

- $\tilde{v}_{WSS}$ is the longitudinal earth relative velocity measurement.
- $R_{nominal}$ is the nominal radius of the wheel.
- ϵ_R is the radius variation coefficient.
- SF_{WSS} is the Scale Factor error coefficient of the tachometer.
- Ω_{WSS} is the angular velocity of the wheel.
- n_{WSS} is a white Gaussian measurement noise.

The Ω_{WSS} angular velocity represents the true angular velocity of the wheel. In order to generate it from the dataset presented in the next section (6.2.2), which contains position, velocity and attitude only, we used the velocity. In that way, we divided the

velocity by an estimated value of the radius of the wheel that was assumed to be varying as a function of the velocity. This variation of the radius has been estimated empirically, using a set of real WSS measurements provided in the framework of the Ph.D. thesis. Finally the angular velocity Ω_{WSS} obtained in that way, reflects the variation of the wheel's radius caused by tires distortion at high velocities.

The WSS measurements were generated at 10Hz.

6.2.1.4 Video Measurement Model

The mathematical model for the optical angular measurements provided by the Video system is described in sections 4.1.8 and 5.5.1.3.

It is reminded in the following:

$$\tan(\tilde{\alpha}_X) = \tan(\alpha_X) + n_X \tag{6.5}$$

$$\tan(\tilde{\alpha}_Y) = \tan(\alpha_Y) + n_Y \tag{6.6}$$

Where:

- $\tilde{\alpha}_X$ and $\tilde{\alpha}_Y$ are the video measurements
- α_X and α_Y are the true geometrical angles
- n_X and n_Y are the white Gaussian measurement noises

The true geometrical angles are computed using the following observation function:

$$\tan(\alpha_X) = h_1(\lambda, \phi, h_B, \varphi, \theta, \psi) \tag{6.7}$$

$$\tan(\alpha_Y) = h_2(\lambda, \phi, h_B, \varphi, \theta, \psi) \tag{6.8}$$

Where:

- (λ, ϕ, h_B) are the Earth geodetic coordinates of the aircraft (latitude longitude and altitude).
- (φ, θ, ψ) are the attitude angles of the aircraft.

Next part presents the results obtained with the implemented solution in different configurations.

The Video angular measurements were generated at 10Hz.

6.2.2 Trajectory Profile

All sensors considered in the study are not included or used in the hybridization navigation solution during all phases of flight. Indeed, they are not always able to provide measurements or they provide measurements that will not be integrated. As a global view, the Figure 43 indicates which sensors are included during which phase of flight as defined in 2.1.

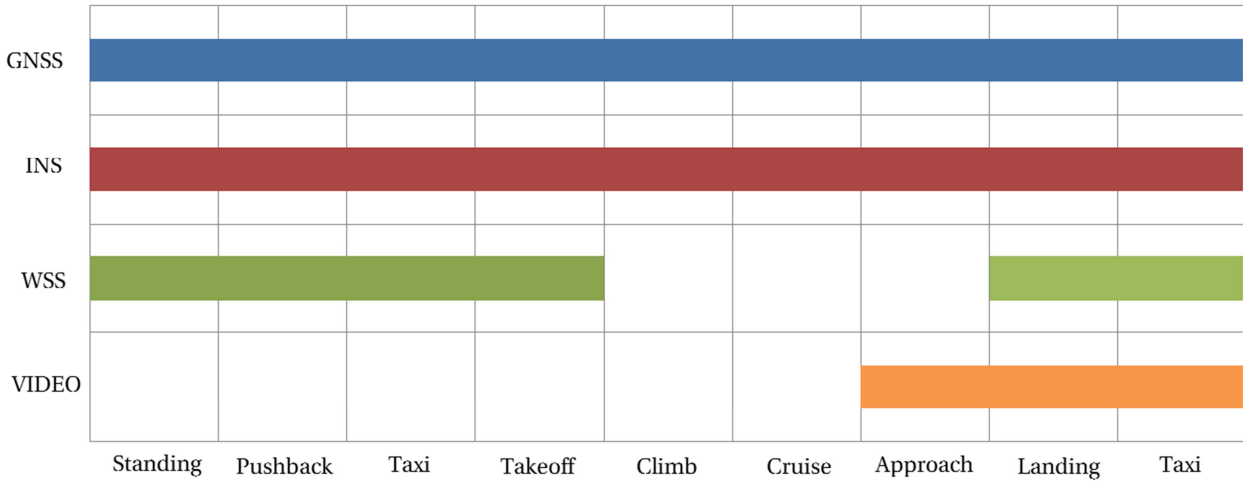

Figure 43 – Inclusion of sensors during phases of flight

As we can see in that figure, the different phases of flight allow proposing several combinations of sensors during an entire flight. This illustration is important so as to keep in mind the potential ability of a navigation solution to switch among the different possible configuration and select the best one. Further comparative performance analyses are conducted in the following.

The trajectory used for the simulations is a Toulouse-Toulouse flight illustrated in Figure 44 and Figure 45. This flight corresponds to a real flight and offers a realistic flight dynamic, a take-off and approach context and a take-off and landing runway rolling. The flight has a duration of two hours and a half. The runway area is indicated in the Figure 44.

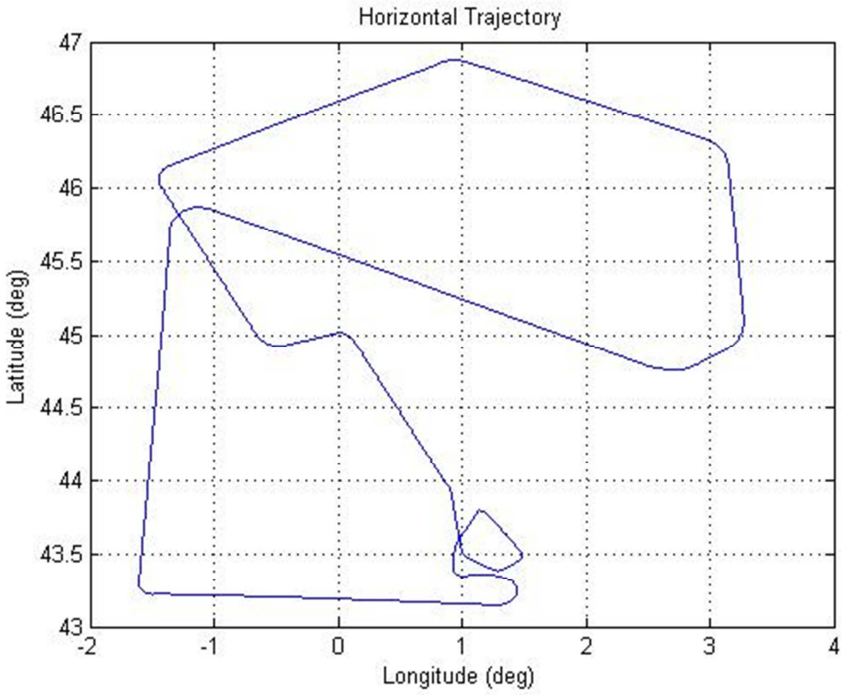

Figure 44 – Horizontal Trajectory Profile

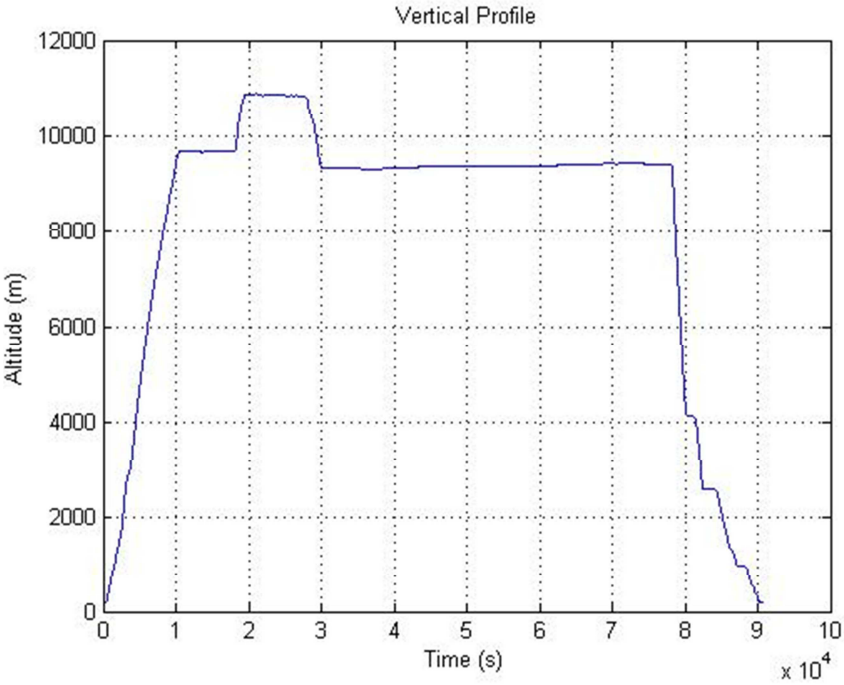

Figure 45 – Altitude Profile

The end of the trajectory is represented in the Figure 46. The runway area, where the WSS measurements are available is illustrated. The red dot represents the instant where the first video measurement can be integrated and the black dot is the moment where the aircraft is aligned with the runway. For the simulations we will focus on the final part of the trajectory composed of the end of the terminal area, the approach area (final approach

segment) and the runway rolling. This part of the trajectory represents the area where all the possible configurations of the filter can be used.

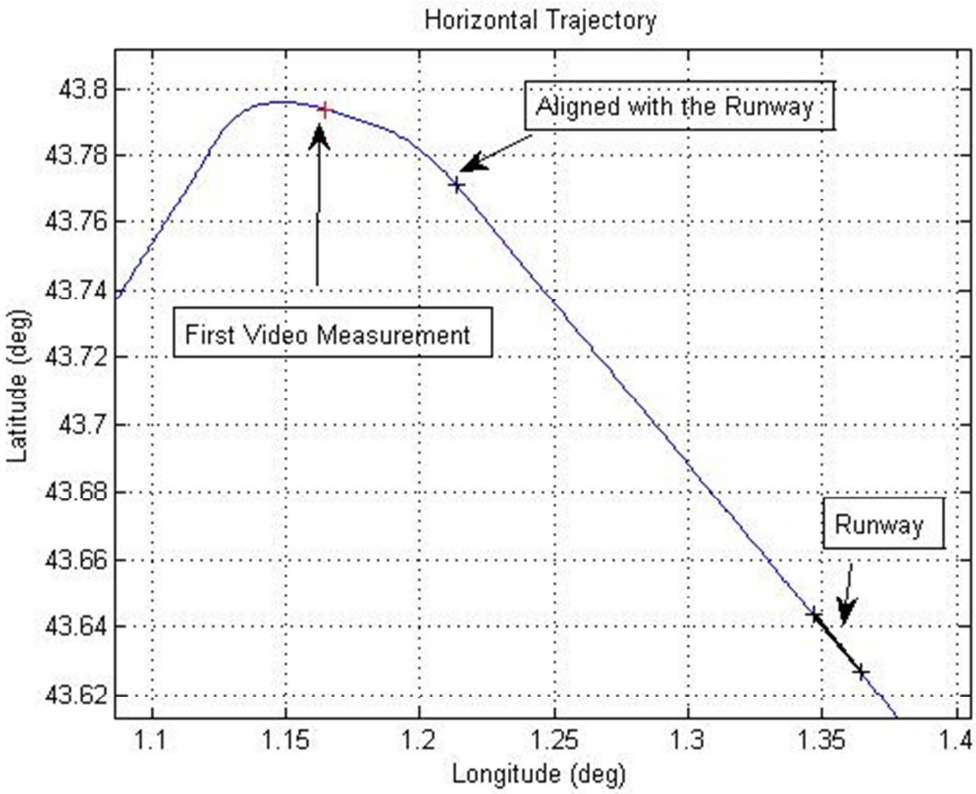

Figure 46 – Zoom on the Trajectory

The data in the simulations have been simulated using measurement models described in 6.2 and from the real trajectory profile recorded during the flight and composed of:

- An accurate reference position.
- The real estimated hybrid velocity as a reference.
- The real estimated hybrid attitude and heading as references.

The basic configuration of the Kalman filter integrating only GNSS measurements (GPS+GALILEO, dual frequency signals) have been validated and tuned correctly. From that configuration we ran a first set of simulation after the addition of the WSS measurements and of the video measurements. In that configuration, one of the satellite geometry (the simulations allow changing the geometry from a rum to another) during the simulation is observable in Figure 47.

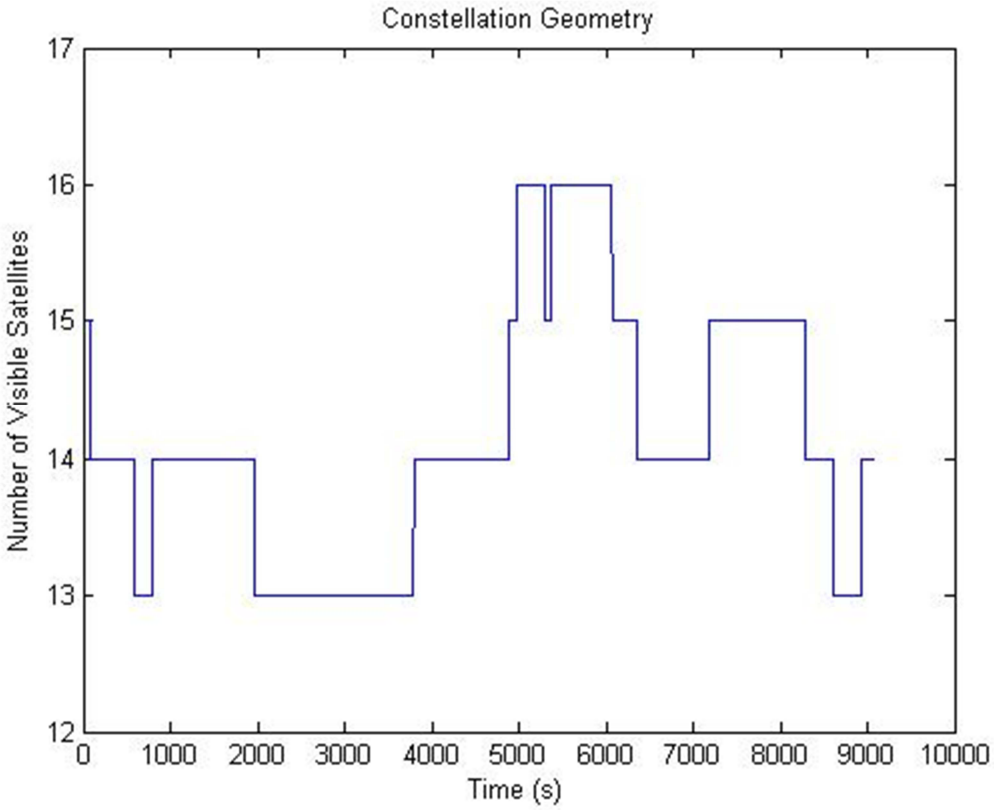

Figure 47 – Geometry of the Constellation

The next part will present an overview of the simulation results by presenting a part of the simulation results and the methodology used for synthetizing our simulation results.

6.3 Simulation Overview

The current section aims at introducing some simulation results that will illustrate the outputs of our hybridization architecture simulator. We remind that the simulator allows to easily combine several sensors that we considered in the study. The GNSS/baro-INS architecture that integrates dual frequency measurements of the two constellations with a class A INS represents the basic configuration of our hybridization filter. In that configuration, the filter has been tuned so that the estimation error is minimized for the parameters of interest: position, velocity and attitude.

In order to give an overview of the estimation results of the filter and of the simulation that we ran, in this part, we consider the augmented configuration with WSS and Video. The configuration which results are illustrated is then GNSS/baro-INS/WSS/VIDEO with the same previous tuning of the filter. That overview aims at introducing some examples of estimation results and describing the process followed for compiling some results criteria. The next section will only focus on the description of some particular scenarios involving one or several combinations of sensors and the presentation of the performance results as it is described in the current section.

Before presenting the results of the simulations, it is important to observe the innovations of the Kalman Filter regarding the Video measurements. Indeed, since we particularly focused on the video measurements as a new innovative way to provide navigation information within an hybridization architecture, it is important to observe the innovation plot as a first validation step. In particular, the zero-mean and white property of the innovations can be verified and provide information on the behavior of the propagation and measurement models. Figure 48 presents the innovation for the two considered targets and for both measurements for each target.

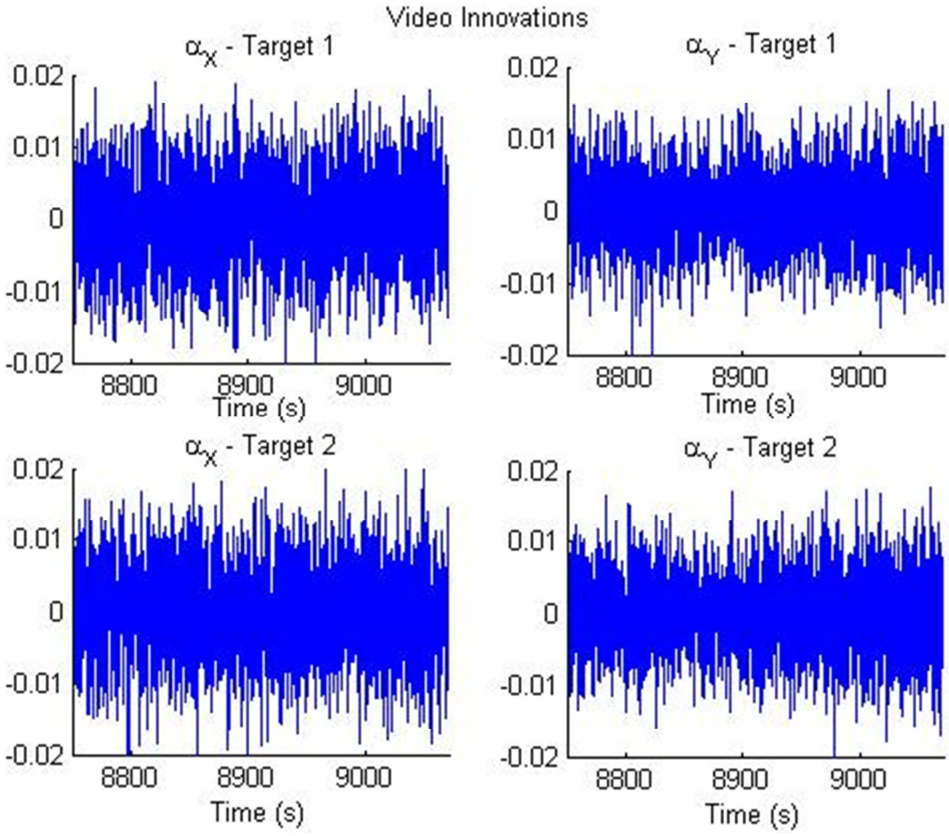

Figure 48 – Video Innovations

We can see on these figures the centered and white noise aspect of the innovations for the video measurements. This step provides us a certain validation of the measurement model implemented that is used for computing the innovations. Further analyses on innovations have been conducted in the framework of the PhD thesis.

In the current part, the simulation overview only focuses on position and altitude error parameters as examples. The EKF estimation of the horizontal and vertical position error is then presented in Figure 49. This figure presents in blue the estimation error along the entire trajectory. The red curve is the $3\hat{\sigma}_{KF}$ limit, where $\hat{\sigma}_{KF}$ is the estimation error covariance estimated by the Kalman Filter. The red dotted line is the similarly the $2\hat{\sigma}_{KF}$.

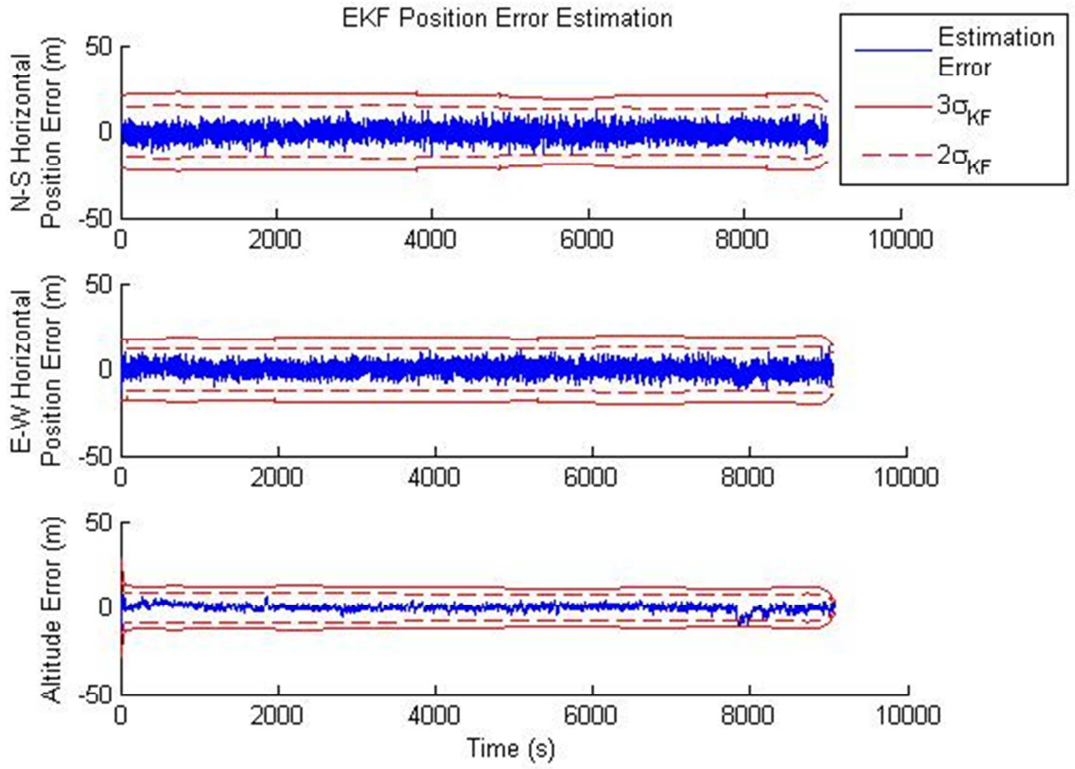

Figure 49 – GNSS/baro-INS/WSS/VIDEO 3-D Position Estimation

The whole trajectory is not considered for the results assessment, as we know existing GNSS/baro-INS hybridizations allows to fulfill the ICAO requirements for En-route down to NPA, and the video-aid and WSS data are available during the last phases of the flight, only. Thus, we focus on the final part of the flight, which is composed of:

- The end of the terminal area, which has a duration of 2 minutes. It starts at $t = 8680$ sec (during the last turn) and ends at $t = 8799$ sec when the aircraft is completely aligned with the runway.
- The final approach segment (when the aircraft is aligned with the runway). This segment starts at $t = 8800$ sec and ends at $t = 9029$ sec (when the aircraft touch the runway.
- The runway rolling area (when the wheels touch the runway). This phase starts at $t = 9030$ sec and ends at $t = 9070$ sec.

These three phases will mainly be used in order to reduce the interest area for the evaluation of the improvement provided by a particular sensor. Indeed, Video measurements start to be integrated at $t = 8750$ sec, in the middle of the first section and are available till the end of the rolling. The runway rolling is the only phase where the WSS measurements are available and may be integrated in the hybridization solution.

As a focus on these three phases, Figure 50 presents a zoomed view of Figure 49.

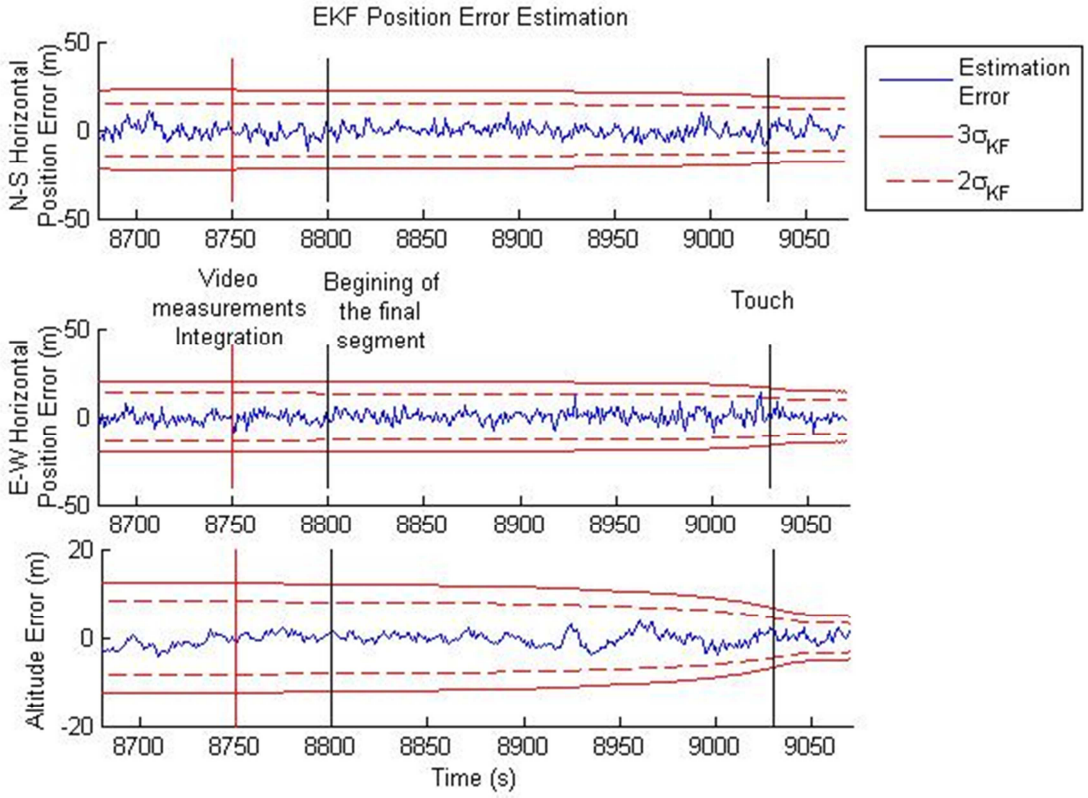

Figure 50 – Zoom on Area of Interest

As expected when introducing new reliable data (moment indicated by the red vertical line for the Video), the estimation uncertainty is reduced. In the same way, when touching the ground and integrating the WSS measurements, the uncertainty decrease again.

In order to assess the performances of the different configurations of the filter, we ran 100 simulations with that same flight path. For each simulation we generated a new draw of GNSS, INS, WSS and Video. In addition, for the GNSS measurements, we changed the initial date of the simulation so as to have a change of satellite geometry.

In the current global GNSS/baro-INS/WSS/VIDEO configuration, for the three parameters presented in this overview, we compute:

- The mean of the estimation error, computed as a function of the time.
- The Root Mean Square of the estimation error, also computed as a function of the time. This is the empirical RMS.
- A mean value of the estimation error covariance, $\hat{\sigma}_{KF}$. This value is obtained by averaging the hundred $\hat{\sigma}_{KF}$-values estimated at each instant.

The mean value of $\hat{\sigma}_{KF}$ allows us comparing the confidence of the filter with the real empirical RMS of the estimation error.

The result of that process is illustrated in Figure 51. Only the final part of the trajectory detailed above is presented.

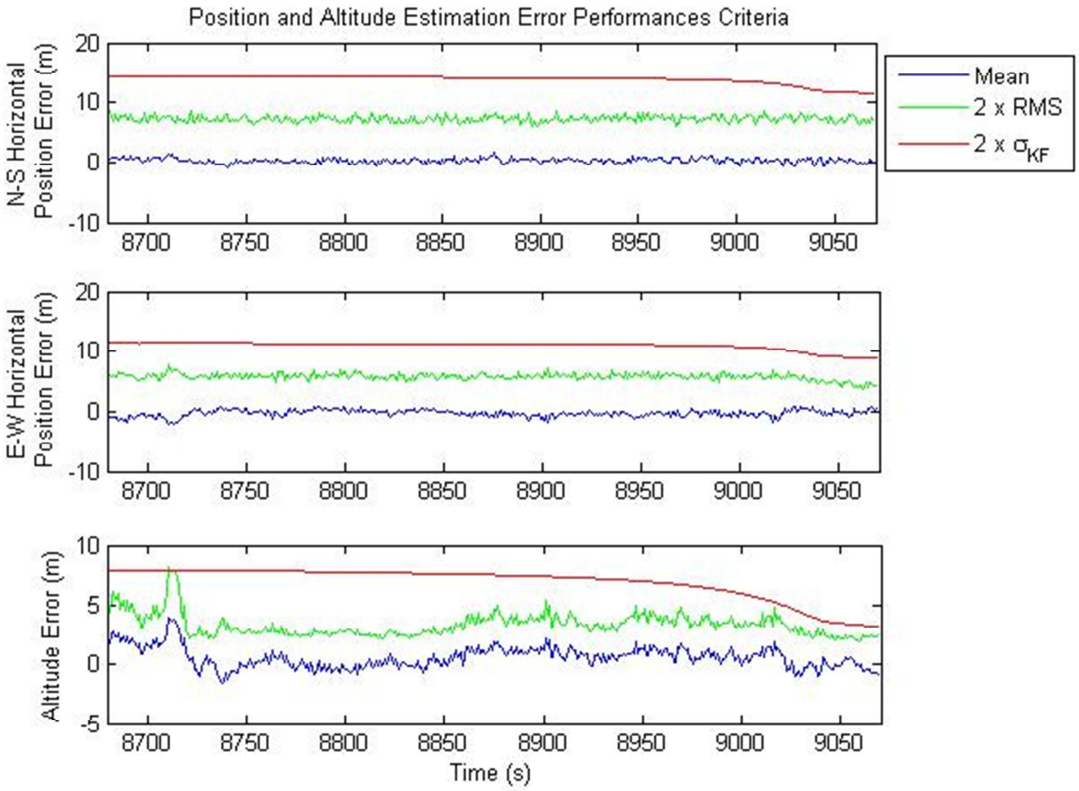

Figure 51 – GNSS/baro-INS/WSS/VIDEO Performance Overview

As we can see on the Figure 51, the averaged value of the estimation error standard deviation estimated by the Kalman filter constantly remains bigger than the empirical RMS of the estimation error. It first means that the filter is under confident regarding the position error estimation represents a good tuning.

The mean estimation error is rather good regarding the horizontal position error. Indeed the mean is around 1 m. Yet, the 95-percentile will be a better criterion for truly assessing the position estimation performance.

The integration of video is done at $t = 8750$ seconds. It does not induce any change in the dynamic of the estimation error but decrease slowly the covariance of the estimation error. In the perspective of the development of an integrity monitoring solution, this decrease of the uncertainty should induce the estimation of smaller protection level.

The integration of WSS is done at $t = 9030$ seconds. Regarding the position, it does not influence the estimation error. However the estimation error covariance predicted by the filter decreases more.

In the framework of this thesis, we focused on assessing the accuracy performances of the filter. In other word, we wanted to find a criterion that can be compared with the accuracy limit introduced in Table 4. This accuracy limit is supposed to represent the 95%-confidence level that contains the estimation error of the considered parameter. In that way, we used as criterion, the 95 percentile of the estimation error computed on the hundred simulations, over a given part of the trajectory.

This 95-percentile criterion is computed for the following parameters:

- N-S Position Error
- E-W Position Error
- Altitude Error
- Horizontal Velocity Error
- Vertical Velocity Error
- Heading Error

Its computation is done on the last part of the trajectory with a duration of 390 seconds. The output of the filter is estimated at a frequency of 1 Hz, and then the interval on which we compute the criterion contain 39000 values of estimation error per parameter.

The results for the GNSS/baro-INS/WSS/VIDEO configuration are presented in Table 9.

Parameters	95-percentile (39000 pts)	Required Accuracy (95%)
N-S Horizontal Position Error (m)	6.33	130
E-W Horizontal Position Error (m)	4.48	130
Altitude Error (m)	3.44	9 to 60
Horizontal Velocity Error (m/s)	3.56	0.5
Vertical Velocity Error (m/s)	0.23	0.15
Heading Error (deg)	0.074	0.4

Table 9 – GNSS/baro-INS/WSS/VIDEO Estimation Error Performances

Regarding the position error 95-percentile computed on this part of the flight, the GNSS/baro-INS/WSS/VIDEO architecture offers good estimations. The velocity, in opposition, does not comply with the required accuracy. The next part will introduce simulations with different combinations in order to identify some potential causes of this high value for velocity error estimation. Regarding the heading estimation, the result is promising.

The overview presented in this section focused on the complete architecture so as to have a global view of the behavior of the filter when all sensors are integrated. However it did not allow targeting the effect of the individual integration of the WSS or the VIDEO.

The next section has a logical progression that starts from the simplest and classic architecture GNSS/baro-INS to the global one addressed in the current part. The goal is to present the results one by one after degradation or integration of a new sensor.

6.4 Performance Assessment

This part introduces the performances assessment results for several scenarios described in the different subsections. The part deals the presentation of specific scenarios simulating the hybridization solution during the flight and including different combinations of the considered sensors. It aims at comparing the cases where a given sensor is and is not integrated and then evaluate the potential improvement provided.

The integration of a sensor to the baseline GNSS/baro-INS architecture is done while conserving the same tuning of the filter. Indeed we assumed that the tuning is related to the inertial class used and any tuning issue after introduction of a sensor could be seen as a future improvement of the filter.

The presented combinations give us an overview of what can be done using the simulator. More combination can be realized as declinations of the presented ones or in integrating new sensors simulators.

Last, the results are presented per parameter as detailed in Table 9.

The configurations considered are:

GNSS/baro-INS Architecture: In that case, the GNSS receiver is only coupled with a baro-INS. Three GNSS receivers and three inertial classes will be tested.

GNSS/baro-INS/WSS Architecture: In that case, WSS velocity measurements will be integrated during the runway rolling phase.

GNSS/baro-INS/VIDEO Architecture: In that case, Video will be integrated to the standard GNSS/baro-INS architecture. The Video system is as described in the thesis and, the camera is assumed to be able to detect and track the two corners of the runway horizon. The runway's horizon corners are chosen in order to have a phase where both Video and WSS data are available.

GNSS/baro-INS/WSS/VIDEO Architecture: In that case, we focus on the global integration architecture. All the considered sensors (GNSS, baro-INS, WSS and Video) are available and will be used during the flight. In that configuration, we obviously focus on the runway rolling because this is the only phase where the global configuration integrate all the measurements at the same time.

6.4.1 GNSS/baro-INS

The current part presents the results obtained with the GNSS/baro-INS configuration. The section starts with the comparison of the following possible integrations of GNSS signals with a class A INS:

- GPS single frequency receiver (this corresponds to the current on-board hybridization for high-end commercial aircraft).
- GPS dual frequency receiver (L5 frequency signal is added in order to cancel most of the ionospheric errors on the pseudorange measurements).
- GPS and GALILEO dual frequency (this configuration corresponds to the most advanced GNSS mode, adding satellite redundancy in addition to dual frequency assumption?).

The synthetized results are presented in Table 10

Parameters	GNSS Receiver	95 percentile (39000 pts)	Required Accuracy (95%)
N-S Horizontal Position Error (m)	GPS single	13.5	130
	GPS dual	9.51	
	GPS + GAL dual	6.34	
E-W Horizontal Position Error (m)	GPS single	9.09	130
	GPS dual	6.61	
	GPS + GAL dual	4.48	
Altitude Error (m)	GPS single	3.07	9 to 60
	GPS dual	3.45	
	GPS + GAL dual	3.41	
Horizontal Velocity Error (m/s)	GPS single	0.41	0.5
	GPS dual	0.56	
	GPS + GAL dual	0.64	
Vertical Velocity Error (m/s)	GPS single	0.15	0.15
	GPS dual	0.18	
	GPS + GAL dual	0.18	
Heading Error (deg)	GPS single	0.061	0.4
	GPS dual	0.061	
	GPS + GAL dual	0.061	

Table 10 – GNSS constellation contribution to current hybridization

As expected, the results show better performance with the two constellations with dual frequency signals for position estimation. However, the horizontal velocity criterion seems to be degraded when then the position gets better. This might be due to the fact that the current tuning of the filter favors the position estimation. In that case, two solutions could be considered. First, a modification of the tuning of the filter could be proposed in order to find the efficient trade-off between position and velocity performance. Then, the measurement error model used for the simulations is a highly conservative model that can

induce these velocity bad estimations. Future simulations could be considered using real measurements for validating the GPS single frequency case.

In a second part, another set of simulations have been done regarding the variation of the inertial class. For these simulations, we considered dual frequency GNSS signals of the GPS and GALILEO constellations. The considered classes are A, B+ and B- (their characteristics are depicted in Table 5).

The results are presented in Table 11.

Parameters	INS Classes	95 percentile (39000 pts)	Required Accuracy (95%)
N-S Horizontal Position Error (m)	A	6.34	130
	B+	6.34	
	B-	6.34	
E-W Horizontal Position Error (m)	A	4.48	130
	B+	4.48	
	B-	4.49	
Altitude Error (m)	A	3.41	9 to 60
	B+	3.40	
	B-	3.37	
Horizontal Velocity Error (m/s)	A	0.64	0.5
	B+	1.14	
	B-	3.16	
Vertical Velocity Error (m/s)	A	0.18	0.15
	B+	0.19	
	B-	0.22	
Heading Error (deg)	A	0.061	0.4
	B+	0.23	
	B-	1.65	

Table 11 – Inertial Class contribution to GNSS/baro-INS hybridization, in a dual frequency and dual constellation case

Regarding the position error estimation, the performance does not change when degrading the INS. This behavior can be explained by the fact that the measurements are directly related to the position parameters. Indeed, in the tight coupling architecture, the GNSS code pseudorange measurements correct in majority the INS position.

In that configuration, we then observe an augmentation of the velocity and attitude estimation errors. It is obviously correlated with the fact that a worse INS, degrades the accelerometers and gyrometers measurements (increase the measurement errors) and induces a less accurate propagation model.

As expected, class A INS offers the better performances but class B+ INS still provides good performances regarding the position and heading parameters. The degradation of the inertial class offers an interesting improvement regarding to the price of the sensors. In compensation, to guarantee a performance level equivalent to that of class A

INS, a solution could be to add other sensors in the hybridization process that may potentially improve velocity and heading estimations.

Finally, the altitude and vertical velocity estimations are not impacted by the change of class. This is due to the fact that the baro-INS loop offers very good performances for the vertical channel compensation of the INS and it is not degraded by a low quality INS.

6.4.2 GNSS/baro-INS/WSS

The previous section illustrated a degradation of the basic GNSS/baro-INS architecture, which is composed of a dual frequency GNSS receiver using signals from GPS and GALILEO constellations and a Class A INS. Now, the current section focusses? on the integration of WSS measurements to this architecture and the comparison of the estimation results using the criteria defined in 6.3 so as to assess the contribution of WSS information.

As presented before, we assume a set of 16 WSS providing longitudinal velocity measurements during runway rolling. In our case, the runway rolling phase has a duration of 40 seconds. In that way, the number of points used for the computation of the 95-percentile is 4000.

The results obtained are presented in Table 12.

Parameters	GNSS (GPS+GAL dual freq) baro-INS Class A + WSS Integration?	95 percentile (4000 pts)	Required Accuracy (95%)
N-S Horizontal Position Error (m)	No	6.32	130
	Yes	6.32	
E-W Horizontal Position Error (m)	No	4.72	130
	Yes	4.71	
Altitude Error (m)	No	2.22	9 to 60
	Yes	2.23	
Horizontal Velocity Error (m/s)	No	0.40	0.5
	Yes	0.54	
Vertical Velocity Error (m/s)	No	0.16	0.15
	Yes	0.16	
Heading Error (deg)	No	0.060	0.4
	Yes	0.076	

Table 12 – WSS contribution to GNSS/baro-INS hybridization

The WSS sensors provide velocity measurements. They naturally should improve the velocity estimation. However, the 95-percentile is not reduced and the velocity estimation does not seem to be better.

Therefore, there has to be reminded that the velocity performance estimation are rather good. This is mainly due to the Class A INS, which combined with GNSS measurements provides very good velocity estimations. Thus, so as to illustrate the contribution provided by the WSS we propose to observe the estimation error standard deviation estimated by the Kalman Filter and presented in Figure 52.

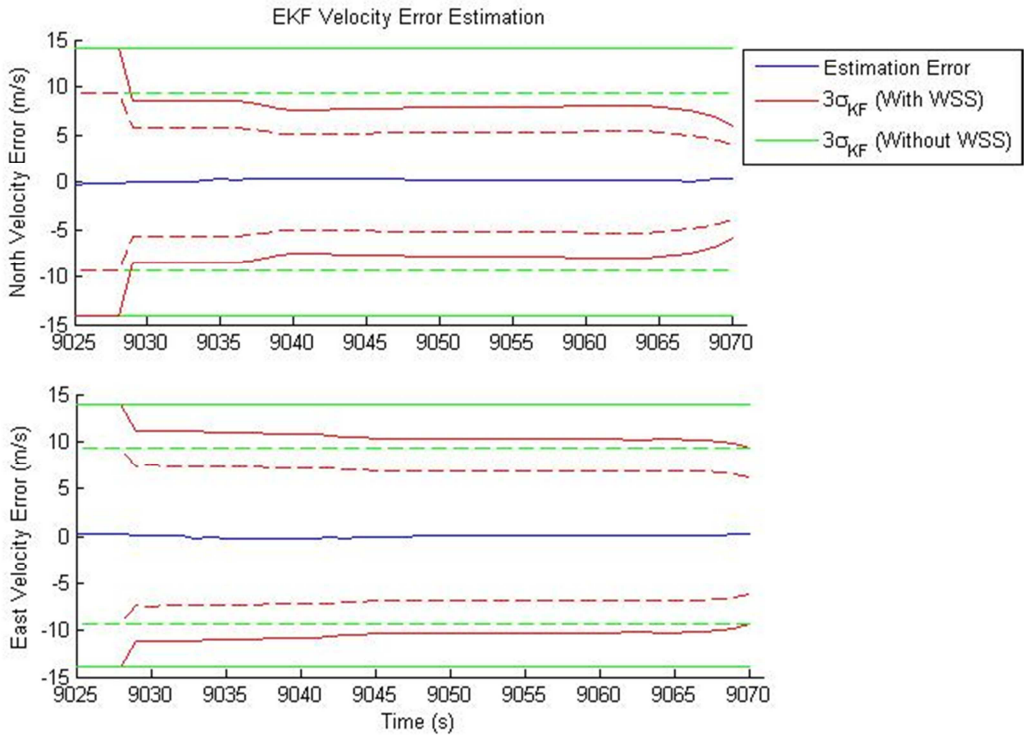

Figure 52 – WSS influence on Velocity Error Covariance

Figure 52 illustrates the influence of the WSS measurements integration on the estimation error covariance of the filter. As explained, the WSS does not improve the estimation of the velocity when using a Class A INS but the filter's covariance is reduced on the runway. The filter covariance being decrease, the reduction of the estimation uncertainty can be promising for a potential integrity monitoring solution.

Therefore, WSS integration is not without interest in such architecture. In fact, it can be used for compensating a less performing INS, such as a Class B+ or B-. Indeed, we also run simulations in order to compare the influence of WSS integration in a GNSS/baro-INS architecture, using a GNSS/baro-INS architecture with a dual frequency GNSS receiver using signals from the GPS and GALILEO constellations and a Class B- INS.

The results are illustrated in Table 13.

Parameters	GNSS (GPS+GAL dual freq) baro-INS Class B- + WSS Integration?	95 percentile (4000 pts)	Required Accuracy (95%)
N-S Horizontal Position Error (m)	No	6.34	130
	Yes	6.34	
E-W Horizontal Position Error (m)	No	4.69	130
	Yes	4.69	
Altitude Error (m)	No	2.37	9 to 60
	Yes	2.39	
Horizontal Velocity Error (m/s)	No	2.08	0.5
	Yes	1.19	
Vertical Velocity Error (m/s)	No	0.15	0.15
	Yes	0.15	
Heading Error (deg)	No	1.54	0.4
	Yes	1.62	

Table 13 – WSS Integration in a GNSS/baro-INS Class B- Architecture

As expected, there is an improvement in the horizontal velocity estimation that can be seen during the runway rolling. However this improvement is not sufficient for reaching the 0.5 m/s value denoted as requirement.

Interest in the WSS remains its usage as a velocity estimate provider for runway's operations. Indeed, the horizontal velocity does not completely reflect the longitudinal velocity improvement that should be improved by the use of WSS.

Finally, the integration in a global hybridization architecture stays promising for the integration of velocity measurements. In addition, the WSS presence and high redundancy on lots of high end aircraft leads to keep this sensor as a system that should be integrated.

6.4.3 GNSS/baro-INS/VIDEO

Similarly to the previous section, the current one focusses on the integration of Video measurements to the baseline architecture and the comparison of the estimation results using the criteria defined in 6.3 so as to assess the contribution of Video. The WSS are assumed to be unavailable.

The Video system is as described in Chapter 4 and assumed to be able to detect and track the two corners of the runway's horizon. During the simulations run, the part of the flight where Video is available has a duration of 320 seconds. In that way, the number of points used for the computation of the 95-percentile is 32000.

The results are presented in Table 14.

Parameters	GNSS (GPS+GAL dual freq) baro-INS Class A- + VIDEO Integration?	95 percentile (32000 pts)	Required Accuracy (95%)
N-S Horizontal Position Error (m)	No	6.34	130
	Yes	6.31	
E-W Horizontal Position Error (m)	No	4.48	130
	Yes	4.50	
Altitude Error (m)	No	3.41	9 to 60
	Yes	3.13	
Horizontal Velocity Error (m/s)	No	0.64	0.5
	Yes	3.61	
Vertical Velocity Error (m/s)	No	0.18	0.15
	Yes	0.22	
Heading Error (deg)	No	0.06	0.4
	Yes	0.08	

Table 14 – Video contribution to GNSS/baro-INS hybridization

The integration of Video data during landing seems at first glance not to improve position and heading estimations. As described in Chapter 4, Video angular measurements are related to the position and attitude parameters; but, as for the WSS measurements, the combination with a class A INS does not allow getting a better estimation.

However, regarding the velocity, the estimation is degraded. In order to try to understand this, the next section will focus on the GNSS/baro-INS/WSS/VIDEO architecture during the runway rolling phase. Indeed, the integration of WSS measurements might compensate the degradation of the velocity estimation and improve the global performance.

6.4.4 GNSS/baro-INS/WSS/VIDEO

This section presents the results of the most complete configuration assuming that all considered sensors can be integrated during a single flight. It is the case where the INS is an ADIRU (class A) and the GNSS receiver is a dual constellation and dual frequency receiver.

For this simulation case, only the runway rolling phase is considered as, this is the only area where Video and WSS are available in the same time. The duration of the phase is thus 40 seconds. In that way, the number of points used for the computation of the 95-percentile is 4000.

This configuration is the global one presented in 6.3. But the results are not exactly the same as in 6.3, as we focus on the runway rolling phase, only: the 95-percentile is computed over a smaller period of time.

The results are presented in Table 15.

Parameters	GNSS (GPS+GAL dual freq) baro-INS Class A- + WSS and VIDEO Integration?	95 percentile (4000 pts)	Required Accuracy (95%)
N-S Horizontal Position Error (m)	No	6.32	130
	Yes	6.30	
E-W Horizontal Position Error (m)	No	4.72	130
	Yes	4.01	
Altitude Error (m)	No	2.22	9 to 60
	Yes	1.78	
Horizontal Velocity Error (m/s)	No	0.40	0.5
	Yes	3.78	
Vertical Velocity Error (m/s)	No	0.16	0.15
	Yes	0.19	
Heading Error (deg)	No	0.060	0.4
	Yes	0.063	

Table 15 – Video and WSS contribution to GNSS/baro-INS hybridization during runway rolling

In that global configuration, which integrates all the considered sensors, the position and altitude parameters estimation seems to be slightly improved.

Regarding the velocity, in spite of the integration of the WSS measurements, there is no improvement and the estimation stays degraded compared to the GNSS/baro-INS solution.

The reason of that bad velocity estimation has not been identified. The fact that the video measurements are delivered at a high rate and are representative of the very high dynamic of the aircraft could possibly be interpreted by the filter as a noisy velocity. In that way, a different tuning of the filter might be a possible axis for investigating about that issue.

6.5 Conclusion

The current chapter presented the accuracy performance on position, velocity and heading estimations, we get with the hybridization architecture proposed in the Ph.D. . It described some simulations runs and the results we obtained when testing the implemented hybridization architecture under different scenarios. We remind this architecture allows combining a GNSS receiver, a baro-INS, a WSS and a Video system in every possible combination. The simulation tool can be configured in different manners and simulate multiple combinations of systems or sensors: it includes a GNSS receiver able to generate single or dual frequency signals from GPS and GALILEO constellations, an IMU and a baro-INS platform whose quality may vary from the class A to the class C-, up to 16 Wheel Speed Sensors and a Video System as described in Chapter 4.

We also validated the baseline architecture implementation combining a GNSS receiver and a baro-INS through the first scenario presented that compared inertial classes and GNSS receiver modes.

It has been shown that, as expected, the position estimation is better when the dual frequency, dual constellation GNSS receiver model is used. In addition, the class A INS provides the best performances. Regarding the velocity, we observed an opposite behavior than the position. This can be reduced by finding a different tuning that guarantees an efficient trade-off between positon and velocity estimation performances. In the current proposed solution, we only focused on integrating code pseudorange measurements. As a potential development, it could be interesting to use phase based methods such as the one described in the WAAS MOPS [ICAO, 2006] to improve velocity estimation.

The WSS integration scenario illustrates the reduction of the filter estimation uncertainty and offers promising results if considering the future development of an integrity monitoring solution. In addition, velocity estimation error is reduced when using WSS in order to compensate a degradation of the INS class. This idea offers also good perspectives regarding the use of less expensive INS.

Regarding the video, its integration does not seem to improve performances of the hybridization architecture during the proposed scenarios. Therefore, more cases needs to be studied and the integration of video could need a different tuning of the global filter. In particular, the video integration could be a lot improved by increasing the optical flow of the features by including additional landmarks. Indeed, when the aircraft is moving toward the runway, the features associated to the runway result in a limited optical flow. The high dynamic of the video measurements should be taken into account regarding its integration within the global architecture. However, it appears to be an interesting aid that still needs to be studied and developed. Indeed, the proposed solution remains one possible usage of a video system. Other methods using video has been identified such as the line-following applications and could be developed in a new simulator.

Finally, some additional discussions should be held about timing issues due to the integration of all these sensors. This item has not been dealt during the PhD since the results are based on simulations.

Chapter 7 : Conclusions and Perspectives

The current chapter has a first part which reminds the conclusions of the previous chapters and concludes the work done during this Ph.D. thesis. It also reminds the major contributions of the thesis.

In a second part, perspectives of future projects that could be led so as to continue the work done during this Ph.D. thesis are addressed.

7.1 Thesis Conclusions

As a first step, it is important to remind that this Ph.D. thesis focused on designing and assessing the performances of a hybridization filter integrating a GNSS receiver, a baro-INS, several WSS and a Video system able to detect runway's corners and provides their corresponding angular coordinates. In that way, several simulation scenarios have been ran in order to estimate the position, altitude, velocity and heading errors of an aircraft during approach and landing.

Aircraft navigation is an application regulated in particular by the ICAO through recommendations and requirements for the actors, the equipment and the systems that aims at navigating the aircraft. The Chapter 2 of the thesis dealt with the identification and definition of the requirements currently established by the ICAO. In addition, it presented a set of requirements issue by AIRBUS that allows extending the previous requirements to several other navigation parameters, such as the velocity or attitude angles. These requirements are those that were considered in the framework of the Ph.D. thesis.

As the thesis focused on the study of future hybridization architectures, we presented in the Chapter 3 an overview of the GNSS/baro-INS hybridization solution currently performed on most of the high end commercial aircraft. For that, we first introduced the principle of inertial navigation and the description of the inertial measurement models. Regarding the IMU models, a simulator of accelerometer and gyrometer measurements have been developed allowing generating IMUs from class A to class C. We also used a strapdown baro-INS algorithm in order to generate inertial estimates of position, velocity and attitude. We validated the estimation results of the baro-INS platform by comparing the drifting errors and the temporal behavior of the estimation errors with the standard performances of real INS.

In a second part, we implemented a GNSS receiver simulator allowing generating code pseudorange measurements of the GPS and GALILEO constellations for single and dual frequency receiver configurations. This GNSS receiver module is entirely configurable

and allows adjusting the measurement error models so as to be in line with the models standardized for the desired applications.

In that chapter, we also detailed the characteristics, the benefits and the drawbacks of the current on-board GNSS/baro-INS. In fact, current hybridization only integrates the GPS L1C/A code pseudorange measurements and is only used for position estimation. The first aim of the Ph.D. thesis was then to integrate more GNSS signals. In particular we focused on integrating signals of the constellation GALILEO, in order to add measurement redundancy. The fact of adding measurements finds a particular interest when dealing with an integrity monitoring solution, but this has not been particularly addressed here. We also focused on integrating dual frequency signals allowing reducing the residual errors on the measurements.

The integration of other sensors within the hybridization architecture first focused on the Wheel Speed Sensors. Many high end commercial aircraft have several WSS but do not use them for hybridized navigation purpose. The idea was then to integrate the WSS velocity measurements within the global architecture and then assess the performances of such a solution. The integration of WSS started with the development of a WSS simulator allowing generating multiple velocity measurements that takes into account the variation of the wheel's radius as a function of the velocity.

The second considered new sensor in the Ph.D. thesis was the video. For this purpose, a state of the art on video based navigation methods has been done and an overview is detailed in Chapter 4. As a conclusion of the state of the art, we identified some key-elements for navigation with video sensors. This state of the art was a first step that led to propose a solution for integrating video within a hybridization architecture. The constraint that we established were simple: we wanted a video sensor able to provide real time measurements that do not depend on any image database not already available on-board. However, the proposed solution assumed that the runway's coordinates are known and that the video system is able to identify and track the corresponding points. For the knowledge of the coordinates, the runway position coordinates and characteristics such as its length, width and orientation can be available on board. Regarding the image processing algorithm, we detailed a preliminary study that aimed at fulfilling this tracking function with promising performances. Therefore, we did not particularly focus on the image processing part during the Ph.D. study but only on the measurement model that such a system could provide. Indeed, we wanted to describe completely the integration process of these measurements and evaluate the potential improvement compared with the current solution.

Further to this state of the art, a video measurement model has been proposed and implemented. The video system proposed is able to provide angular coordinates of targets of known locations in the scenery around the runway. As interesting targets, we focused on the runway's corners assuming that their locations could be known with a good accuracy when having the location and geometric characteristic of the runway. The visibility of these targets depends on the environment around the airport but we could assume that such a

system could provide good performance of detection during the entire final approach segment.

Among all these assumptions, one in particular was very restrictive concerning the potential feasibility of such a solution. In effect, without an appropriate image processing algorithm the solution could not be realizable. In that way, we also started a study in order to assess the feasibility of that algorithm. This study presented in the Chapter 4 showed that very good results could be obtained regarding the detection of the runway in a dense urban area. Further more detailed studies need to be done and the tracking ability should also be studied but promising results have been shown.

Thus, assuming this video system feasibility, we focused on the proposed video measurement model and presented a detailed geometrical model that acted as a generating function for the video measurements. As a first step, we only distorted this measurement model with an additive white Gaussian noise that modeled the several error sources affecting the pixels detection: image processing errors, camera resolution, targets location errors or image noise. For further studies, this measurement model can be refined and developed in order to suit better some specific elements of the reality.

Once these sensors simulators have been developed, we implemented an Extended Kalman Filter architecture assuming a wander azimuth inertial mechanization and potentially integrating a GNSS receiver, a baro-INS, a WSS and a video system as described in the thesis. The interest of this architecture is the fact that we can easily switch between the combinations and choose or not to integrate the different sensors. In addition, the EKF structure also allows, in the future, implementing other Kalman architectures.

The Chapter 5 introduced the detailed equations of the proposed algorithm in the Ph.D. thesis. It described the solution by presenting the architecture, the theoretical model of the filter and introducing the state vector and state space model equations. The baro-INS wander mechanization error equations are provided and the observation functions for the subset of considered sensors are presented.

Finally, the performances of several combinations of sensors have been assessed during the final part of a trajectory performed by a real flight of an A380. The part of the trajectory considered was the final part of the flight. This part was composed of the last turn, the final approach segment and the runway rolling. For the assessment of performances we focused on an accuracy parameter, which is the 95-percentile of the estimation error for the considered parameters: the horizontal position along the North-South direction, the horizontal position along the East-West direction, the altitude, the horizontal velocity, the vertical velocity and the heading angle. We used as requirements the accuracy bound defined in Table 4 of Chapter 2. For some particular scenarios, we also presented the filter's output illustrated by the estimation error and the estimation error covariance.

The basic architecture composed of the GNSS receiver and of the baro-INS platform has been tuned before the simulations and this tuning has been used as a reference. Indeed, we also used the simulations to validate or identify some changes that can be made about the tuning.

Regarding the additional sensors, the WSS showed an important interest regarding the estimation of the velocity parameter. When using a class A INS the improvement does not seem to be on the accuracy but on the covariance of the Kalman filter. But, for a degraded INS, we showed that the WSS is improving the estimation. Regarding the video contribution, most of the results in the scenario showed that the proposed video solution does not improve our filter performances accuracy. The interest still remains in the availability of an additional sensor that can operate during an approach as soon as the runway becomes visible. In such conditions, these measurements can be integrated in the simulated architecture and augment the solution. Besides, the small number of features used in the proposed method limits the optical flow of the video measurements. The use of additional landmark could constitute a good solution for increasing the optical flow and improving the performance when integrating the video measurements.

In most of the simulations, we also showed that the basic combination remains a very powerful solution. This is mainly because of the very high quality of the class A INS, which can, maintain a good performance level even during coasting. Thus, when integrated with this type of INS, the additional sensors such as WSS and video integrated as proposed, seem not to provide improvement of the solution for approach and rolling on runway after landing. In addition, we could imagine using in the future some phase based methods with phase pseudorange measurements so as to improve velocity estimations. This could help compensating the lack of accuracy on the velocity estimations.

The integration of these sensors within a global architecture has been done with a global view to build a functional hybridization simulator. The idea was to be able to switch easily from a combination to another and to add some potential future sources of measurements. Indeed, the overall objective is to make available a global filter that aims at integrating most of the measurements that can be found on board in order to estimate most of the navigation parameters. That estimation would be done by selecting the most appropriate architecture and selection of sensors considering the phase of flight, the environment, the sensors availability and the requirements. Such a choice can be addressed in simulations like those presented in the Chapter 6 and offers performances comparisons when multiplying the possible architectures. Finally, this modular architecture appears as a powerful tool in the framework of hybridization studies aiming at simulating several coupling architectures and integrating various measurement sources.

Therefore, those results showed us that as a continuation axis for our works should be to try to build a switching function that switches progressively from a solution to another (this part is detailed in the perspectives). This solution should reduce the fast change in the estimation results and offer a more performing solution.

7.2 Perspectives

Further studies can be conducted in the following of this thesis on several axes. A lot of subjects have been studied during the Ph.D. and some of them have been analyzed under particular assumptions or goals that can be refined or enlarged.

As a first step one of the most important points is that we assumed that data provided by the simulated GNSS receiver are not faulty or have been monitored. However, the first future work to consider as a way forward is to implement an integrity monitoring solution. The first step could be done by using an existing AAIM algorithm. A second step should be to focus on the monitoring of the other sources of measurement of the implemented architecture. It also requires the definition of threat models for the considered sensors.

The filter used for the final results of the Ph.D. was an extended Kalman filter. However, the equations for testing an Unscented Kalman filter have also been implemented but without an efficient tuning. This variation could be studied in the future, just as the possible implementation of other filters. The implemented solution offers the possibility to simply switch between the architectures. Then it is not needed to implement a whole new filter. The particular case of the UKF might be really interesting because of the absence of linearization. In case of an observation function with high non-linearity, especially the proposed video solution, it should improve the solution performance and reduce the linearization errors.

Another point that can be refined in the following concerns the nominal measurement error model of the video measurements. This part was not developed in the thesis because we only focused on the type of measurement provided by the video system and on the possibilities for their integration. Finally, additional components of the video error model can be detailed and could be added to the state vector. In particular, incertitude on the target's position can be modeled as a bias estimated by the filter.

Regarding the image processing algorithm, which development was not a goal of the thesis, the beginning of a feasibility study has been presented. The development of such an image processing algorithm could be considered in a future study. In addition, the multiplication of features that could be detected by the system could be increased for a better optical flow.

Most of the combinations presented in the results illustrate the fact that when a measurement appears during the flight, it induces a change in the dynamic of the estimated parameter. This is partially caused by the direct and immediate use of the sensor measurement. Some studies have been found in the literature proposing to build a bank of filters, each being in a given configuration (integrating a given set of sensors). The idea is then to switch slowly from a filter to another when a sensor becomes available or when one of the filters estimates a better solution. One of the considered solutions could be to add a

state in each filter corresponding to the weight associated to the filter's output. The final solution is then the weighted sum of all the filters estimations.

As an alternative to the integrity monitoring algorithm, there is a process called consolidation, which aims at using the redundancy of systems or sensors in order to build the best output possible from the set of systems/sensors. As an example, consolidating three INS, could lead to providing only one INS output built from the three other. Indeed, consolidation improves robustness of the solution by using the redundancy of the systems and potentially allowing the detection of erroneous systems. The consolidation process could simply be done taking the mean value, choosing one the system (based on a given criteria), taking a weighted sum of the different systems… Consolidation also increases the possible combination of sensors by applying the process directly on the systems or on the results of the hybridization process. On one hand, hybridization could be done integrating all consolidated systems and in the other hand, a consolidation can be done between the outputs of several hybridization solutions.

Finally, more studies can be conducted using the implemented architecture simply by adding other systems or sensors, changing the type of filter, or the measurement models. Phase pseudorange measurements and phase based methods should be considered for being integrated and improving the velocity estimation performances. Real video and WSS measurements can also be considered for validating the architecture and obtaining additional results. A specific degraded case could be assessed that simulate a GNSS outage during an intended operation or before starting an operation. In that way, the ability of a specific architecture to compensate a signal loss could be considered and demonstrated.

Bibliography

[Aggarwal et al., 2010] P. Aggarwal, Z. Syed, A. Noureldin and N. El-Sheimy, *MEMS-Based Integrated Navigation*, 2010.

[AIRBUS, 2009] AIRBUS, *Navigation Performances for A/C Position Function*, Oct. 2009.

[AIRBUS, 2011] AIRBUS, *ADR & IR - Parameters characteristics*, 2011.

[AIRBUS, 2012] AIRBUS, *Navigation Requirement and Architecture for Surface Operations*, Feb. 2012.

[Angeli et al., 2009] A. Angeli, S. Doncieux, J.A. Meyer and D. Filliat, *Visual topological SLAM and global localization*, in Proceedings of IEEE International Conference on Robotics and Automation, 2009, pp. 4300–4305.

[Azinheira and Rives, 2008] J.R. Azinheira and P. Rives, *Image-Based Visual Servoing for Vanishing Features and Ground Lines Tracking: Application to a UAV Automatic Landing*, published in International Journal of Optomechatronics, 2008.

[Ben Afia, 2013] A. Ben Afia, *Rapport d'études sur les méthodes d'hybridation et de surveillance d'intégrité*, 2013.

[Ben Afia et al., 2014] A. Ben Afia, V. Gay-Bellile, A.-C. Escher, D. Salos, L. Soulier, L. Deambrogio and C. Macabiau, *Review and classification of vision-based localisation techniques in unknown environments*, published in IET Radar, Sonar & Navigation, May 2014.

[Betz and Kolodziejski, 2009] J.W. Betz and K.R. Kolodziejski, *Generalized theory of code tracking with an early-late discriminator part I: lower bound and coherent processing*, published in IEEE Transactions on Aerospace and Electronic Systems, 2009, vol. 45, pp. 1538–1556.

[Bibuli et al., 2008] M. Bibuli, G. Bruzzone, M. Caccia, G. Indiveri and A.A. Zizzari, *Line following guidance control: Application to the Charlie unmanned surface vehicle*, in Proceedings of IEEE/RSJ International Conference on Intelligent Robots and Systems, 2008, pp. 3641–3646.

[Blaer and Allen, 2002] P. Blaer and P. Allen, *Topological mobile robot localization using fast vision techniques*, in Proceedings of IEEE International Conference on Robotics and Automation, 2002, vol. 1, pp. 1031–1036.

[Bourquardez and Chaumette, 2007] O. Bourquardez and F. Chaumette, *Visual servoing of an airplane for auto-landing*, in Proceedings of IEEE/RSJ International Conference on Intelligent Robots and Systems, 2007, pp. 1314–1319.

[Cesetti et al., 2010] A. Cesetti, E. Frontoni, A. Mancini, P. Zingaretti and S. Longhi, *A Vision-Based Guidance System for UAV Navigation and Safe Landing using Natural Landmarks*, published in Journal of Intelligent and Robotic Systems, Jan. 2010, vol. 57, pp. 233–257.

[Cheng et al., 2013] C. Cheng, V. Calmettes, B. Priot, Q. Pan and J.-Y. Tourneret, *Vision Aided INS/GNSS Integration for Improving the Robustness of a Navigation System for Mini Unmanned Aerial Vehicles*, in Proceedings of ION ITM, 2013, pp. 780 – 791.

[Conte and Doherty, 2008] G. Conte and P. Doherty, *An integrated UAV navigation system based on aerial image matching*, in Proceedings of IEEE Aerospace Conference, 2008, pp. 1–10.

[Coutard et al., 2011] L. Coutard, F. Chaumette and J.-M. Pflimlin, *Automatic landing on aircraft carrier by visual servoing*, published in IEEE/RSJ International Conference on Intelligent Robots and Systems, 2011.

[Damary et al. O. Damary, N. Drapeau and T. Gallico, *Acquisition et analyse d'image - Détection de droites et de cercles dans une image*.

[DeSouza and Kak, 2002] G.N. DeSouza and A.C. Kak, *Vision for mobile robot navigation: a survey*, published in IEEE Transactions on Pattern Analysis and Machine Intelligence, Feb. 2002, vol. 24, pp. 237 –267.

[Dieter et al., 2003] G.L. Dieter, G.E. Hatten and J. Taylor, *MCS Zero Age of Data Measurement Techniques*, in Proceedings of 35th ION PTTI, 2003, pp. 103–116.

[Doehler and Korn, 2003] H.U. Doehler and B. Korn, *Robust position estimation using images from an uncalibrated camera*, in Proceedings of 22nd Digital Avionics Systems Conference, 2003, vol. 2, pp. 9–D.

[Ebcin and Veth, 2007] S. Ebcin and M. Veth, *Tightly-coupled image-aided inertial navigation using the unscented Kalman filter*, in Proceedings of 20th ION GNSS, 2007, pp. 1851 – 1860.

[El-Diasty and Pagiatakis, 2009] M. El-Diasty and S. Pagiatakis, *A rigorous temperature-dependent stochastic modelling and testing for mems-based inertial sensor errors*, published in Sensors, 2009, vol. 9, pp. 8473–8489.

[ESA, 2005] ESA, *GALILEO Integrity Concept*, 2005.

[EUROCAE, 2010] EUROCAE, *MOPS for Airborne Open Service Galileo Satellite Receiving Equipment*, 2010.

[Farrel and Barth, 1998] J. Farrel and M. Barth, *The global positioning system and inertial navigation*, 1998.

[Fraundorfer et al., 2007] F. Fraundorfer, C. Engels and D. Nistér, *Topological mapping, localization and navigation using image collections*, in Proceedings of IEEE/RSJ International Conference on Intelligent Robots and Systems, 2007, pp. 3872–3877.

[Gaspar et al., 2000] J. Gaspar, N. Winters and J. Santos-Victor, *Vision-based navigation and environmental representations with an omnidirectional camera*, published in IEEE Transactions on Robotics and Automation, 2000, vol. 16, pp. 890–898.

[Giebner, 2003] M.G. Giebner, *Tightly-coupled image-aided inertial navigation system via a kalman filter*, 2003.

[Goncalves et al., 2010] T. Goncalves, J. Azinheira and P. Rives, *Homography-based visual servoing of an aircraft for automatic approach and landing*, in Proceedings of IEEE International Conference on Robotics and Automation, 2010, pp. 9–14.

[Hagen and Heyerdahl, 1992] E. Hagen and E. Heyerdahl, *Navigation by optical flow*, in Proceedings of 11th IAPR International Conference on Pattern Recognition - Conference A:, 1992, vol. 1, pp. 700–703.

[Huang, 2008] H. Huang, *Bearing-only SLAM - A Vision-Based Navigation System for Autonomous Robots*, Apr. 2008.

[ICAO, 1991] ICAO, *ICAO News Release, PIO 11/91 and 12/91*, 1991.

[ICAO, 1991] ICAO, *MOPS for Airborne Supplemental Navigation Equipment Using GPS*, Jul. 1991.

[ICAO, 2003] ICAO, *Minimum Aviation System Performance Standards Required Navigation Performance for Area Navigation*, Oct. 2003.

[ICAO, 2004] ICAO, *Minimum Aviation System Performance Standards for the LAAS*, Dec. 2004.

[ICAO, 2005] ICAO, *ICAO Convention - Annex 2: Rules of the Air*, 2005.

[ICAO, 2006] ICAO, *ICAO Convention - Annex 10: Aeronautical Telecommunications - Volume 1: Radio Navigation Aids*, 2006.

[ICAO, 2006] ICAO, *MOPS for GPS/WAAS Airborne Equipment*, Dec. 2006.

[ICAO, 2008] ICAO, *Perfomance-Based Navigation (PBN) Manual*, 2008.

[ICAO, 2009] ICAO, *MOPS for GPS/ABAS Airborne Equipment*, Apr. 2009.

[ICAO, 2010] ICAO, *Phase of Flight Definitions and Usage Notes*, 2010.

[ICAO, 2010] ICAO, *ICAO Convention - Annex 6: Operation of Aircraft - Part 1: International Commercial Air Transport - Aeroplanes*, 2010.

[Jan, 2003] S.-S. Jan, *Aircraft Landing Using a Modernized Global Positioning System and the Wide Area Augmentation System*, 2003.

[Jia, 2008] Y. Jia, *Aerobot/Robot Vision-based Navigation*, Jun. 2008.

[Jia et al., 2008] Z. Jia, A. Balasuriya and S. Challa, *Autonomous Vehicles Navigation with Visual Target Tracking: Technical Approaches*, published in Algorithms, Dec. 2008, vol. 1, pp. 153–182.

[Jorgensen, 1989] P.S. Jorgensen, *An assessment of ionospheric effects on the GPS user*, published in Navigation, 1989, vol. 36, pp. 195–204.

[Kaplan and Hegarty, 2006] E.D. Kaplan and C.J. Hegarty, *Understanding GPS - Principles and Applications*, 2006.

[Kasdin and Walter, 1992] N.J. Kasdin and T. Walter, *Discrete simulation of power law noise [for oscillator stability evaluation]*, in Proceedings of IEEE Frequency Control Symposium, 1992, pp. 274–283.

[Kayton and Fried, 1997] M. Kayton and W.R. Fried, *Avionics Navigation Systems*, May 1997.

[Kenneth, 2008] G. Kenneth, *Introduction to Inertial Navigation and Kalman filtering*, Jun. 2008.

[Konaka et al., 2001] E. Konaka, T. Suzuki and S. Okuma, *Line following control of two wheeled vehicle by symbolic controller*, in Proceedings of 40th IEEE Conference on Decision and Control, 2001, vol. 1, pp. 514–515.

[Le Bras et al., 2009] F. Le Bras, T. Hamel, C. Barat and R. Mahony, *Nonlinear Image-Based Visual Servo controller for automatic landing guidance of a fixed-wing Aircraft*, in Proceedings of European Control Conference, 2009, pp. 1836–1841.

[Li, 2009] T. Li, *Use of Wheel Speed Sensors to Enhance a Reduced IMU Ultra-Tight GNSS Receiver*, 2009.

[Macabiau et al., 2006] C. Macabiau, L. Moriella, M. Raimondi, C. Dupouy, A. Steingaß and A. Lehner, *GNSS Airborne Multipath Errors Distribution Using the High Resolution Aeronautical Channel Model and Comparison to SARPs Error Curve*, in Proceedings of ION NTM, 2006.

[Maini and Aggarwal, 2009] R. Maini and H. Aggarwal, *Study and comparison of various image edge detection techniques*, published in International journal of image processing (IJIP), 2009, vol. 3, pp. 1–11.

[Maitre, 1985] H. Maitre, *Un panorama de la transformation de Hough*, 1985.

[Martineau, 2008] A. Martineau, *Performance of Receiver Autonomous Integrity Monitoring (RAIM) for Vertically Guided Approaches*, 2008.

[McAndrew, 2004] A. McAndrew, *An introduction to digital image processing with matlab notes for scm2511 image processing*, published in school of computer science and Mathematics, Victoria university of technology, 2004, pp. 1–264.

[Merino et al., 2006] L. Merino, J. Wiklund, F. Caballero, A. Moe, J.R.M. De Dios, P.E. Forssen, K. Nordberg and A. Ollero, *Vision-based multi-UAV position estimation*, published in IEEE Robotics and Automation Magazine, 2006, vol. 13, pp. 53–62.

[Miller et al., 2008] A. Miller, M. Shah and D. Harper, *Landing a UAV on a runway using image registration*, in Proceedings of IEEE International Conference on Robotics and Automation, 2008, pp. 182–187.

[Mirisola et al., 2007] L.G.B. Mirisola, J. Lobo and J. Dias, *3D map registration using vision/laser and inertial sensing*, in Proceedings of European Conference on Mobile Robots, 2007.

[Mirisola and Dias, 2009] L.G.B. Mirisola and J. Dias, *Exploiting attitude sensing in vision-based navigation for an airship*, published in Journal of Robotics, 2009, vol. 2009.

[Montloin, 2011] L. Montloin, *GNSS integrity monitoring in the presence of singular events: State of the art report*, 2011.

[Morvan, 2009] Y. Morvan, *Acquisition, Compression and Rendering of Depth and Texture for Multi-View Video*, 2009.

[Murphy and Booth, 2000] T. Murphy and J. Booth, *GBAS SARPs Review and Validation of Airborne Multipath Requirements*, 2000.

[Neri, 2011] P. Neri, *Use of GNSS signals and their augmentations for Civil Aviation navigation during approaches with vertical guidance and precision approaches - Présentation*, 2011.

[OFCM, 2005] OFCM, *Federal Meteorological Handbook No. 1 Surface Weather Observations and Reports*, 2005.

[Parkinson and Spilker, 1996] B.W. Parkinson and J.J. Spilker, *Global Positioning System: Theory and Applications*, 1996.

[Raquet and Giebner, 2003] M.J.F. Raquet and C.M. Giebner, *Navigation Using Optical Measurements of Objects at Unknown Locations*, in Proceedings of ION 59th Annual Meeting/CIGTF 22nd Guidance Test Symposium, Jun. 2003.

[Ressouche and Decneudt, 2014] A. Ressouche and K. Decneudt, *Etude des techniques de traitement video pour le positionnement*, 2014.

[Riisgaard and Blas, 2005] S. Riisgaard and M.R. Blas, *SLAM for Dummies - A Tutorial Approach to Simultaneous Localization and Mapping*, 2005.

[Rives and Azinheira, 2004] P. Rives and J.R. Azinheira, *Linear structures following by an airship using vanishing point and horizon line in a visual servoing scheme*, in Proceedings of IEEE International Conference on Robotics and Automation, 2004, vol. 1, pp. 255–260.

[Sabater, 2009] N. Sabater, *Reliability and accuracy in stereovision Application to aerial and satellite high resolution images*, décembre 2009.

[Salos, 2012] D. Salos, *Integrity monitoring applied to the reception of GNSS signals in urban environments*, 2012.

[Schertler, 2012] K. Schertler, *Towards a Robust and Efficient Runway Detection for Image Based Landing*, 2012.

[Segvic et al., 2007] S. Segvic, A. Remazeilles, A. Diosi and F. Chaumette, *Large scale vision-based navigation without an accurate global reconstruction*, in Proceedings of IEEE Conference on Computer Vision and Pattern Recognition, 2007, pp. 1–8.

[Seo et al., 2004] J. Seo, J.G. Lee and C.G. Park, *A New Error Compensation Scheme For INS Vertical Channel*, in Proceedings of 16th IFAC Symposium on Automatic Control in Aerospace, Jun. 2004.

[Silveira et al., 2003] G.F. Silveira, J.R. Azinheira, P. Rives and S.S. BUENO, *Line following visual servoing for aerial robots combined with complementary sensors*, in Proceedings of 11th International Conference on Advanced Robotics, Jul. 2003.

[Sinopoli et al., 2001] B. Sinopoli, M. Micheli, G. Donato and T.J. Koo, *Vision based navigation for an unmanned aerial vehicle*, in Proceedings of IEEE International Conference on Robotics and Automation, 2001, vol. 2, pp. 1757–1764.

[Stephens and Thomas, 1995] S.A. Stephens and J.B. Thomas, *Controlled-root formulation for digital phase-locked loops*, published in IEEE Transactions on Aerospace and Electronic Systems, 1995, vol. 31, pp. 78–95.

[Taylor and Barnes, 2005] J. Taylor and E. Barnes, *GPS Current Signal-in-Space Navigation Performance*, in Proceedings of ION NTM, Jan. 2005.

[THAV, 2009] THAV, *Part 1 - Rapport Final Opportunites Technologiques NAVPRO 2eme edition*, Nov. 2009.

[Ulrich and Nourbakhsh, 2000] I. Ulrich and I. Nourbakhsh, *Appearance-based place recognition for topological localization*, in Proceedings of IEEE International Conference on Robotics and Automation, 2000, vol. 2, pp. 1023–1029.

[Urmson et al., 2002] C.P. Urmson, M.B. Dias and R.G. Simmons, *Stereo vision based navigation for sun-synchronous exploration*, in Proceedings of IEEE/RSJ International Conference on Intelligent Robots and Systems, 2002, vol. 1, pp. 805–810.

[Veth, 2006] M.J. Veth, *Fusion of imaging and inertial sensors for navigation*, 2006.

[Veth and Raquet, 2007] M. Veth and J. Raquet, *Two-dimensional stochastic projections for tight integration of optical and inertial sensors for navigation*, in Proceedings of ION NTM, 2007, pp. 587 – 596.

[Vezinet et al., 2013] J. Vezinet, A.-C. Escher, A. Guillet and C. Macabiau, *State of the Art of Image-aided Navigation Techniques for Aircraft Approach and Landing*, in Proceedings of ION ITM, 2013.

[Vezinet et al., 2014] J. Vezinet, A.-C. Escher, A. Guillet and C. Macabiau, *Video Integration in a GPS/INS Hybridization Architecture for Approach and Landing*, in Proceedings of IEEE/ION PLANS, 2014.

[Wang and Fan, 2009] B. Wang and S. Fan, *An Improved CANNY Edge Detection Algorithm*, 2009, pp. 497–500.

[Wang et al., 2006] J.M. Wang, C.T. Tsai, S. Cherng and S.W. Chen, *Omni-directional camera networks and data fusion for vehicle tracking in an indoor parking lot*, in Proceedings of IEEE International Conference on Video and Signal Based Surveillance, 2006, pp. 45–45.

[Woodman, 2007] O.J. Woodman, *An introduction to inertial navigation*, 2007.

[Yinger et al., 2003] C.H. Yinger, W.A. Feess, V. Nuth and R.N. Haddad, *GPS Accuracy Versus Number of NIMA Stations*, in Proceedings of ION GPS/GNSS, 2003, pp. 9–12.

Appendix A: Reference Frames Definition

Inertial navigation involves several reference frames. Their description is extracted from [Farrel and Barth, 1998]. An illustration of the different frames considered is presented in Figure 53.

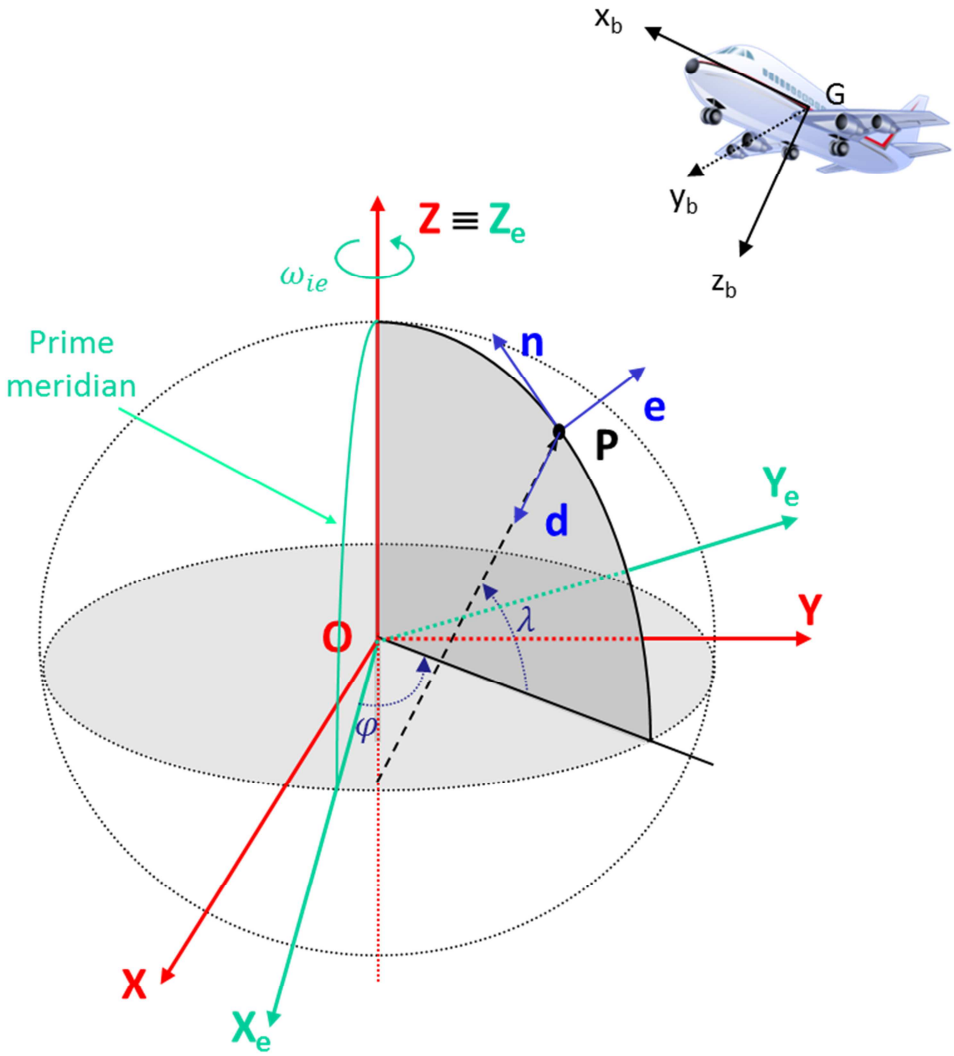

Figure 53 – Coordinate and reference frames

(X_i, Y_i, Z_i) is the ***inertial frame (i-frame)***. It is defined as a reference Galilean frame in which Newton's laws of motion may apply. The origin of the inertial frame is given coincident with the Earth's center of mass, the X axis points toward the vernal equinox, the Z axis extends through the Earth's spin axis and the Y axis is defined to complete the right-handed coordinate system.

(X_e, Y_e, Z_e) is the ***Earth-centered earth-fixed frame (ECEF-frame or e-frame).*** Its origin is fixed to the center of the Earth. The coordinate axis is fixed to the Earth and the Z_e axis is aligned with the Z_i axis of the inertial frame. Then the ECEF frame rotates relative to the inertial frame at a frequency of:

$$\omega_{e/i} \approx 7.292115 \times 10^{-5} rad/s \tag{A.1}$$

In the *e-frame*, two common coordinate systems can be used:

- The ECEF Cartesian coordinates system (X_e, Y_e, Z_e).
- The ECEF geodetic coordinates system that uses the latitude, longitude and altitude parameters (λ, ϕ, h).

The relationship between the two sets of coordinates is:

$$\begin{cases} x_e = (R_N + h) \cdot \cos\lambda \cdot \cos\phi \\ y_e = (R_N + h) \cdot \cos\lambda \cdot \sin\phi \\ z_e = \left((1 - e^2) \cdot R_N + h\right) \cdot \sin\lambda \end{cases} \tag{A.2}$$

Where R_N is the transverse radius of curvature.

(n, e, d) is the ***Geographic navigation frame (NED-frame or n-frame).*** The geographic frame is defined locally, relative to the Earth's geoid. The d axis points toward the interior of the ellipsoid along the ellipsoid normal. The n axis points toward the North and the e axis points in the East direction to complete the orthogonal, right-handed frame. The frame origin is the projection of the platform origin onto the Earth's geoid.

The inertial rotation rate of the Earth expressed in the *n-frame* is:

$$\omega_{e/i}^{n} = \begin{bmatrix} \omega_{e/i} \cdot \cos(\lambda) \\ 0 \\ -\omega_{e/i} \cdot \sin(\lambda) \end{bmatrix} \tag{A.3}$$

(x_b, y_b, z_b) is the ***body or mobile frame (b-frame or m-frame).*** The body frame is rigidly attached to the vehicle of interest, usually at a fixed point such as the center of gravity of the vehicle. The x_b axis is defined in the forward direction. The y_b axis is defined pointing to the right of the vehicle. And the z_b axis is defined pointing to the bottom of the vehicle, in order to complete the right-handed orthogonal frame.

(X_p, Y_p, Z_p) is the ***platform frame (p-frame)*** defined by the positions of the IMU sensors (gyroscopes), in case of a strapdown platform mechanisation**.** In the current study we will consider that the platform frame is perfectly aligned with the body frame.

(X_w, Y_w, Z_w) is the ***wander azimuth frame (w-frame).*** Wander azimuth reference frames solve the high latitude problem faced by the geographic frame. The definition is expressed in terms of the angular velocity of the frame with respect to the earth frame. In that way when the instantaneous rotation vector of the *n-frame* with respect to the *e-frame* is:

$$\omega_{n/e}^{n} = \begin{bmatrix} \dot{\phi} \cdot \cos(\lambda) \\ -\dot{\lambda} \\ -\dot{\phi} \cdot \sin(\lambda) \end{bmatrix} \tag{A.4}$$

The instantaneous rotation vector of the *w-frame* with respect to the *e-frame* is:

$$\omega_{w/e}^{n} = \begin{bmatrix} \dot{\phi} \cdot \cos(\lambda) \\ -\dot{\lambda} \\ 0 \end{bmatrix} \tag{A.5}$$

Finally, the wander azimuth angle at instant k is computed with the following relationship:

$$w(k) = w(0) + \big(\phi(k) - \phi(0)\big) \cdot \sin(\lambda) \tag{A.6}$$

The Z axis of the *n-frame* and the Z axis of the *w-frame* are aligned and they are illustrated in Figure 54. The wander angle is denoted w in the figure.

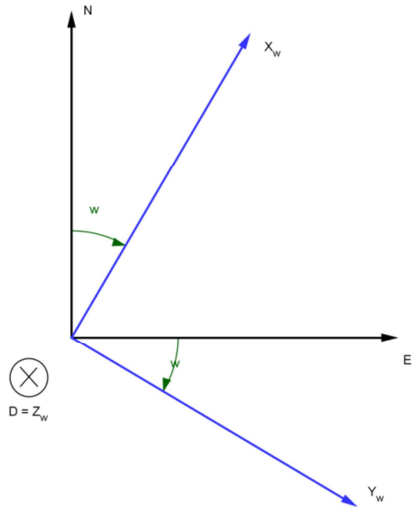

Figure 54 – *n-frame* and *w-frame*

The wander azimuth frame is a navigation frame. In order to dissociate it from the geographic navigation frame (*n-frame*), we denote it the *w-frame.*

The coordinates of a vector v expressed in the *n-frame*, (v_n, v_e, v_d), are linked to those of the same vector expressed in the *w-frame*, (v_x, v_y, v_z), through the relationships (A.7) and (A.8).

$$\begin{aligned} v_n &= v_x \cdot \cos w - v_y \cdot \sin w \\ v_e &= v_x \cdot \sin w + v_y \cdot \cos w \end{aligned} \tag{A.7}$$

$$\begin{aligned} v_x &= v_n \cdot \cos w + v_e \cdot \sin w \\ v_y &= -v_n \cdot \sin w + v_e \cdot \cos w \end{aligned} \tag{A.8}$$

Appendix B: Wheel Speed Sensor Measurement Model

The current appendix proposes some additional information on the Wheel Speed Sensor such as a better description of the measurement model and an analysis of real data.

B.1 WSS Measurement Model

B.1.1 Sensed Data

The basic principle of a tachometer (or Wheel Speed Sensor) is that the sensor generates a sinusoidal signal whose frequency depends on the angular velocity of the wheels. The relation between the frequency of that signal f and wheel rotation speed Ω_{Wheel} is as follows:

$$\Omega_{Wheel} = 3600 \times 2\pi \times \frac{f}{N_{Cycle}} \tag{B.1}$$

Where:

- Ω_{Wheel} is the wheel speed velocity in rad/s.
- f is the frequency of the sinusoidal signal generated by the sensor.
- N_{Cycle} is the number of teeth of the sensor (it defines the resolution of the sensor but has an impact on its size).

Then the linear velocity provided by a WSS is related to the rotation speed as follows:

$$v_{WSS} = R \times \Omega_{Wheel} \tag{B.2}$$

Where:

- v_{WSS} is the linear velocity of the wheel in m/s.
- R is the nominal radius of the wheel.
- Ω_{Wheel} is the wheel speed velocity in rad/s.

In real conditions, the radius of the wheel is not a constant value and varies as a function of several parameters (velocity, pressure, temperature, materials,...). The model used in the PhD thesis takes into consideration a variation of the radius that has been empirically estimated based on real measurements (see section B.1.3).

B.1.2 Nominal Measurement Error Model

The wheel speed measurement error model is composed of three components:

$$v_{WSS} = (R + \epsilon_R) \cdot (1 + SF_{WSS}) \cdot \Omega_{Wheel} + n_{WSS} \tag{B.3}$$

Where:

- v_{WSS} is the WSS velocity
- R is the nominal radius of the wheel.
- ϵ_R is a bias on the nominal radius of the wheel.
- SF_{WSS} is a Scale Factor coefficient.
- Ω_{Wheel} is the wheel rotation speed.
- n_{WSS} is the White Gaussian Centered measurement noise.

B.1.2.1. Scale Factor

As for the IMU measurement models, the Scale factor is the ratio of change in output to a change in the intended input to be measured. It is evaluated as the slope of the straight trend line that can be fitted to input-output data [Aggarwal et al., 2010].

B.1.2.2. Nominal Radius Bias

Under the assumption that the measurement provided by the wheel speed sensor is a wheel speed angular velocity multiplied by the nominal value of the radius of the wheel. We have to consider that this nominal value is not exactly known. In that case, a constant bias ϵ_R is added for this parameter in order to model the eventual change in the radius of the wheels (caused by a change in the pressure of the tires, in the temperature, in the weather or any other environment effect)

B.1.3 Radius Variation Model

In addition to the bias on the expected value of the nominal radius of the wheels, there is a non-constant variation of the radius of the wheel due to several parameters such as the velocity of the aircraft, the temperature, the pressure, the state of the runway,…

So as to correctly model this variation of the radius, we assumed that, due to this variation, a difference can be seen between the linear velocity provided by the WSS and the true linear velocity of the aircraft. This assumption traduces with the following equations:

$$v_{true} = (R + \Delta R) \cdot \Omega_{Wheel} \tag{B.4}$$

$$v_{WSS} = R \times \Omega_{Wheel} \tag{B.5}$$

Where :

- v_{true} is the true linear velocity of the aircraft.
- v_{WSS} is the WSS velocity.
- R is the nominal radius of the wheel.
- ΔR is the radius variation coefficient.
- Ω_{Wheel} is the wheel rotation speed.

Those equations signify that the true linear velocity is related to the wheel rotation speed with the true value of the radius $R_{true} = R + \Delta R$. In the other hand, the linear velocity provided by the WSS is computed by multiplying the rotation speed with the nominal radius.

During the PhD thesis, real WSS data were provided. Those data were recorded during a real flight and they are presented in the next section. With the knowledge of the velocity reference data (considered as true), we empirically determined the value of the ΔR coefficient as a function of the velocity as presented in the following equation:

$$\frac{\Delta R}{R} = \frac{v_{true}}{v_{WSS}} - 1 \tag{B.6}$$

Figure 55 illustrates in blue the criteria introduced in equation (B.6) as a function of the velocity.

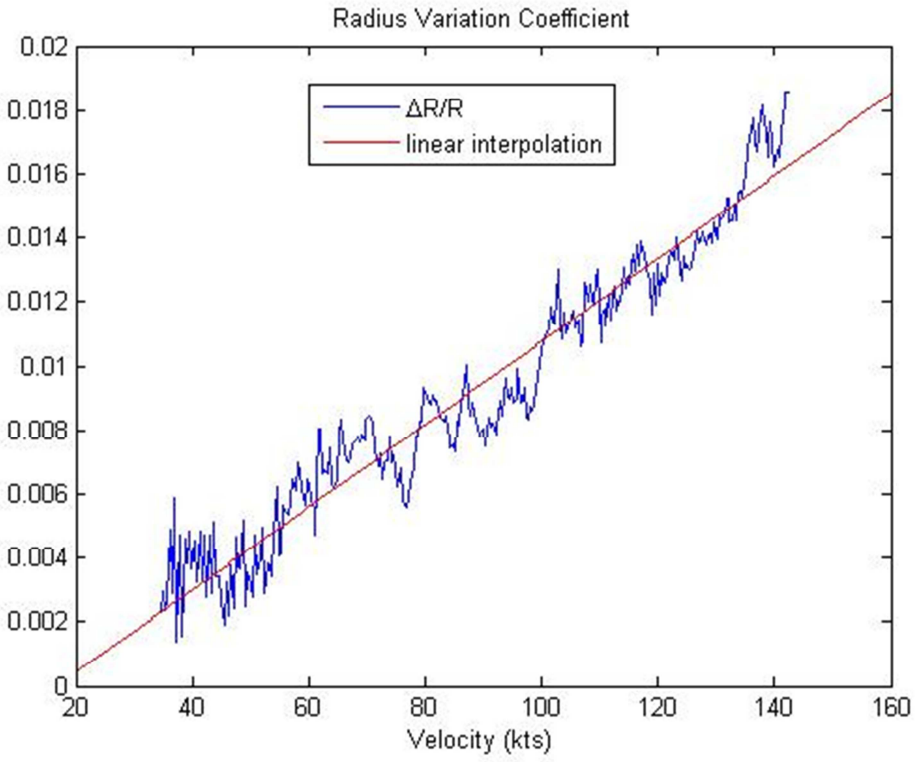

Figure 55 – Radius Variation Coefficient Linear Regression

As we can see in this figure, the $\frac{\Delta R}{R}$ ratio exhibits a slow variation as a function of the velocity (expressed in kts) and therefore can be modeled as a linear function. On the other hand, the fast variation of the ratio will not be taken into account in the model. The linear function model is illustrated in red in Figure 55.

As the measurement model introduced in (B.3) involves the wheel rotation speed Ω_{Wheel} and our reference trajectory data only contains linear velocity, we derived a reference wheel rotation speed by dividing the linear velocity by the $R + \Delta R$ radius. In definitive, the generated Ω_{Wheel} parameter is implicitly impacted by the changing behavior of the radius of the wheels as a function of the velocity. In a second step, the measurement model is used with the Ω_{Wheel} so as to generated v_{WSS} data.

In the future, the ΔR parameter model could be refined using more real data or with a more complex model.

B.2 Real WSS Data Illustration

The availability of real WSS measurements recorded during the real flight allowed us to model some realistic behavior of WSS measurements (as depicted in the previous section). In particular, it helped in estimating a parameter that describes the dependency of the radius of the wheels with respect to the velocity of the aircraft. In addition, it also allowed us to compare the simulated measurements with real ones. In that way, Figure 56 presents a comparison between the real measurements and the simulated ones using the previously described model. Figure 57 illustrates the difference between the simulated velocity and the real measurement.

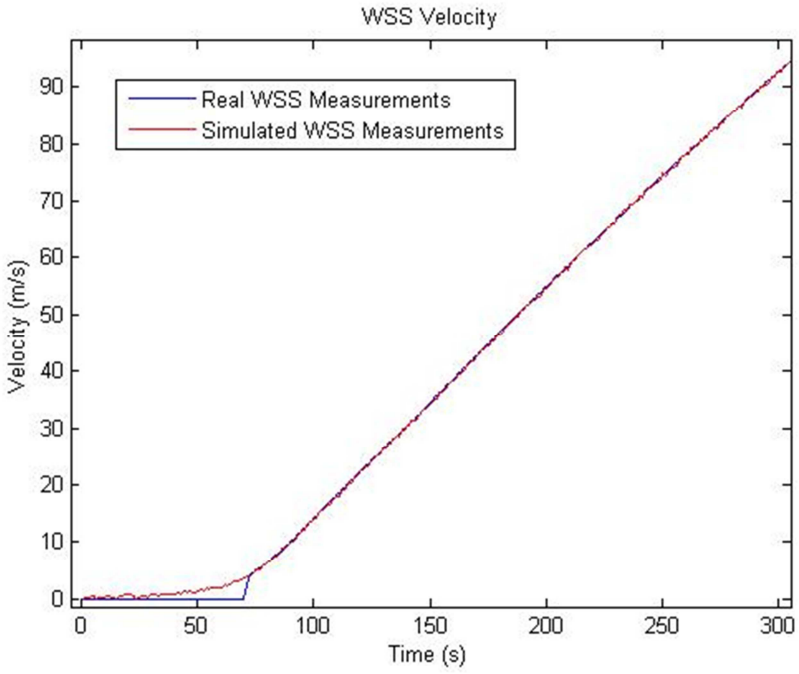

Figure 56 – WSS Velocity Real and Simulated Measurements Comparison

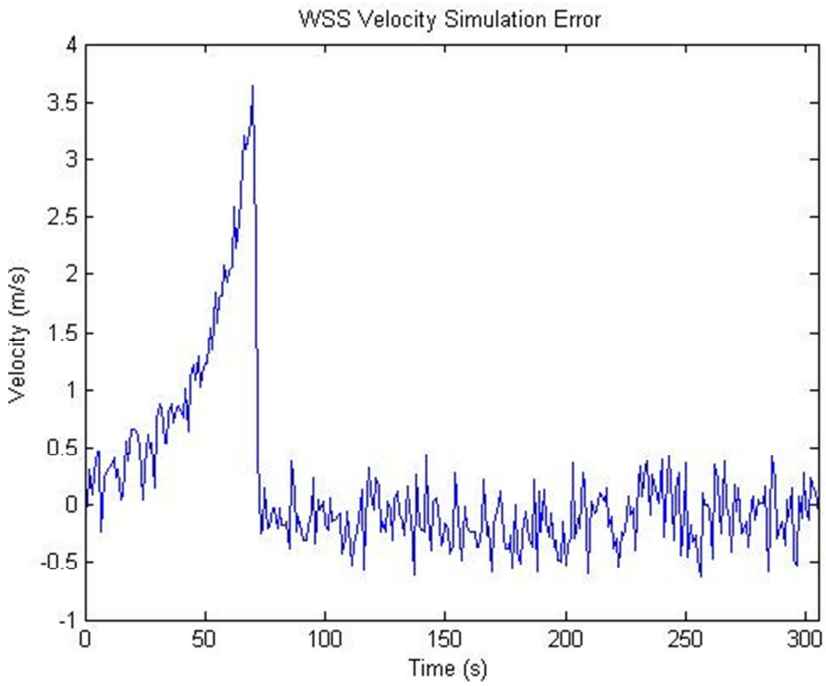

Figure 57 – WSS Velocity Simulation Error

The first observation that we can make on the real data is that the WSS measurements seems to have a minimal velocity threshold (around 7m/s) under which no measurements are provided. No assumptions regarding this "dead zone" have been considered because we do not consider a velocity under that threshold during the simulations.

In the error plot, in addition to the illustration of the threshold of the dead zone, we can observe that a small offset seems to be still present between the real measurements and the simulated ones. A future development can be done by improving the model of the variation of the radius in function of the time or in function of the velocity.

Appendix C: EKF Equations and State Transition Equations

This appendix presents the detailed equations of the Extended Kalman Filter introduced in Chapter 5. It also presents the detailed equation for the state transition model.

C.1 Extended Kalman Filter Equations

A continuous non-linear stochastic system can be modeled with the two following equations:

$$\dot{X}(t) = f(X,t) + U(t) \tag{C.1}$$

$$Y(k) = h(X,k) + V(k) \tag{C.2}$$

Where:

- X is the state vector of the system.
- Y is the observation vector.
- f is the state transition function (or dynamic matrix).
- h is the observation function.
- U is the additive process noise vector, assumed centered, white and Gaussian.
- V is the additive observation noise vector, assumed centered, white and Gaussian.
- t is the continuous time variable.

(C.1) and (C.2) are respectively denoted the state transition model and the observation model.

Let us consider $\hat{X}(t_k)$ the estimated value of the state at instant t_k. Using the state transition model (C.1), $\hat{X}(t_k)$ verifies:

$$\dot{\hat{X}}(t_k) = f\left(\hat{X}, t_k\right) \tag{C.3}$$

Then, let us introduce $\delta X(t) = X(t) - \hat{X}(t_k)$ the estimation error of the state at instant t.

A Taylor series first order expansion of the state transition function f around the estimated state $\hat{X}(t_k)$ leads to:

$$f(X,t) = f\left(\hat{X}, t_k\right) + \left.\frac{\partial f}{\partial X}\right|_{X=\hat{X}(t_k)} \cdot \left(X(t) - \hat{X}(t_k)\right) \tag{C.4}$$

Let us denote $\dot{\hat{X}}(t_k) = f\left(\hat{X}, t_k\right)$, equation (C.4) becomes:

$$f(X,t) = \dot{\hat{X}}(t_k) + F(t) \cdot \delta X(t) \tag{C.5}$$

By using the prediction equation of the Kalman Filter introduced in 5.2.2.1, the state estimate becomes:

$$\hat{X}_{k|k-1} = \hat{X}(t_k) + \delta\hat{X}_{k|k-1} \tag{C.6}$$

A Taylor series first order expansion of the observation function h around the previous estimate of the state $\hat{X}_{k|k-1}$ (also called the predicted state) leads to:

$$h(X,k) = h\left(\hat{X}, k\right) + \underbrace{\left.\frac{\partial h}{\partial X}\right|_{X=\hat{X}_{k|k-1}}}_{H(k)} \cdot \left(X(k) - \hat{X}_{k|k-1}\right) \tag{C.7}$$

Let us then replace $f(X,t)$ by its Taylor series expansion, (C.4), in the equation (C.1). The equation becomes:

$$\dot{X}(t) = \dot{\hat{X}}(t_k) + F(t) \cdot \delta X(t) + U(t) \tag{C.8}$$

The state propagation equation can be rewritten using the error state vector δX as:

$$\delta\dot{X} = F(t) \cdot \delta X(t) + U(t) \tag{C.9}$$

That last equation represents the linearized state propagation equation of a Kalman Filter whose state vector is the error state vector δX and propagation matrix is F.

In the same way, let's then replace $h(X,k)$ by its Taylor series expansion, (C.7), in the equation (C.2). The equation becomes:

$$Y(k) = h\left(\hat{X}, k\right) + H(k) \cdot \left(X(k) - \hat{X}_{k|k-1}\right) + V(k) \tag{C.10}$$

Denoting $h\left(\hat{X}_{k|k-1}\right) = h\left(\hat{X}, k\right)$, and developing (C.6), we obtain:

$$Y(k) = h\left(\hat{X}_{k|k-1}\right) + H(k) \cdot X(k) - H(k) \cdot \hat{X}_{k|k-1} + V(k) \tag{C.11}$$

Thus, the introduction of $\hat{X}(t_k)$ in the equation leads to:

$$Y(k) = h\left(\hat{X}_{k|k-1}\right) + H(k) \cdot \left[X(k) - \hat{X}(t_k) + \hat{X}(t_k)\right] - H(k) \cdot \hat{X}_{k|k-1} + V(k) \tag{C.12}$$

Then,

$$Y(k) = h\left(\hat{X}_{k|k-1}\right) + H(k) \cdot \delta X(k) + H(k) \cdot \left[\hat{X}(t_k) - \hat{X}_{k|k-1}\right] + V(k) \tag{C.13}$$

Let's introduce $\tilde{V}(k) = h\left(\hat{X}_{k|k-1}\right) - H(k) \cdot \delta\hat{X}_{k|k-1}$, the predicted measurement. (C.13) becomes:

$$Y(k) - \tilde{V}(k) = H(k) \cdot \delta X(k) + V(k) \tag{C.14}$$

That last equation represents the linearized observation equation of a Kalman Filter whose state vector is the error state vector δX, observation matrix is H and measurement is $Y(k) - \tilde{V}(k)$.

Equations (C.9) and (C.14) constitute a linear state space system that can be solved using a Kalman Filter. This implies that estimation of a state X of a nonlinear system using the EKF equations is similar to the estimation of the error state vector δX of the linearized system using the more simple KF equations.

The innovation vector, considering KF equations, is then computed as:

$$I(k) = Y(k) - \tilde{V}(k) - H(k) \cdot \delta\hat{X}_{k|k-1} \tag{C.15}$$

And using the predicted measurement expression:

$$I(k) = Y(k) - h\left(\hat{X}_{k|k-1}\right) + H(k) \cdot \delta\hat{X}_{k|k-1} - H(k) \cdot \delta\hat{X}_{k|k-1} \tag{C.16}$$

Finally it can be simplified as:

$$I(k) = Y(k) - h\left(\hat{X}_{k|k-1}\right) \tag{C.17}$$

C.2 State Transition Equations

C.2.1 Position Error Propagation Equation

The aircraft velocity expressed in the *n-frame* velocity is related to the aircraft geodetic position rate vector as follows:

$$\begin{bmatrix} v_N \\ v_E \end{bmatrix} = \begin{bmatrix} (R_M + h) & 0 \\ 0 & (R_N + h) \cdot \cos(\lambda) \end{bmatrix} \cdot \begin{bmatrix} \dot{\lambda} \\ \dot{\phi} \end{bmatrix} \tag{C.18}$$

Where:

- R_M is the radius of curvature along a meridian at a given latitude: $R_M = \frac{a \cdot (1-e^2)}{(1-e^2 \cdot \sin^2(\lambda))^{1.5}}$.
- R_N is the transverse radius of curvature: $R_N = \frac{a}{(1-e \cdot \sin^2(\lambda))^{0.5}}$.
- a is the equatorial radius: $a = 6378137m$.
- e is the eccentricity: $e = 0.0818$.

Then:

$$\begin{bmatrix} \dot{\lambda} \\ \dot{\phi} \end{bmatrix} = \begin{bmatrix} \frac{1}{R_M + h} & 0 \\ 0 & \frac{1}{(R_N + h) \cdot \cos(\lambda)} \end{bmatrix} \cdot \begin{bmatrix} v_N \\ v_E \end{bmatrix} \tag{C.19}$$

The differentiation of the relation leads to:

$$\begin{aligned} d\dot{\lambda} &= \frac{dv_N}{R_M + h} \\ d\dot{\phi} &= \frac{dv_E}{(R_N + h) \cdot \cos(\lambda)} \end{aligned} \tag{C.20}$$

Then, using the coordinate conversion equation (5.14), we obtain:

$$\begin{aligned} d\dot{\theta}_E &= -\frac{dv_N}{R_M + h} \\ d\dot{\theta}_N &= \frac{dv_E}{R_N + h} \end{aligned} \tag{C.21}$$

A projection in the *w-frame* induces:

$$\begin{aligned} d\dot{\theta}_x \cdot \sin w + d\dot{\theta}_y \cdot \cos w &= -\frac{dv_x \cdot \cos w - dv_y \cdot \sin w}{R_M + h} \\ d\dot{\theta}_x \cdot \cos w - d\dot{\theta}_y \cdot \sin w &= \frac{dv_x \cdot \sin w + dv_y \cdot \cos w}{R_N + h} \end{aligned} \tag{C.22}$$

And finally the horizontal angular position error propagation equation is:

$$\begin{aligned} d\dot{\theta}_x &= dV_x \cdot \cos w \cdot \sin w \cdot \left(\frac{1}{R_N + h} - \frac{1}{R_M + h}\right) + dV_y \cdot \left(\frac{\sin^2 w}{R_M + h} + \frac{\cos^2 w}{R_N + h}\right) \\ d\dot{\theta}_y &= -dV_x \cdot \left(\frac{\cos^2 w}{R_M + h} + \frac{\sin^2 w}{R_N + h}\right) + dV_y \cdot \cos w \cdot \sin w \cdot \left(\frac{1}{R_M + h} - \frac{1}{R_N + h}\right) \end{aligned} \tag{C.23}$$

We can introduce the radius of curvature in the X_w and Y_w directions (X-axis and Y-axis of the *w-frame*) as follows:

$$\begin{aligned} \frac{1}{R_x + h} &= \frac{\cos^2 w}{R_M + h} + \frac{\sin^2 w}{R_N + h} \\ \frac{1}{R_y + h} &= \frac{\sin^2 w}{R_M + h} + \frac{\cos^2 w}{R_N + h} \end{aligned} \tag{C.24}$$

And by defining $\frac{1}{R_{xy}+h} = \cos w \cdot \sin w \cdot \left(\frac{1}{R_N+h} - \frac{1}{R_M+h}\right)$, we obtain the following matrix form presented in 5.4.1.1:

$$\begin{bmatrix} d\dot{\theta}_x \\ d\dot{\theta}_y \end{bmatrix} = \begin{bmatrix} \frac{1}{R_{xy} + h} & \frac{1}{R_y + h} \\ -\frac{1}{R_x + h} & -\frac{1}{R_{xy} + h} \end{bmatrix} \cdot \begin{bmatrix} dv_x \\ dv_y \end{bmatrix} \tag{C.25}$$

C.2.2 Velocity Error Propagation Equation

C.2.2.1. Earth-relative velocity in inertial coordinates

If we define the mobile position vector in the earth frame as R^e, then the earth relative velocity of the mobile expressed in the *i-frame* is:

$$v_e^i = \left(\frac{d}{dt} R^e\right)^i \tag{C.26}$$

The relationship between the two coordinates of R in the *i-frame* and the *e-frame* coordinates systems is:

$$R^e = R_{i2e} \cdot R^i \tag{C.27}$$

Then by using the transport rate expression, the derivative of (C.27) leads to the following relationship, expressed in the *i-frame* coordinates system:

$$\left(\frac{d}{dt} R^e\right)^i = v_e^i = \omega_{i/e}^i \wedge R^i + \left(\frac{d}{dt} R^i\right)^i \tag{C.28}$$

Rewritten as follows:

$$\left(\frac{d}{dt}R^i\right)^i = v_e^i - \omega_{i/e}^i \wedge R^i \tag{C.29}$$

Or:

$$\left(\frac{d}{dt}R^i\right)^i = v_e^i + \omega_{e/i}^i \wedge R^i \tag{C.30}$$

Thus, a second derivation of (C.28) expressed in the *i-frame* coordinates system leads to:

$$\left(\frac{d^2}{dt^2}R^i\right)^i = \frac{d}{dt}v_e^i + \frac{d}{dt}\left(\omega_{e/i}^i \wedge R^i\right) \tag{C.31}$$

And after development:

$$\left(\frac{d^2}{dt^2}R^i\right)^i = \frac{d}{dt}v_e^i + \underbrace{\frac{d}{dt}\left(\omega_{e/i}^i\right)}_{0} \wedge R^i + \omega_{e/i}^i \wedge \left(\frac{d}{dt}R^i\right)^i \tag{C.32}$$

By replacing $\left(\frac{d}{dt}R^i\right)^i$ by its expression in (C.30), we obtain:

$$\left(\frac{d^2}{dt^2}R^i\right)^i = \frac{d}{dt}v_e^i + \omega_{e/i}^i \wedge \left(v_e^i + \omega_{e/i}^i \wedge R^i\right) \tag{C.33}$$

And after development:

$$\left(\frac{d^2}{dt^2}R^i\right)^i = \dot{v}_e^i + \omega_{e/i}^i \wedge v_e^i + \omega_{e/i}^i \wedge \omega_{e/i}^i \wedge R^i \tag{C.34}$$

That last equation leads to the expression of the derivative of the Earth's relative velocity in inertial coordinates:

$$\dot{v}_e^i = \frac{d^2}{dt^2}R^i - \omega_{e/i}^i \wedge v_e^i + \omega_{e/i}^i \wedge \omega_{e/i}^i \wedge R^i \tag{C.35}$$

That can be rewritten as:

$$\dot{v}_e^i = f^i + G^i + \omega_{e/i}^i \wedge \omega_{e/i}^i \wedge R^i - \omega_{e/i}^i \wedge v_e^i \tag{C.36}$$

Where:

- f^i is the non-gravitational acceleration or specific force
- G^i is the Gravitational acceleration
- $-\omega_{e/i}^i \wedge \omega_{e/i}^i \wedge R^i$ is the centrifugal acceleration
- $-\omega_{e/i}^i \wedge v_e^i$ is the Coriolis acceleration

By introducing the local gravity vector g^i (containing the centrifugal acceleration), (C.36) becomes:

$$\dot{v}_e^i = f^i + g^i - \omega_{e/i}^i \wedge v_e^i \tag{C.37}$$

C.2.2.2. Earth-relative velocity in wander azimuth frame coordinates

In the same way as for the previous part, the Earth's relative velocity vector v_e satisfies the following relationship between the *w-frame* and the *i-frame* coordinates systems:

$$v_e^w = R_{i2w} \cdot v_e^i \tag{C.38}$$

The application of the Coriolis theorem leads to:

$$\dot{v}_e^w = R_{i2w} \cdot \left(\omega_{i/w}^i \wedge v_e^i + \dot{v}_e^i\right) \tag{C.39}$$

Then replacing $\dot{v}_e^i$ by its expression in equation (C.37):

$$\dot{v}_e^w = R_{i2w} \cdot \left(\omega_{i/w}^i \wedge v_e^i + f^i + g^i - \omega_{e/i}^i \wedge v_e^i\right) \tag{C.40}$$

And after development:

$$\dot{v}_e^w = \omega_{i/w}^w \wedge v_e^w + f^w + g^w - \omega_{e/i}^w \wedge v_e^w \tag{C.41}$$

Finally, the earth-relative velocity differential equation expressed in wander coordinates can be written as:

$$\dot{v}_e^w = f^w + g^w - \left(\omega_{w/e}^w + 2\omega_{e/i}^w\right) \wedge v_e^w \tag{C.42}$$

Appendix A presents the expression of the angular velocity of the *w-frame* relative to the *e-frame* expressed in the *n-frame* coordinates system:

$$\omega_{w/e}^{n} = \begin{bmatrix} \dot{\phi} \cdot \cos(\lambda) \\ -\dot{\lambda} \\ 0 \end{bmatrix} \tag{C.43}$$

Using (C.19), that expression becomes:

$$\omega_{w/e}^{n} = \begin{bmatrix} \dfrac{v_E}{R_N + h} \\ -\dfrac{v_N}{R_M + h} \\ 0 \end{bmatrix} \tag{C.44}$$

Finally, using (C.44) and (A.3), (C.42) can be rewritten as:

$$\dot{v}_e^w = R_{m2w} \begin{bmatrix} f_x \\ f_y \\ f_z \end{bmatrix}^m + R_{n2w} \begin{bmatrix} \xi_g \\ -\eta_g \\ g \end{bmatrix}^n - R_{n2w} \left(\begin{bmatrix} \dfrac{V_E}{R_N + h} \\ -\dfrac{V_N}{R_M + h} \\ 0 \end{bmatrix}^n + 2 \begin{bmatrix} \omega_{e/i} \cos\lambda \\ 0 \\ -\omega_{e/i} \sin\lambda \end{bmatrix}^n \right) \wedge \begin{bmatrix} v_x \\ v_y \\ v_z \end{bmatrix}^w \tag{C.45}$$

Where:

- $\begin{bmatrix} f_x \\ f_y \\ f_z \end{bmatrix}^m$ are the components of the specific force of the mobile expressed in the mobile frame f^m.
- $\begin{bmatrix} \xi_g \\ -\eta_g \\ g \end{bmatrix}^n$ is the local gravity vector expressed in the *n-frame* g^n.

Equation (C.45) is the differential equation that describes the INS velocity dynamic. The next part will deal with the establishment of the INS velocity error equation in the *w-frame*.

C.2.3 *Earth-Relative Velocity Error Propagation Equation in Wander Azimuth Frame Coordinates System*

First of all, we need to define the alignment error impact on the rotation matrices. Indeed, the estimation error of the R_{m2w} rotation matrix can be denoted as follows:

$$\delta R_{m2w} = R_{m2w} - \hat{R}_{m2w} \tag{C.46}$$

The rotation matrix error can be described by a the rotation matrix associated to the alignment angles errors, $d\phi$. In that way, the small angle transformation allows us to write:

$$\delta R_{m2w} = (d\phi \wedge) \cdot R_{m2w} \tag{C.47}$$

Where $d\phi = \begin{bmatrix} d\phi_x \\ d\phi_y \\ d\phi_z \end{bmatrix}$ and $(d\phi \wedge)$ its skew symmetric matrix.

The true rotation matrix is then related with the estimated one as follows:

$$R_{m2w} = (1 + d\phi \wedge)\hat{R}_{m2w} \tag{C.48}$$

Then using (C.48) and (C.42) and, introducing the estimation error of the different terms, we obtain:

$$\begin{aligned} \hat{\dot{v}}_e^w + \delta\dot{v}_e^w = {} & (I + d\phi \wedge)\hat{R}_{m2w}\left(\tilde{f}^m + \delta\tilde{f}^m\right) + R_{n2w}(\hat{g}^n + \delta g^n) \\ & -R_{n2w}\left(\delta\omega_{w/e}^n + 2\delta\omega_{e/i}^n\right) \wedge \hat{v}_e^w - R_{n2w}\left(\hat{\omega}_{w/e}^n + 2\hat{\omega}_{e/i}^n\right) \wedge \delta v_e^w \\ & -R_{n2w}\left(\hat{\omega}_{w/e}^n + 2\hat{\omega}_{e/i}^n\right) \wedge \hat{v}_e^w - R_{n2w}\left(\delta\omega_{w/e}^n + 2\delta\omega_{e/i}^n\right) \wedge \delta v_e^w \end{aligned} \tag{C.49}$$

Where the second order term, $R_{n2w}\left(\delta\omega_{w/e}^n + 2\delta\omega_{e/i}^n\right) \wedge \delta v_e^w$, will be neglected in the following.

The development of the terms of the first line leads to:

$$\begin{aligned} \hat{\dot{v}}_e^w + \delta\dot{v}_e^w = {} & \hat{R}_{m2w}\tilde{f}^m + \hat{R}_{m2w}\delta f^m + (d\phi \wedge)\hat{R}_{m2w}\tilde{f}^m + (d\phi \wedge)\hat{R}_{m2w}\delta\tilde{f}^m \\ & +R_{n2w}\hat{g}^n + R_{n2w}\delta g^n \\ & -R_{n2w}\left(\delta\omega_{w/e}^n + 2\delta\omega_{e/i}^n\right) \wedge \hat{v}_e^w - R_{n2w}\left(\hat{\omega}_{w/e}^n + 2\hat{\omega}_{e/i}^n\right) \wedge \delta v_e^w \\ & -R_{n2w}\left(\hat{\omega}_{w/e}^n + 2\hat{\omega}_{e/i}^n\right) \wedge \hat{v}_e^w - R_{n2w}\left(\delta\omega_{w/e}^n + 2\delta\omega_{e/i}^n\right) \wedge \delta v_e^w \end{aligned} \tag{C.50}$$

Where the other second order term, $(d\phi \wedge)\hat{R}_{m2w}\delta\tilde{f}^m$, is also neglected in the following.

In equation (C.50), we can isolate the zero order terms and establish:

$$\hat{\dot{v}}_e^w = \hat{R}_{m2w}\tilde{f}^m + R_{n2w}\hat{g}^n - R_{n2w}\left(\hat{\omega}_{w/e}^n + 2\hat{\omega}_{e/i}^n\right) \wedge \hat{v}_e^w \tag{C.51}$$

And the first order terms describe the velocity error propagation equation:

$$\begin{aligned} \delta\dot{v}_e^w = {} & \hat{R}_{m2w}\delta f^m + (d\phi \wedge)\hat{R}_{m2w}\tilde{f}^m + R_{n2w}\delta g^n \\ & -R_{n2w}\left(\delta\omega_{w/e}^n + 2\delta\omega_{\mathrm{e/i}}^{\mathrm{n}}\right) \wedge \hat{v}_e^w - R_{n2w}\left(\hat{\omega}_{w/e}^n + 2\hat{\omega}_{e/i}^n\right) \wedge \delta v_e^w \end{aligned} \tag{C.52}$$

Where we can denote:

- $-\tilde{f}^w \wedge d\phi = (d\phi \wedge)\hat{R}_{m2w}\tilde{f}^m$
- $\hat{v}_e^w \wedge \left(\delta\omega_{w/e}^w + 2\delta\omega_{e/i}^w\right) = R_{n2w}\left(\delta\omega_{w/e}^n + 2\delta\omega_{\mathrm{e/i}}^{\mathrm{n}}\right) \wedge \hat{v}_e^w$
- $\hat{R}_{m2w}\delta f^m = \delta f^w$

Based on these simplifications, equation (C.52) becomes:

$$\delta\dot{v}_e^w = \delta f^w - \tilde{f}^w \wedge d\phi + \delta g^w + \hat{v}_e^w \wedge \left(\delta\omega_{w/e}^w + 2\delta\omega_{e/i}^w\right) - \left(\hat{\omega}_{w/e}^w + 2\hat{\omega}_{e/i}^w\right) \wedge \delta v_e^w \tag{C.53}$$

That equation represents the final form of the INS velocity error propagation in the *w-frame*. It will be used for establishing the velocity transition matrix as explained in the following.

From [Farrel and Barth, 1998] the local gravity vector expressed in the *n-frame* depends on the latitude and altitude and, can be defined as:

$$g_n(\lambda, h) = g_n(\lambda, 0) \cdot \left(\frac{R_E}{R_E + h}\right)^2 \tag{C.54}$$

Where:

- $g_n(\lambda, 0) = g_0 \cdot \frac{\left(1+k\cdot\sin^2\lambda\right)}{\sqrt{1-e^2\cdot\sin^2\lambda}}$
- $k = \frac{b\cdot\gamma_P}{a\cdot\gamma_E} - 1 \approx 0.00193185$ is a geometrical parameter related to the reference ellipsoid.

The approximation of this model [Farrel and Barth, 1998] with a first order Taylor series expansion gives: $g_n(\lambda, h) = g_0 \cdot \left(1 - \frac{2h}{R_E}\right)$.

Thus the estimation of the local gravity vector is:

$$\hat{g} = \begin{bmatrix} 0 \\ 0 \\ g_0 \end{bmatrix} + \begin{bmatrix} 0 \\ 0 \\ -\frac{2g_0}{R_E} \end{bmatrix} \cdot \begin{bmatrix} \hat{\lambda} \\ \hat{\phi} \\ \hat{h} \end{bmatrix} + \begin{bmatrix} \xi_g \\ -\eta_g \\ o(h) \end{bmatrix} \tag{C.55}$$

And $\delta g = \begin{bmatrix} 0 \\ 0 \\ -\frac{2g_0}{R_E} \end{bmatrix} \cdot \begin{bmatrix} \lambda \\ \phi \\ h \end{bmatrix} + \begin{bmatrix} e_N \\ e_E \\ e_D \end{bmatrix}$.

$\begin{bmatrix} e_N \\ e_E \\ e_D \end{bmatrix}$ is the gravity model error. If the gravity model error is not modelled in the state vector, these errors are included in the velocity state noise vector. We will consider that case in our implementation.

Then we can define the baro-altitude dynamic matrix by:

$$F_{velo/baro} = \begin{bmatrix} 0 & 0 & 0 \\ 0 & 0 & 0 \\ 0 & 0 & -\dfrac{2g_0}{a} \end{bmatrix} \tag{C.56}$$

The computation of the rotation velocity vector error, $\delta\omega^w_{w/e} + 2\delta\omega^w_{e/i}$,, is done with the formula of the partial derivatives, as follows:

$$\delta\omega^w_{w/e} = \left[\frac{\partial\omega^w_{w/e}\left((\lambda,\phi,h),v^w_e\right)}{\partial(\lambda,\phi,h)}, \frac{\partial\omega^w_{w/e}\left((\lambda,\phi,h),v^w_e\right)}{\partial v^w_e}\right] \cdot \begin{bmatrix}\delta(\lambda,\phi,h)\\ \delta v^w_e\end{bmatrix} \tag{C.57}$$

$$\delta\omega^w_{e/i} = \left[\frac{\partial\omega^w_{e/i}\left((\lambda,\phi,h),v^w_e\right)}{\partial(\lambda,\phi,h)}, \frac{\partial\omega^w_{e/i}\left((\lambda,\phi,h),v^w_e\right)}{\partial v^w_e}\right] \cdot \begin{bmatrix}\delta(\lambda,\phi,h)\\ \delta v^w_e\end{bmatrix} \tag{C.58}$$

Using (A.3) and (A.5), and the expression of $R_{n2w} = \begin{bmatrix} \cos w & \sin w & 0 \\ -\sin w & \cos w & 0 \\ 0 & 0 & 1 \end{bmatrix}$, we can compute the rotation velocity vectors expressed in the *w-frame* coordinate system by:

$$\omega^w_{w/e} = R_{n2w}\omega^n_{w/e} = \begin{bmatrix} \dfrac{v_E\cos w}{R_N+h} - \dfrac{v_N\sin w}{R_M+h} \\ -\dfrac{v_E\sin w}{R_N+h} - \dfrac{v_N\cos w}{R_M+h} \\ 0 \end{bmatrix} \tag{C.59}$$

$$\omega^w_{e/i}\& = R_{n2w}\cdot\omega^n_{w/e} = \begin{bmatrix} \omega_{e/i}\cos\lambda\cos w \\ -\omega_{e/i}\cos\lambda\sin w \\ -\omega_{e/i}\sin\lambda \end{bmatrix} \tag{C.60}$$

And compute their partial derivatives:

$$\frac{\partial\omega^w_{w/e}}{\partial(\lambda,\phi,h)} = \begin{bmatrix} 0 & 0 & -\dfrac{v_E\cos w}{(R_N+h)^2} + \dfrac{v_N\sin w}{(R_M+h)^2} \\ 0 & 0 & \dfrac{v_E\sin w}{(R_N+h)^2} + \dfrac{v_N\cos w}{(R_M+h)^2} \\ 0 & 0 & 0 \end{bmatrix} \tag{C.61}$$

$$\begin{aligned}\frac{\partial \omega_{w/e}^{w}}{\partial v_e^w} &= \frac{\partial \omega_{w/e}^{w}}{\partial v_e^n} \cdot \frac{\partial v_e^n}{\partial v_e^w} \\ &= \begin{bmatrix} -\dfrac{\sin w}{R_M+h} & \dfrac{\cos w}{R_N+h} & 0 \\ -\dfrac{\cos w}{R_M+h} & -\dfrac{\sin w}{R_N+h} & 0 \\ 0 & 0 & 0 \end{bmatrix} \cdot \begin{bmatrix} \cos w & \sin w & 0 \\ -\sin w & \cos w & 0 \\ 0 & 0 & 1 \end{bmatrix} \\ &= \begin{bmatrix} -\dfrac{\sin w \cos w}{R_M+h} + \dfrac{\sin w \cos w}{R_N+h} & \dfrac{\sin w \sin w}{R_M+h} + \dfrac{\cos w \cos w}{R_N+h} & 0 \\ -\dfrac{\sin w \sin w}{R_M+h} - \dfrac{\cos w \cos w}{R_N+h} & \dfrac{\sin w \cos w}{R_M+h} - \dfrac{\sin w \cos w}{R_N+h} & 0 \\ 0 & 0 & 0 \end{bmatrix}\end{aligned} \tag{C.62}$$

that is to say

$$\frac{\partial \omega_{e/i}^{w}}{\partial(\lambda,\phi,h)} = \begin{bmatrix} -\omega_{e/i}\sin\lambda\cos w & 0 & 0 \\ \omega_{e/i}\sin\lambda\sin w & 0 & 0 \\ -\omega_{e/i}\cos\lambda & 0 & 0 \end{bmatrix} \tag{C.63}$$

$$\frac{\partial \omega_{e/i}^{w}}{\partial v_e^w} = [0] \tag{C.64}$$

Finally:

$$\begin{aligned}\frac{\partial \omega_{w/e}^{w}}{\partial(\theta_x,\theta_y,h)} &= \frac{\partial \omega_{w/e}^{w}}{\partial(\lambda,\phi,h)} \cdot \frac{\partial(\lambda,\phi,h)}{\partial(\theta_x,\theta_y,h)} \\ &= \begin{bmatrix} 0 & 0 & -\dfrac{V_E\cos w}{(R_N+h)^2} + \dfrac{V_N\sin w}{(R_M+h)^2} \\ 0 & 0 & -\dfrac{V_E\sin w}{(R_N+h)^2} + \dfrac{V_N\cos w}{(R_M+h)^2} \\ 0 & 0 & 0 \end{bmatrix} \cdot \begin{bmatrix} -\sin w & -\cos w & 0 \\ \dfrac{cos\, w}{\cos\lambda} & -\dfrac{\sin w}{\cos\lambda} & 0 \\ 0 & 0 & 1 \end{bmatrix} \\ &= \begin{bmatrix} 0 & 0 & -\dfrac{V_E\cos w}{(R_N+h)^2} + \dfrac{V_N\sin w}{(R_M+h)^2} \\ 0 & 0 & -\dfrac{V_E\sin w}{(R_N+h)^2} + \dfrac{V_N\cos w}{(R_M+h)^2} \\ 0 & 0 & 0 \end{bmatrix}\end{aligned} \tag{C.65}$$

$$\begin{aligned}\frac{\partial \omega_{e/i}^{w}}{\partial(\theta_x,\theta_y,h)} &= \frac{\partial \omega_{e/i}^{w}}{\partial(\lambda,\phi,h)} \cdot \frac{\partial(\lambda,\phi,h)}{\partial(\theta_x,\theta_y,h)} \\ &= \begin{bmatrix} -\omega_{e/i}\sin\lambda\cos w & 0 & 0 \\ \omega_{e/i}\sin\lambda\sin w & 0 & 0 \\ -\omega_{e/i}\cos\lambda & 0 & 0 \end{bmatrix} \cdot \begin{bmatrix} -\sin w & -\cos w & 0 \\ \dfrac{\cos w}{\cos\lambda} & -\dfrac{\sin w}{\cos\lambda} & 0 \\ 0 & 0 & 1 \end{bmatrix} \\ &= \begin{bmatrix} \omega_{e/i}\sin\lambda\cos w\sin w & \omega_{e/i}\sin\lambda\cos w\cos w & 0 \\ -\omega_{e/i}\sin\lambda\sin w\sin w & -\omega_{e/i}\sin\lambda\sin w\cos w & 0 \\ \omega_{e/i}\cos\lambda\sin w & \omega_{e/i}\cos\lambda\cos w & 0 \end{bmatrix}\end{aligned} \tag{C.66}$$

In definitive the rotation velocity error term is as follows:

$$\begin{aligned}\delta\omega^w_{w/e} + 2\delta\omega^w_{e/i} &= \left(\frac{\partial\omega^w_{w/e}}{\partial(\theta_x,\theta_y,h)} + 2\frac{\partial\omega^w_{e/i}}{\partial(\theta_x,\theta_y,h)}\right)\cdot d(\theta_x,\theta_y,h) + \left(\frac{\partial\omega^w_{w/e}}{\partial v^w_e} + 2\frac{\partial\omega^w_{e/i}}{\partial v^w_e}\right)\cdot dv^w_e \\ &= \underbrace{\begin{bmatrix} 2\omega_{e/i}\sin\lambda\cos w\sin w & 2\omega_{e/i}\sin\lambda\cos w\cos w & -\frac{V_E\cos w}{(R_N+h)^2} + \frac{V_N\sin w}{(R_M+h)^2} \\ -2\omega_{e/i}\sin\lambda\sin w\sin w & -2\omega_{e/i}\sin\lambda\sin w\cos w & \frac{V_E\sin w}{(R_N+h)^2} + \frac{V_N\cos w}{(R_M+h)^2} \\ 2\omega_{e/i}\cos\lambda\sin w & 2\omega_{e/i}\cos\lambda\cos w & 0 \end{bmatrix}}_{F_{velo/pos\ 1}} \cdot \begin{bmatrix} d\theta_x \\ d\theta_y \\ dh \end{bmatrix} \\ &+ \underbrace{\begin{bmatrix} -\frac{\sin w\cos w}{R_M+h} + \frac{\sin w\cos w}{R_N+h} & \frac{\sin w\sin w}{R_M+h} + \frac{\cos w\cos w}{R_N+h} & 0 \\ -\frac{\sin w\sin w}{R_M+h} - \frac{\cos w\cos w}{R_N+h} & \frac{\sin w\cos w}{R_M+h} - \frac{\sin w\cos w}{R_N+h} & 0 \\ 0 & 0 & 0 \end{bmatrix}}_{F_{velo/velo\ 1}} \cdot \begin{bmatrix} dV_x \\ dV_y \\ dV_z \end{bmatrix}\end{aligned} \tag{C.67}$$

And for the final term of the equation:

$$\omega^w_{w/e} + 2\omega^w_{e/i} = \begin{bmatrix} 2\omega_{e/i}\cos\lambda\cos w + \frac{V_E\cos w}{R_N+h} - \frac{V_N\sin w}{R_M+h} \\ -2\omega_{e/i}\cos\lambda\sin w - \frac{V_E\sin w}{R_N+h} - \frac{V_N\cos w}{R_M+h} \\ -2\omega_{e/i}\sin\lambda \end{bmatrix} \tag{C.68}$$

The skew symmetric matrix associated to the vector defined in (C.68) will be denoted $F_{velo/velo\ 2}$. It constitutes the second term of the matrix that relates the derivative of the velocity error to the velocity error, denoted $F_{velo/velo}$.

The velocity error transition matrix is then described by the sub-matrices detailed previously and is as follows:

$$F_{velo\ INS} = [F_{velo/pos} \quad F_{velo/velo} \quad F_{velo/att} \quad F_{velo/bg} \quad F_{velo/ba}] \tag{C.69}$$

With:

- $F_{velo/pos} = (\hat{v}^w_e \wedge)F_{velo/pos\ 1} + F_{velo/baro}$, is the position error to velocity error derivative transition matrix. $F_{velo/pos\ 1}$ and $F_{velo/baro}$ are defined respectively in (C.67) and (C.56).
- $F_{velo/velo} = (\hat{v}^w_e \wedge)F_{velo/velo\ 1} - F_{velo/velo\ 2}$ is the velocity error to velocity error derivative transition matrix. $F_{velo/velo\ 1}$ and $F_{velo/velo\ 2}$ are defined respectively in (C.67) and (C.68)

- $F_{velo/att} = \left(-\tilde{f}^w \wedge\right)$ is the attitude error to velocity error derivative transition matrix (defined thanks to equation (C.53)).
- $F_{velo/bg} = 0$ is the gyrometer measurement error to velocity error derivative transition matrix (defined thanks to equation (C.53)(C.94)).
- $F_{velo/ba} = \hat{R}_{m2w}$ is the accelerometer measurement error to velocity error derivative transition matrix (defined thanks to equation (C.94)).

C.2.4 Alignment Error Propagation Equation

The rotation matrix differential equation can be described as follows [Farrel and Barth, 1998]:

$$\dot{R}_{m2w} = R_{m2w} \cdot \Omega^m_{m/w} \tag{C.70}$$

Then its derivation leads to:

$$\delta\dot{R}_{m2w} = \delta R_{m2w}\Omega^m_{m/w} + R_{m2w}\delta\Omega^m_{m/w} \tag{C.71}$$

Reminding that,

$$R_{m2w} = (I + d\phi \wedge)\hat{R}_{m2w} \tag{C.72}$$

Or after development:

$$R_{m2w} = \hat{R}_{m2w} + (d\phi \wedge)\hat{R}_{m2w} \tag{C.73}$$

With

$$\delta R_{m2w} = (d\phi \wedge)\hat{R}_{m2w} \tag{C.74}$$

And its derivation leads to:

$$\delta\dot{R}_{m2w} = \left(d\dot{\phi} \wedge\right)\hat{R}_{m2w} + (d\phi \wedge)\hat{\dot{R}}_{m2w} \tag{C.75}$$

Identification of (C.71) and (C.75)(C.74) leads to:

$$\delta R_{m2w}\Omega^m_{m/w} + R_{m2w}\delta\Omega^m_{m/w} = \left(d\dot{\phi} \wedge\right)\hat{R}_{m2w} + (d\phi \wedge)\hat{\dot{R}}_{m2w} \tag{C.76}$$

Using (C.74) and (C.70), it can be rewritten:

$$(d\phi \wedge)\widehat{R}_{m2w}\Omega^m_{m/w} + R_{m2w}\delta\Omega^m_{m/w} = (d\dot{\phi} \wedge)\widehat{R}_{m2w} + (d\phi \wedge)\widehat{R}_{m2w}\widehat{\Omega}^m_{m/w} \tag{C.77}$$

After a reorganization:

$$(d\phi \wedge)\widehat{R}_{m2w}\left(\Omega^m_{m/w} - \widehat{\Omega}^m_{m/w}\right) + \widehat{R}_{m2w}\delta\Omega^m_{m/w} + \delta R_{m2w}\delta\Omega^m_{m/w} = (d\dot{\phi} \wedge)\widehat{R}_{m2w} \tag{C.78}$$

And a simplification:

$$(d\phi \wedge)\widehat{R}_{m2w}\delta\Omega^m_{m/w} + \widehat{R}_{m2w}\delta\Omega^m_{m/w} + \delta R_{m2w}\delta\Omega^m_{m/w} = (d\dot{\phi} \wedge)\widehat{R}_{m2w} \tag{C.79}$$

We can neglect the second order terms $(d\phi \wedge)\hat{R}_{m2w}\delta\Omega^m_{m/w}$ and $\delta R_{m2w}\delta\Omega^m_{m/w}$ and rewrite as follows:

$$(d\dot{\phi} \wedge)\widehat{R}_{m2w} = \widehat{R}_{m2w}\delta\Omega^m_{m/w} \tag{C.80}$$

Thus, we multiply both side by $\hat{R}_{w2m}$, and obtain:

$$\left(d\dot{\phi} \wedge\right) = \hat{R}_{m2w}\delta\Omega^m_{m/w}\hat{R}_{w2m} \tag{C.81}$$

That finally leads to the vector differential equation or alignment error propagation equation:

$$d\dot{\phi} = \hat{R}_{m2w}\delta\omega^m_{m/w} \tag{C.82}$$

The composition of the rotation velocity error vectors allows introducing $\delta\omega^m_{m/i}$, which is the gyrometer measurement error. Equation (C.82) is then:

$$d\dot{\phi} = \hat{R}_{w2m}\left(\delta\omega^m_{m/i} - \delta\omega^m_{w/i}\right) \tag{C.83}$$

The expression of the rotation velocity error vector $\delta\omega^m_{w/i}$ can be deduced from the expression of $\omega^m_{w/i}$. So we can write:

$$\omega^m_{w/i} = R_{w2m}\,\omega^w_{w/i} \tag{C.84}$$

Then introducing the estimation error we have:

$$\widehat{\omega}^m_{w/i} + \delta\omega^m_{w/i} = \left(\hat{R}_{w2m} + \delta R_{w2m}\right)\left(\widehat{\omega}^w_{w/i} + \delta\omega^w_{w/i}\right) \tag{C.85}$$

That, after development, this leads to:

$$\widehat{\omega}_{w/i}^{m} + \delta\omega_{w/i}^{m} = \hat{R}_{w2m}\widehat{\omega}_{w/i}^{w} + \hat{R}_{w2m}\delta\omega_{w/i}^{w} + \delta R_{w2m}\widehat{\omega}_{w/i}^{w} + \delta R_{w2m}\delta\omega_{w/i}^{w} \tag{C.86}$$

We neglect the second order term, $\delta R_{w2m}\delta\omega_{w/i}^{w}$, so as to obtain:

$$\widehat{\omega}_{w/i}^{m} + \delta\omega_{w/i}^{m} = \widehat{\omega}_{w/i}^{m} + \hat{R}_{w2m}\delta\omega_{w/i}^{w} + \delta R_{w2m}\widehat{\omega}_{w/i}^{w} \tag{C.87}$$

The first order terms verify then:

$$\delta\omega_{w/i}^{m} = \hat{R}_{w2m}\delta\omega_{w/i}^{w} + \delta R_{w2m}\widehat{\omega}_{w/i}^{w} \tag{C.88}$$

And using (C.74):

$$\delta\omega_{w/i}^{m} = \hat{R}_{w2m}\delta\omega_{w/i}^{w} + (d\phi\wedge)\hat{R}_{w2m}\widehat{\omega}_{w/i}^{w} \tag{C.89}$$

Thus, the law of inversion of the vector product leads to:

$$\delta\omega_{w/i}^{m} = \hat{R}_{w2m}\delta\omega_{w/i}^{w} - \hat{R}_{w2m}(d\phi\wedge)\widehat{\omega}_{w/i}^{w} \tag{C.90}$$

And after factorization:

$$\delta\omega_{w/i}^{m} = \hat{R}_{w2m}\left(\delta\omega_{w/i}^{w} - (d\phi\wedge)\widehat{\omega}_{w/i}^{w}\right) \tag{C.91}$$

Then, replacing the expression of $\delta\omega_{w/i}^{m}$ in (C.83), the alignment error propagation equation is given by:

$$d\dot{\phi} = \hat{R}_{m2w}\left(\delta\omega_{m/i}^{m} - \hat{R}_{w2m}\delta\omega_{w/i}^{w} + \hat{R}_{w2m}(d\phi\wedge)\widehat{\omega}_{w/i}^{w}\right) \tag{C.92}$$

And after simplification:

$$d\dot{\phi} = \hat{R}_{m2w}\delta\omega_{m/i}^{m} - \delta\omega_{w/i}^{w} + (d\phi\wedge)\widehat{\omega}_{w/i}^{w} \tag{C.93}$$

Finally, the INS alignment error propagation equation is:

$$d\dot{\phi} = -\widehat{\Omega}_{w/i}^{w}d\phi + \hat{R}_{m2w}\delta\omega_{m/i}^{m} - \delta\omega_{w/i}^{w} \tag{C.94}$$

As for the velocity equations, the computation of $\delta\omega_{w/i}^{w}$ and $\widehat{\Omega}_{w/i}^{w}$ is done from (A.3) and (A.5). Then knowing that $\omega_{w/i}^{w} = \omega_{w/e}^{w} + \omega_{e/i}^{w}$, and denoting $\Omega_{w/i}^{w}$ the corresponding skew-symmetric matrix and are as follows:

$$\omega_{w/i}^{w} = \begin{bmatrix} \omega_{e/i}\cos\lambda\cos w + \dfrac{v_E\cos w}{R_N+h} - \dfrac{v_N\sin w}{R_M+h} \\ -\omega_{e/i}\cos\lambda\sin w - \dfrac{v_E\sin w}{R_N+h} - \dfrac{v_N\cos w}{R_M+h} \\ -\omega_{e/i}\sin\lambda \end{bmatrix} \tag{C.95}$$

And the partial derivatives are as follows:

$$\begin{aligned} \delta\omega_{w/i}^{w} = & \underbrace{\begin{bmatrix} \omega_{e/i}\sin\lambda\cos w\sin w & \omega_{e/i}\sin\lambda\cos w\cos w & -\dfrac{v_E\cos\alpha}{(R_N+h)^2} + \dfrac{v_N\sin\alpha}{(R_M+h)^2} \\ -\omega_{e/i}\sin\lambda\sin w\sin w & -\omega_{e/i}\sin\lambda\sin w\cos w & +\dfrac{v_E\sin\alpha}{(R_N+h)^2} + \dfrac{v_N\cos\alpha}{(R_M+h)^2} \\ \omega_{e/i}\cos\lambda\sin w & \omega_{e/i}\cos\lambda\cos w & 0 \end{bmatrix}}_{F_{pos\,1}} \cdot \begin{bmatrix} d\theta_x \\ d\theta_y \\ dh \end{bmatrix} \\ & + \\ & \underbrace{\begin{bmatrix} -\dfrac{\sin w\cos w}{R_M+h} + \dfrac{\sin w\cos w}{R_N+h} & \dfrac{\sin w\sin w}{R_M+h} + \dfrac{\cos w\cos w}{R_N+h} & 0 \\ -\dfrac{\cos w\cos w}{R_M+h} - \dfrac{\sin w\sin w}{R_N+h} & \dfrac{\sin w\cos w}{R_M+h} - \dfrac{\sin w\cos w}{R_N+h} & 0 \\ 0 & 0 & 0 \end{bmatrix}}_{F_{velo\,1}} \cdot \begin{bmatrix} dv_x \\ dv_y \\ dv_z \end{bmatrix} \end{aligned} \tag{C.96}$$

The alignment error transition matrix F_{att} is then described as follows:

$$F_{att} = [F_{att/pos} \quad F_{att/velo} \quad F_{att/att} \quad F_{att/bg} \quad F_{att/ba}] \tag{C.97}$$

With:

- $F_{att/pos} = -F_{pos\,1}$ is the position error to attitude error derivative transition matrix. $F_{pos\,1}$ is the matrix defined in equation (C.96)
- $F_{att/velo} = -F_{velo\,1}$ is the position error to attitude error derivative transition matrix. $F_{velo\,1}$ is the matrix defined in equation (C.96)
- $F_{att/att} = \left(-\hat{\Omega}_{w/i}^{w}\right)$ is the attitude error to attitude error derivative transition matrix (defined thanks to equation (C.94)).
- $F_{att/bg} = \hat{R}_{m2w}$ is the gyrometer measurement error to attitude error derivative transition matrix (defined thanks to equation (C.94)).
- $F_{att/ba} = 0$ is the accelerometer measurement error to attitude error derivative transition matrix (defined thanks to equation (C.94)).

Appendix D: EKF Observation Functions Linearization

This Appendix details the computations to obtain the linearized observation matrix H from the observation functions introduced in 5.5.1.

First let us remind that the equations of the EKF introduced in Chapter 5:

$$\delta\dot{X}(t) = F(t) \cdot \delta X(t) + U(t) \tag{D.1}$$

$$Z(t) = H(t) \cdot \delta X(t) + V(t) \tag{D.2}$$

Where:

- δX is the error state vector, defined as: $\delta X = X - \hat{X}$ with X is the true state and $\hat{X}$ is the estimated state.
- F is the linearized propagation matrix.
- Z is the observation vector.
- H is the linearized observation matrix.
- U is the process noise vector, assumed centered, white and Gaussian.
- V is the observation noise vector, assumed centered, white and Gaussian.

As presented in Chapter 5, the linearized observation matrix H is the Jacobian of the observation function h computed around the predicted aircraft state $\hat{X}_{k|k-1}$. This predicted state is obtained after the prediction stage of the Extended Kalman Filter by compensating the inertial position, velocity and attitude of the aircraft $\hat{X}_{INS}$ with the current estimation of the inertial errors given by the error state vector $\delta\hat{X}_{k|k-1}$.

The linearized observation matrix is thus defined by:

$$H = \left.\frac{\partial h}{\partial X}\right|_{\hat{X}_{k|k-1}=\hat{X}_{INS}+\delta\hat{X}_{k|k-1}} \tag{D.3}$$

For sake of simplification in the notation, the linearization point $\hat{X}_{k|k-1} = \hat{X}_{INS} + \delta\hat{X}_{k|k-1}$ will be implied in the following.

D.1 GNSS Observation Matrix

The derivative of the GNSS observation function from satellite i (see 5.5.1.1) is given by:

$$\frac{\partial h^i_{GNSS}}{\partial X} = \begin{bmatrix} \frac{\partial \rho^i}{\partial \theta_x} & \frac{\partial \rho^i}{\partial \theta_y} & \frac{\partial \rho^i}{\partial h_B} & 0 & \cdots & 0 & \overbrace{1}^{b_H} & 0 & \overbrace{0}^{1^{st}\,meas} & \cdots & 0 & \overbrace{1}^{i^{th}\,meas} & 0 & \cdots & 0 \end{bmatrix} \tag{D.4}$$

Where b_H is the receiver clock bias.

We can then compute its components as follows:

$$\frac{\partial \rho^i}{\partial(\theta_x, \theta_y, h_B)} = \frac{\partial \rho^i}{\partial(x,y,z)} \times \frac{\partial(x,y,z)}{\partial(\lambda,\phi,h_B)} \times \frac{\partial(\lambda,\phi,h_B)}{\partial(\theta_x,\theta_y,h_B)} \tag{D.5}$$

Where (x, y, z) are the Cartesian coordinates of the receiver's antenna in the *e-frame*.

Thus, from (5.39), we have:

$$\frac{\partial \rho^i}{\partial(x,y,z)} = \begin{bmatrix} \frac{x^i - x}{\rho^i} & \frac{y^i - y}{\rho^i} & \frac{z^i - z}{\rho^i} \end{bmatrix} \tag{D.6}$$

From (A.2), we get:

$$\frac{\partial(x,y,z)}{\partial(\lambda,\phi,h_B)} = \begin{bmatrix} -(R_B + h) \cdot \sin\lambda \cdot \cos\phi & -(R_B + h) \cdot \cos\lambda \cdot \sin\phi & \cos\lambda \cdot \cos\phi \\ -(R_B + h) \cdot \sin\lambda \cdot \sin\phi & (R_B + h) \cdot \cos\lambda \cdot \cos\phi & \cos\lambda \cdot \sin\phi \\ \left((1 - e^2) \cdot R_B + h\right) \cdot \cos\lambda & 0 & \sin\lambda \end{bmatrix} \tag{D.7}$$

And from (5.14) and (5.15), we get:

$$\frac{\partial(\lambda,\phi,h_B)}{\partial(\theta_x,\theta_y,h_B)} = \begin{bmatrix} -\sin w & -\cos w & 0 \\ \frac{\cos w}{\cos\lambda} & -\frac{\sin w}{\cos\lambda} & 0 \\ 0 & 0 & 1 \end{bmatrix} \tag{D.8}$$

As illustrated in (D.4), the partial derivative of the observation function with respect to the receiver clock bias and time-correlated measurement bias are equal to one.

D.2 WSS Observation Matrix

The derivative of the WSS i observation function (see 5.5.1.2) is:

$$\frac{\partial h^i_{WSS}}{\partial X} = \begin{bmatrix} 0 & 0 & 0 & 0 & \frac{\partial h^i_{WSS}}{\partial v_x} & \frac{\partial h^i_{WSS}}{\partial v_y} & \frac{\partial h^i_{WSS}}{\partial v_z} & \frac{\partial h^i_{WSS}}{\partial \phi_x} & \frac{\partial h^i_{WSS}}{\partial \phi_y} & \frac{\partial h^i_{WSS}}{\partial \phi_z} & 0 & \ldots & 0 \end{bmatrix} \tag{D.9}$$

We can then compute its components as follows:

$$\begin{aligned}\frac{\partial h^i_{WSS}}{\partial(v_x, v_y, v_z)} &= \frac{\partial(R_{w2m} \cdot v^w_{m/e})}{\partial(v_x, v_y, v_z)} \\ &= \frac{\partial R_{w2m}}{\partial(v_x, v_y, v_z)} \cdot \hat{v}^w_{m/e} + \frac{\partial v^w_{m/e}}{\partial(v_x, v_y, v_z)} \cdot \hat{R}_{w2m}\end{aligned} \tag{D.10}$$

With:

$$\frac{\partial v^w_{m/e}}{\partial(v_x, v_y, v_z)} = 1 \tag{D.11}$$

And

$$\frac{\partial R_{w2m}}{\partial(v_x, v_y, v_z)} = 0 \tag{D.12}$$

And for the other component:

$$\begin{aligned}\frac{\partial h^i_{WSS}}{\partial(\phi_x, \phi_y, \phi_z)} &= \frac{\partial(R_{w2m} \cdot v^w_{m/e})}{\partial(\phi_x, \phi_y, \phi_z)} \\ &= \frac{\partial R_{w2m}}{\partial(\phi_x, \phi_y, \phi_z)} \cdot \hat{v}^w_{m/e} + \frac{\partial v^w_{m/e}}{\partial(\phi_x, \phi_y, \phi_z)} \cdot \hat{R}_{w2m}\end{aligned} \tag{D.13}$$

we get

$$\frac{\partial v^w_{m/e}}{\partial(\phi_x, \phi_y, \phi_z)} = 0 \tag{D.14}$$

And

$$\frac{\partial R_{w2m}}{\partial(\phi_x, \phi_y, \phi_z)} = -\hat{R}_{w2m} \tag{D.15}$$

D.3 VIDEO Observation Matrix

The derivative of the target i video observation function (see 5.5.1.3) is given by:

$$\frac{\partial h^i_{video}}{\partial X} = \begin{bmatrix} \frac{\partial h^i}{\partial \theta_x} & \frac{\partial h^i}{\partial \theta_y} & \frac{\partial h^i}{\partial h_B} & 0 & 0 & 0 & 0 & \frac{\partial h^i}{\partial \phi_x} & \frac{\partial h^i}{\partial \phi_y} & \frac{\partial h^i}{\partial \phi_z} & 0 & \cdots & 0 \end{bmatrix} \tag{D.16}$$

For sake of simplification in the notations, h_{video} will be denoted h, in the following.

Based on the law of the composition of partial derivatives, we have the following relationships for the first three elements:

$$\frac{\partial h^i}{\partial \theta_x} = \frac{\partial h^i}{\partial f_x} \cdot \frac{\partial f_x}{\partial g_x} \cdot \frac{\partial g_x}{\partial k} \cdot \left(\frac{\partial k}{\partial \lambda} \cdot \frac{\partial \lambda}{\partial \theta_x} + \frac{\partial k}{\partial \phi} \cdot \frac{\partial \phi}{\partial \theta_x} \right) + \frac{\partial h^i}{\partial f_y} \cdot \frac{\partial f_y}{\partial g_y} \cdot \left(\frac{\partial g_y}{\partial \lambda} \cdot \frac{\partial \lambda}{\partial \theta_x} + \frac{\partial g_y}{\partial \phi} \cdot \frac{\partial \phi}{\partial \theta_x} \right) \tag{D.17}$$

$$\frac{\partial h^i}{\partial \theta_y} = \frac{\partial h^i}{\partial f_x} \cdot \frac{\partial f_x}{\partial g_x} \cdot \frac{\partial g_x}{\partial k} \cdot \left(\frac{\partial k}{\partial \lambda} \cdot \frac{\partial \lambda}{\partial \theta_y} + \frac{\partial k}{\partial \phi} \cdot \frac{\partial \phi}{\partial \theta_y} \right) + \frac{\partial h^i}{\partial f_y} \cdot \frac{\partial f_y}{\partial g_y} \cdot \left(\frac{\partial g_y}{\partial \lambda} \cdot \frac{\partial \lambda}{\partial \theta_y} + \frac{\partial g_y}{\partial \phi} \cdot \frac{\partial \phi}{\partial \theta_y} \right) \tag{D.18}$$

$$\frac{\partial h^i}{\partial h_B} = \frac{\partial h^i}{\partial f_x} \cdot \frac{\partial f_x}{\partial g_x} \cdot \frac{\partial g_x}{h_B} \tag{D.19}$$

And for the next three, we have:

$$\frac{\partial h^i}{\partial \phi_x} = \frac{\partial h^i}{\partial f_x} \cdot \frac{\partial f_x}{\partial \theta} \cdot \frac{\partial \theta}{\partial \phi_x} + \frac{\partial h^i}{\partial \varphi} \cdot \frac{\partial \varphi}{\partial \phi_x} \tag{D.20}$$

$$\frac{\partial h^i}{\partial \phi_y} = \frac{\partial h^i}{\partial f_x} \cdot \frac{\partial f_x}{\partial \theta} \cdot \frac{\partial \theta}{\partial \phi_y} + \frac{\partial h^i}{\partial \varphi} \cdot \frac{\partial \varphi}{\partial \phi_y} \tag{D.21}$$

$$\frac{\partial h^i}{\partial \phi_z} = \frac{\partial h^i}{\partial f_x} \cdot \frac{\partial f_x}{\partial \theta} \cdot \frac{\partial \theta}{\partial \phi_z} + \frac{\partial h^i}{\partial f_y} \cdot \frac{\partial f_y}{\partial \psi} \cdot \frac{\partial \psi}{\partial \phi_z} \tag{D.22}$$

The dependency of h^i with respect to f_x, f_y and φ has been depicted in 5.5.1.3. Then the partial derivatives may be expressed as:

$$\frac{\partial h^i}{\partial (f_x, f_y)} = \begin{bmatrix} \cos(\varphi) & \sin(\varphi) \\ -\sin(\varphi) & \cos(\varphi) \end{bmatrix} \tag{D.23}$$

$$\frac{\partial h^i}{\partial \varphi} = \begin{bmatrix} -f_x \cdot \sin(\varphi) + f_y \cdot \cos(\varphi) \\ -f_x \cdot \cos(\varphi) - f_y \cdot \sin(\varphi) \end{bmatrix} \tag{D.24}$$

In the same way, the dependency of f_x with respect to g_x and $\tan(\theta)$ leads to the following expressions for the partial derivatives:

$$\frac{\partial f_x}{\partial g_x} = \frac{1 + \tan^2(\theta)}{(\tan(\theta) - g_x)^2} \tag{D.25}$$

$$\frac{\partial f_x}{\partial \tan(\theta)} = -\frac{1 + g_x^2}{(\tan(\theta) - g_x)^2} \tag{D.26}$$

Then by introducing the dependency with θ:

$$\frac{\partial f_x}{\partial \theta} = \frac{\partial f_x}{\partial \tan(\theta)} \cdot \frac{\partial \tan(\theta)}{\partial \theta} \tag{D.27}$$

$$\frac{\partial \tan(\theta)}{\partial \theta} = 1 + \tan^2(\theta) = \frac{1}{\cos^2(\theta)} \tag{D.28}$$

Identically, we have the following partial derivatives for f_y:

$$\frac{\partial f_y}{\partial g_y} = \frac{1 + \tan^2(\psi)}{\left(1 + \tan(\psi) \cdot g_y\right)^2} \tag{D.29}$$

$$\frac{\partial f_y}{\partial \tan(\psi)} = -\frac{1 + g_y^2}{\left(1 + \tan(\psi) \cdot g_y\right)^2} \tag{D.30}$$

And

$$\frac{\partial f_y}{\partial \psi} = \frac{\partial f_y}{\partial \tan(\psi)} \cdot \frac{\partial \tan(\psi)}{\partial \psi} \tag{D.31}$$

$$\frac{\partial \tan(\psi)}{\partial \psi} = 1 + \tan^2(\psi) = \frac{1}{\cos^2(\psi)} \tag{D.32}$$

The partial derivatives for g_x are as follows:

$$\frac{\partial g_x}{\partial k} = \frac{R_C \cdot (R_E + h_B) \cdot \cos w - R_C^2}{\left((R_E + h_B) - R_T \cdot \cos w\right)^2} \tag{D.33}$$

$$\frac{\partial g_x}{\partial h_B} = -\frac{R_T \cdot \sin w}{\left((R_E + h_B) - R_T \cdot \cos w\right)^2} \tag{D.34}$$

And for g_y, they are:

$$\frac{\partial g_y}{\partial \lambda} = -\frac{\cos\left(\frac{\Delta\lambda}{2}\right) \cdot \sin\left(\frac{\Delta\phi}{2}\right)}{2 \cdot \sin^2\left(\frac{\Delta\lambda}{2}\right)} = -\frac{g_y}{2 \cdot \tan\left(\frac{\Delta\lambda}{2}\right)} \tag{D.35}$$

$$\frac{\partial g_y}{\partial \phi} = \frac{1}{2} \cdot \frac{\cos\left(\frac{\Delta\phi}{2}\right)}{\sin\left(\frac{\Delta\lambda}{2}\right)} \tag{D.36}$$

The partial derivative of k with respect to λ and ϕ are:

$$\frac{\partial k}{\partial \lambda} = \frac{\sin(\Delta\lambda) \cdot \cos(\Delta\phi)}{\sqrt{1 - \cos^2(\Delta\lambda) \cdot \cos^2(\Delta\phi)}} = \frac{\sin(\Delta\lambda) \cdot \cos(\Delta\phi)}{\sin(k)} \tag{D.37}$$

$$\frac{\partial k}{\partial \phi} = \frac{\cos(\Delta\lambda) \cdot \sin(\Delta\phi)}{\sin(k)} \tag{D.38}$$

And finally using (5.13) and (5.15), we have:

$$\frac{\partial(\lambda, \phi)}{\partial(\theta_x, \theta_y)} = \begin{bmatrix} -\sin w & -\cos w \\ \dfrac{\cos w}{\cos \lambda} & -\dfrac{\sin w}{\cos \lambda} \end{bmatrix} \tag{D.39}$$

For the last term, we assume that:

$$\frac{\partial(\varphi, \theta, \psi)}{\partial(\phi_x, \phi_y, \phi_z)} = \begin{bmatrix} 1 & 0 & 0 \\ 0 & 1 & 0 \\ 0 & 0 & 1 \end{bmatrix} \tag{D.40}$$

The quick development of air traffic has led to the improvement of approach and landing operations by using flexible flight paths and by decreasing the minima required to perform these operations. Most of the aircraft operations are supported by the GNSS augmented with GBAS, SBAS and ABAS. SBAS or GBAS allow supporting navigation operations down to precision approaches. However, these augmentations do require an expensive network of reference receivers and real-time broadcast to the airborne user. To overcome, the ABAS system integrates on-board information provided by an INS so as to enhance the performance of the navigation system. In that scheme, INS is coupled with a GPS receiver in a GPS/baro-INS hybridization solution that is already performed on current commercial aircraft. This solution allows reaching better performance in terms of accuracy, integrity, availability and continuity than the two separated solutions. However the most stringent requirements for precision approaches or automatic landings cannot be fulfilled with the current hybridization. The main idea of this PhD study is then to extend the hybridization process by including other sensors already available on commercial aircraft or not and, to assess the performance reached by a global hybridization architecture. It aims at providing most of the navigation parameters in all operations with the required level of performance. The operations targeted by this hybridization are precision approaches, with a particular focus on CAT III precision approach and roll out on the runway. The study of video sensor has been particularly focused on in the thesis. Indeed video based navigation is a complete autonomous navigation opportunity only based on sensors that provide information from the dynamic of the vehicle and from the observation of the scenery. Moreover, from a possible compensation of any loss or degradation of a navigation system to the improvement of the navigation solution during the most critical operations, the interests of video are numerous.

Keywords : *GNSS, INS, Multi-sensor Hybridization, Video-based Navigation*

Un développement rapide et une densification du trafic aérien ont conduit à l'introduction de nouvelles opérations d'approches et d'atterrissage utilisant des trajectoires plus flexibles et des minimas plus exigeants. La plupart des opérations de navigation aérienne sont actuellement réalisées grâce au GNSS, augmenté par les systèmes GBAS, SBAS et ABAS qui permettent d'atteindre des opérations d'approches de précision (pour GBAS et SBAS). Cependant ces systèmes nécessitent la mise en place d'un réseau de station de référence relativement couteux et des diffusions constantes de messages aux utilisateurs de l'espace aérien. Afin de surmonter ces contraintes, le système ABAS intègre à bord des informations fournies par les systèmes de navigation inertielle (INS) ainsi améliorant les performances de navigation. Dans cette logique, les avions commerciaux actuels utilisent une solution de couplage des deux systèmes appelée hybridation GPS/baro-INS. Cette solution permet d'atteindre des niveaux de performance en termes de précision, intégrité, disponibilité et continuité supérieurs aux deux systèmes pris séparément. Malheureusement, les niveaux d'exigences requis par les opérations de précision ou les atterrissages automatiques ne peuvent pas encore être totalement couverts par les solutions d'hybridation actuelles. L'idée principale de cette thèse a été d'étendre le processus d'hybridation en incluant d'autres capteurs ou systèmes actuellement disponibles ou non à bord et d'évaluer les niveaux de performance atteints par cette solution de filtre d'hybridation global. L'objectif ciblé est de pouvoir fournir la plupart des paramètres de navigations pour les opérations les plus critiques avec le niveau de performance requis par les exigences OACI. Les opérations ciblées pendant l'étude étaient les approches de précision (en particulier les approches CAT III) et le roulage sur la piste. L'étude des systèmes vidéo a fait l'objet d'une attention particulière pendant la thèse. La navigation basée sur la vidéo est une solution autonome de navigation de plus en plus utilisée de nos jours axée sur des capteurs qui mesurent le mouvement du véhicule et observent l'environnement. Que cela soit pour compenser la perte ou la dégradation d'un des systèmes de navigation ou pour améliorer la solution existante, les intérêts de l'utilisation de la vidéo sont nombreux.

Mots-clés : *GNSS, INS, Hybridation Multi-capteurs, Navigation Basée sur la Vidéo*